Atomic-scale modeling of diffusion in concentrated alloys

Pamela Camilos

To cite this version:

Pamela Camilos. Atomic-scale modeling of diffusion in concentrated alloys. Materials Science [cond-mat.mtrl-sci]. Université Paris-Saclay, 2022. English. NNT : 2022UPASP125 . tel-04368956

HAL Id: tel-04368956
https://theses.hal.science/tel-04368956v1

Submitted on 2 Jan 2024

THESE DE DOCTORAT

NNT : 2022UPASP125

Atomic-scale modeling of diffusion in concentrated alloys

Modélisation à l'échelle atomique de la diffusion dans les alliages concentrés

Thèse de doctorat de l'université Paris-Saclay

École doctorale n° 564, physique en Île-de-France (PIF)
Spécialité de doctorat : Physique
Graduate School : Physique
Référent : Faculté des sciences d'Orsay

Thèse préparée dans l'unité de recherche **SRMP, Service de Recherches de Métallurgie Physique (Université Paris-Saclay, CEA)**, sous la direction de **Maylise NASTAR**, directrice de recherche du CEA, et le co-encadrement de **Thomas SCHULER**, ingénieur chercheur du CEA

Thèse soutenue à Paris-Saclay, le 22 novembre 2022, par

Pamela CAMILOS

Composition du jury

Membres du jury avec voix délibérative

Sergiy DIVINSKI Professeur, University of Münster	Président
Enrique MARTINEZ-SAEZ Professeur associé, Clemson University	Rapporteur & Examinateur
Ludovic THUINET Maître de conférences, HDR, Université de Lille, UMET	Rapporteur & Examinateur
Philippe MAUGIS Professeur, Aix-Marseille Université, IMN2P	Examinateur
Céline VARVENNE Chargée de recherche CNRS, Aix-Marseille Université, CINaM	Examinatrice

université
PARIS-SACLAY

ÉCOLE DOCTORALE
Physique en
Île-de-France (PIF)

Titre : Modélisation à l'échelle atomique de la diffusion dans les alliages concentrés

Mots clés : diffusion, coefficients de transport, alliages concentrés, interdiffusion, diffraction des rayons X, alliage FeCr

Résumé : L'objectif de cette thèse est d'étudier la diffusion dans les alliages concentrés à l'aide de modèles à l'échelle atomique. Notre travail se divise en deux grandes parties.

Dans la première étude, nous avons modélisé l'interdiffusion dans des multicouches nanométriques Fe/Cr à l'aide d'un modèle Monte Carlo cinétique à l'échelle atomique (AKMC) développé précédemment, et nous avons simulé leurs profils de diffraction de rayons X (DRX). Nous avons comparé les profils de concentration et les épaisseurs de couches aux mesures expérimentales obtenues par nos collaborateurs. Nous avons constaté que le modèle AKMC reproduit l'interdiffusion dans la région riche en Fe et aux interfaces à 500°C avec un accord satisfaisant avec les résultats expérimentaux. Les profils DRX étaient en bon accord qualitatif avec les profils expérimentaux, malgré le fait que les profils DRX expérimentaux décroient globalement plus rapidement, à 450°C et 500°C, en particulier au début du recuit. Nous avons constaté qu'une analyse des profils DRX basée sur l'interférence des rayons X nous permet d'identifier la partie de la multicouche qui affecte principalement chaque satellite DRX. En raison de l'asymétrie de diffusion, la décroissance du logarithme des intensités des satellites DRX est linéaire pendant un intervalle de temps spécifique et avec un taux de décroissance différent pourchaque satellite. Nous avons pu séparer l'évolution de la multicouche en différents régimes cinétiques, chacun attribué à l'interdiffusion dans une région spécifique de la multicouche, et extraire à partir des simulations et des expériences, des coefficients d'interdiffusion à 450°C et 500°C, et à différentes valeurs de concentration : région riche en Cr, région riche en Fe, aux interfaces, et à des concentrations proches des limites de solubilité. Les valeurs obtenues à 500°C sont en accord satisfaisant avec les valeurs calculées par une méthode d'atténuation d'ondes. Les observations expérimentales ont montré la présence de dislocations misfit ainsi qu'une possibilité de croissance partiellement cohérente des multicouches. Pour une étude plus complète, nous devons prendre en compte dans nos simulations la présence de dislocations et les propriétés élastiques de l'alliage. Cela peut en outre aider à faire le lien entre la mobilité de l'interface, les distances interplaires et l'interdiffusion.

Dans la deuxième étude, nous avons développé un modèle à l'échelle atomique pour la diffusion dans les alliages concentrés dans un cadre plus général. Nous avons étendu la reformulation de la théorie du champ moyen auto-cohérent et le code KineCluE aux alliages concentrés, et mis en œuvre une procédure d'échantillonnage pour réduire la taille de l'espace de configuration. La procédure d'échantillonnage est basée sur le remplissage des sites de l'environnement à partir d'un réservoir d'atomes en fonction de leur composition moyenne, combiné à un algorithme de pseudo temps de résidence qui privilégie les configurations les plus stables thermodynamiquement. Notre modèle introduit une façon originale d'explorer un espace de configuration connecté. Nous avons appliqué notre modèle à des alliages binaires avec différentes énergies d'ordre. Dans les alliages sans interactions, nous avons trouvé un bon accord avec les résultats de la littérature lorsque les fréquences de saut des différentes espèces atomiques sont du même ordre de grandeur. Dans les alliages où les interactions thermodynamiques sont non nulles, avec une tendance à l'ordre ou à la démixion, nous avons trouvé un bon accord avec les simulations AKMC pour les faibles valeurs absolues d'énergies d'ordre. L'implémentation actuelle de notre modèle ne peut pas être utilisée pour étudier avec précision la diffusion dans les alliages qui présentent un ordre à longue distance important, et une étude plus approfondie devra être menée pour optimiser la procédure d'échantillonnage et pour appliquer notre modèle à des alliages plus réalistes.

Title : Atomic-scale modeling of diffusion in concentrated alloys

Keywords : diffusion, transport coefficients, concentrated alloys, interdiffusion, X-ray diffraction, FeCr alloy

Abstract : The aim of this thesis is to study diffusion in concentrated alloys using atomic-scale models. Our work is divided in two main parts. In the first part, we combine Atomic Kinetic Monte Carlo (AKMC) with X-ray diffraction (XRD) to calculate concentration dependent interdiffusion coefficients, and in the second part we develop a general atomic-scale model to calculate transport coefficients in multi-component alloys.

In the first study, we modeled interdiffusion in Fe/Cr nanometric multilayers using a previously developed AKMC model and we simulated their corresponding XRD profiles. We compared the concentration profiles and layer thicknesses to experimental multilayers which were studied by our experimental collaborators. We found that the AKMC model reproduces interdiffusion in the Fe-rich region and at the interfaces at 500°C, with overall satisfactory agreement with the experimental results. The XRD profiles were in good qualitative agreement with the experimental profiles, while experimental XRD profiles exhibit an overall faster decay at 450°C and 500°C, especially at the beginning of annealing. We found that an analysis of multilayer XRD profiles based on interference of X-rays allows us to identify the part of the multilayer which affects predominantly each XRD satellite. We also found that, due to diffusion asymmetry, the decay of the logarithm of XRD satellite intensities is linear during specific time ranges of annealing, with a decay rate specific to each satellite. We were able to separate the evolution of the multilayer into different kinetic regimes, each attributed to diffusion in a specific region of the multilayer, and extract, from the simulations and the experiments, interdiffusion coefficients at 450°C and 500°C, and at different concentration ranges : in high Cr concentration, in high Fe concentration, at the interfaces, and at concentrations close to the solubility limits. We found that the values obtained at 500°C are in satisfactory agreement with values calculated using a wave attenuation method. Experimental observations showed the presence of misfit dislocations and a possible partial coherency growth of the multilayers. For a more complete study, we need to take into account in our simulations the presence of dislocations and the elastic properties of the alloy. This can further help make the link between interface mobility, interplanar spacing and interdiffusion.

In the second study, we developed an atomic-scale model for diffusion in concentrated alloys in a more general framework. We extended the Self-Consistent Mean-Field theory reformulation and the KineCluE code to concentrated alloys, and implemented a sampling procedure to reduce the size of the configuration space. The sampling procedure is based on filling environment sites from a reservoir of atoms based on their average composition, combined with a pseudo residence-time algorithm which favors the most thermodynamically stable configurations. Our model introduces an original way to explore a connected configuration space. We applied our model to binary alloys with different ordering energies. In non-interacting alloys, we found good agreement with the literature results when the jump frequencies of the different atomic species were within the same order of magnitude. In interacting alloys with both ordering and clustering tendencies, we found good agreement with AKMC simulations for low values of ordering energies. The current implementation of our model cannot be used to study accurately diffusion in alloys with long-range order and a further study needs to be conducted to optimize the sampling scheme and apply the model to more realistic alloys.

Acknowledgment

I would like to thank all the jury members for accepting to judge this work. I thank them for all the time and attention they put into reading the manuscript, attending the defense, and asking relevant and interesting questions. I thank you for the conversations we shared during and after the defense, and I hope to meet you again in conferences or collaborative works.

I thank my thesis supervisors Maylise Nastar and Thomas Schuler for giving me the chance to work on this project and for their continuous assistance during these 3 and a half years. I also thank you for taking the time to read and correct my manuscript, and I hope I learned to no longer use “consist on”. I thank Maylise for her scientific enthusiasm and passion, for sharing her knowledge and experience with me, for encouraging me to tackle different topics in parallel and for making me a better researcher. I thank Thomas for his daily availability, guidance, advice and patience. Thank you for all the diffusion, coding and personal talks we shared and which were always enlightening to me on many levels. Thank you for introducing me to KineCluE, for trusting me to code in it and for all the scientific insight you brought to coding. I am looking forward to meeting you again within a scientific format, or while running a marathon.

I would like to also thank the many collaborators for the insightful meetings we had which helped shape this project and advance my work and understanding. I especially thank Frédéric Soisson for his constant availability and helpfulness regarding the Monte Carlo model and for sharing all his knowledge on FeCr alloys with me. I also thank the experimentalists Maxime Vallet, Estelle Meslin, Gladice Magnifouet-Tchinda and Véronique Pierron-Bohnes, who helped me understand interdiffusion from an experimental point of view and who provided the interdiffusion project with important scientific results.

I thank the permanents and non-permanents of the lab for the environment they provided and for making the coffee/tea breaks much more entertaining. I would like to especially mention and thank: my office-mate Xixi for being my first friend in the lab and for accompanying me during these three years; Orane for all the interesting conversations we had; Liangzhao for making my first year and last month enjoyable with football and gaming talks; Anruo for her big heart and all the game development talks (thank you for the Switch games!); and last but not least Daphné, for the support, for the morning coffee breaks and for stealing Xixi’s office to keep me company whenever I worked late. I am also very grateful for the friendships I made with Yunho, Quentin, Savneet, Thomas B., Guilhem, and many others.

Outside of the lab, my friends Alan and Remik provided a great deal of support and huge source of fun, laughter and craziness throughout these three years. From passing by my place for 10 minutes to check up on me, to taking quick walks in the park, you have made writing the manuscript much more enjoyable.

I cannot but thank my life partner Charbel for being the greatest support, both at the office and outside of it. He was there during all the personal and professional ups and downs of the PhD, and he made it much easier for me to go through this journey. I am very grateful for the delicious and heart-warming meals he cooked for me and which always managed to lift my mood up.

Lastly, I thank my parents, without whom I wouldn't have been able to follow an education path I was passionate about nor come to France and pursue this PhD. I thank my sister for being a great support throughout all these years, for being kindhearted and caring when I needed it the most, and for always welcoming me in Metz to enjoy its coffee shops.

This project has received funding from the *European Union's Horizon 2020 research and innovation programme* under grant agreement No *800945* — NUMERICS — H2020-MSCA-COFUND-2017

Contents

3 Extending SCMF-d and KineCluE to concentrated alloys 144

Introduction

Materials have long been made and used by humans. The progress of materials science contributed to the progress of humanity, all the while progressing with it. While metals were first used in their raw form, it was then discovered that alloys consisting of a mixture of specific elements could have better overall properties (tensile strength, resistance to fracture, oxidation, etc...). Alloys also evolved from dilute alloys formed by adding a small concentration of elements to a main metal element, to concentrated alloys formed by mixing equal or near-equal proportions of two or more elements. Nowadays, in most applications, metals are no longer used in their pure forms, as we can optimize the composition of alloys with respect to the application of interest. There is a great variety of alloys and alloy properties, and they are used in different applications based on the macroscopic constraints and conditions of the application (temperature, pressure, volume, etc...). While properties of alloys used to be optimized based on macroscopic experimentation and observation, it is now known that macroscopic properties result from the microscopic state of the alloy. Atoms are constantly moving in a material at finite temperature, which leads to atomic jumps and a redistribution of atoms. These changes at the atomic scale affect the macroscopic properties of materials. For example, a local chromium depletion in stainless steel can make the depleted area more sensitive to corrosion. Additionally, alloys have different phases at different temperatures and compositions, and each phase can have different properties. Diffusion properties allow the evolution of the material from one phase to another and explain how and at which rate alloy properties change. Materials used in nuclear applications are faced with potential variations of temperature, stress and irradiation, which may change the initial phase of the material and hence its properties. Even at steady-state, it is enough to modify the microstructure [1] and phase diagrams [2]. This can weaken the material and render it unsuitable for the application for which it was originally designed. These variations result from irradiation which creates defects in the material [3,4]. These defects (mainly vacancies and interstitials and their clusters) diffuse in the alloy and can lead to segregation or precipitation [5–7]. The concentration of these defects depends on the irradiation conditions, temperature and microstructure. Next generation reactors and fusion reactors under development, such as ITER (International Thermonuclear Experimental Reactor), will operate up to higher irradiation doses, hence producing more defects in the material. This will require materials that are even more withstanding to irradiation damage and temperature. To ensure the mechanical strength of these reactor materials throughout their operation time, it is necessary to understand and to be able to predict the consequences of atomic diffusion in them.

FeCr based alloys (FeCrC, FeNiCr, etc...) are currently largely used in the nuclear and energy industry, and constitute good candidates for next generation nuclear and fusion reactors. The reason is that FeCr alloys are characterized by good mechanical properties and resistance to corrosion, and, more importantly, they have good resistance to void swelling under irradiation. However, FeCr alloys decompose at certain temperatures and concentrations, and this new phase can increase the alloy's chances of corrosion and weaken it [8,9]. There is however little data on the diffusion properties of the FeCr alloy at high Cr concentrations and at low temperatures [9], which further limits its applications to certain domains of temperature and concentration.

High-entropy alloys (HEA) show great potential in many applications, including nuclear applications, as they can have high corrosion and irradiation resistance as well as high strength. These alloys are a special class of multi-component alloys which have five or more elements mixed in comparable proportions. HEA triggered huge scientific interest recently [10, 11], but diffusion is still not well understood in this type of alloys. Until recently, diffusion in HEA was thought to be sluggish [12], which made them of great technological interest for high-temperature applications. However, there now exists a convincing amount of scientific works which show that diffusion in HEA is not necessarily sluggish, and that it can rather be accelerated in some cases by increasing the number of elements [10]. Therefore, before being able to use HEA in environments with high irradiation and temperature, we need to properly understand their diffusion properties. These properties are not unique in this class of alloys, and a study is required for each type of HEA alloy as a function of the alloying elements and the defects mediating diffusion. Hence the interest of developing a general theoretical model which can be applied to all, or at least a big portion, of these alloys, and to a variety of potential experimental conditions.

Diffusion is quantified by the Onsager matrix (also known as the transport coefficients matrix) which links the macroscopic flux to the driving forces of diffusion [13, 14]. Diffusion experiments do not allow us to calculate the full Onsager matrix except in very special experimental conditions [15]. Theoretical methods have therefore been developed. Numerical approaches, like Monte Carlo and Molecular Dynamics simulations, are a powerful tool to study diffusion. For instance, a Monte Carlo model has been developed to study the decomposition in FeCr alloys, and takes into account the effect of temperature, magnetism and concentration on the atomic-scale diffusion properties [8, 9, 16]. Nevertheless, as we shall explain in detail, numerical approaches have their limitations when it comes to calculating transport coefficients, and analytical models have been developed to try and fill the remaining gaps. Models have been developed at different scales and by relying on a variety of alloy properties. It is known that geometrical and kinetic correlations arise in diffusing systems due to interactions between the different chemical species, and because diffusion is mediated by a small number of defects [17]. It was found that calculating kinetic correlations analytically is a difficult task. While many efforts have been made to study diffusion in alloys, analytical models have been able to predict the full Onsager matrix mainly in dilute alloys [18]. In concentrated alloys, kinetic correlations become more challenging to calculate as the number of components increases. Progress has been mainly made in the case of a non-interacting concentrated alloy [19, 20] and in simple and specific cases of concentrated alloys [21, 22]. In both cases, models have been mostly applied in the case of a binary alloy. The need for a general model which predicts the full Onsager matrix in any concentrated alloy is still present.

The aim of this thesis is to tackle this problem specifically in the case of a FeCr alloy, by relying on Monte Carlo simulations and X-ray diffraction profiles, and from a more general theoretical point of view, by studying the atomic diffusion in a multicomponent alloy. Monte Carlo simulations allow us to work on a specific alloy and compare with experimental works, which provides a macroscopic vision of diffusion. A general theory allows us, on the other hand, to work on a greater variety of applications, but it comes with challenging technical difficulties and relies on Monte Carlo simulations to test the validity of its hypotheses and approximations.

In the first chapter, we present a detailed bibliographical study on the experimental, numerical and theoretical works that have been done so far to study diffusion in alloys in general, and in concentrated alloys in particular. We discuss in detail interdiffusion experiments and how they can be combined with other experimental and theoretical methods in order to obtain interdiffusion coefficients. We show the strength and limitations of Monte Carlo simulations in calculating transport coefficients, and why the problem of diffusion has been mostly solved in the case of dilute alloys, but not in the general case of concentrated alloys. We finally present a detailed summary of the models that have been developed for concentrated alloys, and compare them based on their approximations, their limitations and the range of applications in which they can be used.

In the second chapter, we study interdiffusion in Fe/Cr nanometric multilayers, and present a general method which combines Atomic Kinetic Monte Carlo simulations and X-ray diffraction profiles to calculate interdiffusion coefficients. Multilayers provide a workaround to performing experiments in reasonable time while at relatively low temperatures [23, 24], which allows us to compare our simulation works with the experimental results obtained by our collaborating teams (Gladice Magnifouet, Véronique Pierron-Bohnes, Maxime Vallet, and Estelle Meslin). We present a previously developed analytical model to otain a concentration independent interdiffusion coefficient from X-ray diffraction profiles [25, 26]. Developing a model based on a concentration dependent interdiffusion coefficient is a highly challenging task, and potentially impossible to solve in the general case. Instead, we show how a concentration independent model, combined with a proper analysis of the X-ray diffraction profile, enables us to calculate interdiffusion coefficients which depend on concentration. We apply this methodology to both the simulated and experimental multilayer X-ray diffraction profiles, and we show that our calculated interdiffusion coefficients are in good agreement with each other and with literature values calculated using a wave-attenuation method.

In the third chapter, we expand our scope of work and develop a new atomic-scale model to study diffusion in concentrated alloys. We present a previously developed theory [22] and code (KineCluE) which have automated the calculation of transport coefficients [18] in the case of dilute alloys. We show how we extend the theoretical framework of this model to apply it to the case of concentrated alloys, as well as its implementation in the KineCluE code. Our model consists in studying diffusing species and a local environment around them in a precise and exact way, and on using an original formulation of a mean-field approximation far from the diffusion species. We apply our model to the case of non-interacting and interacting binary alloys with both ordering and clustering tendencies. Our results are in good agreement with the literature results, especially for low absolute values of ordering energies and when the different atomic jump frequencies are not too different. We show that alloys in which long-range order is important require the treatment of larger environments around diffusing species, which increases the size of the configuration space that we need to study. Computational memory limitations require us to sample the configuration space to reduce the size of the system. We present our sampling scheme and analyze the sampled concentration and probability distributions, as well as the accuracy of the sampling in the case of a non-interacting alloy. We then discuss the remaining open-questions regarding how to perform an accurate and efficient sampling before it can be applied to more realistic alloys.

Chapter 1

Bibliographical study on diffusion in alloys

1.1 Introduction to chapter 1

The concept of diffusion flux was first introduced in 1807 by Fourier while studying heat transfer in metals [27]. Since then, flux became a fundamental concept to describe any transport phenomena. The flux represents the rate at which some physical quantity crosses a plane of unit area per unit time. The nature of the physical quantity depends on the transport phenomena that is being studied, and can represent a variety of things going from particles and atoms to pedestrians and cars (Table 1.1). For Fourier it was heat, while for Fick it was matter transport [28]. To study matter transport, i.e. diffusion, in alloys, we are interested in the flux of the different atomic species that constitute the alloy, including point defects which are usually the diffusion mediators. The driving force for diffusion is the chemical potential gradients of atomic species. Onsager's thermodynamics of irreversible processes [13, 14] established the phenomenological laws that relate the flux and the driving forces through transport coefficients and what is known as the Onsager matrix. Random walk theories have also been established to study diffusion as a consequence of successive atom jumps. The difficulty in studying diffusion generally lies in calculating kinetic correlations which arise because atoms interact with each other and because diffusion is usually mediated by a limited number of point defects which deviates diffusion from a completely random walk.

The Onsager matrix is hard to determine experimentally in solids. Some diffusion experiments allow for the calculation of the full transport matrix only in specific cases. Diffusion experiments are also usually only feasible at high temperatures in order to observe and measure the phenomena of interest in a reasonable amount of time. Transport coefficients are not necessarily linear in temperature and we cannot always extrapolate their values to low temperatures from high temperature experiments. Numerical methods, especially Monte Carlo simulations, are a powerful tool to study diffusion [8, 16, 29–37]. They are versatile in structure, jump mechanisms, concentration and temperature. However, Monte Carlo simulations do not allow us to study unstable systems and can present numerical errors and kinetic trapping, especially when calculating the off-diagonal terms of the matrix. Several analytical models have been developed to overcome these problems.

In dilute alloys, which are composed of one main chemical element and a small number of impurities, analytical models already exist and allow for the computation of the full Onsager matrix. Le Claire and Lidiard's n-jump frequency models and their generalization [38–41] are famous examples to study impurity diffusion. Trinkle's Onsager code [42] and Schuler's KineCluE code [18] are other examples which allow the computation of transport coefficients in an automated way for a variety of crystal structures, point defects and jump mechanisms. Concentrated alloys on the other hand, are composed of at least two elements that are present in relatively high concentrations (i.e. concentrations above 1%). The reason why models developed for dilute alloys cannot be used in the case of concentrated alloys is because the medium around diffusing species becomes chemically heterogeneous and the set of different jump frequencies becomes a lot bigger. Since thermodynamic interactions and jump mechanisms are usually influenced by the surroundings, this heterogeneity increases the number of different interactions and jumps in the alloy. This further introduces kinetic correlations that are usually hard to calculate. Currently, models have mainly been developed to study diffusion in non-interacting concentrated alloys. These belong to a class of Random Alloy (RA) models [19, 20, 36, 43–45] which cannot be applied to the more general case of interacting alloys. The Path Probability Method (PPM) [21, 46, 47] and the Self-Consistent Mean-Field (SCMF) theory [22, 48–50] were developed to study diffusion in an interacting concentrated alloy, with both theories taking into account short-range order and computing the full Onsager matrix.

In this chapter, we try to summarize some of the most important breakthroughs in the concepts and theory of diffusion. In Sec. 1.2, we present the phenomenological law of Onsager and treat some special cases of it, such as Fick's laws of diffusion. We also try to summarize the most commonly used diffusion coefficients and show in which case each one is used. In Sec. 1.3, we present some of the most important diffusion experiments and show their limitations in computing the full Onsager matrix in the general case. In Sec. 1.4, we discuss the main differences between different statistical ensembles which are needed for a theoretical macroscopic description of diffusion. Section 1.5 discusses the basics of Monte Carlo simulations and how they can be used to calculate transport coefficients. In Sec. 1.6, we present the problematic of analytically calculating kinetic correlations, how it can be done in the case of a dilute alloy, and the theoretical challenges it generates in concentrated alloys. We lastly present, in Sec. 1.7, the analytical models developed to study diffusion in non-interacting (RA) and interacting (PPM and SCMF) concentrated alloys. We will also present the strengths, applicability and limitations of each of these methods, and try to compare them among each other.

1.2 Phenomenological laws of diffusion

1.2.1 Onsager's diffusion laws

A system subjected to some driving forces $\vec{\mathcal{F}}_j$ is driven to a non-equilibrium state. As a consequence, a net flux $\vec{J}^i$ of a quantity i is established to cancel these forces out, until the system reaches a steady state in which the net flux and the driving forces become zero. Note that this final state is not necessarily the same as the equilibrium state. This is true if the driving force is not maintained. In the framework of thermodynamics of irreversible processes (TIP), the driving force is maintained constant and therefore the steady-state has a non-zero flux. It is assumed that, when driving forces are sufficiently small, the system is in a steady-state state that is close enough to the equilibrium state so that the fluxes are linearly proportional to the driving forces. It can be shown that the proportionality coefficients are equilibrium properties that are independent of the driving forces [51]. The net flux vector of i can therefore be written as

$$\vec{J^i} = -\sum_j L_{ij} \vec{\mathcal{F}_j}, \tag{1.1}$$

where the L_{ij} coefficients are the transport coefficients, also known as the Onsager coefficients. Note that, when the driving force vanishes, the flux also becomes null. The nature of the i (subsequently $\vec{J^i}$) and $\vec{\mathcal{F}_j}$ quantities depends on the transport phenomena that is being studied, as shown in Table 1.1.

phenomena	i	driving force $\vec{\mathcal{F}_i}$
chemical diffusion	atoms	chemical potential gradient
fluid flow	liquid	pressure gradient
heat conduction	heat	temperature gradient
electrical conduction	charge	electric field
pedestrian flow	pedestrians	self-driving force

Table 1.1: Examples of matter transport phenomena and their associated matter and driving force.

In the rest of the manuscript, we will be exclusively interested in diffusion in alloys which requires the study of the net flux of atomic species β as a consequence of the chemical potential gradients $\vec{\nabla}\mu_\alpha$ of all species α present in the system, such that the flux equation (Eq. 1.1) becomes

$$\vec{J^\beta} = -\sum_\alpha L_{\beta\alpha} \frac{\vec{\nabla}\mu_\alpha}{k_B T}, \tag{1.2}$$

where k_B is the Boltzmann constant, and T is the temperature. Note that the transport coefficients form a square matrix with diagonal coefficients $L_{\beta\beta}$ and off-diagonal coefficients $L_{\beta\alpha}$. A diagonal coefficient relates the flux of a species to the driving force that originates from the same species. The off-diagonal coefficient relates the flux of a species to the driving forces originating from other species and shows the existence of a kinetic flux coupling, such that a species diffuses under the influence of other species. As a consequence of the second principle of thermodynamics, the Onsager matrix is a positive definite matrix, and therefore

$$L_{\alpha\alpha} \geq 0 \qquad \text{and} \qquad L_{\alpha\alpha}L_{\beta\beta} - L_{\alpha\beta}^2 \geq 0. \tag{1.3}$$

Onsager further proved in 1931 [13, 14], through his reciprocal relations, that the transport matrix is symmetric, except in cases where time-reversal is not symmetric, leading to

$$L_{\alpha\beta} = L_{\beta\alpha}. \tag{1.4}$$

In chemical diffusion, detailed balance at the microscopic scale entails that the probability of the system being in a state n and transitioning into a state m is equal to the probability of being in state m and transitioning into state n. Time reversal is symmetric when detailed balance is verified, and is not symmetric otherwise, like in the case of diffusion under irradiation with forced relocations of atoms [52]. The importance of this relation lies in the fact that, for a matrix of size N, we only need to determine $N\left(N+1\right)/2$ independent coefficients.

1.2.2 Special cases of the Onsager equation

In the general case, the challenge is to calculate the full transport coefficient matrix. There are many special cases of the Onsager equation, each associated with a different type of diffusion coefficient. In some of these cases, there exist experimental and/or theoretical tools to determine the transport or diffusion coefficients. In this section, we will summarize some of the most important cases along with commonly used diffusion coefficients.

1.2.2.1 Chemical diffusion coefficient

Onsager's law can be re-written as a function of the concentration gradients. The chemical potential can generally be expressed as a function of concentration through the relation

$$\mu_\alpha = \mu_\alpha^{ref} + k_B T \ln \gamma_\alpha C_\alpha, \tag{1.5}$$

where μ_α^{ref} is a reference chemical potential for species α, γ_α is the activity coefficient and C_α is the volume concentration of species α. Note that the chemical potential has to always be calculated with respect to a reference, and hence the need for μ_α^{ref}. The activity coefficient quantifies the deviation from an ideal solid solution in which there are no interactions, such that $\gamma_\alpha = 1$ when interactions can be neglected (e.g. random alloys). The chemical potential gradient can then be calculated as

$$\begin{aligned} \frac{\vec{\nabla}\mu_\alpha}{k_B T} &= \vec{\nabla}\ln\gamma_\alpha + \vec{\nabla}\ln C_\alpha & (1.6)\\ &= \frac{1}{C_\alpha}\left(1 + \frac{d\ln\gamma_\alpha}{d\ln C_\alpha}\right)\vec{\nabla}C_\alpha & (1.7)\\ &= \frac{1}{C_\alpha}\Phi_\alpha\vec{\nabla}C_\alpha, & (1.8)\end{aligned}$$

where $\Phi_\alpha = 1 + d\ln\gamma_\alpha / d\ln C_\alpha$ is the thermodynamic factor of species α. The flux of β can hence be written as a function of the concentration gradients

$$\vec{J^\beta} = -\sum_\alpha \frac{L_{\beta\alpha}}{C_\alpha}\Phi_\alpha\vec{\nabla}C_\alpha. \tag{1.9}$$

If we consider that there is no cross-diffusion then all non-diagonal transport coefficients are null and the flux of β becomes proportional to the concentration gradient of β

$$\vec{J^\beta} = -\frac{L_{\beta\beta}}{C_\beta}\Phi_\beta\vec{\nabla}C_\beta. \tag{1.10}$$

This is known as Fick's first law of diffusion [28], in which the flux of a species depends only on its own concentration gradient and is not affected by the presence of other species

$$\vec{J^\beta} = -D_\beta^c\vec{\nabla}C_\beta. \tag{1.11}$$

The proportionality constant D^c_β is known as the **chemical diffusion coefficient** of β and is identified using Eq. 1.10 as

$$D^c_\beta = -\frac{L_{\beta\beta}}{C_\beta}\Phi_\beta. \tag{1.12}$$

Note that the chemical diffusion coefficient has to include the effect of the interactions between atoms. Fick's law is a special case of Onsager's law and is applicable when there is no cross-diffusion. One of the most important questions is whether or not the off-diagonal coefficients are small enough to be neglected, which would greatly simplify the problem by using Fick's law. On one hand, it is easier to measure concentration gradients than chemical potential gradients, and on the other hand, there are fewer parameters to calculate; for N species, there are N diffusion coefficients in comparison with $N(N+1)/2$ transport coefficients. This is why Fick's law is often used experimentally. However, in many cases, cross-diffusion coefficients are important and cannot be neglected. Experiments done by Darken (Sec. 1.3.3) and Anthony (Sec. 1.3.4) showed that the flux of a species is not necessarily null when its concentration gradient is. The off-diagonal transport coefficients cannot be neglected when there is vacancy drag effect (which happens when the vacancy and solute diffuse in the same direction, entailing that the vacancy drags the solute with it) and therefore Fick's law cannot be used when studying cases like non-equilibrium interfacial segregations [53]. Several studies have also showed that diffusion in nanoscale binary systems does not always follow Fick's law [54,55]. Percolation phenomena as well cannot be correctly studied if kinetic couplings are ignored. Therefore, one of the most important questions to answer when studying diffusion, is whether or not the cross terms are small enough to neglected, since removing them would greatly simplify the problem. In the general case, these terms cannot be neglected.

1.2.2.2 Tracer diffusion coefficient

In the case of a dilute alloy in which there are no interactions between atoms ($\Phi_\alpha = 1$) and no flux coupling, for a species A, the flux expression 1.9 reduces to a special case of Fick's first law of diffusion

$$\vec{J}^A = -\frac{L_{AA}}{C_A}\vec{\nabla}C_A, \tag{1.13}$$

with

$$D^*_A = \frac{L_{AA}}{C_A}, \tag{1.14}$$

known as the **tracer diffusion coefficient**. The tracer diffusion coefficient is also known as the **self-diffusion coefficient** when A is an isotope in a homogeneous A matrix (often labeled A^*), and as the **impurity diffusion coefficient** when A is a solute found in a very low concentration in a homogeneous B matrix. In both cases, the tracer diffusion coefficient can be measured experimentally as a function of the tracer concentration gradient, as is shown in Sec. 1.3.1.

1.2.2.3 Interdiffusion in a binary alloy

We can consider the case of a binary alloy AB in which we can assume either diffusion via direct exchange between A and B atoms, either diffusion via point defects (for example vacancies) such that the concentrations of point defects is too low with respect to the concentration of A and B. In these two cases, we can write $C_A + C_B \simeq C_{at}$, where C_{at} is the total number of atoms per unit volume, and $\vec{\nabla} C_A = -\vec{\nabla} C_B$. This leads to the thermodynamic factors of the two species being equal $\Phi_A = \Phi_B = \Phi_{AB}$. The flux of species A can be calculated as a function of its concentration gradient, even if we take into account the off-diagonal term in the 2×2 Onsager matrix

$$\begin{aligned}
\vec{J}^A &= -\frac{L_{AA}}{C_A}\Phi_A \vec{\nabla} C_A - \frac{L_{AB}}{C_B}\Phi_B \vec{\nabla} C_B \\
&= -\frac{L_{AA}}{C_A}\Phi_{AB}\left(1 - \frac{C_A L_{AB}}{C_B L_{AA}}\right)\vec{\nabla} C_A \\
&= -D_A^c\left(1 - \frac{C_A L_{AB}}{C_B L_{AA}}\right)\vec{\nabla} C_A \\
&= -D_A^I \vec{\nabla} C_A. \qquad (1.15)
\end{aligned}$$

The proportionality factor

$$D_A^I = D_A^c\left(1 - \frac{C_A L_{AB}}{C_B L_{AA}}\right), \qquad (1.16)$$

is known as the **intrinsic diffusion coefficient**. Note that this is not equivalent to using Fick's law because the cross-diffusion coefficient L_{AB} is not necessarily null, even though the equation has the same form as Fick's equation. The only approximation done here with respect to Onsager's general law is considering $C_A + C_B \simeq C_{at}$. The intrinsic diffusion coefficient of species B can be written by analogy in the same way

$$\vec{J}^B = -D_B^I \vec{\nabla} C_B, \qquad (1.17)$$

with

$$D_B^I = D_B^c\left(1 - \frac{C_B L_{AB}}{C_A L_{BB}}\right). \qquad (1.18)$$

Each intrinsic diffusion coefficient quantifies the diffusion of one species. When interdiffusion is mediated by vacancies, atomic planes move at Kirkendall's velocity and the flux of species A and B observed in the reference frame of the laboratory can be written as a function of one coefficient, $\tilde{D}_{AB}$, such that

$$\vec{J}^A_{lab} = -\tilde{D}_{AB}\vec{\nabla} C_A \quad \text{and} \quad \vec{J}^B_{lab} = -\tilde{D}_{AB}\vec{\nabla} C_B, \qquad (1.19)$$

where

$$\tilde{D}_{AB} = X_A D_B^I + X_B D_A^I, \qquad (1.20)$$

is known as the **interdiffusion coefficient** and quantifies the intermixing of both species. Here, $X_\alpha = C_\alpha / C_{at}$ is the atomic fraction of species α. Kirkendall's experiment and the derivation of the interdiffusion coefficient are explained in detail in the experimental section (Sec. 1.3.2). There are several ways to calculate the interdiffusion coefficient from an experimental or simulated concentration profile, like the Boltzmann-Matano construction [56, 57], the Sauer-Freise analysis [58], and den Broeder's method [59]. This is further discussed in Sec. 1.3.2.

1.3 Diffusion experiments

To quantify diffusion, it is necessary to calculate the transport coefficients or the diffusion coefficients. Experiments have long been the best available tool to better understand diffusion and to measure diffusion properties. Different types of diffusion experiments have been proposed to calculate the previously defined diffusion coefficients. It is not always easy to reconcile theory and experiment due to difficulties that may arise experimentally to apply theoretical approximations and assumptions. In general in an experiment, one can impose, measure and control a concentration gradient and not a chemical potential gradient. Therefore, diffusion experiments are usually done by forcing on the system a concentration gradient and observing its response to it. Fluxes need to be expressed as a function of concentration gradients, and the diffusion coefficients that are measured are those of Eq. 1.11. Additionally, diffusion at room temperature is slow and one would need to run an experiment for an unreasonably long time before observing the evolution of the system. To overcome this difficulty, experiments are usually performed at high temperatures or in nanometric materials. We will highlight in this section some of the most important experimental breakthroughs in diffusion. We will present tracer diffusion experiments which allow the calculation of diffusion properties related to a single atom, and interdiffusion experiments which allow the measurement of interdiffusion coefficients and correlation factors of collective atoms. We will also talk about Anthony's experiment which presents the ideal conditions to calculate the full Onsager matrix experimentally.

1.3.1 Tracer diffusion experiments

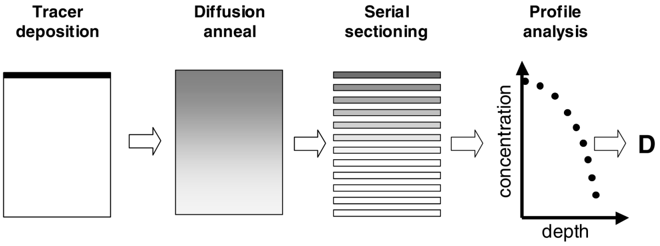

Figure 1.1: Main steps of a tracer diffusion experiment. Image taken from [17].

Self-diffusion, followed by impurity diffusion, is the easiest type of diffusion to study both theoretically and experimentally. In tracer diffusion experiments, Fick's equations can be used (Eq. 1.11) which requires only the knowledge of a concentration gradient. The assumptions made require a small enough amount of the tracer species to diffuse in a chemically homogeneous matrix of A (it can also be a matrix of AB, ABC, etc...) such that the presence of the tracer does not interact with the bulk matrix. In a self-diffusion experiment, an isotope of A labeled as A^* is introduced, such that isotope atoms are either stable and distinguished by their mass, either unstable and distinguished by their radioactivity. In impurity diffusion, a very small amount of a different species B is introduced and distinguished by its different chemical nature. Let us assume the more general case of a tracer B in a homogeneous A matrix. One of the most fundamental laws of diffusion is the continuity equation, also known as the mass conservation law,

$$\frac{\partial C_B\left(\vec{r}, t\right)}{\partial t} + \vec{\nabla} \vec{J}^B = 0, \tag{1.21}$$

where $C_B\left(\vec{r}, t\right)$ is the local concentration of species B at position $\vec{r}$ and time t. Combining the continuity equation with Fick's first law of diffusion gives

$$\frac{\partial C_B\left(\vec{r}, t\right)}{\partial t} = \vec{\nabla}\left(D_B \vec{\nabla} C_B\left(\vec{r}, t\right)\right). \tag{1.22}$$

In such a chemically homogeneous system, and if $\vec{\nabla} C_B$ is not too high, one can assume that the diffusion coefficient is homogeneous in space, and we obtain an equation known as Fick's second law of diffusion

$$\frac{\partial C_B\left(\vec{r}, t\right)}{\partial t} = D_B \Delta C_B\left(\vec{r}, t\right). \tag{1.23}$$

Note that here, Δ represents the Laplacien operator. Therefore, the diffusion coefficient is the proportionality constant that links the time evolution of the concentration field to its second derivative with respect to space. The solution to such equation in a semi-infinite system (tracer deposited on the surface) has the Gaussian form

$$C_B\left(\vec{r}, t\right) = \frac{C_b^S}{d\sqrt{\pi}} \exp\left(-\frac{\vec{r}^2}{2d^2}\right), \tag{1.24}$$

where C_B^S is the initial number of B atoms per unit surface, d is the diffusion distance of an atom B, whose diffusion coefficient is D_B, during time t

$$d = \sqrt{2D_B t}. \tag{1.25}$$

In such Gaussian distribution, the distance $2d$ represents the standard deviation and is equal to the distribution's full width at half maximum. Calculating D_B requires then the knowledge of the evolution of the concentration profile with the diffusion distance. The experimental procedure (Fig. 1.1) is conceptually simple and consists in depositing a very thin layer of tracer atoms on the surface of a homogeneous sample (semi-infinite system), followed by an isothermal annealing during a time t so that tracer atoms diffuse into the volume. The sample is then sectioned into layers parallel to the surface of deposition and the tracer concentration in each sample is calculated using an experimental technique adapted to the type of isotopes used. This allows us to construct the concentration-depth profile and calculate from it the diffusion coefficient using Eq. 1.25 as

$$D_B = \frac{d^2}{2t}. \tag{1.26}$$

Therefore, tracer diffusion experiments allow the calculation of tracer (self-diffusion and impurity) diffusion coefficients and correlation factors that are related to a single tracer atom.

1.3.2 Interdiffusion experiments

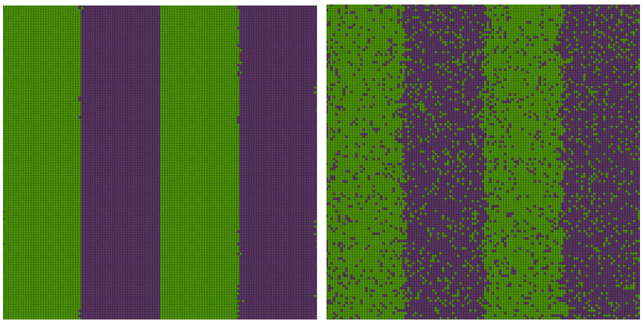

Figure 1.2: Example of the distribution of atoms in a multilayer before (left) and after (right) annealing. Image simulated using Atomic Kinetic Monte Carlo.

Interdiffusion experiments consist in studying diffusion between different atomic layers, for example between a layer containing A atoms and a layer containing B atoms, by studying the time evolution of the different concentration profiles (Fig. 1.2). Nowadays, interdiffusion experiments are done either at high temperatures, or in nanometric multilayers [60]. The most famous interdiffusion experiment is the one done by Kirkendall in 1939 during his thesis, and published later in 1942 [61,62], and which lead him to prove that diffusion is mediated by vacancies, at a time when direct exchange and ring mechanism were thought to be the only diffusion mechanisms. In his experiment, Kirkendall introduced inert markers at an interface between copper and brass (CuZn alloy) and observed that these markers (i.e. the interface), which were expected to stay immobile, shifted positions during the experiment (Fig. 1.3). This is a consequence of the difference in intrinsic diffusion coefficients of A and B that must be compensated by the presence of a third species in the system, the vacancy. Few years later in 1948, Darken [63] established the theoretical framework to describe what is known as the Kirkendall effect.

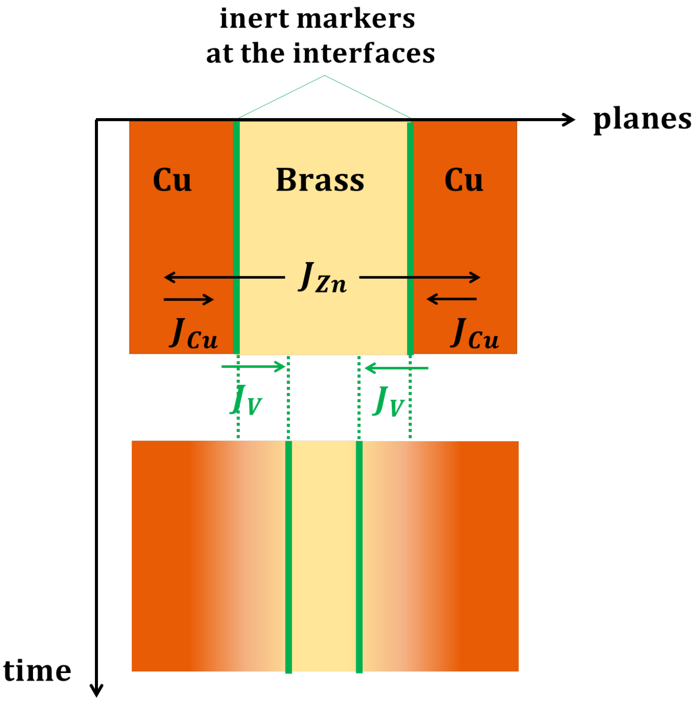

Figure 1.3: Schematic representation of Kirkendall's interdiffusion experiment. After annealing, a flux of vacancies towards the brass layer compensates for the difference in Zn and Cu fluxes, which leads to the disappearance of atomic planes in the brass-rich layer and as a consequence to the interface shift towards the brass layer.

A net flux of vacancies compensates for the difference in atomic fluxes

$$\vec{J}^V = -\left(\vec{J}^A + \vec{J}^B\right). \tag{1.27}$$

Since vacancies are always at their equilibrium concentration, there is creation and elimination of vacancies at different parts of the crystal which means that some atomic sites, and eventually atomic planes, disappear and appear at different places. The consequent movement of atomic planes is assimilated to Kirkendall's velocity $\vec{v}_K$ and is directly linked to the flux of vacancies through the moving planes. The previously determined flux expressions of A and B as a function of the intrinsic diffusion coefficients (Eq. 1.15 and Eq. 1.17) are intrinsic fluxes that do not take into consideration this movement of planes, and are therefore calculated relative to the moving lattice planes. If we were to calculate the flux of A in the frame of reference of an observer in the laboratory, it is simply a function of $\vec{J}^A$ and the velocity of the planes with respect to the laboratory, which is $\vec{v}_K$

$$\vec{J}^A_{lab} = \vec{J}^A + \vec{v}_K C_A. \tag{1.28}$$

Kirkendall's velocity is directly linked to the flux of vacancies observed in the reference frame of the laboratory

$$\vec{v}_K = \frac{\vec{J}^V_{lab}}{C_{sites}}, \tag{1.29}$$

where C_{sites} is the total number of sites per unit volume. Since the vacancy concentration is considered too low with respect to the sites concentration, Kirkendall's velocity becomes a function of $\vec{J}^V$

$$\vec{v}_K = \frac{\vec{J}^V}{C_{sites}} + \vec{v}_K \frac{C_V}{C_{sites}} \simeq \frac{\vec{J}^V}{C_{sites}}. \tag{1.30}$$

Combining this equation with Eq. 1.27, Eq. 1.15, and Eq. 1.17, $\vec{v}^K$ can be expressed as a function of the intrinsic diffusion coefficients and the concentration gradient of one of the two species

$$\vec{v}_K = \frac{1}{C_{sites}} \left(D_A^I - D_B^I\right) \vec{\nabla} C_A. \tag{1.31}$$

The flux vector of A in the laboratory can be written as a function of the A concentration gradient by replacing $\vec{v}_K$ and $\vec{J}^A$ with their expressions in Eq. 1.28

$$\vec{J}^A_{lab} = -\left(X_A D_B^I + X_B D_A^I\right) \vec{\nabla} C_A, \tag{1.32}$$

where $X_\alpha = C_\alpha / C_{sites}$ is the atomic fraction of species α. The flux of B in the frame of reference of the laboratory can be written by analogy as

$$\vec{J}^B_{lab} = -\left(X_A D_B^I + X_B D_A^I\right) \vec{\nabla} C_B. \tag{1.33}$$

The fluxes of both A and B species are proportional to their corresponding species concentration gradient, and can both be written as a function of the same proportionality constant $\tilde{D}_{AB}$ such that

$$\vec{J}^A_{lab} = -\tilde{D}_{AB} \vec{\nabla} C_A \quad \text{and} \quad \vec{J}^B_{lab} = -\tilde{D}_{AB} \vec{\nabla} C_B, \tag{1.34}$$

with

$$\tilde{D}_{AB} = X_A D_B^I + X_B D_A^I, \tag{1.35}$$

known as the interdiffusion coefficient. Note that we find a Fickian law with effective diffusion coefficients. The interdiffusion coefficient is the same for both species and it describes the behavior of intermixing of both species. Note that the fluxes of A and B in the reference frame of the laboratory are equal in magnitude but are in opposite directions. The interdiffusion coefficient can also be written explicitly as a function of concentrations, transport coefficients and the common thermodynamic factor

$$\tilde{D}_{AB} = \left(\frac{C_A^2 L_{AA} + C_B^2 L_{BB} - 2 C_A C_B L_{AB}}{C_A C_B} \right) \Phi_{AB}. \tag{1.36}$$

Note that in this case, the thermodynamic factor can be expressed as a function of the second-order derivative of the free energy G,

$$\Phi_{AB} = \frac{C_A C_B}{k_B T C_{at}} \frac{d^2 G}{d C_A^2} = \frac{C_A C_B}{k_B T C_{at}} \frac{d^2 G}{d C_B^2}, \tag{1.37}$$

where C_{at} is the atomic concentration. Since the second order derivative of G depends on its curvature, the thermodynamic factor can be negative, leading to negative intrinsic diffusion coefficients and a negative interdiffusion coefficient. The interdiffusion coefficient can be measured in several parts of the multilayers as a function of the local concentration, using for example the Boltzmann-Matano [56,57], the Sauer-Freise [58], or the den Broeder [59] method. One needs to make sure that the volume is constant and that the local concentration gradient is small enough to consider a constant local concentration where the interdiffusion coefficient is being measured. From the evolution of the interdiffusion coefficient with respect to concentration (Eq. 1.35) and from Kirkendall's velocity measured from the marker's velocity (Eq. 1.31), the intrinsic diffusion coefficients can be obtained. Therefore, an interdiffusion experiment allows the calculation of the concentration dependent interdiffusion coefficient that describes the behavior of intermixing of both species, and the concentration dependent intrinsic diffusion coefficients that describe the diffusion of each species separately in a homogeneous solid solution. Because of its simplicity, this approach is widely used to calculate interdiffusion and intrinsic diffusion coefficients. However, from the intrinsic diffusion coefficients we can only measure a linear combination of the $L_{\alpha\beta}$ coefficients and not the full Onsager matrix. Anthony's experiment (next paragraph) showed that in some alloys one can obtain a third equation which allows us to calculate all transport coefficients.

Over the past years, there has been great interest in studying interdiffusion in nanometric multilayers, because their small size is a workaround to performing diffusion experiments at low temperature in reasonable times [60]. Multilayers are additionally characterized by an interface mobility and an X-ray diffraction profile with satellites around the main Bragg peak due to composition modulations. Calculating interdiffusion coefficients from interface mobility and X-ray diffraction patterns [55,60,64–66]. Since the shift in position of the interface is directly related to the asymmetry in fluxes (as explained in this section), several models are being developed to calculate interdiffusion coefficients based on the observable interface shift [55, 64–67]. On the other hand, X-ray diffraction profiles are sensitive to the composition and lattice parameter profiles, which change during interdiffusion. The intensity of XRD satellite peaks decreases with annealing [60] and this decay is directly related to interdiffusion. Interdiffusion, multilayer compositions, X-ray diffraction profiles and interface mobility are closely linked. Therefore, interdiffusion experiments can be combined with other experimental and theoretical tools for a better understanding of the link between the atomic scale and the macroscopic scale, and the calculation of interdiffusion coefficients. In Chapter 2, we will discuss the theory of simulating X-ray diffraction profiles of multilayers and the challenges that arise to make the link between the interdiffusion coefficients and the measurable concentration profile and satellite intensities.

1.3.3 Darken's experiment

In 1941, Darken conducted an interdiffusion experiment in a bilayer of a ternary FeCSi alloy, such that the concentration in silicon and iron is different in the two layers and the concentration in carbon is the same in both. After annealing, Darken observed that the C concentration decreased in the Si-rich layer and increased in the other layer. This experiment is a simple and clear proof that the flux of a species is not necessarily null if its concentration gradient is null (Fick's laws of diffusion, Eq. 1.11), and that the true driving force of diffusion is a chemical potential gradient (the general laws of Onsager, Eq. 1.2) that arises not only from a concentration gradient but also from the thermodynamic interactions between the different species. In the general case, Fick's laws are not sufficient and flux couplings cannot be neglected.

1.3.4 Anthony's experiment

Anthony's experiment provides an experimental way to measure the full Onsager matrix. The conditions of this particular diffusion experiment make it possible to obtain, in addition to the two equations obtained in a regular interdiffusion experiment, an equation which relates all atomic transport coefficients, and therefore allow the calculation of all transport coefficients of a binary alloy. In 1970, Anthony observed in a alumina based alloy the segregation of impurities in vacancy sinks, and was able to measure the ratio of impurity flux to vacancy flux (AlCu [68], AlZn [69]). The experiment consists in slowly quenching a dilute aluminum based alloy (AB) from a temperature close to its melting temperature to room temperature. This slow process of cooling down increases the concentration of vacancies in the alloy and forces them to diffuse to the surface to get eliminated there. However, alumina forms an oxide layer on the surface and prevents the elimination of vacancies, and therefore, vacancies precipitate at the surface in the form of cavities. The solutes B are either depleted or enriched near these cavities, depending on whether the vacancy drags B atoms with it (drag effect) or if they diffuse in opposite directions. This is known as the inverse Kirkendall effect since in this case it is the induced vacancy flux which affects the diffusion of A and B. The ratio of vacancy flux to B flux is calculated by measuring the ratio of the volume of the cavities to the volume of the B atoms near the cavities and by assuming fluxes are proportional to $\nabla\mu_V$ only. A new equation linking the transport coefficients is obtained since the flux ratio is

$$\frac{\vec{J}_B}{\vec{J}_V} = \frac{L_{AB} + L_{BB}}{L_{AA} + 2L_{AB} + L_{BB}}. \tag{1.38}$$

Combining this equation with the equations previously obtained in the interdiffusion experiment, one can calculate all three transport coefficients L_{AA}, L_{AB} and L_{BB}, necessary for a full description of diffusion in a binary alloy. This experiment is of great importance because it provides the missing equation to calculate the full Onsager matrix experimentally. The alloys used by Anthony is his experiment were aluminum alloys AlX (X=Zn, Mg, Cd, Si, Ge), copper alloys CuX (X=Zn, Mn, Ag, In) and gold alloys AgX (X=Zn, Cu), and his experiment could not be reproduced with other alloys as no voids were observed at the oxide/substrate interface because of the low concentration of vacancy precipitation at the surfaces.

1.3.5 Limitations

The modern era of technology and computation marked the switch from experimentally assisted theories, to computationally assisted experiments. Previously, theories were being developed mainly to explain the scientific phenomena observed in experiments, while nowadays, modeling and simulation are essential to guide researchers in their choice of experiments and setups. When it comes to studying diffusion, at low temperatures species diffuse rather slowly. As a consequence, in order to observe interesting phenomena, experiments need to be performed in very small systems or for an unreasonable period of time and for a considerable amount of resources. Therefore, experiments do not allow us to observe nor predict the long-term consequences of atoms diffusing in big systems at low temperatures. They are usually limited to either the range of high temperatures, or to small dimensional systems like nanometric multilayers [60]. To extrapolate high temperature results to low temperatures is a quick assumption that does not take into account that diffusion properties - such as the diffusion coefficient - do not necessarily have an Arrhenius evolution as a function of temperature, nor that the different phases of an alloy can have different properties at different temperatures and that diffusion mechanisms with other activation energies can be activated at high temperature (see Fig. 1.4). Therefore, we cannot always extrapolate the results of high temperature experiments to low temperatures. A solution would be to instead study diffusion in nanometric systems, however such systems can have very different behavior from the bulk material due to their very small size [70]. Attempts to accelerate diffusion lead to studying diffusion under irradiation, however this usually leads to the production of additional defects which involves additional fluxes and flux couplings that need to be taken into account. One of the main limitations is therefore that diffusion properties are not necessarily linear in temperature, concentration or size. Experimental setups can be cumbersome in light of the different samples, temperatures and conditions that need to be tested, all while controlling sample pollution and contamination issues. Besides all this, in the general case, the main reason diffusion experiments are insufficient is that they do not allow us to measure the full Onsager matrix in solids. Anthony's experiment is a special case in which we can, and only in such systems can we measure enough diffusion coefficients to compute the full Onsager matrix. For all these reasons, and thanks to the progress of *ab initio* methods and pseudo-potentials that can provide accurate atomic-scale data, scientists in this field have started to rely greatly on numerical and analytical methods. Numerical approaches include most importantly Monte Carlo simulations (Section 1.5) and Molecular Dynamics, that can simulate diffusion within a bigger range of temperature in a more reasonable time and can compute the full Onsager matrix in many more cases. Analytical models (Sections 1.6 and 1.7) have been developed with the aim to give further insight on the problem and to express the Onsager coefficients as a function of measurable quantities. While numerical methods have their own limitations, analytical approaches are challenging, especially when studying diffusion in concentrated alloys. The next sections will focus on the most important advancements made in modeling and simulation of diffusion in alloys.

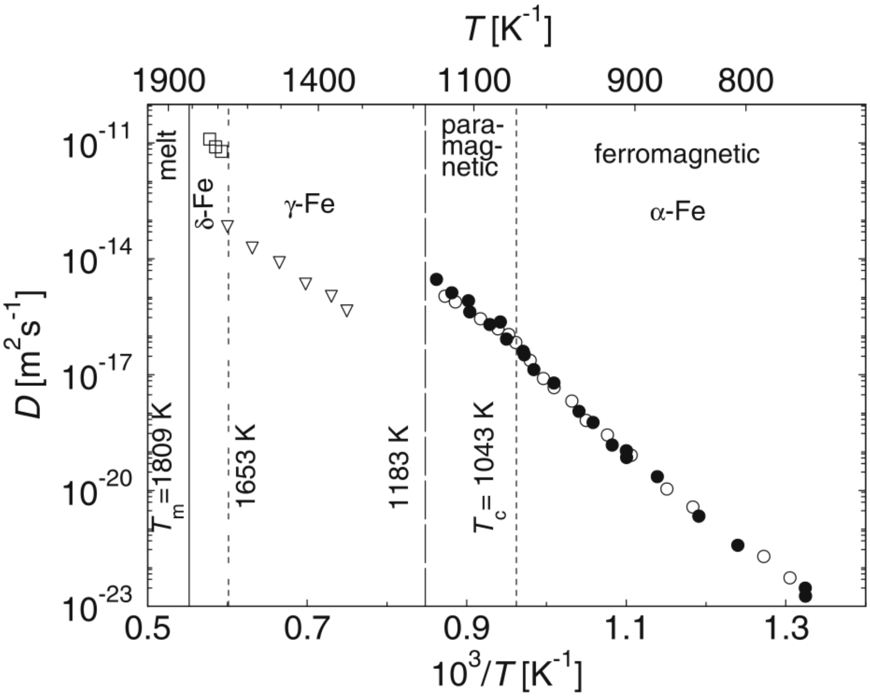

Figure 1.4: Self-diffusion coefficient as a function of temperature in the $\alpha-$, $\gamma-$ and $\delta-$phases of Fe, measured experimentally: full circles [71]; open circles [72]; triangles [73]; squares [74]. This image was taken from [17].

1.4 Statistical ensembles

While we are usually interested in the macroscopic state and evolution of a system, to each macroscopic state corresponds in fact several microscopic states in which the system can be. The probability that the system is in a specific microscopic state is not the same for all states, and a macroscopic property is the average of this property over all microscopic states weighted by their probabilities. Statistical physics provides the mathematical framework to quantify the macroscopic behavior of a system. Each system is described by a statistical ensemble, and the type of this ensemble depends on the macroscopic constraints. The three most important ensembles are the microcanonical ensemble (MCE), the canonical ensemble (CE) and the grand canonical ensemble (GCE). In each ensemble, variables are either fixed or can vary, however the ensemble can always be quantified by a probability distribution over the microscopic states. Throughout this manuscript, we will be working with canonical and grand-canonical ensembles, depending on the constraints of the system under study. It is therefore practical to define a general probability distribution which can be applied to any statistical ensemble. We define the generalized energy E_n of a microscopic state n of the system, and we write the probability distribution of n as a function of E_n,

$$P_n = \frac{1}{Z} \exp\left(-\frac{E_n}{k_B T}\right), \tag{1.39}$$

where k_B is the Boltzmann constant, T is the temperature, and Z is the partition function of the corresponding system which guarantees the normalization of the probability distribution

$$Z = \sum_n \exp\left(-\frac{E_n}{k_B T}\right). \tag{1.40}$$

Equations 1.39 and 1.40 are valid for micro-canonical, canonical and grand-canonical ensembles, and it is the definition of the generalized energy which differs from one ensemble to the other.

An MCE is isolated and cannot exchange energy or particles with its environment. The total energy and number of particles are fixed, and the generalized energy is independent of the state of the system and is always null

$$E_n|_{MCE} = 0. \tag{1.41}$$

Note that all microstates have equal probabilities. A CE represents a closed system in contact with a thermostat at fixed temperature, and cannot exchange particles with its environment. This means that the temperature and number of particles are fixed, while the energy can vary in the microstates. The generalized energy is equal to the internal energy H_n,

$$E_n|_{CE} = H_n. \tag{1.42}$$

A GCE represents an open system which can exchange energy and particles with its environment. The chemical potential is fixed, while the energy and number of atoms can vary between the microstates. The generalized energy is a function of the internal energy and the chemical potential of species

$$E_n|_{GCE} = H_n - \sum_\alpha N_n^\alpha \mu_\alpha, \tag{1.43}$$

where N_n^α is the number of atoms of species α in n, and μ_α is the chemical potential of species α. The GCE partition function can be expressed as a function of the CE partition function, by grouping together all microstates that have the same number of atoms

$$Z|_{GCE} = \sum_n \exp\left(-\frac{H_n - \sum_\alpha N_n^\alpha \mu_\alpha}{k_B T}\right) \tag{1.44}$$

$$= \sum_{\{N^\alpha\}} \exp\left(\frac{\sum_\alpha N^\alpha \mu_\alpha}{k_B T}\right) \sum_{n:N_n^\alpha=\{N^\alpha\}} \exp\left(-\frac{H_n}{k_B T}\right) \tag{1.45}$$

$$= \sum_{\{N^\alpha\}} \exp\left(\frac{\sum_\alpha N^\alpha \mu_\alpha}{k_B T}\right) Z|_{CE}^{\{N^\alpha\}}. \tag{1.46}$$

Here, the sum over $\{N^\alpha\}$ is a sum over specific combinations of number of atoms α, and $Z|_{CE}^{\{N^\alpha\}}$ is the canonical partition function at fixed number of atoms equal to $\{N^\alpha\}$. In this manuscript, we will use a CE to study systems in which the number of atoms is the same in all states of the system, and a GCE when the number of atoms can fluctuate.

In each ensemble, many relationships exist between the different thermodynamic quantities. For the sake of brevity, we will only mention here the ones which will be used in this manuscript. Each ensemble is characterized by a thermodynamic potential energy which describes the state of the system. The partition functions can be written as a function of these thermodynamic potentials. In the canonical ensemble, the thermodynamic potential is the free energy F,

$$Z|_{CE} = \sum_n \exp\left(-\frac{H_n}{k_B T}\right) = \exp\left(-\frac{F}{k_B T}\right). \tag{1.47}$$

If in addition to the CE constraints (fixed N and T), the pressure is also fixed in the system (i.e. in an isobaric ensemble), the canonical partition function can instead be written as a function of the Gibbs free energy G,

$$Z|_{CE} = \exp\left(-\frac{G}{k_B T}\right), \tag{1.48}$$

where $G = \sum_\alpha N^\alpha \mu_\alpha$. In the GCE, the grand potential $\mathcal{A}$ is the thermodynamic potential and the partition function can be written as

$$Z|_{GCE} = \sum_n \exp\left(-\frac{H_n - \sum_\alpha N_n^\alpha \mu_\alpha}{k_B T}\right) = \exp\left(-\frac{\mathcal{A}}{k_B T}\right), \tag{1.49}$$

where $\mathcal{A} = -PV$, is a function of the pressure and volume of the system.

1.5 Monte Carlo simulations of diffusion in alloys

1.5.1 Basis of the method

Monte Carlo is a stochastic modeling tool that has been widely used in materials science in general and in studying diffusion in alloys in particular [8,16,29–37]. The probabilistic method consists in studying the discrete time evolution of a system towards its equilibrium state through a series of consecutive jumps or exchanges. It relies on the principle of ergodicity and on detailed balance[1] to ensure that all states of the system can be explored and that the equilibrium state is reached by the end of the simulation. The system can however be trapped in some local minima instead. In general, the total number of possible configurations of a system is too big for all of them to be found, and rather a connected sample of the most probable configurations is explored (importance sampling).

From an initial configuration of the system, a connected trajectory is created through successive jumps that occur based on a specific jump frequency model and stochastic algorithm. These two parameters determine if a jump (a state transition of the system) is chosen or not by comparing its success probability to a randomly generated number. The accuracy of the Monte Carlo relies mainly on the sophistication of the implemented jump model and its ability to properly describe the behavior of the real alloy. Monte Carlo simulations can be a very powerful tool when the thermodynamic properties and jump mechanisms are determined accurately (experimentally and/or using *ab initio* methods) and implemented properly in the

simulation. An optimal choice of the stochastic algorithm based on the problem at hand ensures that the simulation is not stuck in a local equilibrium state and

---

[1] In some cases, such as when there are radiation-induced ballistic jumps, atomic exchanges which do not satisfy the detailed balance are simulated instead.

that it converges to the correct global equilibrium state, with the least number of jumps.

Simulations can be done in the canonical or grand canonical ensemble, while they are mostly done in the canonical ensemble because it is easier to simulate a fixed number of atoms of each species. The probability distribution of a configuration n is equal to its equilibrium probability

$$P_n^0 = \frac{1}{Z} \exp\left(-\frac{E_n}{k_B T}\right), \tag{1.50}$$

where E_n is the energy of configuration n which includes thermodynamic interactions, and Z is the partition function. The system evolves according to the master equation

$$\frac{dP_n}{dt} = \sum_m \left(P_m W_{mn} - P_n W_{nm}\right), \tag{1.51}$$

where W_{nm} is the jump frequency which transitions the system from configuration n to configuration m. The master equation shows that the time evolution of the probability of being in a configuration is equal to the probability of transitioning to it (from another configuration) minus the probability of transitioning out of it (to another configuration). At equilibrium, these two latter probabilities are equal and the global detailed balance is verified

$$\sum_m P_m^0 W_{mn} = P_n^0 \sum_m W_{nm}. \tag{1.52}$$

When a jump and its reverse jump have the same probability of occurring, this is described by the microscopic detailed balance equation

$$P_n^0 W_{nm} = P_m^0 W_{mn}. \tag{1.53}$$

This jump frequency from n to m is calculated using transition state theory (TST) [75] as

$$W_{nm} = \Gamma_{nm} \exp\left(-\frac{\Delta E_{nm}}{k_B T}\right), \tag{1.54}$$

where Γ_{nm} is the attempt frequency (assumed equal to Γ_{mn}), and k_B and T are the usual Boltzmann constant and temperature respectively (Fig. 1.5). The exponential part of the jump frequency corresponds to the transition probability

$$w_{nm} = \exp\left(-\frac{\Delta E_{nm}}{k_B T}\right), \tag{1.55}$$

and the energy ΔE_{nm} is calculated based on the energetic model that was implemented. The transition probabilities between two configurations have to respect detailed balance (Eq. 1.52) to ensure that the system reaches a stationary state after a sufficient number of jumps (dP_n/dt in Eq. 1.51 becomes null). The necessary number of jumps required to reach convergence is not trivial to determine and usually depends on the system and on the size of the Monte Carlo box (usually of the order of a 10^6). In general, the simulation results are averaged by dividing it in several observations which are called Monte Carlo blocks and calculating the properties of interest in each block. In each block, a total number of jump attempts N_s is made such that at each time-step i one jump is attempted and either accepted or refused. The choice of the jump depends on the implemented algorithm (we will present in Sec. 1.5.2 two of the most widely used algorithms, the Metropolis algorithm [76] and the time residence algorithm [77]). The number of Monte Carlo blocks is usually of the order of 10^6 blocks, while the number of attempt jumps depends on the number of species and is usually at least 100 per atom that can potentially jump to ensure convergence. This becomes harder to guarantee when the different jump frequencies are very different, say 4 orders of magnitude different. This makes it particularly difficult to ensure a good statistics to calculate off-diagonal transport coefficients in highly correlated systems. In the theoretical limit of percolation phenomena for example, when the different jump frequencies ratio in a binary alloy is infinite (in practice above 10^4), it is hard to accurately calculate the correlation factor of species [33, 36]. Usually, the more correlated diffusion is, the longer are the trajectories that need to be considered, and the harder it is to ensure convergence.

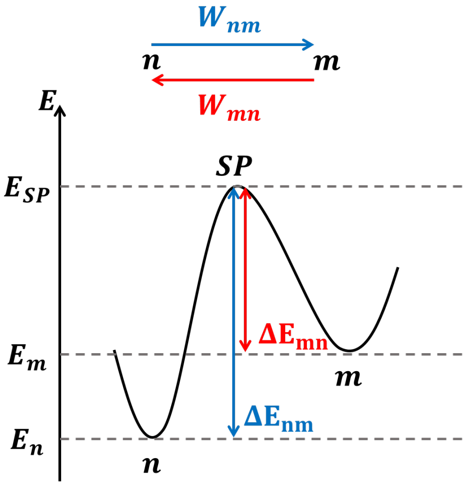

Figure 1.5: Schematic representation of the system's transition probability between states n and m. Here, the migration barrier for a jump from n to m is $\Delta E_{nm} = E_{SP} - E_n$, and its corresponding jump frequency is $W_{nm} = \Gamma_{nm} \exp\left(-\Delta E_{nm}/\left(k_B T\right)\right)$, where E_{SP} is the energy of the saddle-point configuration, and E_n is the energy of configuration n. Note that, in the general case, $\Delta E_{nm} \neq \Delta E_{mn}$ and $W_{nm} \neq W_{mn}$.

1.5.2 Algorithms

1.5.2.1 Metropolis algorithm

The Metropolis algorithm [76] is based on picking one accessible configuration at each time-step and deciding whether or not the system transitions to it by comparing its transition probability to a random probability. Sampling of the configurations is based on their thermodynamic weight and, in theory, the sampled configuration space will be mostly formed of the most stable configurations. It is based on a rejection versus acceptance algorithm and physical Monte Carlo time increases constantly at each time-step.

1. Start with an initial configuration;
2. Find the set of all N_m configurations $\{m_k; k \in [1, N_m]\}$ that are accessible from the current configuration n based on the implemented jump model;

3. Pick a random number $r \in [0, N_m]$ and pick the corresponding configuration m_r;
4. Calculate the transition probabilityw_{nm_r} (Eq. 1.55 with $\Delta E_{nm} = E_m - E_n$);
   (a) If $w_{nm_r} \geq 1$: the system transitions to configuration m_r;
   (b) If $w_{nm_r} < 1$: pick a random probability $P \in [0, 1[$, and:
      i. if $w_{nm_r} \geq P$: the system transitions to configuration m_r;
      ii. if $w_{nm_r} < P$: the system stays in configuration n;
5. Increment Monte Carlo time by a constant Monte Carlo time-step δt;
6. Go back to step 2.

Step 4 ensures that the system always transitions to more or equally stable configurations (corresponding to $\Delta E_{nm} \leq 0$), and transitions to a less stable configuration only if its transition probability is greater than a random transition probability, which means if its corresponding transition energy is lower than a randomly chosen transition energy (the random energy being $-k_B T \ln(P)$). Therefore, the algorithm explores mostly thermodynamically stable configurations, and occasionally less stable configurations.

1.5.2.2 Residence-time algorithm

The residence-time algorithm [77] is based on picking one accessible configuration at each time-step based on the transition probability to it compared to the transition probabilities to other accessible configurations. Sampling of the configurations is based on their transition rate and, in theory, the sampled configuration space will be mostly formed of the most stable configurations[2]. It is based on an acceptance algorithm and physical Monte Carlo time does not increase in a constant manner at each time-step.

1. Start with an initial configuration;
2. Find the set of all N_m configurations $\{m_k;\ k \in [1, N_m]\}$ that are accessible from the current configuration n based on the implemented jump model;
3. Calculate the set of all transition frequencies $\{W_{nm_k};\ k \in [1, N_m]\}$ (Eq. 1.54 with $\Delta E_{nm} = E_{SP} - E_n$);
4. Pick a random probability $P \in [0, 1[$;
5. Form a list of all transition frequencies (Fig. 1.6) and pick the r-th transition which satisfies
$$\sum_{k=1}^{r-1} W_{nm_k} < P \sum_{k=1}^{N_m} W_{nm_k} \leq \sum_{k=1}^{r} W_{nm_k}; \tag{1.56}$$
6. The system transitions to configuration m_r;
7. Increment Monte Carlo time by the average residence time $\delta t_n = 1/\sum_{k=1}^{N_m} W_{nm_k}$;

---

[2] In fact, it is most probable trajectories, i.e. trajectories in which the saddle-point configurations have the lowest energies, which are sampled. There is usually a correlation between configuration energies and saddle-point energies (at least qualitatively), and in most cases it is indeed the most stable configurations which are sampled.

8. Go back to step 2;

Step 5 ensures that the system transitions to a configuration with a probability proportional to its transition probability. Step 7 ensures that the transition time depends on the configuration that the system is in and on the total transition probability out of it. Therefore, the more stable a configuration is, the longer it should take to transition out of it, and the physical Monte Carlo time is adjusted accordingly without making the actual computational time longer. Therefore, trajectories are built mostly according to the highest transition probabilities, and occasionally according to lower transition probabilities, and transition time is adjusted according to the stability of configurations.

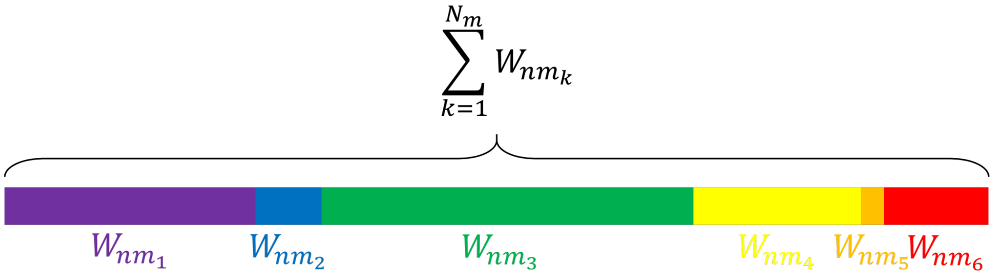

Figure 1.6: Scheme that shows how the residence-time algorithm works in the case of 6 possible transitions from a configuration n. Transition frequencies are stacked in a line such that the length of a probability is proportional to its value W_{nm_k}. A point is randomly chosen along the line and the code transitions to configuration m_k which corresponds to the W_{nm_k} on which the random point falls. This guarantees that the probability of transitioning to a configuration is proportional to its value.

1.5.2.3 Choice of algorithm

The advantage of using the Metropolis algorithm is that at each time-step only one transition probability is calculated which saves computation time compared to the residence-time algorithm in which all transition probabilities are calculated. The disadvantage of using the Metropolis algorithm is, however, that when the transition is rejected, no configurations are chosen and the system remains in the same configuration. In contrast, using the residence-time algorithm guarantees that at every-time step a transition is made. The Metropolis algorithm can therefore waste computational time and include a lower number of jumps in the statistics, as compared to the residence-time algorithm.

The Metropolis algorithm is not suitable for cases when the energetic landscape presents sharp local minima as the system will most likely remain in the same configuration for several time-steps. Also, when studying diffusion at low temperatures, most transition probabilities are low and will be rejected, making the Metropolis algorithm unsuitable in such cases.

The residence-time algorithm is not suitable for cases when the number of transition probabilities is high or when there is a big difference in transition probabilities. Even though the state of the system changes at each step, it can still get stuck in local minima. When a saddle-point energy is low, the system will transition back and forth between two configurations and will not evolve to a new area of phase space. Instead of getting stuck in one configuration like the Metropolis algorithm, it will get stuck in a small sample of configurations.

Regardless of the algorithm, transition probabilities verify detailed balance and the system should converge towards its equilibrium state. Both algorithms have their advantages and disadvantages, and depending on the system that is being studied, and more specifically depending on the jump frequency model and energy landscape, one of the two might be more or less suitable to use. For example, to study decomposition phenomena in FeCr alloys, the residence-time algorithm is better because, on one hand, the number of possible transitions via the vacancy mechanism are low, and, on the other hand, decomposition is studied at relatively low temperatures which could result in low transition probabilities and make the Metropolis less suitable [9].

1.5.3 Time re-normalization problem

In the case of a vacancy-mediated diffusion mechanism, we need at least one vacancy in the Monte Carlo box for atoms to exchange with it. The size of a Monte Carlo box being usually of the order of 1 million, the resulting vacancy concentration is of the order of 10^{-6}. This is much higher than the real vacancy concentration (which can be of the order of magnitude of 10^{-13} in FeCr alloys at 770K [9]). A higher number of vacancies leads to more frequent vacancy exchanges and a faster atomic diffusion, leading to higher absolute values of the transport coefficients. Time re-normalization is therefore crucial to fix this problem and obtain accurate transport coefficients. The correction to the Monte Carlo can be done at each time-step i according to

$$t_i = t_i^{MC} \frac{C_V^{MC}}{C_V}, \tag{1.57}$$

where t_i^{MC} and t_i are respectively the time measured at time-step i in the Monte Carlo simulation and the real physical time, and C_V^{MC} and C_V are respectively the average vacancy concentration in the Monte Carlo simulation box and the real average vacancy concentration. Note that the average vacancy concentration in the real alloy is equal to its equilibrium value $C_V = C_V^{eq}$. The ratio of average concentrations C_V^{MC}/C_V^{eq} can be approximated by the ratio of local concentrations in an environment α inside which we know how to calculate the equilibrium concentration, $C_V^{MC}(\alpha)/C_V^{eq}(\alpha)$, and which is assumed to be the same in all environments. The real physical time becomes

$$t_i = t_i^{MC} \frac{C_V^{MC}(\alpha, \delta t)}{C_V^{eq}(\alpha)}. \tag{1.58}$$

Here, $C_V^{eq}(\alpha) = \exp\left(-\frac{E_V^f(\alpha)}{k_B T}\right)$ is a function of $E_V^f(\alpha)$, the vacancy formation energy in α. $C_V^{MC}(\alpha, \delta t)$ is calculated in an environment α during the time-step δt. The chosen environment has to be well representative of the system to ensure a big enough statistics. Equivalently, δt has to be big enough for the vacancy to explore all the possible environments, and small enough with respect to the evolution of the alloy's structure. In the general case, the choice of α should not affect the simulation itself, and the real physical time calculated from it should still be of the same order of magnitude regardless of our choice. For more detail on the time re-normalization problem, please refer to [78].

1.5.4 Calculating transport coefficients

1.5.4.1 The Einstein-Smoluchowski formula: diffusion coefficients

In the case of isotropic diffusion and in the absence of a driving force, Einsten [79] and Smoluchowski [80] established independently the relationship between the diffusion coefficient D_α of an atom of species α and its total mean-square displacement vector, $\vec{r}_\alpha\left(t\right)$, during a time t,

$$D_\alpha = \lim_{t\to\infty} \frac{\left\langle \vec{r}_\alpha\left(t\right)^2 \right\rangle}{6t}. \tag{1.59}$$

The brackets here represent an ensemble average that is measured at equilibrium, and time needs to be long enough for an accurate calculation. This relationship can be used to calculate the diffusion coefficient in a Monte Carlo simulation in which the system is already at equilibrium. Atomic displacements can be measured at each Monte Carlo step and the total displacement of an atom α can be calculated in each Monte Carlo block as the sum of its N_s successive displacements that happen at each step i,

$$D_\alpha = \frac{\left\langle \left(\sum_{i=1}^{N_s} \vec{r}_{\alpha,i}\right)^2 \right\rangle}{6t}, \tag{1.60}$$

where t_i is the time at step i, such that the total time $t = \sum_{i=1}^{N_s} t_i$. The brackets represent an average over the different Monte Carlo blocks. Note that Monte Carlo blocks represent various parts of the trajectory. Averaging over blocks is a time average, and using the ergodicity principle, it is equivalent to an ensemble average. To improve the convergence of D_α, it can also be calculated by averaging the sum of displacements of α over all identical atoms α present in the simulation box, such that

$$D_\alpha = \frac{\left\langle \sum_{k=1}^{N_\alpha} \left(\sum_{i=1}^{N_s} \vec{r}_{\alpha_k,i}\right)^2 \right\rangle}{6N_\alpha t}, \tag{1.61}$$

where N_α is the total number of α atoms. Correlations between successive jumps of the same species α are taken into account, and this can be seen in the $\vec{r}_{\alpha,i}\vec{r}_{\alpha,j}$ term when expanding the square of the sum

$$\left(\sum_{i=1}^{N_s} \vec{r}_{\alpha,i}\right)^2 = \sum_{i=1}^{N_s} \vec{r}^{\,2}_{\alpha,i} + 2\sum_{i=1}^{N_s-1}\sum_{j=i+1}^{N_s} \vec{r}_{\alpha,i}\vec{r}_{\alpha,j}. \tag{1.62}$$

This allows for the calculation of the diffusion coefficient from atomic displacements while implicitly taking into account kinetic correlation effects. This demonstrates the power of the Monte Carlo simulations because, as will be further discussed in Sec. 1.6.1, calculating correlations analytically is not a trivial task.

1.5.4.2 The Allnatt formula: transport coefficients

In 1982, in the case of isothermal diffusion on a lattice of total volume V, Allnatt established the link between transport coefficients and equilibrium fluctuations of atomic positions using a generalized Einstein formula [81]. The $L_{\beta\alpha}$ coefficient is calculated as a function of the mean-square displacement of atoms β and α at equilibrium,

$$L_{\beta\alpha} = \lim_{t\to\infty} \frac{\left\langle \vec{R}_{\beta}(t)\,\vec{R}_{\alpha}(t) \right\rangle}{6Vt}, \tag{1.63}$$

where t is the time during which the collective displacement vector of atoms of species α is $\vec{R}_{\alpha}(t)$. The brackets represent a thermodynamic average and time needs to be long enough for an accurate calculation. This relationship can be used in Monte Carlo simulations in which the system has already converged towards equilibrium and by assuming that the measurement time is long enough. Note that the displacement of all atoms of species α is related to the displacement of one atom of species α (discussed in the previous paragraph, Sec. 1.5.4.1) through

$$\vec{R}_{\alpha}(t) = \sum_{k=1}^{N_{\alpha}} \vec{r}_{\alpha_k}(t), \tag{1.64}$$

where N_{α} is the total number of α atoms. The total equilibrium fluctuations of atomic positions of atoms α can be calculated after N_s steps as

$$\vec{R}_{\alpha}(t) = \sum_{i=1}^{N_s} \vec{R}_{\alpha,i} = \sum_{i=1}^{N_s}\sum_{k=1}^{N_{\alpha}} \vec{r}_{\alpha_k,i}, \tag{1.65}$$

and the transport coefficient as

$$L_{\beta\alpha} = \frac{\left\langle \left(\sum_{i=1}^{N_s}\sum_{k=1}^{N_{\beta}} \vec{r}_{\beta_k,i}\right)\left(\sum_{i=1}^{N_s}\sum_{k=1}^{N_{\alpha}} \vec{r}_{\alpha_k,i}\right)\right\rangle}{6Vt}, \tag{1.66}$$

where the brackets indicate an average over the different blocks. Here, the $L_{\beta\alpha}$ coefficient takes into account kinetic correlations between successive jumps, and therefore, there is no need to explicitly model them in the simulation. Note that, in the case of 1 α atom in the box (very dilute case), the relationship between the diagonal transport coefficient and the tracer diffusion coefficient established in Eq. 1.14, is found here again

$$L_{\alpha\alpha} = C_{\alpha}\frac{\left\langle \left(\sum_{i=1}^{N_s} \vec{r}_{\alpha,i}\right)^2 \right\rangle}{6t} = C_{\alpha}D_{\alpha}, \tag{1.67}$$

where $C_{\alpha} = 1/V$ is the volume concentration of α.

1.5.5 Limitations

Monte Carlo simulations have been widely used to compute transport coefficients and correlation factors in alloys [9, 16, 29–32, 35]. Even though Monte Carlo simulations are a very powerful tool, they still have some limitations when it comes to computing transport coefficients. It is not always easy to generate a big enough statistics that gives converged results, especially when calculating off-diagonal transport coefficients in correlated systems. Kinetic trapping in local energy basins can arise depending on the energetic landscape and the chosen algorithm. In these cases, a large number of steps is needed to properly sample the configuration space and for the calculated coefficients to converge, even though many efforts have been done to try and overcome these trapping problems [82–88]. Performing a complete study on the effect of several parameters (composition, temperature, interaction energies) on the transport coefficients becomes computationally heavy. Furthermore, there are some cases in which we cannot calculate diffusion coefficients using Monte Carlo simulations. Diffusion coefficients are calculated after a system has reached equilibrium which means we cannot calculate accurate diffusion coefficients in systems under decomposition. In unstable systems, for example, in supersaturated solid solutions, the decomposition of the system will happen at the same time as the diffusion coefficient is being calculated and there is no way to verify that enough steps were made to converge the value of the diffusion coefficient. Furthermore, even though off-lattice methods exist (e.g. k-ART [89], which requires an interatomic potential and is much heavier computationally), simulations are usually performed on a rigid lattice which disables us from modeling strained systems, inclusions and dislocations.

Analytical models allow us to overcome these obstacles. Atomic-scale analytical models in particular, allow us to explicitly make the link between measurable quantities, like the diffusion coefficients, and atomic quantities, like jump frequencies, interaction energies, and formation energies. This enables us to have access to atomic scale data, to better understand the diffusion process, and finally to make predictions at different scales in an accurate and efficient way. Yet, they are often limited by the complexity of the system that can be addressed, in terms of defects and jump mechanisms. The next two sections will focus on some of the most important analytical models that were developed to study diffusion in alloys in general, and diffusion in concentrated alloys in particular, as well as all the difficulties that arise in the latter case.

1.6 Correlation factors

The difficulty in analytically calculating transport coefficients lies mainly in calculating the correlated part of the coefficients. Even though jumps are random, successive jumps depend on the direction of preceding jumps. For instance, a tracer that can only move by exchanging with a vacancy will move according to the direction from which the vacancy comes to exchange with it. While in Monte Carlo simulations correlation factors can be directly calculated as a function of the displacement of atoms (Sec. 1.6.1 and Sec. 1.6.2), analytical models of diffusion require us to explicitly formulate and calculate them. In self-diffusion in a one component system, all jump frequencies are the same and correlations arise solely from geometrical effects. In such a case, the random walk theory is enough to accurately calculate correlation factors. In some simple cases of dilute alloys where the number of different jump frequencies is low, the Le Claire model can be used to approximate in a simple manner the correlation factor (Sec. 1.6.3). In the general cases of dilute alloys and concentrated alloys, the number of jump frequencies is too high to use the Le Claire model and it is necessary to build a model that couples the thermodynamics and the kinetics of the system for a proper calculation of transport coefficients (Sec. 1.6.4).

1.6.1 Correlations in the Einstein equation

Combining Eq. 1.60 and Eq. 1.62, the diffusion coefficient of an atom of species α as given by Einstein and Smoluchowski (Sec. 1.5.4.1) is divided in two terms,

$$D_\alpha = \frac{\sum_{i=1}^{N_s} \left\langle \vec{r}^2_{\alpha,i} \right\rangle}{6t} + \frac{2\sum_{i=1}^{N_s-1} \sum_{j=i+1}^{N_s} \left\langle \vec{r}_{\alpha,i}\vec{r}_{\alpha,j} \right\rangle}{6t}. \tag{1.68}$$

The first term, $\sum_{i=1}^{N_s} \left\langle \vec{r}^2_{\alpha,i} \right\rangle$, is a thermodynamic average of all individual jumps of atom α and does not take into account how these jumps are connected. The second term, $\sum_{i=1}^{N_s-1} \sum_{j=i+1}^{N_s} \left\langle \vec{r}_{\alpha,i}\vec{r}_{\alpha,j} \right\rangle$, is an average of displacement vector products of all consecutive jumps i and j. For each jump i, one has to find all possible jumps after i, which takes into account correlations between consecutive jumps. Even though individual jumps follow a Markovian process and are random, the sequences of consecutive jumps do not necessarily have the same probability of being formed. This latter term therefore takes into account all the possible trajectories and their different probabilities, making it hard to calculate. Enumerating and studying all possible individual jumps of an atom analytically is not always easy, but it remains much easier than enumerating and studying all possible trajectories. This term is in general negative because consecutive exchanges between two atoms are more likely to happen in the opposite direction. This is further explained in Fig. 1.7. Correlations can be quantified by introducing the correlation factor of species α, f_α, which represents the deviation of the total diffusion coefficient from the non-correlated diffusion coefficient

$$D_\alpha = f_\alpha D^0_\alpha. \tag{1.69}$$

Here, D^0_α is the uncorrelated diffusion coefficient of α and is equal to the diffusion coefficient that one would obtain in a crystal of the same structure if consecutive jumps were not correlated

$$D^0_\alpha = \frac{\left\langle \sum_{i=1}^{N_s} \vec{r}^2_{\alpha,i} \right\rangle}{6t}, \tag{1.70}$$

and the correlation factor is

$$f_\alpha = 1 + 2\frac{\left\langle \sum_{i=1}^{N_s-1} \sum_{j=i+1}^{N_s} \vec{r}_{\alpha,i}\vec{r}_{\alpha,j} \right\rangle}{\left\langle \sum_{i=1}^{N_s} \vec{r}^2_{\alpha,i} \right\rangle}. \tag{1.71}$$

Note that $0 \leq f_\alpha \leq 1$, and the closer the correlation factor is to 0 the more correlated the diffusion ($D_\alpha \rightarrow 0$), and the closer it is to 1 the less correlated the diffusion ($D_\alpha \rightarrow D^0_\alpha$). Correlation factors therefore reduce the efficiency of diffusion with respect to a non-correlated one and slow down the diffusion process ($D_\alpha \leq D^0_\alpha$).

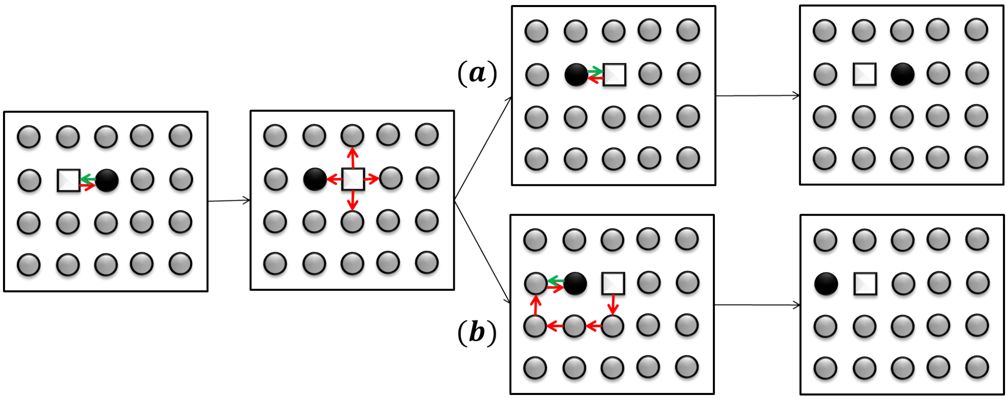

Figure 1.7: A first exchange between a vacancy (white square) and tracer α atom (black circle) puts the vacancy to the right of atom α. The probability that the vacancy exchanges with α from the right side, $P(a) = (1/z)$, is higher than exchanging with it from any other side, e.g. from the left $P(b) = (1/z)^5$, $z = 4$ being the coordination number. Even though a vacancy jump in any direction has an equal probability of $(1/z)$, the number of jumps the vacancy needs to make to exchange with α from the right (with the fewest number of jumps) is lower than the number of jumps required to exchange with α from any other direction (with the fewest number of jumps), making the exchange from the right more probable. Note that this only concerns tracer atoms α whose movement relies on a vacancy exchanging with them.

1.6.2 Correlations in the Onsager formalism

Using Allnatt's formalism, the diagonal transport coefficient of collective atoms of species α is

$$L_{\alpha\alpha} = \frac{\left\langle \left(\sum_{i=1}^{N_s} \vec{R}_{\alpha,i}\right)^2 \right\rangle}{6Vt} = \frac{\left\langle \sum_{i=1}^{N_s} \vec{R}_{\alpha,i}^2 \right\rangle}{6Vt} + \frac{\left\langle 2\sum_{i=1}^{N_s-1} \sum_{j=i+1}^{N_s} \vec{R}_{\alpha,i}\vec{R}_{\alpha,j} \right\rangle}{6Vt}. \tag{1.72}$$

By analogy with the treatment of diffusion coefficients, the correlated transport coefficient can be written as a function of the un-correlated coefficient multiplied by the correlation factor

$$L_{\alpha\alpha} = f_{\alpha\alpha}^{(\alpha)} L_{\alpha\alpha}^0, \tag{1.73}$$

where the un-correlated transport coefficient is a function of individual jumps only

$$L_{\alpha\alpha}^0 = \frac{\left\langle \sum_{i=1}^{N_s} \vec{R}_{\alpha,i}^2 \right\rangle}{6Vt}, \tag{1.74}$$

and the correlation factor is given by

$$f_{\alpha\alpha}^{(\alpha)} = \frac{L_{\alpha\alpha}}{L_{\alpha\alpha}^0} = 1 + 2\frac{\left\langle \sum_{i=1}^{N_s-1} \sum_{j=i+1}^{N_s} \vec{R}_{\alpha,i}\vec{R}_{\alpha,j} \right\rangle}{\left\langle \sum_{i=1}^{N_s} \vec{R}_{\alpha,i}^2 \right\rangle}. \tag{1.75}$$

The off-diagonal correlation factor $f_{\beta\alpha}^{(\gamma)}$ quantifies the deviation of the transport coefficient $L_{\beta\alpha}$, with respect to the coefficient $L_{\gamma\gamma}^0$ which one would obtain in the case of a random walk in a crystal of the same structure containing only γ atoms (of the form of Eq. 1.74, and where γ is either α or β). This off-diagonal correlation factor can also be calculated

$$f_{\beta\alpha}^{(\gamma)} = \frac{L_{\beta\alpha}}{L_{\gamma\gamma}^{0}} = \frac{\left\langle \left(\sum_{i=1}^{N_s} \vec{R}_{\beta,i}\right) \left(\sum_{i=1}^{N_s} \vec{R}_{\alpha,i}\right) \right\rangle}{\left\langle \sum_{i=1}^{N_s} \vec{R}_{\gamma,i}^{2} \right\rangle}. \tag{1.76}$$

The difficulty in calculating f_α, $f_{\alpha\alpha}^{(\alpha)}$ and $f_{\alpha\beta}^{(\gamma)}$ (Eq. 1.71, 1.75 and 1.76) analytically lies in calculating the averages of successive displacement vectors of atoms. Calculating the terms in the averages requires us to find all the possible trajectories of the atoms that are being followed, which is not feasible in the general case of many-body diffusion. Despite the fact that it is difficult to calculate correlation factors analytically, they are significant in many cases (see Fig. 1.13), especially at low temperatures, and must be taken into account for a full description of the diffusion phenomena. The following sections will show some methods to calculate correlation factors in dilute alloys, and the challenges that arise to calculate them in concentrated alloys.

1.6.3 Correlation factors of tracer atoms

The first studies to calculate correlation factors focused on studying the diffusion of a solute atom by means of a vacancy mechanism in pure (self-diffusion) or very dilute (impurity diffusion) alloys. Let us consider a vacancy V diffusing in a homogeneous matrix of A atoms containing a tracer B ($B = A^*$ in the case of self-diffusion and $B \neq A$ in the case of impurity diffusion).

1.6.3.1 Self-diffusion

In the case of self-diffusion, the tracer A^* has the same properties as A, and therefore all atoms in the crystal are the same. As seen in 1.6.1 and 1.6.2, the diffusion coefficient and the diagonal transport coefficient (which, in this case, is directly proportional to the diffusion coefficient) deviate from the random-walk coefficients and show a correlated tracer diffusion. Figure 1.7 shows how and why correlation effects arise, even when all matrix atoms are the same, due to geometrical effects. Note that it is only the tracer's diffusion that is correlated, while the vacancy's diffusion is a non-correlated random walk since at all times it can jump in any direction with equal probability (Fig. 1.8).

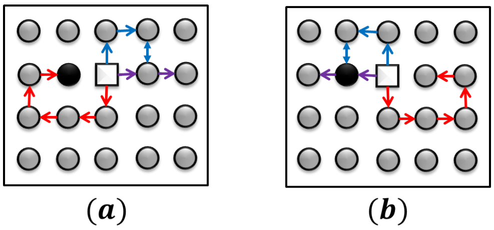

Figure 1.8: The probability that a vacancy (white square) jumps in any direction is equal to $1/z$, z being the coordination number. This is true whether the vacancy is exchanging with a matrix atom (gray circle) or with an isotope (black circle). A red trajectory drawn in (a) occurs with the same probability as the red trajectory drawn in (b), and which represents a trajectory which is symmetric to it with respect to the vertical plane. This is true for any trajectory in the system (e.g. blue trajectories and purple trajectories also have the same probabilities in (a) and (b)). For every couple of displacements $\vec{r}_{V,i}\vec{r}_{V,j}$ there exists an $\vec{r}_{V,j}\vec{r}_{V,i}$ that occurs with the same probability. These two terms cancel out for all trajectories and the correlated part of Eq. 1.68 becomes null.

As a first approximation, the self-diffusion correlation factor can be calculated as the fraction of vacancy exchanges that take the vacancy away from the tracer in a way to randomize its direction with respect to the tracer. Let z be the coordination number of the crystal. After a first exchange with the tracer, a vacancy has $(z-1)$ possibilities of exchanging with a matrix atom and one possibility of exchanging back with the tracer. Let us approximate the problem by considering that all $V-A$ exchanges take the vacancy sufficiently far from the tracer so that the vacancy is dissociated from it and its direction is randomized. Among $(z+1)$ possible jumps, there are $(z-1)$ jumps that take the vacancy away from the tracer. This allows us to calculate a first-order approximation of the correlation factor as

$$f_0 \equiv f_{A^*} = \frac{z-1}{z+1}. \tag{1.77}$$

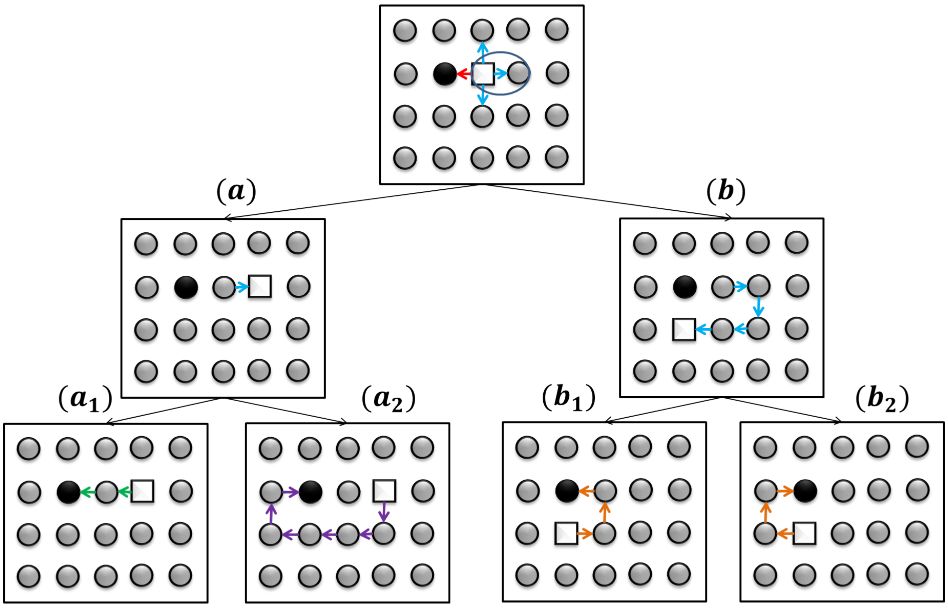

Figure 1.9: A vacancy (white square) escapes from a tracer (black circle) by jumping away from it (blue arrows). An escape jump to the right can eventually lead the vacancy to a scenario (a) or (b), among other possibilities. Diffusion is being studied along the horizontal axis. In (a), the vacancy can come back from a non-random direction to exchange with the tracer, as explained in Fig. 1.7. The first jump shown in (a) was not efficient in randomizing the position of the vacancy with respect to the tracer's position. In (b), the probability that the vacancy comes back from the right or left of the tracer are equal. The trajectory shown in (b) was efficient in randomizing the position of the vacancy. Therefore, only a fraction of the initial blue arrow jump to the right is indeed an escape frequency, and the real value is lower than $(z-1)$, z being the coordination number.

The results are not very accurate as expected, since not all $(z-1)$ jumps with A will be effective in randomizing the direction of the vacancy with respect to the tracer. This can be better seen in Fig. 1.9. However, the results remain within a 10% relative error, and given its simplicity, this approximation is a good fast way to estimate the self-diffusion correlation factor. For a better accuracy, trajectories longer than 2 jumps need to be considered, and the correlation factor converges with increasing size of the longest considered trajectory. Note again that the self-diffusion correlation factor is only a function of the crystalline structure. More sophisticated models now exist to calculate it accurately and there are databases of self-diffusion correlation factors of different crystalline structures. The next paragraph will focus on the more general case of impurity diffusion which can also be applied to the case of self-diffusion.

1.6.3.2 Impurity diffusion

In the case of self-diffusion, correlations are purely geometrical, while in the case of impurity diffusion, the difference in vacancy exchange rates with a solute B and a matrix atom A in the vicinity of B leads to additional correlations. In 1955, Le Claire and Lidiard developed an n-jump frequency model to study solute diffusion via the vacancy mechanism in dilute alloys by expressing all quantities as a function of vacancy concentrations and vacancy jump frequencies [38–41]. The number of vacancy jump frequencies in the model, n, depends on the crystalline structure and the number of different frequencies that are considered around the solute. The simplest models consider vacancy jump frequencies between only two types of configurations: those in which the vacancy and the tracer are $1nn$, and those in which they are dissociated (i.e. at any distance beyond $1nn$). The 4 frequency model in SC, the 4 frequency model in BCC, and the 5 frequency model in FCC (Fig. 1.10 and Table 1.2) are such examples. Configurations where the vacancy and tracer are $2nn$ or further apart can also be included which increases the accuracy but also the complexity of the calculation. For example, in the BCC structure, there is a 6 frequency model which includes $2nn$ configurations.

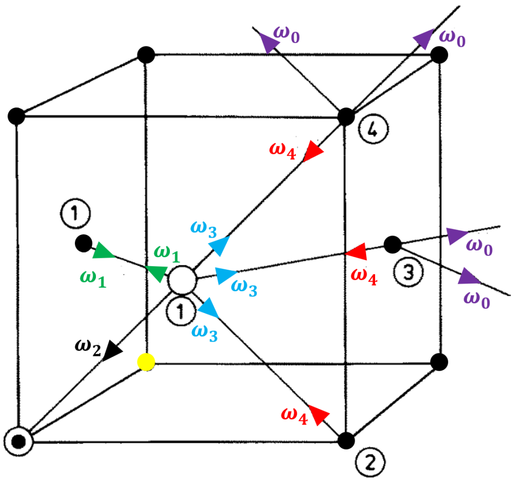

Figure 1.10: The 5 different types of vacancy exchange frequencies in a FCC crystal in which only $1nn$ and dissociated configurations are considered. Image taken from [41].

	exchanging species	relative initial position	relative final position	multiplicity
w_0	$V-A$	∞	∞	$\approx Nz/2 \rightarrow \infty$
w_1	$V-A$	$1nn$	$1nn$	2
w_2	$V-B$	$1nn$	$1nn$	1
w_3	$V-A$	$1nn$	∞	5
w_4	$V-A$	∞	$1nn$	5

Table 1.2: The five types of vacancy exchange frequencies in a FCC crystal in which only $1nn$ and dissociated configurations are considered. The pair of species involved in the exchanged is given in the second column where V, A and B represent respectively the vacancy, the matrix atom and the tracer. The relative initial and final positions of the vacancy with respect to the tracer B are given in the third and fourth columns, and the multiplicity of each exchange (i.e. the number of such exchanges) is given in the last column.

In transition state theory [75], jump frequencies are thermally activated events expressed as

$$w_i = \nu_i \exp\left(-\frac{H_i}{k_B T}\right), \tag{1.78}$$

where H_i is the activation enthalpy and ν_i is the attempt frequency which takes into account the vibrational entropy contribution. Furthermore, detailed balance can be written for reverse jumps (for example jumps related to w_3 and w_4)

$$P_{1nn} w_3 = P_\infty w_4, \tag{1.79}$$

where

$$P_{1nn} = \exp\left(-\frac{E_V^f + E_{BV}}{k_B T}\right), \tag{1.80}$$

is the probability of a configuration in which the vacancy and the tracer are $1nn$, and

$$P_\infty = \exp\left(-\frac{E_V^f}{k_B T}\right), \tag{1.81}$$

is the probability of any other configuration. Here, E_v^f and E_{BV} are respectively the formation energy of a vacancy and the interaction energy of a nearest-neighboring pair of a vacancy and a tracer B. This allows the expression of jump frequency ratios as a function of interaction energies

$$\frac{w_4}{w_3} = \exp\left(-\frac{E_{BV}}{k_B T}\right). \tag{1.82}$$

In 1959, Manning [90] showed that, within the n-jump frequency model and in the case of diffusion in isotropic crystals, the tracer correlation factor of an atom of species α can be rigorously written as

$$f_\alpha = \frac{H}{2w_\alpha + H}, \tag{1.83}$$

where w_α corresponds to the exchange frequency between the vacancy and α (here denoted as w_2), and H represents the effective escape frequency of the vacancy from α. The escape frequency is the frequency at which the vacancy diffuses away from α in a way that randomizes the next vacancy-α exchange direction. Therefore, jumps that allow the vacancy to come back and exchange with the tracer from a non-random direction are not included in H. The tracer correlation factor quantifies therefore the competition between the vacancy-tracer jump frequency and the vacancy escape frequency. Figure 1.11 shows the variation of the tracer correlation factor as a function of w_α/H. Let us consider the two extreme cases. When $w_\alpha/H \ll 1$, the vacancy exchange rate with the impurity is much lower than the escape frequency, the vacancy will perform a random-walk by exchanging mostly only with matrix atoms, and it will so frequently exchange with them that its direction will be randomized before its next exchange with the solute. The diffusion of the solute will then be similar to an uncorrelated diffusion and $f_\alpha \to 1$. In the opposite case when $w_\alpha/H \gg 1$, after a first exchange with the solute the vacancy will prefer to exchange with it again which will cancel out its displacement. This will lead to another reverse jump happening with high probability and so on. The solute will therefore mostly keep moving back and forth between two positions, leading to a net displacement of zero and a highly correlated diffusion, $f_\alpha \to 0$.

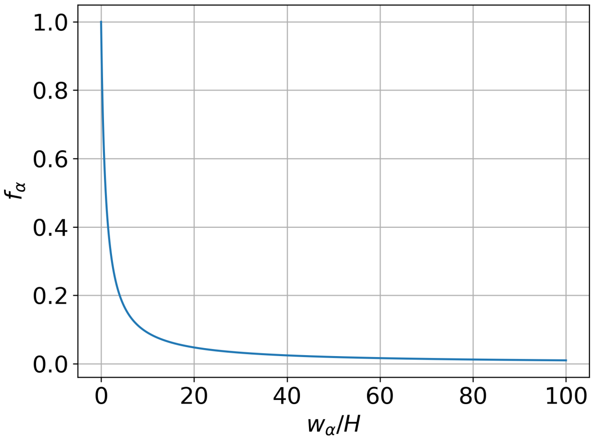

Figure 1.11: Evolution of the tracer correlation factor f_α as a function of the ratio of tracer-vacancy exchange frequency w_α to vacancy escape frequency H.

Manning further derived analytical expressions of H as a function of the jump frequencies and as a function of $F(k)$, which represents the fraction of dissociated vacancy jumps that are effective in randomizing the vacancy's direction with respect to the tracer. k is usually a jump frequency ratio and the value of $F(k)$ depends on the crystalline structure and on the value of k (See [90,91] for references). For example, in the case of a 5-jump frequency model in the FCC structure, the escape frequency is obtained by Manning as

$$H = 2w_1 + w_3 F\left(w_4/w_0\right), \tag{1.84}$$

with

$$F(k) = 7 - \frac{10k^4 + 180.5k^3 + 927k^2 + 1341k}{2k^4 + 40.2k^3 + 254k^2 + 597k + 436}, \tag{1.85}$$

where $k = w_4/w_0$ represents the competition of a dissociated vacancy between jumping further away from the tracer and jumping back close to it.

Note that these relations can be applied to the case of self-diffusion by considering all jump frequencies w_i to be equal. In this case, the n-jump frequency model is more accurate than the first approximation presented in Sec. 1.6.3.1 because it better approximates the escape frequency.

The works of Lidiard and Le Claire [38–41] have made the n-jump frequency model a widely used method because it provides a simple analytical solution, it takes as input atomic-scale data that can be calculated relatively easily using ab-initio methods, and it gives a good estimate of the correlation factors in pure and dilute alloys despite its simplicity [92]. The limitations of this model is that it is only valid for tracer diffusion via vacancy mechanisms and that it assumes a null vacancy-solute interaction energy when they are at a distance greater than $1nn$. Extending the model beyond the $1nn$ configurations has been done in some cases, however this increases the number of jump frequencies that have to be taken into account making the analytical expressions harder to manipulate.

1.6.4 Challenges in modeling diffusion in concentrated alloys

The challenge in calculating transport coefficients in concentrated alloys relies mainly on calculating correlations. In order to properly take into account correlations, it is necessary to construct the different trajectories made up of successive atom jumps. In order to do this, we need to find the different jump frequencies and construct a graph between the various configurations of the system through these jump frequencies. For a given graph in the dilute system, each configuration or jump frequency is degenerated with respect to the occupation of matrix sites. We can reduce the degeneracy by assuming short-range interactions. However, in a concentrated system where several species are present at similar concentrations, the spatial distribution of species over the available sites in any configuration can vary greatly in space. A jump frequency depends on the surrounding of the jumping species and therefore varies depending on their location in the lattice. The short-range and long-range environments around diffusing species are heterogeneous, and as a consequence, the number of possible configurations and jump frequencies to consider becomes too large to enumerate them, let alone to construct the graph of the trajectories that link them. The total number of configurations of a system in the Grand Canonical ensemble depends on the number of ways the different atomic species and point defects can be arranged on the lattice. Therefore, the number of configurations is closely related to the number of different species ($N_{species}$ species in an $N_{species}$-component system), the number of defects ($N_{defects}$, number of vacancies for example), and the total number of sites N_{sites}. If the system contains one vacancy at a specific site, the number of possible configurations is equal to the number of ways we can arrange the atomic species on the remaining $N_{sites} - 1$ sites. The number of configurations in this case is equal to $\Omega_{species} = N_{species}^{N_{sites}-1}$, and scales with the number of components in the system and the number of sites in it.

In dilute alloys, simplifications could be made by assuming that diffusing defects are surrounded by a homogeneous medium, which reduces the number of configurations to the number of different ways of arranging defects on a uniform lattice. This number is further reduced because most configurations of defects on a uniform lattice are symmetrically equivalent. Additionally, since the environment around diffusing species is uniform, a lot of the jump frequencies become identical and translational invariance allows us to treat only a fraction of the configuration space. For instance, the n-jump frequency model of Le Claire and Lidiard shows that in the case of a vacancy diffusing in a dilute system, the number of jump frequencies can be reduced to less than a dozen. If we were to apply the n-jump frequency model to a concentrated alloy, jump frequencies that were previously equivalent become different due to the difference in the environment surrounding the tracer-vacancy pair, and the multiplicity of most jump frequencies in Table 1.2 will be 1 (few will be equivalent by symmetry). This means that for each unique configuration of the system, we would have to consider an infinite number of jump frequencies. For example, in a ternary (3-component system of RBG) FCC crystal in which the vacancy has 17 nearest and second-nearest neighbors (other than the tracer), there are more than 100 million different ways to arrange the species R, B and G in these 17 sites, leading to more than 100 million different configurations, most of which will be symmetrically unique. This further leads to more than 1 billion different jump frequencies to consider. One of the possible configurations is shown in Figure 1.12. Is is therefore impossible to analytically study the case of concentrated alloys using the n-jump frequency model, even when we only consider $1nn$ pairs.

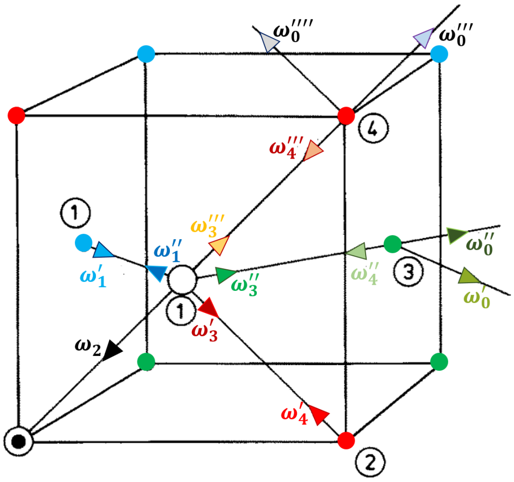

Figure 1.12: The different types of vacancy exchange frequencies in a FCC crystal in the case of a ternary alloy RBG (red, blue, and green circles). Jump frequencies do not only depend on the relative positions of the vacancy and impurity, but also on the type of species the vacancy is exchanging with, and on their surrounding. Jump frequencies that were equivalent in the homogeneous matrix are no longer so, and the five unique jump frequencies drawn in Figure 1.10 become 13 in this case. Note that Fig. 1.10 represents the only possible configuration of the system, while this figure represents one of the million possible configurations.

One way to approach the problem would be to approximate the heterogeneous medium around diffusing species (the vacancy and the solute which is being treated explicitly) by one average homogeneous medium having properties that are the average of those of the initial system [93]. This reduces the concentrated alloy to an average dilute alloy, which allows us to study it using any of the tools developed for dilute alloys. However, this approach neglects all correlations that arise from the difference in interactions between different atomic species. A vacancy surrounded by A and B atoms will exchange with each with a different frequency, and the diffusion of the vacancy will be correlated, while a vacancy surrounded by a hypothetical average M species will exchange with all atoms with the same frequency and its diffusion will be uncorrelated, as we showed in Sec. 1.6.3. Several analytical models have been developed in this mean-field spirit, and each of them relies on a different definition or interpretation of the mean-field to reproduce and calculate the correlations [19,21,22]. Each of these models also relies on a different set of kinetic and thermodynamic assumptions and approximations. In the next section, we choose to detail three of these models.

1.7 Analytical models of diffusion in concentrated alloys

The development of analytical models of diffusion in concentrated alloys has been an ongoing work for many years now, the goal being to express the Onsager coefficients as a function of measurable quantities. Because of all the difficulties of modeling concentrated alloys, the first models focused on treating non-interacting alloys. Manning [19, 20] was the first to introduce the random alloy model in which a vacancy diffuses in a non-interacting alloy such that the vacancy jump frequency depends only on the species with which it is exchanging. The relations derived by Manning allow the expression of the transport coefficients as a function of tracer diffusion coefficients. In the case of a binary random alloy, knowing the self diffusion correlation factor, the tracer and vacancy correlation factors can be obtained using a very simple analytical formula. Despite its simplicity, Manning's model is in good agreement with Monte Carlo simulations [29–32], except when the off-diagonal transport coefficients are negative, as his model fails to predict a negative $L_{\alpha\beta}$. Other methods have been developed in the same spirit to study correlations in a random alloy in what is known as the "random lattice gas" models [43,44]. These methods often yield more accurate tracer correlation factors, however, they are also much more complex to use than Manning's analytical result. The difficulty is usually to reproduce with high accuracy the tracer correlation factor of the fastest diffusing species because it is the species whose diffusion is the most correlated. Another challenge is to reproduce the percolation phenomena which occurs when the exchange frequency of the vacancy with one of the species is infinitely big compared to the other frequencies (Fig. 1.13).

Kikuchi was on the other hand the first to develop an analytical model to treat interacting alloys [21, 46, 94]. His Path Probability Method (PPM) was mainly used to study order-disorder transitions. This PPM is limited to a statistical pair approximation and the generalization beyond it is complex theoretically. It was only extended once to a triangle approximation but only in a 2D structure [95]. When applied to a random alloy, a revised version of the PPM showed satisfactory results in comparison with Monte Carlo simulations but remained less accurate than Manning's model [47].

Vaks et al. later used a different approach based on a master equation which describes the evolution of the non-equilibrium probability distribution of the system [96,97]. His model, however, predicts a diagonal Onsager matrix, and therefore neglects cross-diffusion coefficients. In more recent years, based on the same formalism, Nastar et al. developed the Self-Consistent Mean-Field (SCMF) theory to study diffusion in interacting alloys [22, 48, 98, 99]. Unlike Vaks, the SCMF manages to compute the full Onsager matrix. In the case of an interacting alloy and a random vacancy concentration, the theory was in general good agreement with Monte Carlo simulations. In the case of a random alloy, a subsequent work by Barbe *et al.* [49] showed that the method yields results in good agreement with Monte Carlo simulations for all range of jump frequency ratios. Even though the SCMF is limited to an alloy with short range order, it allows for the calculation of single and collective correlation factors in both cases of an interacting and non-interacting alloy.

In the following parts, we will discuss in more detail the three models that are most important for a full understanding of the evolution of analytical models of diffusion in concentrated alloys: the RA model, the PPM, and the SCMF theory.

In an effort to properly compare these three approaches, we will show as briefly as possible the theory behind each one of them and address the advantages and disadvantages of each method.

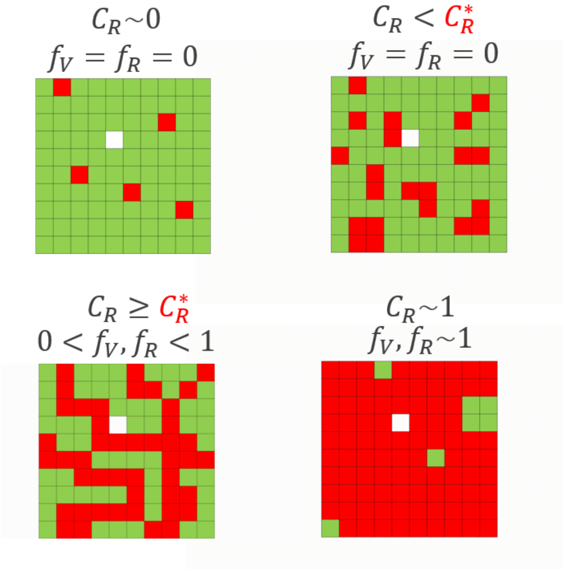

Figure 1.13: Schematic representation of the percolation phenomena in a binary alloy RG. Red, green and white squares represent respectively atoms of species R, atoms of species G and the vacancy. Let w_α be the exchange frequency of the vacancy with an atom of species α, and let us consider the case of an infinite jump frequency ratio w_R/w_G, such that the vacancy can only exchange with atoms of species R. The net displacement of the vacancy is non-null only if the vacancy can exchange with an infinite connected cluster of R atoms. When the R concentration C_R is low and below a structure specific concentration C_R^*, known as the percolation threshold or the critical percolation concentration, an infinite connected cluster of R atoms cannot form. In this case, the vacancy exchanges with R atoms in a small closed system and its net diffusion is null and the vacancy correlation factor f_V, as well as the tracer correlation factor f_R, are null. When the R concentration increases above the percolation threshold, the higher its concentration, the closer the diffusion is to an un-correlated walk. In this case, the vacancy correlation factor converges towards 1.

1.7.1 Manning's Random Alloy model (RA)

One of the most used models to study tracer-vacancy diffusion in concentrated alloys is the random alloy (RA) model developed by Manning in 1971 [19, 20]. Manning managed to calculate the vacancy and solute correlation factors by approximating the concentrated alloy by a random alloy containing only tracer atoms and a vacancy (or a very low concentration of vacancies). A random alloy is an alloy in which there are no interactions between its components nor between its components and defects (vacancy). Therefore, there are no preferential sites for atoms to occupy, and for a given alloy concentration, all configurations of the system have the same energy regardless of the atomic distribution. This type of alloy is also known as an ideal solid solution.

The model

Manning approximates the heterogeneous medium of a concentrated alloy by a hypothetical average homogeneous dilute alloy containing a tracer atom of each α component of the alloy. All sites, other than the ones with a tracer atom, are occupied by an average atom M, whose properties are the average of those of the chemical species. The tracer atoms are sufficiently diluted in the matrix to consider that each tracer is surrounded by M atoms only. Since there is only one environment surrounding the vacancy-tracer pair, the jump frequency w_α of a vacancy with an α atom is the same anywhere in the system. This approximates the real jump frequency which usually depends on the atoms surrounding the vacancy-α pair. Manning considers the jump frequency of a vacancy with an atom M to be the average of all w_α frequencies, each weighted by the atomic fraction of the corresponding α

$$W_M = \sum_\alpha X_\alpha w_\alpha, \tag{1.86}$$

where X_α is the atomic fraction α. In order to calculate the tracer correlation factor using an equation of the form of Eq. 1.83, one needs to calculate the escape frequency H_α of a vacancy away from an atom α. Manning considers that the escape frequency depends only on the geometry of the crystal and on the vacancy correlation factor

$$H = f_V H_0, \tag{1.87}$$

where H_0 is the escape frequency in a pure M crystal, and f_V is the vacancy correlation factor in the random alloy. This can be justified by the fact that, on one hand, there are no thermodynamic interactions between V and α, and on the other hand, the jump frequency W_M of exchanging with any atom other than α, does not depend on α. Therefore, the vacancy escape frequency is the same for all α atoms. One can go further and say that it is the same even if the α atom is replaced by an M atom. In this case, the system is equivalent to a pure M crystal. We have shown that in a pure crystal correlations arise only from geometrical effects (Sec. 1.6.3.1), and using Eq. 1.83 the escape frequency in a pure M crystal can be calculated as a function of the self-diffusion correlation factor f_0 as

$$H_0 = \frac{2W_M f_0}{1-f_0}. \tag{1.88}$$

Equation 1.87 can be intuitively understood. If the movement of the vacancy is not correlated (i.e. $f_V = 1$), then the escape frequency of the vacancy in the random alloy is equal to its escape frequency in a pure M crystal. On the other hand, the higher the correlations, the less efficient is the diffusion of the vacancy, which reduces the rate of its escape proportionally to the strength of correlations. In the limit of very high correlations (i.e. $f_V = 0$), the vacancy's net diffusion is null and so is its escape frequency. Manning further separates the total vacancy correlation factor into partial vacancy correlation factors that arise from each species separately

$$f_V = \frac{\sum_\alpha X_\alpha w_\alpha f_V^\alpha}{\sum_\alpha X_\alpha w_\alpha}, \tag{1.89}$$

where f_V^α is the partial vacancy correlation factor related to α. All of Manning's approximations reduce the number of different jump frequencies from an infinite number to $(N_{species}+1)$, where $N_{species}$ is the number of different α species, and the additional frequency is the vacancy escape frequency H. In a single-component system, the self-diffusion correlation factor, f_0, can be written as a function of the vacancy escape frequency (Eq. 1.83), which enables us to calculate this quantity from it as

$$H = \frac{2 f_0 f_V W_M}{1 - f_0}. \tag{1.90}$$

Remember that, as seen previously in Sec. 1.6.3.1, the self-diffusion correlation factor is a geometrical factor that can be determined based on the structure and an accurate database has already been established for different crystalline structures [100]. The correlation factor of tracer α is calculated using Eq. 1.83, where the vacancy-tracer exchange frequency is w_α and the escape frequency is given in Eq. 1.90

$$f_\alpha = \frac{f_0 f_V W_M}{w_\alpha \left(1 - f_0\right) + f_0 f_V W_M}. \tag{1.91}$$

Manning interestingly finds a relationship between the tracer correlation factor and the vacancy correlation factor. This equation is valid for all α species separately, and forms a system of non-linear $N_{species}$ independent equations with $(N_{species} + 1)$ correlation factors to be calculated. Vacancy flux equations derived on one hand using vacancy drift velocities, and on the other hand using atom fluxes, allow Manning to express the vacancy correlation factor as a function of the tracer correlation factors and obtain an additional equation to complete the system of Eq. 1.91. A brief summary of this work is detailed below, and for more details, one can refer to Manning's paper [19]. The vacancy flux compensates for the tracer fluxes through

$$\vec{J}_V = -\sum_\beta \vec{J}_\beta, \tag{1.92}$$

and both $\vec{J}_V$ and $\vec{J}_\beta$ can be expressed as a function of transport coefficients. Furthermore, since vacancies are at equilibrium in the system, there is no driving force related to a vacancy concentration or chemical potential gradient, and the vacancy flux depends on the vacancy equilibrium concentration and on the average vacancy drift velocity

$$\vec{J}_V = C_V \left\langle \vec{v}_F \right\rangle_V = C_V \sum_\alpha \left\langle \vec{v}_F \right\rangle_V^\alpha, \tag{1.93}$$

where C_V is the vacancy concentration per unit volume at equilibrium, $\left\langle \vec{v}_F \right\rangle_V = \sum_\alpha \left\langle \vec{v}_F \right\rangle_V^\alpha$ is the average vacancy drift velocity vector, and $\left\langle \vec{v}_F \right\rangle_V^\alpha$ is the average contribution to the vacancy drift velocity that results from the driving force of species α, $\vec{F}_V^\alpha = -\vec{\nabla}\mu_\alpha / \left(k_B T\right)$. The vacancy drift velocity is calculated using the general Nernst-Einstein equation which is valid for cubic crystals for a very low vacancy concentration, and Manning finds the final form of the vacancy flux (Eq. 1.93) to be

$$\vec{J}_V = -\sum_\alpha L_{V\alpha} \frac{\vec{\nabla}\mu_\alpha}{k_B T}, \tag{1.94}$$

with

$$L_{V\alpha} = X_\alpha D_\alpha \frac{f_V^\alpha}{f_\alpha}. \tag{1.95}$$

Here, D_α is the tracer diffusion coefficient of species α, and the passage from w_α to D_α happens by expressing the tracer diffusion coefficient as (see Sec. 1.6.1)

$$D_\alpha = f_V D_\alpha^0, \tag{1.96}$$

with the un-correlated part of the diffusion coefficient being

$$D_\alpha^0 = \frac{l^2 w_\alpha}{6}, \tag{1.97}$$

where l is the displacement distance. Manning also finds the expression of the flux of species α as

$$\vec{J}_\beta = -\sum_\alpha L_{\beta\alpha} \frac{\vec{\nabla}\mu_\alpha}{k_B T}, \tag{1.98}$$

where the transport coefficients are given as a function of the diffusion coefficients

$$\begin{cases} L_{\beta\beta} = X_\beta D_\beta \left[1 + \dfrac{(1-f_0)\, X_\beta D_\beta}{f_0 \sum_\alpha X_\alpha D_\alpha} \right], \\ \\ L_{\beta\alpha} = X_\beta D_\beta \left[\dfrac{(1-f_0)\, X_\alpha D_\alpha}{f_0 \sum_\alpha X_\alpha D_\alpha} \right], \qquad \alpha \neq \beta. \end{cases} \tag{1.99}$$

Using the flux equality (Eq. 1.92), a relation between the tracer correlation factor and the partial vacancy correlation factors is found

$$f_\alpha = f_0 f_V^\alpha. \tag{1.100}$$

This equation shows that, when the vacancy diffusion around α is not correlated (i.e. $f_V^\alpha = 1$), the tracer correlation factor is equal to the self-diffusion correlation factor, $f_\alpha = f_0$. This makes sense because the tracer's diffusion is vacancy-mediated, and in this case correlations are only geometrical. In the opposite case of a highly correlated vacancy diffusion around α (i.e. $f_V^\alpha = 0$), the diffusion of the tracer is also highly correlated ($f_A = 0$). In general, Eq. 1.100 states that the tracer's diffusion is f_0 times more correlated than the vacancy around it. Replacing Eq. 1.100 in Eq. 1.89, a relationship between the vacancy and tracer correlation factors is found

$$f_V = \frac{\sum_\alpha X_\alpha w_\alpha f_\alpha}{f_0 \sum_\alpha X w_\alpha}. \tag{1.101}$$

A system of $(N_{species} + 1)$ independent equations with $(N_{species} + 1)$ correlation factors is formed from Eq. 1.91 and Eq. 1.101

$$\begin{cases} f_\alpha = \dfrac{f_0 f_V W_M}{w_\alpha (1-f_0) + f_0 f_V W_M} \quad , \forall \alpha \\ \\ f_V = \dfrac{\sum_\alpha X_\alpha w_\alpha f_\alpha}{f_0 \sum_\alpha X_\alpha w_\alpha}. \end{cases} \tag{1.102}$$

By solving this system of equations, Manning's model allows for the calculation of all correlation factors (tracer and vacancy) in a self-consistent manner. Note that Manning's off-diagonal coefficients are always positive (all the terms in Eq. 1.99 are positive), and therefore his model is limited to cases where the cross coefficients are positive. For example, his model cannot be used to study drag phenomena.

Results

Manning applied his model to the case of a binary random alloy AB and calculated the vacancy and tracer correlation factors as a function of concentration for different values of the vacancy jump frequency ratio w_A/w_B. In this case, the vacancy escape frequency from any atom is calculated (using Eq. 1.90 and Eq. 1.102) as

$$H = \frac{X_A w_A + X_B w_B}{1 - f_0} - w_A - w_B + \left[\left(\frac{X_A w_A + X_B w_B}{1 - f_0} - w_A - w_B \right)^2 + \frac{4 w_A w_B f_0}{1 - f_0} \right]^{1/2} . \tag{1.103}$$

The tracer correlation factors of $\alpha \in [A, B]$,

$$f_\alpha = \frac{H}{2w_\alpha + H}, \tag{1.104}$$

and the vacancy correlation factor,

$$f_V = \frac{\sum_\alpha X_\alpha w_\alpha f_\alpha}{f_0 \sum_\alpha X_\alpha w_\alpha}, \tag{1.105}$$

are given in their general form and can be easily calculated knowing the vacancy escape frequency H. These analytical expressions are very simple to use directly, and are only a function of the concentrations and jump frequencies. It is therefore no surprise that they have been extensively used since.

Several Monte Carlo simulations of a vacancy-tracer diffusion in a binary random alloy have been performed to test the validity of the Manning model in different crystalline structures: SC [31], BCC [29,31] and FCC [30–32]. The conclusions of all the comparisons are consistent. They showed that Manning's model accurately reproduces the vacancy correlation factor and the fastest and slowest tracer correlations factors at all concentrations for a jump frequency ratios w_A/w_B are below 10. In the range of higher jump frequency ratios, the vacancy correlation factor exhibits a small but non-negligible deviation below the critical percolation concentration, while the tracer correlation factors deviate in a more noticeable manner. The percolation concentration found by Manning is equal to $(1 - f_0)$ and is a good first approximation of the exact value in several structures. In all cases, Manning's model captures the percolation phenomena behavior of the correlation factors and predicts a percolation limit within satisfying accuracy. In the case of a BCC ternary alloy in which the maximum jump frequency ratio is 100, Belova *et al.* [33] showed that the collective transport coefficients of Manning's theory are in semi-quantitative agreement with Monte Carlo simulations, and that off-diagonal transport coefficients are the least accurate ones.

Conclusion

The beauty of Manning's model is its simplicity. Despite its simplicity, the binary random alloy model provides a very good approximation of the correlation factors of the vacancy and of both the slowest and fastest tracers. The agreement is less satisfying when the jump frequency ratios are high, but it still manages to predict a satisfying percolation threshold. To globally reproduce the percolation phenomena one needs to properly describe both short and long range order through the exchange frequencies, and as will be shown in later models, this is not a trivial task. Manning's model manages to do this despite its simplicity which is one of its major fortes. The model's general agreement with Monte Carlo simulations shows that the average frequencies introduced in the model are able to well reproduce the exact vacancy-tracer exchange frequencies and the exact vacancy escape frequency, or at least the ratio between them. The RA model has however its limitations. More importantly, the RA model is only valid for alloys in which thermodynamic interactions can be neglected and in which diffusion is mediated by a low concentration of vacancies. Extending the model to ordered alloys in general is not trivial and may be impossible.

1.7.2 Other random alloy models

Since 1971, many works have been inspired by Manning's random alloy model in hopes of both generalizing it and improving its accuracy. The main limitation of Manning's model is that it is not a good approximation in the case of interacting alloys. Belova *et al.* [101] extended the model to an ordered binary alloy that has two random sublattices and in which intrasublattice jumps are not allowed. This limits the model to ordered alloys in which jumps happen within each sublattice independently and in which the distribution of atoms on each sublattice can be approximated by a random distribution.

Bocquet [102] applied the random alloy model to the case of dumb-bell intestitial diffusion but, even though the results were in reasonable agreement with Monte Carlo simulations, he found that there is not a general simple analytical solution in this case. Besides the fact that the random alloy applies mainly in the case of a vacancy-mediated diffusion, another of the model's limitations is that it treats alloys with a low vacancy concentration. This has been addressed by Moleko and Allnatt in 1988 [103], in a work in which they extend the random alloy model to an arbitrary vacancy concentration. This type of model is known as the "random lattice gas" model, however their results were not accurate for high vacancy concentrations. Among the "random lattice gas" based models, it is worth noting those developed in 1986 by Holdsworth and Elliott (HE) [43], in 1989 by Moleko, Allnatt and Allnatt (MAA) [44], and in 2016 by Paul *et al.* (Manning+HE) [36]. The HE model applies to a multicomponent alloy and for a general vacancy concentration, and the combined Manning+HE model was tested in the case of a ternary alloy. The HE results obtained in the case of a binary random alloy are in general good agreement with Monte Carlo simulations, especially for the slow diffusing species, and in better agreement than Manning's model. The main drawback of the HE method is its theoretical complexity. The MAA can be applied to any vacancy concentration, and, even though it presents the best accuracy at all jump frequency ratios in the case of binary alloys, it cannot in practice be extended to alloys with more than three components. A theoretically lighter version was later presented by Allnatt *et al.* [45]. They calculated with this new version tracer correlation factors of the fastest and slowest diffusing species in binary, ternary, quaternary and quinary alloys. By comparing their results to Monte Carlo simulations, they found that their model is less accurate than the original MAA, but that it still well reproduces the tracer correlation factor of the fastest (with high accuracy) and slowest diffusing species (with less accuracy). Even though this new MAA-light can treat alloys with more than three components, it still requires an iterative numerical calculation for alloys with five or more components. This method is more complex to use than the combined Manning and HE theory, however it is much more accurate, especially for the fast diffusing species which is usually the hardest to reproduce with accuracy.

It is worthwhile to note that Moleko and Allnatt [103] derived the following exact analytical relations between the tracer correlation factors and the jump frequencies

$$\sum_{\beta} f^{(\alpha)}_{\alpha\beta} \frac{w_\alpha}{w_\beta} = 1, \tag{1.106}$$

and this relation should be used to verify the validity of a diffusion model applied to a random alloy. In a binary alloy, this reduces the number of tracer correlation factors needed to be calculated to just one factor.

All the above mentioned models were restrained to the case of a random alloy because their generalization to the case of an interacting alloy was too complicated. The next two paragraphs will focus on two methods that were developed to calculate all the transport coefficients in an interacting alloy.

1.7.3 Kikuchi's Path Probability Method (PPM)

The method

The Path Probability Method (PPM) developed by Kikuchi in 1966 [21] was the first method to allow the calculation of the full Onsager matrix in an interacting concentrated alloy and the expression of transport coefficients as a function of measurable microscopic quantities. A few years earlier in 1951, Kikuchi had developed the Cluster Variation Method (CVM) to approximate the entropy and free energy of an order-disorder system at equilibrium [104]. In the CVM, a cluster of a finite size is chosen and used to represent the whole system along with smaller sized clusters that are included in it. The level of approximation is controlled by the size of the biggest cluster introduced - point, pair, triangle, tetrahedron, etc... At equilibrium, a configuration of the system is described by a set of state variables $\{\alpha\}$ whose definition depends on the approximation. In the point approximation, the state variables represent site occupation probabilities, in the pair approximation they represent nearest-neighbors pair occupation probabilities, and so on. The energy of a configuration is written as a function of $\{\alpha\}$, $E(\{\alpha\})$, and its probability is written as

$$P(\{\alpha\}) = \frac{1}{Z} \exp\left(-\frac{E(\{\alpha\}) - TS(\{\alpha\})}{k_B T}\right), \tag{1.107}$$

where the entropy, $S(\{\alpha\})$, is obtained as a function of the state variables by calculating the number of ways of filling the lattice sites with clusters of specific atomic species. Z is the partition function of the system, and it is expressed as a function of the free energy $F(\{\alpha\})$ as

$$Z = \sum_{\{\alpha\}} \exp\left(-\frac{E(\{\alpha\}) - TS(\{\alpha\})}{k_B T}\right) = \exp\left(-\frac{F(\{\alpha\})}{k_B T}\right). \tag{1.108}$$

Using the variational principle, the most probable configuration of the system is found by minimizing the free energy with respect to the state variables

$$\frac{\partial F(\{\alpha\})}{\partial \{\alpha\}} = 0, \tag{1.109}$$

and equilibrium quantities can then be deduced. Note that minimizing the free energy is equivalent to maximizing the probability $P(\{\alpha\})$, and therefore to finding the most probable state of the system

$$Z \approx \max\left[\exp\left(-\frac{E(\{\alpha\}) - TS(\{\alpha\})}{k_B T}\right)\right]. \tag{1.110}$$

The CVM was then extended to out-of-equilibrium time-dependent processes, in what is known as the PPM. In the PPM, the state variables are time-dependent, $\alpha\left(t\right)$, and additional variables named "path variables", $A\left(t_0, t_0+\Delta t\right)$, are introduced to describe the change in the cluster configuration that is happening between times t_0 and $t_0+\Delta t$. The probability of a certain state of the system occuring at time $t_0+\Delta t$, $P\left[A\left(t_0, t_0+\Delta t\right)\right]$, is calculated as the probability that a path $A\left(t_0, t_0+\Delta t\right)$ occurs during Δt. The PPM then consists in expressing this path probability as a function of microscopic quantities and maximizing it to find the most probable path. The path variables should then satisfy the condition

$$\frac{\partial P\left[A\left(t_0, t_0+\Delta t\right)\right]}{\partial A}=0. \tag{1.111}$$

The state variables, the path variables and the path probabilities are written depending on the problem at hand. The path probability is usually written as a function of several parameters such as the entropy term calculated using the CVM, a transition rate factor, an exponential of interaction energies, a diffusion activity term and the lattice coordination number. The path probability is then maximized with respect to the path variables by fixing the initial state variables of the system. Then the time evolution of the state variables can be deduced. By considering the steady state close to equilibrium, the flux is then directly calculated as the net current of atoms jumping in a given direction or through a specific site or plane, and the transport coefficient matrix is deduced. The PPM consists then in finding the most probable path that a cluster configuration takes to change with time. The way the PPM is built as the dynamic version of the CVM ensures a coherence between the thermodynamic and kinetic approximations by ensuring the same level of approximations in both. However, as will be shown later in its applications, this makes the method too complex to be used beyond the pair approximation and prevents a good description of the paths. For more details on the theory behind the PPM, the reader can refer to one of these reviews by Sato [105] and Akbar [106].

Applications

Throughout the years, the PPM has been used to study thermal diffusion, chemical diffusion and tracer diffusion, but mostly it has been used within the pair approximation to study second-order phase transitions in BCC binary alloys [107–109]. In the first paper [21], the PPM was applied by Kikuchi to study relaxation towards equilibrium of an order-disorder AB system and the relaxation time was calculated in the case of a disordered equilibrium state. Kikuchi [94] also used it to study vacancy diffusion in an ordered BCC ternary alloy analytically, and he calculated the isotope diffusion coefficient in a binary BCC alloy as a function of concentration and degree of order for different temperatures and interaction energies. An application to the BCC AgMg alloy showed agreement with experimental results. Therefore, in addition to calculating transport coefficients of interacting concentrated alloys, the PPM allows the study of phase transformations of spinodal decomposition. The method was however limited to the pair approximation in most cases, which cannot be used, for example, to study FCC alloys with first-order transitions. The first attempt to extend the PPM beyond the pair approximation was made by McCoy *et al.* in 1982 [95]. They used a triangle approximation in the simplest case of a 2D triangular lattice. They showed how a lot of complexities arise to find the proper independent state variables and construct the path probabilities. Another attempt was made by Wada et al. to extend the PPM to a triangle approximation to study the kinetics of a 2D ferromagnetic Ising system [110]. Even though in theory the PPM can be extended beyond the pair approximation, it remains a difficult task because the number of independent state variables increases and one cannot visualize the different possible paths and their constraints necessary to write and solve the equations. Even though the PPM showed satisfactory results in studying several diffusion problems, in particular second-order phase transitions in BCC binary alloys, it has shown some limitations when calculating correlation factors. These limitations are not only due to the pair approximation but also to the PPM formalism itself. This will be further discussed below.

Kikuchi [46] studied the general case of diffusion via a vacancy mechanism in a binary solid solution AB using the pair approximation model. He calculated the correlation factors for a BCC structure in the special cases of self-diffusion, impurity diffusion, and tracer diffusion in a concentrated random alloy.

- In the case of self-diffusion, the calculated correlation factor has the same form as a first-order approximation, $f_0 = (z-1) \,/\, (z+1)$, $z = 8$ being the coordination number in a BCC structure. This value deviates by around 7% from the exact one, and the discrepancy is due to the pair approximation that considers in this case trajectories of one jump (as was seen in Fig. 1.9). The calculated escape frequency is calculated by considering that a vacancy that just jumped from site i to site j has a zero probability of returning to the site j after it has exchanged with one of its $(z-1)$ neighboring sites. The calculated escape frequency is

$$H = (z-1)\,\hat{w}, \tag{1.112}$$

with $\hat{w}$ being the jump frequency which includes the effect of the surrounding atoms. In reality, the probability of a vacancy returning after a first jump away from the tracer is not null because not all $(z-1)$ jumps will be effective in randomizing the position of the vacancy, and the PPM therefore overestimates the escape frequency.

- In the case of impurity diffusion, the escape frequency from impurity B calculated using the PPM is the same as the one calculated in the case of self-diffusion, since all sites except the one occupied by B are occupied by A atoms, so that

$$H_B = (z-1)\,\hat{w}_A. \tag{1.113}$$

This is also a higher frequency than the real one and overestimates the correlation factor.

- In the case of a binary random alloy, the correlation factor of tracer A^* was calculated and compared to Manning's for a jump frequency ratio w_A/w_B ranging between 0.1 and 10^3. The two methods are in good agreement for ratios lower or equal to 10, while the PPM deviates from Manning's results for higher ratios. In particular, the PPM does not reproduce the critical percolation concentration and the correlation factor is not null for concentrations below the critical concentration. Again, this is caused by an overestimation of the escape frequency; below the critical concentration, a connected cluster of A atoms that extends to infinity cannot form and the escape frequency from A should be null, whereas in the PPM the escape frequency is greater than zero and obtained as

$$H_A = (z-1)\,\frac{2q_B\hat{w}_B + q_A\left(\hat{w}_A + \hat{w}_B\right)}{2q_B\hat{w}_A + q_A\left(\hat{w}_A + \hat{w}_B\right)}\hat{w}_B, \tag{1.114}$$

where q_α is an equilibrium quantity proportional to the probability of finding an α atom as a nearest-neighbor of the vacancy. It is true that in most real alloys the jump frequency ratios are below 10, however, failing to reproduce the percolation phenomena reveals the method's inability to properly reproduce long-range order. Note that these deviations from the expected correlation factors are not only due to the pair approximation but also to the formalism itself, and to how the CVM was extended.

Revised PPM

The failure of the PPM in predicting the percolation phenomena and its underperformance compared to the CVM at the same level of approximation is due to the fact that, in the PPM, the state variables and the path probabilities are averaged with respect to the ensemble of states and not with respect to the real space. The real space is assumed to be constructed by translating replicas of the ensemble averaged states which results in a homogeneous space. This explains why the PPM yields satisfactory results when the system is represented by a homogeneous lattice and the fluctuations of energies and jump frequencies are small. This also means that the PPM works best when the diffusion of a large number of atoms is being followed, because then the space average becomes more accurate. This also means that the PPM cannot predict precise correlations between consecutive transitions of configurations, which are needed to follow the diffusion of a single atom, like in the case of tracer correlation calculations. Furthermore, in a random binary alloy, as long as both species are present in an averaged state of the system, there are no restrictions that prevent an infinitely connected cluster of A atoms to form, even if the A composition is below its critical percolation value. In 1983, Kikuchi introduced a correction to the PPM in the pair approximation by replacing ensemble averages with time averages [47]. This allows the PPM to predict the time evolution of a single system instead of an ensemble system, and therefore the behavior of a small number of atoms. This revised version of yields the same values as the CVM of the correlation factor in the cases of self-diffusion and impurity diffusion. In the case of a random binary alloy, the accuracy of the newly calculated correlation factors is greatly improved for all jump ratios and the percolation phenomena is well described. This revised PPM has not been extensively applied to transport phenomena problems and its generalization beyond the pair approximation is theoretically very complex and has not been done.

Conclusion

The PPM allows the expression of transport coefficients as a function of measurable microscopic quantities. The system is represented by state variables, the most probable path is found by maximizing the path probability function, and the time evolution of the averaged system is studied. It provides control over the approximation by choosing the size of the cluster, however it was mostly used within the pair approximation, and the attempts to extend it beyond that showed great theoretical complexity. The PPM is a good method for modeling second order phase transformations which are homogeneous in space. The revised version of the PPM replaces ensemble averages with time averages and allows for the study of the time evolution of a single system. The revised PPM is a good method to use when the diffusion of a small number of atoms is followed, like in the case of tracer diffusion. It has been mainly applied to the case of a random binary alloy and only within the pair approximation due to its complexity. Even though the PPM and its revised version allow the study of both tracer and non-tracer diffusion, the system dependence of all state variables and path functions make this method hard to generalize to complex systems, even within the pair approximation model.

1.7.4 Nastar's Self-Consistent Mean-Field theory (SCMF-o)

A more recent model is the Self-Consistent Mean-Field theory, which was developed in 2000 by Nastar *et al.* [22] to calculate the transport coefficients in alloys. In this thesis, we will call this original formulation of the Self-Consistent Mean-Theory by the abbreviation SCMF-o. Several subsequent works have extended this theory to other approximations or systems, which allowed for its application to a great variety of diffusion problems [48–50, 98, 99, 111–114]. The theory considers a stationary system in a state close to a homogeneous equilibrium driven by stationary chemical potential gradients. The distribution function is defined as a correction to the equilibrium distribution in the same way as Vaks [97] defined it, however, unlike the work of Vaks where the Onsager matrix is diagonal, the SCMF-o manages to compute the full Onsager matrix. The correction to the equilibrium distribution function is written as a function of unknown effective interactions to be calculated. A master equation defines the time evolution of the system and microscopic detailed balance is assumed at equilibrium. The stationnarity condition allows the calculation of the unknown effective interactions as a linear function of the chemical potential gradients by dividing each configuration into finite sized clusters surrounded by a mean-field. These effective interactions are used in a self-consistent manner to calculate the flux as a linear function of chemical potential gradients, and a symmetric non-diagonal Onsager matrix is obtained. To simplify the theoretical framework of this method and to make it more accessible, Schuler *et al.* reformulated it in 2020 and implemented it in an open-source code called KineCluE [18]. However, their reformulation was limited to dilute alloys and one of the main objectives of this thesis is to extend KineCluE to concentrated alloys. In Chapter 3, we will present the new formulation and its implementation in the KineCluE code, and we will present the work done within this thesis to extend KineCluE to concentrated alloys. Therefore, the theoretical details of the SCMF-o theory needed for an understanding of Chapter 3 are outlined below.

Distribution function

Consider a system in the Grand Canonical ensemble, in which n represents one configuration of the system in which all atomic positions are occupied by well defined atomic species up to infinity. The physical Hamiltonian H_n of n is given by

$$H_n = \frac{1}{2!} \sum_{i,j,\alpha,\beta} V_{ij}^{\alpha\beta} n_i^\alpha n_j^\beta + \frac{1}{3!} \sum_{i,j,k,\alpha,\beta,\gamma} V_{ijk}^{\alpha\beta\gamma} n_i^\alpha n_j^\beta n_k^\gamma + ..., \tag{1.115}$$

where n_i^α is the occupation number of site i with atomic species α ($n_i^\alpha = 1$ if site i is occupied by species α, and 0 otherwise), and $V_{ij...}^{\alpha\beta...}$ is the thermodynamic interaction between atomic species α, β, ... occupying sites i, j, ... At equilibrium, the probability of a configuration n is given by a Boltzmann distribution of the form

$$P_n^0 = \exp\left(-\frac{H_n - \sum_{i,\alpha} n_i^\alpha \mu^\alpha - \Omega}{k_B T}\right), \tag{1.116}$$

with μ^α being the chemical potential of species α. Note that, at equilibrium, chemical potentials are homogeneous. Ω is a normalization constant, such that

$$\Omega = k_B T \ln Z, \tag{1.117}$$

where k_B is the Boltzmann constant, T is the temperature, and Z is the partition function of the system

$$Z = \sum_n \exp\left(-\frac{H_n - \sum_{i,\alpha} n_i^\alpha \mu^\alpha}{k_B T}\right). \tag{1.118}$$

The model assumes the presence of uniform and stationary chemical potential gradients (CPG) driving the system out of equilibrium. As a consequence, fluxes of the different species present in the system arise. The chemical potential gradients are taken small enough for the system to be in an out-equilibrium state close to the homogeneous equilibrium state, and for fluxes to be written as a linear function of the CPG. The out-of-equilibrium probability of a configuration n is considered to be a deviation of the equilibrium probability

$$P_n = P_n^0 \delta P_n, \tag{1.119}$$

and the deviation δP_n has the same mathematical form as the equilibrium probability, except that now, the chemical potential is not homogeneous

$$\delta P_n = \exp\left(-\frac{h_n - \sum_{i,\alpha} n_i^\alpha \delta\mu_i^\alpha - \delta\Omega}{k_B T}\right). \tag{1.120}$$

Here $\delta\mu_\alpha$ and $\delta\Omega$ include the corrections needed on respectively the chemical potentials and the normalization constant, while h_n includes all other corrections. To calculate h_n, they use the Cluster Expansion Theorem [115] which shows that any function of n can be written as a Hamiltonian function

$$h_n = \frac{1}{2!} \sum_{i,j,\alpha,\beta} \nu_{ij}^{\alpha\beta} n_i^\alpha n_j^\beta + \frac{1}{3!} \sum_{i,j,k,\alpha,\beta,\gamma} \nu_{ijk}^{\alpha\beta\gamma} n_i^\alpha n_j^\beta n_k^\gamma + ... \tag{1.121}$$

h_n is called the effective Hamiltonian and $\nu_{i,j,...}^{\alpha,\beta,...}$ are called the N-body effective interactions, which are not a Hamiltonian or interactions in the thermodynamic sense. In fact, they represent the deviation from equilibrium caused by the driving forces and are therefore kinetic properties. Jump mechanisms change the configuration n of the system to a configuration m. The time evolution of the out-of-equilibrium distribution function is described by means of master equations

$$\forall n,\ \frac{dP_n}{dt} = \sum_m \left(P_m W_{mn} - P_n W_{nm}\right), \tag{1.122}$$

where W_{nm} is the transition frequency from a configuration n to a configuration m. The master equation describes the microscopic evolution of the probability of each configuration n as the probability of being in any configuration m and transitioning to a configuration n minus the probability of being in configuration

n and transitioning to any configuration m. It is therefore the difference between the probability of transitioning out of configuration n and the probability of transitioning into it. At equilibrium, the distribution function is stationary

$$\forall n,\ \frac{dP_n^0}{dt} = \sum_m \left(P_m^0 W_{mn} - P_n^0 W_{nm}\right) = 0, \tag{1.123}$$

and the global detailed balance holds

$$\forall n,\ \sum_m P_m^0 W_{mn} = P_n^0 \sum_m W_{nm}. \tag{1.124}$$

Furthermore, microscopic detailed balance is supposed to hold, which implies that

$$\forall n,\ \forall m,\ P_m^0 W_{mn} = P_n^0 W_{nm}. \tag{1.125}$$

Note that microscopic detailed balance (Eq. 1.125) implies general detailed balance (Eq. 1.124), while the opposite is not true.

Transport coefficients The flux of species β from site i to site j, $J_{i\to j}^{\beta}$, is calculated using the continuity equation (Eq. 1.21) applied locally

$$\frac{dX_i^\beta}{dt} = -\sum_j J_{i\to j}^{\beta}, \tag{1.126}$$

where X_i^β is the atomic fraction of β at site i. The macroscopic flux of β is calculated in cubic crystals as

$$J^\beta = \frac{a}{V_{at}} \sum_j J_{i\to j}^{\beta}, \tag{1.127}$$

where a is the lattice parameter, and V_{at} is the atomic volume per site. The site concentration can be calculated as the average of site occupancy

$$X_i^\beta = \sum_n P_n n_i^\beta = \left\langle n_i^\beta \right\rangle. \tag{1.128}$$

In order to calculate the time evolution of the site concentration

$$\frac{dX_i^\beta}{dt} = \frac{d}{dt}\sum_n P_n n_i^\beta = \sum_n \frac{dP_n}{dt} n_i^\beta, \tag{1.129}$$

one needs to calculate the time evolution of the out-of-equilibrium distribution function. Note that the inversion between the sum and the derivative can be made because the phase space is constant over time. Combining Eq. 1.122 with Eq. 1.119 and using the microscopic detailed balance (Eq. 1.125), the time evolution of P_n can be calculated as

$$\frac{dP_n}{dt} = P_n^0 \sum_m W_{nm}\left(\delta P_m - \delta P_n\right). \tag{1.130}$$

The difference in the deviations from equilibrium $\delta P_m - \delta P_n$ needs to be calculated. Since the system is considered close to equilibrium, $P_n \simeq P_n^0$, $\delta P_n \simeq 1$, and equivalently $h_n - \sum_{i,\alpha} n_i^\alpha \delta\mu_i^\alpha - \delta\Omega$ vanishes at equilibrium. A first-order Taylor expansion can be made of the exponential of δP_n so that it becomes

$$\delta P_n \simeq 1 - \frac{h_n - \sum_{i,\alpha} n_i^\alpha \delta\mu_i^\alpha - \delta\Omega}{k_B T}. \tag{1.131}$$

The difference in deviations becomes

$$\delta P_m - \delta P_n \simeq \frac{h_n - h_m + \sum_{i,\alpha} (m_i^\alpha - n_i^\alpha)\,\delta\mu_i^\alpha}{k_B T}. \tag{1.132}$$

Remember that it was assumed that the chemical potential gradients are constant, which allows us to express $\delta\mu_i^\alpha$ in terms of the macroscopic chemical potential gradient $\vec{\nabla}\mu_\alpha$, and as a function of a reference chemical potential $\delta\mu_r^\alpha$, which is the chemical potential of α at a reference point r where its value is known

$$\delta\mu_i^\alpha = \delta\mu_r^\alpha + \vec{\nabla}\mu^\alpha \vec{ri}. \tag{1.133}$$

The product in Eq. 1.132 becomes

$$\sum_{i,\alpha} (m_i^\alpha - n_i^\alpha)\,\delta\mu_\alpha^i = \delta\mu_\alpha^r \sum_{i,\alpha} (m_i^\alpha - n_i^\alpha) + \sum_{i,\alpha} (m_i^\alpha - n_i^\alpha)\,\vec{\nabla}\mu_\alpha \vec{ri}. \tag{1.134}$$

The first sum is null since the number of atoms of each species is considered to be the same in all configurations of the system

$$\sum_{i,\alpha} (m_i^\alpha - n_i^\alpha) = \sum_\alpha (m^\alpha - n^\alpha) = N_{at} - N_{at} = 0, \tag{1.135}$$

where N_{at} is the total number of atoms in the system. The second sum can be expressed in terms of the total displacement vector of species α from configuration n to m, $\vec{d}_{nm}$, by writing for each α

$$\sum_i (m_i^\alpha - n_i^\alpha)\,\vec{ri} = \sum_i \left[\vec{ri} - \left(\vec{ri} + \vec{d}_{mn}^{\alpha i}\right)\right] = -\vec{d}_{mn}^\alpha = \vec{d}_{nm}^\alpha. \tag{1.136}$$

Note that $\vec{d}_{nm}^{\alpha i}$ is the displacement vector of species α between configurations n and m, such that α was at site i in configuration n and moved a distance of $\left\|\vec{d}_{nm}^{\alpha i}\right\|$ from site i in configuration m. The difference in deviations from equilibrium probabilities can now be written as

$$\delta P_m - \delta P_n \simeq \frac{h_n - h_m}{k_B T} + \sum_\alpha \vec{d}_{nm}^\alpha \cdot \frac{\vec{\nabla}\mu_\alpha}{k_B T}. \tag{1.137}$$

The time evolution of the site concentration is deduced by replacing the above equation in Eq. 1.130 and Eq. 1.129

$$\frac{dX_i^\beta}{dt} = \sum_n P_n^0 n_i^\beta \sum_m W_{nm} \left(\frac{h_n - h_m}{k_B T} + \sum_\alpha \vec{d}_{nm}^\alpha \cdot \frac{\vec{\nabla}\mu_\alpha}{k_B T} \right). \tag{1.138}$$

The sum over configurations m that are accessible from configuration n can be rewritten as a sum over jumps that take atom β from site i in configuration n to site j in configuration m

$$\frac{dX_i^\beta}{dt} = \sum_n P_n^0 n_i^\beta \sum_{j \neq i} m_j^\beta W_{nm} \left(\frac{h_n - h_m}{k_B T} + \sum_\alpha \vec{d}_{nm}^\alpha \cdot \frac{\vec{\nabla}\mu_\alpha}{k_B T} \right). \tag{1.139}$$

The flux from site i can be finally expressed as a function of the homogeneous gradient of chemical potential and the unknown effective Hamiltonians

$$\sum_j J_{i\to j}^{\beta} = \sum_n P_n^0 n_i^{\beta} \sum_{j\neq i} m_j^{\beta} W_{nm} \left(\frac{h_m - h_n}{k_B T} - \sum_{\alpha} \vec{d}_{nm}^{\alpha} \cdot \frac{\vec{\nabla}\mu_{\alpha}}{k_B T} \right), \tag{1.140}$$

or equivalently as a function of the effective interactions

$$\begin{aligned} \sum_j J_{i\to j}^{\beta} = \sum_n P_n^0 n_i^{\beta} \sum_{j\neq i} m_j^{\beta} W_{nm} & \left[\frac{1}{2!} \sum_{i,j,\alpha,\beta} \frac{\nu_{ij}^{\alpha\beta}}{k_B T} \left(m_i^{\alpha} m_j^{\beta} - n_i^{\alpha} n_j^{\beta} \right) \right. \\ & \left. + \frac{1}{3!} \sum_{i,j,k,\alpha,\beta,\gamma} \frac{\nu_{ijk}^{\alpha\beta\gamma}}{k_B T} \left(m_i^{\alpha} m_j^{\beta} m_k^{\gamma} - n_i^{\alpha} n_j^{\beta} n_k^{\gamma} \right) + \ldots \right] \\ & - \sum_n P_n^0 n_i^{\beta} \sum_{j\neq i} m_j^{\beta} W_{nm} \sum_{\alpha} \vec{d}_{nm}^{\alpha} \cdot \frac{\vec{\nabla}\mu_{\alpha}}{k_B T}. \end{aligned} \tag{1.141}$$

Note that this flux can also be expressed as an ensemble average over the equilibrium distribution function

$$\sum_j J_{i\to j}^{\beta} = \left\langle n_i^{\beta} \sum_{j\neq i} m_j^{\beta} W_{nm} \left(\frac{h_m - h_n}{k_B T} - \sum_{\alpha} \vec{d}_{nm}^{\alpha} \cdot \frac{\vec{\nabla}\mu_{\alpha}}{k_B T} \right) \right\rangle. \tag{1.142}$$

As can be seen in the two equations above, to calculate the flux, it is necessary to first determine the effective Hamiltonians, or equivalently the effective interactions.

Effective interactions The SCMF-o finds a self-consistent way to calculate the effective interactions as a linear function of the chemical potential gradients and then reinjects them into the flux equations to obtain the full Onsager matrix. In a stationary system, even though the system is evolving at the microscopic level, the distribution probability remains constant, and therefore

$$\forall n, \ \frac{dP_n}{dt} = 0. \tag{1.143}$$

Effective interactions cannot in theory be calculated from this stationnarity equation because it is a function of a large number of interactions. Instead of applying stationnarity to the distribution function, the SCMF-o constructs a set of kinetic equations by applying the stationnarity principle to a finite number of moments of the distribution function and calculates from each one of them an effective interaction. The moments of order 1, 2, 3, ... are defined as $\langle n_i^{\alpha} \rangle_{oe}^{(1)}$, $\left\langle n_i^{\alpha} n_j^{\beta} \right\rangle_{oe}^{(2)}$, $\left\langle n_i^{\alpha} n_j^{\beta} n_k^{\gamma} \right\rangle_{oe}^{(3)}$, ... such that

$$\langle n_i^{\alpha} \rangle_{oe}^{(1)} = \sum_n P_n n_i^{\alpha} = X_i^{\alpha}, \tag{1.144}$$

$$\left\langle n_i^{\alpha} n_j^{\beta} \right\rangle_{oe}^{(2)} = \sum_n P_n n_i^{\alpha} n_j^{\beta}, \tag{1.145}$$

$$\left\langle n_i^{\alpha} n_j^{\beta} n_k^{\gamma} \right\rangle_{oe}^{(3)} = \sum_n P_n n_i^{\alpha} n_j^{\beta} n_k^{\gamma}, \ldots \tag{1.146}$$

and so on, such that the brackets here $\langle . \rangle_{oe}$ represent averages over the out-of-equilibrium distribution function. Note that the first moment is equal to the site concentration X_i^α. Under steady-state conditions, all these moments become independent of time and the stationnarity principle can be applied to them. The kinetic approximation in the SCMF-o consists in truncating the effective Hamiltonian to a finite number of effective interactions, n_ν, and in calculating each of the n_ν effective interactions from its corresponding stationnarity equation. In other words, the N-th order effective interaction $\nu_{ijk...}^{\alpha\beta\gamma...}$ is calculated from the N-th moment stationnarity equation

$$\frac{d\left\langle n_i^\alpha n_j^\beta n_k^\gamma ... \right\rangle_{oe}^{(N)}}{dt} = \frac{d}{dt}\sum_n P_n n_i^\alpha n_j^\beta n_k^\gamma ... = \sum_n \frac{dP_n}{dt} n_i^\alpha n_j^\beta n_k^\gamma ... = 0. \tag{1.147}$$

This allows for the calculation of a finite number of effective interactions. For example, if a pair approximation is used for the effective interactions, all effective interactions other than $\nu_{ij}^{\alpha\beta}$ are considered to be null and there is only a 2-body effective interaction to be calculated. From the 2^{nd} moment stationnarity equation (Eq. 1.145),

$$\left\langle n_i^\alpha m_j^\beta W_{nm} \left[\frac{1}{2!} \sum_{i,j,\alpha,\beta} \frac{\nu_{ij}^{\alpha\beta}}{k_B T} \left(m_i^\alpha m_j^\beta - n_i^\alpha n_j^\beta \right) \right] \right\rangle = \left\langle n_i^\alpha m_j^\beta W_{nm} \sum_\alpha \vec{d}_{nm}^\alpha \cdot \frac{\vec{\nabla}\mu_\alpha}{k_B T} \right\rangle, \tag{1.148}$$

and $\nu_{ij}^{\alpha\beta}$ are obtained as a linear function of the chemical potential gradients by solving the linear system of equations of the form of Eq. 1.148. Note that, even though we assumed a pair approximation for effective interactions, we made no approximations on the distance between two species (i.e. sites i and j do not have to be first nearest-neighbors sites). In the same way, any N-body effective interaction is obtained as a linear function of the chemical potential gradients by solving the system of linear equations formed by the N moment stationnarity equations.

Back to the transport coefficients As shown in the previous paragraph, the effective interactions can be calculated as a linear function of the driving forces by using the stationnarity of the moments of the distribution function. To simplify the notations, the sum over all effective interactions that appears in the flux equation 1.141 (sum in brackets) can be written as a linear function of the chemical potential gradients

$$\nu_{ij}^{\alpha\beta} = \sum_\alpha \vec{\kappa}_{ij,\alpha} \cdot \vec{\nabla}\mu_\alpha, \tag{1.149}$$

such that $\vec{\kappa}_{ij,\alpha}$ is the calculated proportionality constant. Using Eq. 1.127 and Eq. 1.141, the macroscopic flux becomes a linear function of the driving force

$$J^\beta = \frac{a}{V_{at}} \sum_n P_n^0 \sum_j n_i^\beta m_j^\beta W_{nm} \sum_\alpha \left(\vec{\kappa}_{ij,\alpha} - \vec{d}_{nm}^\alpha \right) \cdot \frac{\vec{\nabla}\mu_\alpha}{k_B T}, \tag{1.150}$$

and the Onsager transport coefficients along a direction $\vec{e}_\mu$ can be identified using Eq. 1.141

$$L^d_{\beta\alpha} = \frac{a}{V_{at}} \sum_n P^0_n \sum_j n^\beta_i m^\beta_j W_{nm} \sum_\alpha \left(\kappa^\mu_{ij,\alpha} - d^{\alpha\mu}_{nm} \right), \tag{1.151}$$

where $\kappa^\mu_{ij,\alpha}$ and $d^{\alpha\mu}_{nm}$ are projections along the CPG direction, $\vec{e}_\mu$. Again, we see that the macroscopic transport coefficients can be calculated as a thermodynamic average over the equilibrium distribution function

$$L^d_{\beta\alpha} = \left\langle \frac{a}{V_{at}} \sum_j n^\beta_i m^\beta_j W_{nm} \sum_\alpha \left(\kappa^\mu_{ij,\alpha} - d^{\alpha\mu}_{nm} \right) \right\rangle. \tag{1.152}$$

Within the framework of the SCMF-o theory, in case the effective interactions are neglected, the Onsager matrix is diagonal (all cross coefficients are null), meaning that the effective interactions contain all the information on kinetic correlations. This is the reason why Vaks' theory lead to a diagonal Onsager matrix [97]. Hence the importance of taking them into consideration. Even though it wasn't formally proven, the more effective interactions are considered, the better the description of correlations and the more precise the result of the SCMF-o is, which allows the choice and control of balance between complexity and precision. The SCMF-o has the great advantage of producing the full Onsager matrix and taking into consideration correlations, as can be seen from the above equations. The only other theory that had managed to achieve these two things was the PPM which was discussed in the previous section (Sec. 1.7.3). Additionally, Eq. 1.152 shows the decoupling in the SCMF-o between the thermodynamic approximation (P^0_n) and the kinetic approximation ($\kappa^\mu_{ij,\alpha}$).

Applications In the first SCMF-o paper [22], Nastar *et al.* applied the theory to the case of a binary alloy AB in which diffusion is mediated by vacancies. A statistical point approximation (Bragg-Williams) was used to describe the short-range order and a pair approximation was assumed for the effective interactions, and they introduced a cut-off radius for the pair distance beyond which effective interactions are assumed to be null. The effective interactions decrease towards zero with the cut-off radius. Self-diffusion correlation factor in a BCC structure converges with increasing cut-off radius. In the case of an interacting alloy, correlation factors calculated using the SCMF-o are in good agreement with Monte Carlo simulations, in both cases of a positive and negative mixing enthalpy. Deviations of 20% of the calculated off-diagonal correlation factors are found at some concentrations and are due to both thermodynamic and kinetic approximations. In the case of a random alloy, for a jump frequency ratio of 1 the theory yields exact results, while for higher ratios the results are less accurate, and in the limit of an infinite ratio, the percolation phenomena is not reproduced. Note that in a random alloy, the Bragg-Williams approximation is exact and therefore the discrepancy is due to the kinetic approximation. Since the year 2000, many subsequent works have been made to improve the SCMF-o theory and apply it to substitutional, interstitial and dumbbell diffusion mechanisms [48–50,98,99,111–114]. In one subsequent work, Barbe *et al.* [49] showed that in the case of a random alloy, using a triplet approximation for the effective interactions and considering only a finite number of triplet effective interactions is enough to reproduce the percolation limit. The solution in this case is numerical and iterative, and correlation factors converge with the number of iterations (STEIPA formalism). The work also showed that the MAA's decoupling scheme applied to their effective Hamiltonians leads to an analytical solution that is simpler than calculating all triplet effective interactions, and that the solution is equivalent to the converged STEIPA. The critical percolation concentration is obtained at $1 - f_0$. In the case of an interacting alloy, the theory was in general good agreement with Monte Carlo simulations, but was less accurate than other theories because of the use of the Bragg-Williams thermodynamic approximation. This, however, made it possible to account for effective interactions beyond the pair approximation and improve on its kinetic description of diffusion. Subsequent applications improved on the thermodynamic approximation by considering the pair approximation. They found that in many cases of vacancy, interstitial and dumbbell diffusion, the use of a pair approximation drastically improved the results with respect to a point approximation. In dilute alloys, it was shown that the transport coefficients can be calculated exactly within a thermodynamic and kinetic pair approximation and for an infinite kinetic cut-off radius. In the case of concentrated alloys, this could not be done and an optimization between thermodynamic and kinetic approximations has to be found as a function of thermodynamic interactions and jump frequency ratios. Additionally, the SCMF-o was able to predict a vacancy drag effect in an FCC structure, in agreement with Monte Carlo observations. Even though the SCMF-o theory was in practice limited to alloys with short range order, it still allowed for the calculation of single and collective correlation factors in both cases of an interacting and non-interacting alloy, with general good agreement with Monte Carlo simulations and other theories. In addition to these applications, the SCMF-o was used to study the kinetics of non-uniform composition fluctuations [23], and the theory managed to predict the qualitative behavior of the composition gradient parameter and the non-linearity of the interdiffusion coefficient, in agreement with Monte Carlo simulations.

Note that Eq. 1.152 is general for the case of any pair of species α and β, and for any transition frequency model, and so in theory, the SCMF-o can be applied to the case of any concentrated alloy. The theoretical difficulty of the SCMF-o resides mainly in constructing and solving simultaneously the n_ν equations with effective interactions up to n_ν-body interactions. One can see that, the bigger the n_ν the more accurate the result should be, but also the more mathematically challenging it will be to find the effective interactions. A great mathematical effort is required to calculate Eq. 1.147 for interactions beyond the pair approximation ($n_\nu > 2$). The thermodynamic interactions, the effective interactions and the transition frequencies depend on the thermodynamic and kinetic approximations, on the crystal's structure, on the number of species and defects, and on the chosen atomic jump model. The difficulty of the analytical calculations is proportional to all these factors. One of the interesting features of the SCMF-o theory, and what mainly differentiates it from the PPM, is that the thermodynamic and kinetic approximations are decoupled. This allows us to consider the appropriate level of approximation for the thermodynamic and kinetic parts separately, leading to a good level of accuracy in both with the least mathematical complexity. For example, a point approximation can be used for thermodynamic interactions, in order to simplify the calculations, while a triplet approximation can be used for the kinetic approximation, which could be necessary to properly evaluate kinetic trajectories and correlations. Despite this great simplification, in practice, a general analytical result is hard to obtain using the SCMF-o, and for each different crystalline structure, diffusing species or jump mechanisms a new development of the equations is required.

Conclusion

Besides the PPM, the SCMF-o is the only method to allow the calculation of the full Onsager matrix in the case of an interacting concentrated alloy, without neglecting off-diagonal coefficients. Very small driving forces are assumed to drive the system to an out-of-equilibrium state close to a homogeneous equilibrium and fluxes are calculated using the continuity equation as a function of concentration. A thermodynamic Hamiltonian describes the thermodynamic interactions while an effective Hamiltonian describes the system's kinetic response to the driving forces. The effective Hamiltonian is a function of effective interactions which contain all the information on kinetic correlations and which can be calculated as a linear function of chemical potential gradients. Stationnarity of the different moments of the distribution function allow the calculation of the effective interactions, which are then used to calculate the transport coefficients. Even though the thermodynamic and kinetic parts are treated simultaneously, their approximations are treated separately. Compared to its most concurrent method, the PPM, the SCMF-o has the advantage of separating thermodynamic and kinetic approximations, giving it the possibility to improve on its kinetic approximation for a greater accuracy of correlation factors, all while being less theoretically challenging. In most applications a point approximation was used for the thermodynamic part while a pair approximation was used for the kinetic part, but other applications required higher level of either or both for accurate results. The SCMF-o was applied in the cases of vacancy and self-interstitial diffusion in different crystalline structures. By adjusting in each case the level of approximations, the SCMF-o was found in a general good agreement with Monte Carlo simulations in the case of interacting and non-interacting alloys. The theoretical challenge in the SCMF-o is to calculate the effective interactions, which becomes harder with the number of defects, components, and levels of approximations. A general analytical formulation cannot be established, and one needs to develop the equations depending on the case to study.

1.7.5 Comparative summary of the models

All three methods, the RA, the PPM and the SCMF-o, constitute a remarkable advancement in the development of analytical methods for the study of diffusion in concentrated alloys. The three methods make it possible to calculate the complete Onsager matrix. The direct comparison between the three methods could only be made in the case of a random binary alloy. The three methods lead to close results at all concentrations and for a wide range of jump frequencies, and in the limit of an infinitely big jump frequency, the three models provide a good description of the percolation phenomena (the PPM after its reformulation, and the SCMF-o after including triplet effective interactions in a decoupled scheme). The PPM and the SCMF-o have additionally the power to study concentrated alloys without neglecting thermodynamic interactions. While these two methods are very similar in nature, they still have their differences, and they are both very different from Manning's approach. In Table 1.3, we make the effort to compare exhaustively several aspects of the three methods. In short, Manning's model is very simple in the case of vacancy diffusion in a non-interacting alloy. Its application to dumb-bell interstitials proved that there are no simple analytical solutions in this case [102]. The PPM and the SCMF-o are more complex but provide the capacity to study interacting alloys. The PPM and the SCMF-o rely on thermodynamic and kinetic approximations that are similar in built and objective. However, the PPM provides coherency between the thermodynamic and kinetic aspects by keeping the same level of approximation in both parts, while the SCMF-o provides the flexibility to separate the two approximations, making it more versatile and less complex. Additionally, the PPM has been widely used to study order-disorder kinetics but it has been only applied in the case of vacancy diffusion, while the SCMF-o's flexibility allowed it to study a greater variety of diffusion mechanisms. Both methods remain however hard to generalize to large cluster systems that include a big number of point defects, and to complex crystalline structures and jump mechanisms.

	RA	PPM	SCMF-o
Description of the system	Tracer of each species embedded in a homogeneous mean-field.	Finite sized cluster embedded in a mean-field.	Finite sized cluster embedded in a mean-field.
Equilibrium probabilities	All configuration probabilities are equal.	Equilibrium probability represented by a Boltzmann distribution.	Equilibrium probability represented by a Boltzmann distribution
Control over thermodynamic approximation	Bragg-Williams approximation.	Level of approximation depends on the size of the biggest cluster and the range of thermodynamic interactions. Mostly used in the pair approximation.	Level of approximation depends on the size of the biggest cluster and the range of thermodynamic interactions. Mostly used in the point approximation.
Time evolution of the system	Evolution of a steady-state system near equilibrium.	Evolution of a steady-state system near equilibrium.	Evolution of a steady-state system near equilibrium.
Kinetic interactions	Represented directly by escape frequencies and partial correlation factors.	Represented by path variables.	Represented by effective interactions.
Control over kinetic approximation	-	Level of approximation depends on the size of the biggest cluster, i.e. has to be the same as the thermodynamic approximation. Only used in the nearest-neighbors pair approximation.	Level of approximation depends on the largest effective interaction. Mostly used in the pair approximation, but also beyond in the triplet approximation.
Applications: types of alloys	Regular solid solution model of concentrated interacting alloys.	Homogeneous non-interacting and interacting concentrated alloys. A revised version allows the extension to heterogeneous concentrated alloys but has only been applied to the case of vacancy-tracer diffusion in a binary random alloy.	Heterogeneous non-interacting and interacting concentrated alloys with short range order.
Applications: jump mechanisms	Vacancy mechanism with very low concentration of vacancies.	Vacancy mechanism.	Vacancy mechanism, direct interstitial mechanism, dumbbell mechanism, ...
Complexity level	Simple.	Hard to generalize to any structure and any jump mechanisms.	Hard to generalize to any structure and any jump mechanisms.

Table 1.3: Comparative summary of different aspects of Manning's RA, Kikuchi's PPM and Nastar's SCMF-o.

1.8 Conclusions of chapter 1

In the general case, we cannot calculate the full Onsager matrix experimentally. Additionally, diffusion experiments are generally only feasible at high temperatures and, in most cases, it is not correct to extrapolate the results to low temperatures. To overcome this obstacle, interdiffusion experiments can be performed in nanometric multilayers, because their small size allows the study of interdiffusion at relatively low temperatures and in reasonable time. Numerical and analytical models were found necessary to fill these gaps. Monte Carlo simulations cannot study unstable systems and they suffer from statistical errors and kinetic trapping, especially when calculating off-diagonal coefficients and when studying highly correlated systems. Analytical methods, on the other hand, are hard to develop for concentrated alloys because of the difficulty of explicitly calculating kinetic correlations, which are measured naturally in numerical methods. This difficulty is due to the size and complexity of the configuration space, hence to simplify and reduce it, models have been developed with various assumptions and approximations. These methods have been applied either to the case of a non-interacting alloy (RA), or to the case of an interacting alloy in specific cases of structures and diffusion mechanisms (PPM and SCMF-o). Even though the PPM and the SCMF-o share a lot of similarities, the SCMF-o provides more flexibility and treats correlations more rigorously, which allowed for its application to a greater variety of diffusion problems. The fact that they are both system specific does not help since the analytical equations have to be reworked from the beginning for each different case. A general and relatively simple analytical method to calculate the full Onsager matrix in concentrated alloys is therefore still missing.

In recent years, the SCMF-o has been reformulated by Schuler *et al.* [18], in what we will call in this thesis the SCMF-d, and it was implemented in an open-source code called KineCluE. The main difference in the SCMF-d lies in the way effective interactions are treated and their new approach allows the treatment of much longer kinetic trajectories. In this work, however, they made the assumption that clusters are sufficiently dilute in a homogeneous matrix which limited their approach to pure and dilute alloys. Nevertheless, this showed the potential of simplifying the SCMF-o and making it more versatile, accessible and fast. The successive advancements in the SCMF-o theory and its reformulation, the SCMF-d, and its implementation in the KineCluE code show the potential of extending the SCMF-d to concentrated alloys.

Therefore, the need for a general model to study diffusion in any concentrated alloy is still present. The aim of the next sections is to provide atomic-scale models to calculate interdiffusion coefficients and transport coefficients in concentrated alloys. In Chapter 2, we present a method to extract concentration dependent interdiffusion coefficients from experimental and simulated nanometric multilayers from their X-ray diffraction profiles, and in Chapter 3, we present a new analytical model, based on the SCMF-d and KineCluE, to compute transport coefficients in concentrated alloys.

Chapter 2

Interdiffusion in Fe/Cr multilayers

2.1 Introduction to chapter 2

In an interdiffusion experiment, a diffusion over a given distance is required to obtain a measurable signal. The typical diffusion distance being $d \sim \sqrt{2Dt}$ and the diffusion coefficient D being typically an Arrhenius form, $D = D_0 \exp\left(-Q/\left(k_B T\right)\right)$, interdiffusion experiments can only be performed at high temperatures. At low temperatures, interdiffusion experiments would require to be performed for an unreasonable amount of time. Nanometric multilayers provide a workaround to access low temperature data by analyzing the evolution of composition waves over time instead of the classical Boltzmann-Matano analysis [57] of interdiffusion experiments. The advantage is that atoms need to diffuse over only a few nanometers to affect the concentration at the center of a layer. Hence the interest in studying interdiffusion in nanometric multilayers. For instance, Fe/Cr multilayers attract a lot of attention because diffusion properties of Fe-Cr alloys are still not well known at low temperatures, yet their $\alpha - \alpha'$ decomposition at industrial temperatures is of high interest [8, 9, 16, 35]. There is also little data on the kinetic properties of Fe-Cr alloys with high Cr concentrations [9], and the interdiffusion coefficient in such system is very concentration dependent [16], making it hard to extrapolate data from high Fe concentrations to high Cr concentrations.

Nanometric multilayers provide two additional interesting features, besides their small size: an interface between the different atomic layers, and a composition modulation. These characteristics lead scientists to develop a wide variety of interface mobility models and to make the link between interdiffusion coefficients and interface shift [55, 64–67]. The particularity of these features can also be seen in X-ray diffraction (XRD) profiles. While XRD profiles of monolayers present a main Bragg peak characteristic of their lattice parameter, XRD profiles of multilayers present satellites around the main Bragg peak due to modulations of concentration and lattice parameter (Fig. 2.1). During annealing, interdiffusion between different atomic species alters the concentration profile and consequently the interplanar spacing profile. This causes XRD satellite peak intensities to decay, but the relationship between interdiffusion and satellite decay is not clear yet. The evolution of the composition and the XRD profiles are relatively easy to obtain experimentally, hence the interest in finding the link between interdiffusion coefficients and the evolution of XRD profiles in multilayers.

The aim of this work is to study interdiffusion in Fe/Cr multilayers and calculate interdiffusion coefficients based on X-ray diffraction profiles. In Sec. 2.2, we present previous analytical works that have been done to study X-ray diffraction in multilayers. These models tried to make the analytical link between composition profile, lattice spacing profile, interdiffusion coefficients, and X-ray satellite peak positions and intensities. In Sec. 2.3, we present the thermodynamic and kinetic properties of FeCr alloys. Then in Sec. 2.4, we talk about the experimental work done by our collaborators to grow Fe/Cr multilayers and characterize them, and the previously developed simulation tools that enabled us to study interdiffusion in Fe/Cr multilayers and to simulate their X-ray profile. In Sec. 2.5, we analyze what each satellite peak represents and which part of the multilayer affects it. In Sec. 2.6, we present a detailed simulation study of interdiffusion in a Fe/Cr multilayer, we analyze composition and X-ray profiles, and calculate interdiffusion coefficients from the decay of satellite intensities, and in Sec. 2.7, we compare our simulation results to the experiment and discuss the common points and differences.

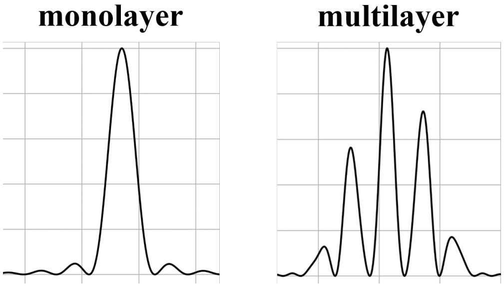

Figure 2.1: Schematic representation of the difference between the X-ray diffraction profiles of a monolayer and a multilayer.

2.2 Previous analytical works on X-ray diffraction in multilayers

The intensity recovered from the diffraction of X-rays on a sample results from the scattering of the incident rays by atoms, and from the interference between these scattered rays. Each atomic species has a different scattering factor which reduces the intensity of the incident ray depending on its wavelength and angle of incidence with respect to the atom's position. The density and type of atoms on an atomic plane determine the intensity of each scattered wave, and the interference between them depends on the relative positions of the planes. This is why, in theory, from the X-ray diffraction profile, we are able to recover both the concentration and interplanar spacing profiles. XRD profiles of multilayers present satellites around the main Bragg peak due to modulations of concentration and lattice parameter. Upon annealing, satellite peak intensities decrease due to interdiffusion and/or strain relaxation. It is known that interdiffusion causes the concentration profile to change, which changes both the scattering factor profile and the interplanar spacing profile. The time evolution of the average scattering factor profile affects the intensity of the diffracted rays, while the time evolution of the interplanar spacing profile changes both the nature and number of planes satisfying Bragg's law. This leads to a change in both the angles at which diffracted rays are constructive as well as the intensity of the satellites. Yet, the relationship between decay rate and interdiffusion parameters, such as the interdiffusion coefficient, is not clearly established. Furthermore, interface mobility occurs in some types of multilayers due to the asymmetry in both interdiffusion and miscibility gap, for example in Cu/Brass multilayers in Kirkendall's experiment (Sec. 1.3.2) or in equiatomic Fe/Cr multilayers (as will be shown later in Sec. 2.3). It is still not clear how interface mobility affects XRD profiles. Several theories have been developed to study interdiffusion in multilayers and to obtain the time evolution of composition profiles from XRD (see [116] for a review). It was DuMond and Youtz [117] who were the first to link X-ray intensity decay to diffusion properties. They determined the diffusion coefficient as a function of the decay rate of satellite intensities and noted the power of this method in calculating very small values of interdiffusion coefficients. Guinier [25] was then the first to consider a sinusoidal modulation of the scattering factor and the inter-planar spacing, and to establish the relation between diffracted intensities and modulation amplitudes. This model was extended to include a sum of several harmonics, and similarly, the composition and distance profiles could be concluded from the X-ray diffracted intensities [118–120]. From the combination of Guinier's theory with a linear diffusion model (Eq. 2.52) in which the interdiffusion coefficient $\tilde{D}$ is assumed constant, the decay rate of satellites can be expressed as a function of a unique interdiffusion coefficient [121–123]. However, in the case of a concentration dependent interdiffusion coefficient $\tilde{D}(C)$, which is the more realistic case, the relationship between decay rate and interdiffusion parameters could not be established yet because the equations rely on a specific function of $\tilde{D}(C)$ and become more difficult to solve. Aubertine *et al.* [124] discussed that in the case of a concentration dependent interdiffusion coefficient in Si/SiGe hetero-structures, calculating the interdiffusion coefficient from the decay of the first order peak doesn't necessarily correspond to calculating it at the mean concentration, nor does it give insight on the range of inter-diffusivity values, i.e. the minimum and maximum values of it. Tsakalakos [125] used a perturbation method to find an approximate analytical solution to a nonlinear diffusion equation (Eq. 2.63) by writing the interdiffusion coefficient as a quadratic function of composition. He gave the solution to the composition variation as a sum of truncated first and second order Fourier components whose time-dependent amplitudes are a function of their amplitudes before annealing, the interdiffusion coefficient, and the period of the multilayer. Intensities of different order X-ray satellites can be deduced from this model since they are proportional to the square of the amplitude of the same order Fourier components. The diffusion parameters and the gradient energy coefficient can then be deduced using a non-linear regression model.

In this section, we will present an overview on the basics of diffraction theory in multilayers (Sec. 2.2.1) and the theoretical advancements made to recover the composition and lattice spacing profiles from XRD profiles, by assuming sinusoidal functions of single harmonics and the more complicated case of several harmonics (Sec. 2.2.2 and Sec. 2.2.3). We will also discuss the theories developed to calculate interdiffusion coefficients from satellite decay rates, in both cases of concentration dependent and concentration independent coefficients (Sec. 2.2.4).

2.2.1 Basics of diffraction theory

In the classical wave method, an X-ray, just like any electromagnetic wave, is composed of oscillating electric $\vec{E}$, and magnetic $\vec{B}$, fields that are orthogonal. Mathematically, an X-ray can be expressed as sinusoidal wave functions that describe its field equations

$$\begin{cases} \vec{E}\left(\vec{r},t\right) = \vec{E}_0 \sin\left(\vec{k}.\vec{r} - wt + \phi_0\right), \\ \vec{B}\left(\vec{r},t\right) = \vec{B}_0 \sin\left(\vec{k}.\vec{r} - wt + \phi_0\right), \end{cases} \tag{2.1}$$

where $\left\|\vec{E}_0\right\|$ and $\left\|\vec{B}_0\right\|$ are the amplitudes of the electric and magnetic fields respectively, and ϕ_0 is the phase shift. The X-ray wavelength is given by $\lambda = 2\pi/\left\|\vec{k}\right\|$, and its frequency by $f = 2\pi/w$. At any point in time, the intensity of the plane wave formed by these two fields is given by the time average of the Poynting vector

$$I = \langle S\left(t\right)\rangle = \left\langle \frac{1}{\mu_0}\left(\vec{E}\times\vec{B}\right)\right\rangle = \frac{1}{2c\mu_0}E_0^2 \propto E_0^2. \tag{2.2}$$

Therefore, the intensity of the X-ray is proportional to the squared amplitude of its electric field. Note that the intensity can also be expressed in an equivalent way in terms of the squared amplitude of the magnetic field, or in terms of the amplitude of both the electric and magnetic fields.

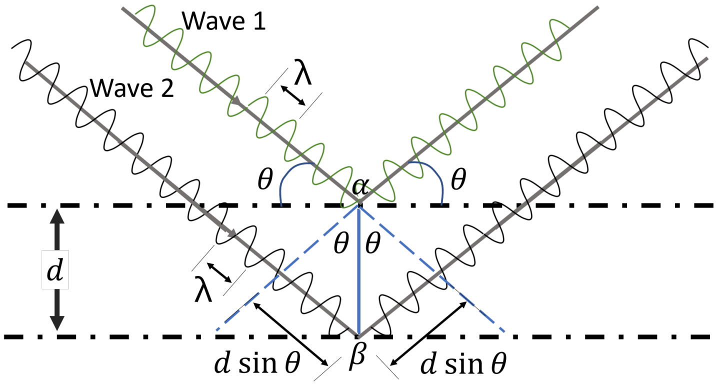

Figure 2.2: Schematic representation of two incident waves with an angle θ that get diffracted by atoms α and β located on two different planes distant by d.

Let us now consider a crystal formed by parallel planes with an equal spacing d between the planes. Let us consider two X-rays emitted by the X-ray source at the same time, and incident on the crystal such that they get diffracted by an atom of species α on plane 1, and by an atom of species β on plane 2, as can be seen in Figure 2.2. Note that diffracted X-rays are mostly emitted by elastic scattering of the atoms' electrons. Both rays, when emitted, have the same wavelength, frequency and phase shift, and can both be described by the above equations (Eq. 2.1 and Eq. 2.2). For example, the electric field of the incident rays when emitted can be expressed as

$$\vec{E}_1^i\left(\vec{r},t\right) = \vec{E}_0 \sin\left(\vec{k}.\vec{r} - wt + \phi_0\right), \tag{2.3}$$

$$\vec{E}_2^i\left(\vec{r},t\right) = \vec{E}_0 \sin\left(\vec{k}.\vec{r} - wt + \phi_0\right), \tag{2.4}$$

where $\vec{E}_1^i\left(\vec{r},t\right)$ and $\vec{E}_2^{\hat{i}}\left(\vec{r},t\right)$ correspond respectively to the electric fields of the first incident ray before it hits atom α and to the second incident ray before it hits atom β. After getting diffracted by the atoms, the ray hitting atom β has to travel a longer distance before reaching the detector. This creates a path difference between the two rays, which we will call $\|\Delta\vec{r}\|$. Using simple geometry, we find that this path difference depends on the planes at which the particles are found and is a function of the distance between the two planes d and of the scattering angle θ, such that

$$\|\Delta\vec{r}\| = 2d\sin\theta. \tag{2.5}$$

As a consequence to this path difference, the two rays reach the detector with a phase difference, even though they were initially emitted with the same phase shift ϕ_0. On the other hand, a wave diffracted by an atom loses some of its energy due to interactions between the wave and the atom, and therefore the amplitude of the diffracted field will be smaller than the emitted one. These interactions not only depend on the atomic species, but also on the X-ray wavelength and on the angle at which the wave hits the atomic planes. The amplitude of the scattered wave will then depend on the diffracting species, the ray wavelength and the scattering angle. This can be quantified by introducing a scattering factor such that the initial amplitude $\left\|\vec{E}_0\right\|$ of a ray of wavelength λ reduces to $\left\|\vec{E}_0\right\| f_\alpha^0(\theta,\lambda)$ after getting diffracted by species α at an angle θ. The electric field of the diffracted rays then becomes

$$\vec{E}_1(\vec{r},t) = \vec{E}_0 f_\alpha^0(\theta,\lambda)\sin\left(\vec{k}.\vec{r} - wt + \phi_1\right), \tag{2.6}$$

$$\vec{E}_2(\vec{r},t) = \vec{E}_0 f_\beta^0(\theta,\lambda)\sin\left(\vec{k}.\vec{r} - wt + \phi_2\right), \tag{2.7}$$

where ϕ_1 and ϕ_2 are the new wave phases. Note that the wavelength and frequency are not affected by the diffraction and remain the same, and that the incident angles θ are the same because planes are assumed to be parallel. When these two individual waves reach the detector, the wave resulting from their superposition is the sum of the two waves such that

$$\begin{aligned}\vec{E}_f(\vec{r},t) &= \vec{E}_1(\vec{r},t) + \vec{E}_2(\vec{r},t)\\ &= \vec{E}_0 f_\alpha^0(\theta,\lambda)\sin\left(\vec{k}.\vec{r} - wt + \phi_1\right) + \vec{E}_0 f_\beta^0(\theta,\lambda)\sin\left(\vec{k}.\vec{r} - wt + \phi_2\right).\end{aligned} \tag{2.8}$$

Instead of using trigonometric functions, we can equivalently express each wave as a complex exponential function. This is equivalent to expressing a wave as a vector instead of a sine function and makes it easier to manipulate waves, especially when performing addition operations on them. This can be done since a sinusoidal function is the imaginary part of a complex exponential function

$$\sin\left(\vec{k}.\vec{r} - wt + \phi\right) = \mathrm{Im}\left[e^{i\left(\vec{k}.\vec{r} - wt + \phi\right)}\right]. \tag{2.9}$$

The superposition of the two waves (Eq. 2.8) becomes

$$\begin{aligned}\vec{E}_f(\vec{r},t) &= \vec{E}_0 f_\alpha^0(\theta,\lambda)\, e^{i\left(\vec{k}.\vec{r} - wt + \phi_1\right)} + \vec{E}_0 f_\beta^0(\theta,\lambda)\, e^{i\left(\vec{k}.\vec{r} - wt + \phi_2\right)}\\ &= \vec{E}_0 e^{i\left(\vec{k}.\vec{r} - wt\right)}\left[f_\alpha^0(\theta,\lambda)\, e^{i\phi_1} + f_\beta^0(\theta,\lambda)\, e^{i\phi_2}\right].\end{aligned} \tag{2.10}$$

Equation 2.10 represents the superposition of two waves, one diffracted by an atom α on plane 1, and the other diffracted by an atom β on plane 2 which is parallel to plane 1. The advantage of using complex exponential functions is that the result we obtained can be generalized for the superposition of any number of waves from any number of planes and from any number and type of species on the planes,

$$\vec{E}_f\left(\vec{r},t\right)=\vec{E}_0 e^{i\left(\vec{k}.\vec{r}-wt\right)}\sum_j e^{i\phi_j}\sum_\alpha N_\alpha\left(j\right)f_\alpha^0\left(\theta,\lambda\right), \tag{2.11}$$

where the sum over j runs over all planes, and the sum over α runs over all atomic species. Here, $N_\alpha\left(j\right)$ represents the number of atoms of species α on plane j. $N_\alpha\left(j\right)$ can be more conveniently written as a function of the concentration $C_\alpha\left(j\right)$ of α on plane j, such that

$$N_\alpha\left(j\right)=C_\alpha\left(j\right)N, \tag{2.12}$$

with N the total number of sites on a plane, which is assumed to be the same for all planes. We can choose a reference plane r with respect to which we calculate the phase differences, and Eq. 2.11 becomes

$$\vec{E}_f\left(\vec{r},t\right)=\vec{E}_0 e^{i\left(\vec{k}.\vec{r}-wt+\phi_r\right)}N\left[\sum_j e^{i\phi_j^{'}}\sum_\alpha C_\alpha\left(j\right)f_\alpha^0\left(\theta,\lambda\right)\right], \tag{2.13}$$

with $\phi_j^{'}=\phi_j-\phi_r$. What we are interested in calculating is the intensity of the diffracted waves since this is what the detector will measure. Recall from Eq. 2.2 that the intensity is proportional to the amplitude squared, which gives us

$$\begin{aligned}I &\propto \left\|\vec{E}_f\left(\vec{r},t\right)\right\|^2 \propto \left\|\vec{E}_0 e^{i\left(\vec{k}.\vec{r}-wt+\phi_r\right)}\sum_j e^{i\phi_j^{'}}\sum_\alpha C_\alpha\left(j\right)f_\alpha^0\left(\theta,\lambda\right)\right\|^2\\ &\propto \left\|\sum_j e^{i\phi_j^{'}}\sum_\alpha C_\alpha\left(j\right)f_\alpha^0\left(\theta,\lambda\right)\right\|^2.\end{aligned} \tag{2.14}$$

To calculate the diffracted intensity we need to calculate the scattering factor $f_\alpha^0\left(\theta,\lambda\right)$ of each species α and the phase difference ϕ_j of each wave diffracted on plane j. There already exists models and datasets for the calculation of the scattering factor. The phase difference on the other hand, can be calculated from the path difference as

$$\phi_j^{'}=\frac{2\pi}{\lambda}\left\|\Delta\vec{r_j}\right\|=\frac{4\pi d_{r,j}\sin\theta}{\lambda}, \tag{2.15}$$

where $d_{r,j}$ is the distance between plane j and a reference plane (r). This distance is often referred to as the perpendicular lattice spacing because it is in the direction perpendicular to the diffracting planes. The lattice spacing between atoms belonging to the same plane is the in-plane lattice spacing. In this manuscript, when it is not specified, the lattice spacing refers to the perpendicular lattice spacing by default. Note that waves diffracted by atoms belonging to the same plane will have the same phase difference since it only depends on the position of the plane with respect to a reference plane and on the scattering angle θ, and not on the species diffracting them. However, these waves will have different intensities depending on the species diffracting them because of the difference in atomic scattering factors. The intensity resulting from the superposition of waves (Eq. **??**) diffracted by atoms α belonging to the same plane j is proportional to

$$I_j\propto\left\|e^{i\phi_j}f\left(j\right)\right\|^2, \tag{2.16}$$

where $f\left(j\right)$ is the average scattering factor of plane j,

$$f\left(j\right)=\sum_{\alpha}C_{\alpha}\left(j\right)f_{\alpha}^{0}\left(\theta,\lambda\right). \tag{2.17}$$

The scattering factor profile $f\left(j\right)$ has therefore the same variation in space as the concentration profile $C_{\alpha}\left(j\right)$. The exact distribution of atoms in the plane does not matter, and only their average planar concentration does. Note that, by definition, constructive interference happens when the amplitude of the superposition of waves takes its maximum value. This is equivalent to a maximum in diffracted intensity, and mathematically corresponds to

$$\forall j,\ e^{i\phi_{j}^{'}}=1, \tag{2.18}$$

and consequently

$$\forall j,\ \phi_{j}^{'}=2n\pi, \tag{2.19}$$

where n is an integer. If we put this condition in Eq. 2.15, we get the well-known Bragg's law

$$2d_{r,j}\sin\theta=n\lambda. \tag{2.20}$$

The incidence angle θ between the emitted ray and the crystal plane is equal to the angle between the crystal plane and the diffracted (Fig. 2.2). Therefore, the angle between the X-ray emitter and the detector is 2θ, and diffraction profiles are drawn as a function of 2θ because it is an easily measurable quantity. For practical reasons, in an X-ray experiment, the detector rotates around the sample and at the same time either the sample or the emitter are rotated. The diffraction pattern is obtained for a range of 2θ values and the different lattice spacings characteristic of the crystal are determined from the 2θ angles at which the most intense rays are detected (Bragg's law, Eq. 2.20). The detected rays form a 2D diffraction pattern of spots with different intensities. The positions of the spots and their relative intensities depend on the crystal lattice and atomic distribution. In order to find dominating lattice spacings in the crystal, a post-processing step is required to transform the 2D diffraction pattern into a 1D profile, in which detected intensities are mapped as a function of the 2θ angle. This 1D profile is easier to analyze because Bragg's law can be directly used to determine the lattice spacing corresponding to each peak. Note that this lattice spacing is often referred to as the perpendicular lattice spacing, which is not necessarily the same as the lattice spacing in the plane. XRD measurements can further be combined with the $\sin^{2}\Psi$ method to study residual stress and calculate perpendicular and in-plane lattice parameters [126].

2.2.2 Guinier's theory with single harmonics

In the previous section we showed that the intensity of rays diffracted from several planes and the angle at which rays are constructive, are both a function of the atomic scattering factor and the interplanar spacing. Interdiffusion in multilayers changes the composition profile, which in turn changes both the atomic scattering profile and the interplanar spacing profile. Interdiffusion therefore alters the intensity and peak positions of the XRD profile. While it is relatively easy experimentally to measure the XRD intensities and peak positions, it is much harder to get information on the composition of the material and the lattice spacings, especially in a non-destructive way like provided by XRD. One can see that XRD has the potential of being a great characterization tool at the atomic scale and an experimental technique that allows the calculation of diffusion coefficients. Modeling XRD and establishing the link between satellite intensities and positions on one hand, and composition, lattice parameter and diffusion properties on the other hand, has therefore attracted a lot of attention. The goal is to find the analytical expression of the time evolution of the scattering factor and of the lattice spacing, and express them as a function of interdiffusion coefficients. From there, we are able to calculate the interdiffusion coefficients from the time evolution of the intensity and the position of each satellite.

Let us consider a multilayer structure of the form $[\alpha/\beta]_r$ with a periodicity Λ, where $[\alpha/\beta]$ is a bilayer formed by one layer of pure α and one layer of pure β, and r is the number of bilayers. Guinier [25] was the first to consider a one-dimensional sinusoidal modulation of the composition. He wrote the composition of species α in the z-direction as

$$C_\alpha(z) = C_\alpha^0 + A\sin\left(\frac{2\pi}{\Lambda}z\right), \tag{2.21}$$

where C_α^0 is the average concentration of species α in the multilayer, and A is the amplitude of the concentration modulation. As shown in Eq. 2.17, the scattering factor of a plane is simply the average of the atomic scattering factors of all atoms, and therefore the composition modulation in a direction z causes a modulation of the same form of the average scattering factor in the same direction

$$\begin{aligned} f(z) &= C_\alpha(z) f_\alpha^0(\theta,\lambda) + [1 - C_\alpha(z)] f_\beta^0(\theta,\lambda) && (2.22)\\ &= \left[C_\alpha^0 + A\sin\left(\frac{2\pi}{\Lambda}z\right)\right] f_\alpha^0(\theta,\lambda) + \left[1 - C_\alpha^0 - A\sin\left(\frac{2\pi}{\Lambda}z\right)\right] f_\beta^0(\theta,\lambda) && (2.23)\\ &= C_\alpha^0 f_\alpha^0(\theta,\lambda) + \left(1 - C_\alpha^0\right) f_\beta^0(\theta,\lambda) + A\sin\left(\frac{2\pi}{\Lambda}z\right)\left(f_\alpha^0(\theta,\lambda) - f_\beta^0(\theta,\lambda)\right). && (2.24)\end{aligned}$$

The scattering factor has the same modulation as the concentration profile, with different average values and amplitudes, such that

$$f(z) = f_0 + A\Delta f\sin\left(\frac{2\pi}{\Lambda}z\right) \tag{2.25}$$

where $f_0 = C_\alpha^0 f_\alpha^0(\theta,\lambda) + (1 - C_\alpha^0) f_\beta^0(\theta,\lambda)$ is the average scattering factor of all atoms in the multilayer, and $\Delta f = f_\alpha^0(\theta,\lambda) - f_\beta^0(\theta,\lambda)$ is the difference between the atomic scattering factors. The interplanar spacing depends on the composition, but there is no general direct relationship between the two. Guinier considered a sinusoidal modulation of the lattice spacing in the z-direction, such that the distance between planes n and $n+1$ is of the form

$$d_{n,n+1} = d_0 + \epsilon d_0 \sin\left(\frac{2\pi}{\Lambda}nd_0\right), \tag{2.26}$$

where d_0 is the average interplanar spacing, and ϵ is a strain parameter to be defined. The interplanar spacing is therefore following the concentration profile.

The period of the multilayer is a function of the average spacing, $\Lambda = Nd_0$, where N is the number of planes in a bilayer. Remember that the goal of this work is to reconstruct the composition and lattice spacing profiles of the multilayers from XRD profiles. The unknowns are therefore A, Λ, d_0 and ϵ, assuming that the average concentration C_α^0 is known and that the scattering factors can be determined. Guinier manages to find an analytical link between the unknowns and the measurable XRD peak positions and intensities. As mentioned in Sec. 2.2.1, the diffraction pattern results from the interference of scattering of rays by atoms' electrons based on their relative positions and scattering factors. A Fourier transform allows the transition between the space domain and the time domain, which can in some situations simplify a mathematical problem. For instance, the amplitude, frequency and phase shift of a wave resulting from the interference of several waves. A Fourier transform of the diffraction pattern transforms the resulting diffracted wave pattern into the separate diffracted waves that make it up. The amplitude of diffracted X-ray waves can be calculated as the Fourier transform of the electronic density along z, $\rho(z)$, by integrating over the reciprocal space

$$A(k) = \int \rho(z) \exp(ikz)\, dz = \int f(z) \sum_n \delta(z - z_n) \exp(ikz)\, dz, \tag{2.27}$$

where $A(k)$ is the amplitude of the diffracted rays at the spacial frequency k, and z_n is the position of plane n with respect to the reference of the z axis. To calculate z_n, let us first consider the reference of the z axis to be at a distance $(\epsilon\Lambda)/(2\pi)$ from the first plane of the multilayer (i.e. from the plane to which corresponds $n = 0$). Therefore, the distance between the first plane ($n = 0$) and the reference plane ($n = r$) is

$$d_{r,0} = -\frac{\epsilon\Lambda}{2\pi}. \tag{2.28}$$

The position of plane n with respect to the position of the first plane can be calculated as the sum over all distances between consecutive planes

$$d_{n,0} = \sum_{j=0}^{n-1} d_{j,j+1}. \tag{2.29}$$

To calculate the position of plane n with respect to the reference of the z axis, we need to add to $d_{n,0}$ the distance from the reference of plane 0

$$z_n = d_{r,0} + \sum_{j=0}^{n-1} d_{j,j+1}. \tag{2.30}$$

By assuming that the deviations between the interplanar spacings are very small, and by approximating the sum over planes k by an integral, the position of plane n is finally

$$\begin{aligned} z_n &\approx -\frac{\epsilon\Lambda}{2\pi} + nd_0 + \epsilon d_0 \int_0^{n-1} \sin\left(\frac{2\pi}{\Lambda} k d_0\right) dk \\ &\approx jd_0 - \frac{\epsilon\Lambda}{2\pi} \cos\left(\frac{2\pi}{\Lambda} n d_0\right). \end{aligned} \tag{2.31}$$

$$A\left(k\right)=FT\left[\left(f_0+A\Delta f\sin\left(\frac{2\pi}{\Lambda}z\right)\right)\sum_n\delta\left(z-nd_0+\frac{\epsilon\Lambda}{2\pi}\cos\left(\frac{2\pi}{\Lambda}nd_0\right)\right)\right] \tag{2.32}$$

$$\int\sum_n\delta\left(z-nd_0+\frac{\epsilon\Lambda}{2\pi}\cos\left(\frac{2\pi}{\Lambda}nd_0\right)\exp\left(ikz\right)\right)dk \tag{2.33}$$

The Fourier transform of $\rho\left(z\right)$ is the convolution of the two transforms of the functions $f\left(z\right)$ and $\sum_{n=-\infty}^{+\infty}\delta\left(z-z_n\right)$. The final result is

$$\begin{aligned}A\left(k\right)=&\sum_n\frac{2\pi f_0}{d_0}\delta\left(k-\frac{2\pi n}{d_0}\right)\\&-\frac{2\pi i f_0}{d_0}\sum_n\left[\left(\frac{\Lambda\epsilon k}{4\pi}-\frac{A\Delta f}{2f_0}\right)\delta\left(k-\frac{2\pi n}{d_0}-\frac{2\pi}{\Lambda}\right)\right.\\&\left.+\left(\frac{\Lambda\epsilon k}{4\pi}+\frac{A\Delta f}{2f_0}\right)\delta\left(k-\frac{2\pi n}{d_0}+\frac{2\pi}{\Lambda}\right)\right].\end{aligned} \tag{2.34}$$

Remember that the diffracted intensity is proportional to the amplitude squared. For each n, the δ functions are non-null for three values of k, to which corresponds three non-null diffracted amplitudes and equivalently three intensity peaks. The values of k at which the intensities are not null, and the values of the associated intensities are given below as a function of n

$$\begin{cases}k_0=\dfrac{2\pi n}{d_0}, & I_0=\left(\dfrac{2\pi f_0}{d_0}\right)^2,\\ k_{+1}=\dfrac{2\pi n}{d_0}+\dfrac{2\pi}{\Lambda}, & I_{+1}\left(k_{+1}\right)=\left(\dfrac{2\pi f_0}{d_0}\right)^2\left(\dfrac{\Lambda\epsilon k_{+1}}{4\pi}-\dfrac{A\Delta f}{2f_0}\right)^2,\\ k_{-1}=\dfrac{2\pi n}{d_0}-\dfrac{2\pi}{\Lambda}, & I_{-1}\left(k_{-1}\right)=\left(\dfrac{2\pi f_0}{d_0}\right)^2\left(\dfrac{\Lambda\epsilon k_{-1}}{4\pi}+\dfrac{A\Delta f}{2f_0}\right)^2.\end{cases} \tag{2.35}$$

The indices (0, +1, and −1) are only to differentiate between the intensity of the central peak of order 0, and the satellite at its left said to be of order −1, and the satellite at its right said to be of order +1. Therefore, Guinier's solution (Eq. 2.35) represents a central peak with a pair of satellites around it, one on each side. The position of the main peak is $\dfrac{2\pi n}{d_0}$ and the satellites are distant from it by $\pm\dfrac{2\pi}{\Lambda}$. Note that the two satellites are equally distant from the main peak, however they do not have the same intensities. The intensity of the satellites ±1 with respect to the central peak's intensity is

$$F_{\pm1}^2\equiv\frac{I_{\pm1}\left(k_{\pm1}\right)}{I_0}=\left(\frac{\Lambda\epsilon k_{\pm1}}{4\pi}\mp\frac{A\Delta f}{2f_0}\right)^2. \tag{2.36}$$

If there is no lattice strain ($\epsilon=0$ and all interplanar spacings are equal to d_0) the intensities of the satellites are both equal to $\left(\dfrac{A\Delta f}{2f_0}\right)^2$. Therefore, an asymmetry in satellite intensities is due to a variation in the lattice spacing between the planes. From the XRD profile, we can calculate the unknown quantities of interest:

- the average lattice spacing d_0 from the position of the main peak, $\dfrac{2\pi n}{d_0}$;
- the periodicity of the multilayer Λ from the distance between the main peak and one of the satellites, $\dfrac{2\pi}{\Lambda}$;
- the modulation amplitude A and the strain ϵ from the intensity of both satellites, by solving the system of two equations with two unknowns (Eq. 2.36),

$$\text{if } \frac{A}{\epsilon} \leq \frac{f_0}{\Delta f}\left(1+\frac{n\lambda}{d_0}\right), \text{ then } \begin{cases} \epsilon = \dfrac{d_0}{n\Lambda}\left(F_{-1}+F_{+1}\right), \\ A = \dfrac{d_0}{n\Lambda}\left(F_{-1}k_{+1}-F_{+1}k_{-1}\right), \end{cases} \tag{2.37}$$

$$\text{if } \frac{A}{\epsilon} \geq \frac{f_0}{\Delta f}\left(1+\frac{n\lambda}{d_0}\right), \text{ then } \begin{cases} \epsilon = \dfrac{d_0}{n\Lambda}\left(F_{-1}-F_{+1}\right), \\ A = \dfrac{d_0}{n\Lambda}\left(F_{-1}k_{+1}+F_{+1}k_{-1}\right). \end{cases} \tag{2.38}$$

  Note that the scattering factors (and hence f_0 and Δf) are known if we know the chemical species of the multilayers and their average composition, which is normally the case.

Remember that the lattice spacing is assumed to follow the concentration profile (Eq. 2.26), but no explicit model was used to make the link between the two. If we were to write the lattice spacing using Vegard's law as an average of the lattice spacings of α and β (d_α and d_β) weighted by their concentrations

$$d_{n,n+1} = C_\alpha(z)\,d_\alpha + \left[1-C_\alpha(z)\right]d_\beta, \tag{2.39}$$

we would obtain that the strain parameter represents

$$\epsilon = A\left(d_\beta - d_\alpha\right)/d_0. \tag{2.40}$$

The strain calculated from the XRD profiles could tell us the validity of such assumption by comparing the calculated value with Eq. 2.40.

Therefore, Guinier's single harmonic model allows for the calculation of the profiles of composition, scattering factor, lattice spacing, from the positions and intensities of the XRD peaks. This model is simple and reproduces a main peak with two satellites equally distant from it and with asymmetric intensities. In many cases, XRD profiles of multilayers present second order satellites which are not reproduced by this model. This model is also limited to sinusoidal profiles of concentration and lattice spacing. Benoudia [26] showed in his thesis that the range of validity of this model depends on the system under study, on the number of planes in the multilayer (its periodicity), and that it applies only within a specific range of values of ϵ and A.

2.2.3 Extension of Guinier's theory to several harmonics

Since a periodic function can be better approximated by a Fourier series, Guinier's model was extended [26] by replacing the sinusoidal function by a sum over several sinusoidal functions. The composition, scattering factor and interplanar spacing profiles are described by

$$C_\alpha(z) = C_\alpha^0 + \sum_{m=1}^{\infty} A_m \sin\left(m\frac{2\pi}{\Lambda}z\right), \tag{2.41}$$

$$f(z) = f_0 + \Delta f \sum_{m=1}^{\infty} A_m \sin\left(m\frac{2\pi}{\Lambda}z\right) \tag{2.42}$$

$$d_{n,n+1} = d_0 + d_0 \sum_{m=1}^{\infty} \epsilon_m \sin\left(m\frac{2\pi}{\Lambda}nd_0\right), \tag{2.43}$$

These modulations can be equivalently expressed as a sum of cosine functions instead of sine functions. The position of the n-th plane can be calculated in the same manner as above

$$z_n \approx nd_0 - \sum_{m=1}^{\infty} \frac{\epsilon_m \Lambda}{m2\pi} \cos\left(m\frac{2\pi}{\Lambda}nd_0\right). \tag{2.44}$$

The diffracted amplitude is also calculated as the Fourier transform of the electron density and has an analogous form

$$A(k) = \sum_n \frac{2\pi f_0}{d_0}\delta\left(k - \frac{2\pi n}{d_0}\right) \tag{2.45}$$

$$-\sum_{m=1}^{\infty}\left\{\frac{2\pi i f_0}{d_0}\sum_n\left[\left(\frac{\epsilon_m k_m}{4\pi/\Lambda} - \frac{A_m\Delta f}{2f_0}\right)\delta\left(k_m - \frac{2\pi n}{d_0} - m\frac{2\pi}{\Lambda}\right)\right.\right. \tag{2.46}$$

$$\left.\left.+\left(\frac{\epsilon_m k_m}{4\pi/\Lambda} + \frac{A_m\Delta f}{2f_0}\right)\delta\left(k_m - \frac{2\pi n}{d_0} + m\frac{2\pi}{\Lambda}\right)\right]\right\}. \tag{2.47}$$

This represents, for each order n, a central intensity peak at $\frac{2\pi n}{d_0}$, surrounded by both sides by peaks with asymmetric intensities and that are distant from the center by $m\frac{2\pi}{\Lambda}$, where m is a positive integer. The position of the central peak and of the satellites of order $\pm m$, as well as their respective intensities are given below

$$\begin{cases} k_0 = \dfrac{2\pi n}{d_0}, & I_0 = \left(\dfrac{2\pi f_0}{d_0}\right)^2, \\ k_{+m} = \dfrac{2\pi n}{d_0} + m\dfrac{2\pi}{\Lambda}, & I_{+m} = \left(\dfrac{2\pi f_0}{d_0}\right)^2\left(\dfrac{\Lambda\epsilon_m k_{+m}}{4\pi} - \dfrac{A_m\Delta f}{2f_0}\right)^2, \\ k_{-m} = \dfrac{2\pi n}{d_0} - m\dfrac{2\pi}{\Lambda}, & I_{-m} = \left(\dfrac{2\pi f_0}{d_0}\right)^2\left(\dfrac{\Lambda\epsilon_m k_{-m}}{4\pi} + \dfrac{A_m\Delta f}{2f_0}\right)^2. \end{cases} \tag{2.48}$$

The intensity of a satellite $\pm m$ with respect to the intensity of the main peak is

$$\frac{I_{\pm m}}{I_0} = \left(\frac{\Lambda\epsilon_m k_{\pm m}}{4\pi m} \mp \frac{A_m\Delta f}{2f_0}\right)^2. \tag{2.49}$$

From the XRD profile, we can calculate the unknown quantities of interest:

- the average lattice spacing d_0 from the position of the main peak, $\frac{2\pi n}{d_0}$;

- the periodicity of the multilayer Λ from the distance between the main peak and any of the satellites $\pm m$, $k_{\pm m} - k_0 = \pm m \frac{2\pi}{\Lambda}$;
- the modulation amplitude A_m and the strain ϵ_m of the m-th order harmonic from the intensity of the $\pm m$ satellites, by solving a system of two equations with two unknowns (Eq. 2.49) for each m separately, in the same way that was done in the case of only order 1 satellites (Sec. 2.2.2)

$$\text{if } \frac{A_m}{\epsilon_m} \leq \frac{f_0}{\Delta f}\left(1 + \frac{n\lambda}{d_0}\right), \text{ then } \begin{cases} \epsilon_m = \frac{d_0}{n\Lambda}\left(F_{-m} + F_{+m}\right), \\ A_m = \frac{d_0}{n\Lambda}\left(F_{-m}k_{+m} - F_{+m}k_{-m}\right), \end{cases} \tag{2.50}$$

$$\text{if } \frac{A_m}{\epsilon_m} \geq \frac{f_0}{\Delta f}\left(1 + \frac{n\lambda}{d_0}\right), \text{ then } \begin{cases} \epsilon_m = \frac{d_0}{n\Lambda}\left(F_{-m} - F_{+m}\right), \\ A_m = \frac{d_0}{n\Lambda}\left(F_{-m}k_{+m} + F_{+m}k_{-m}\right). \end{cases} \tag{2.51}$$

Several works have used this method to predict experimental composition and interplanar spacing profiles from XRD peak intensities and positions [118–120]. Benoudia [26] tested the validity of this model in the case of Mo/V and Cu/Ni multilayers. In each case, he considered a specific sinusoidal modulation of composition and lattice spacing, he simulated the XRD profiles of the multilayer and calculated the composition and lattice spacing profiles by applying Guinier's theory to the diffracted intensities and he compared the calculated profiles to the initially input profiles. He found that this model cannot be applied to Mo/V multilayers and leads to erroneous composition and lattice spacing profiles, while in the case of Cu/Ni multilayers, the calculated profiles were in good agreement with the input profiles. It is interesting to note that in Guinier's theory and in the extension to several harmonics, the position and intensity of the main peak do not depend on the concentration, scattering factor or lattice spacing profiles, and rather they only depend on the average values of the lattice spacing and scattering factor of the α components of the multilayer. This means that the main peak of an XRD profile of a Fe/Cr multilayer will always be the same, regardless of the distribution of atoms in the different planes.

2.2.4 Calculating interdiffusion coefficients

To calculate interdiffusion coefficients from XRD profiles, we need to express the composition modulation as a function of interdiffusion coefficients. This can be done if the interdiffusion coefficient $\tilde{D}$, does not depend on the concentration. In the case of a concentration dependent interdiffusion coefficient, the problem becomes harder to solve because of the need of an analytical function of the interdiffusion coefficient as a function of concentration, $\tilde{D}(C)$. This requires finding one general solution for any mathematical form of $\tilde{D}(C)$, which is not trivial and is not necessarily feasible. Therefore, there is still no general analytical solution to determine $\tilde{D}(C)$ from XRD profiles.

2.2.4.1 Concentration independent coefficient

When the interdiffusion coefficient does not depend on concentration, Glicksman [127] solved Fick's second law of diffusion in a direction z

$$\frac{\partial C_\alpha(z,t)}{\partial t} = \tilde{D}\frac{\partial^2 C_\alpha(z,t)}{\partial z^2}, \tag{2.52}$$

by separating the time and space variables, $C(z,t) = Z(z)\,T(t)$, and by then writing the solution using a Fourier series to express the concentration as a sum of sinusoidal functions. Initial and boundary conditions lead to an analytical solution of the form

$$C_\alpha(z,t) = \frac{C_\alpha(0,0)\,4h}{\Lambda} + \frac{2C_\alpha(0,0)}{\pi}\sum_{m=1}^{\infty}\frac{1}{m}\cos\left(m\frac{4\pi h}{\Lambda}\right)\sin\left(m\frac{2\pi z}{\Lambda}\right)\exp\left(-\frac{4m^2\pi^2\tilde{D}}{\Lambda^2}t\right). \tag{2.53}$$

From Guinier's theory with several harmonics (Sec. 2.2.3), if strain is assumed to be null ($\epsilon_m = 0$), satellites $\pm m$ have the same intensity

$$I_{\pm m} = \left(\frac{2\pi f_0}{d_0}\right)^2\left(\frac{A_m\Delta f}{2f_0}\right)^2, \tag{2.54}$$

and to calculate these satellite intensities we need to identify the composition modulation A_m. Eq. 2.53 can be written in the form

$$C_\alpha(z,t) = C_\alpha^0 + \gamma - \sum_{m=1}^{\infty}A_m\sin\left(m\frac{2\pi z}{\Lambda}\right), \tag{2.55}$$

where the scaling constant

$$\gamma = \frac{C_\alpha(0,0)\,4h}{\Lambda} - C_\alpha^0, \tag{2.56}$$

only shifts the profile, and where the modulations are identified as

$$A_m = \frac{2C_\alpha(0,0)}{\pi}\frac{1}{m}\cos\left(m\frac{4\pi h}{\Lambda}\right)\exp\left(-\frac{4m^2\pi^2\tilde{D}}{\Lambda^2}t\right). \tag{2.57}$$

Injecting this expression of A_m in the intensity equation (Eq. 2.54), we obtain the $\pm m$ satellite intensity as a function of time and the interdiffusion coefficient

$$I_{\pm m}(t) = \left(\frac{2\pi f_0}{d_0}\right)^2\left(\frac{\Delta f}{2f_0}\right)^2\frac{2C_\alpha(0,0)}{\pi m^2}\cos^2\left(m\frac{4\pi h}{\Lambda}\right)\exp\left(-\frac{8m^2\pi^2\tilde{D}}{\Lambda^2}t\right). \tag{2.58}$$

Since in Guinier's theory the intensity of the main peak only depends on the average lattice spacing and the average scattering factor, therefore it remains constant throughout interdiffusion

$$\forall t,\ I_0(t) = \left(\frac{2\pi f_0}{d_0}\right)^2. \tag{2.59}$$

The intensity of a satellite at a time t, normalized with respect to the main peak's intensity at time t is

$$\frac{I_{\pm m}(t)}{I_0(t)} = \left(\frac{\Delta f}{2f_0}\right)^2\frac{2C_\alpha(0,0)}{\pi m^2}\cos^2\left(m\frac{4\pi h}{\Lambda}\right)\exp\left(-\frac{8m^2\pi^2\tilde{D}}{\Lambda^2}t\right). \tag{2.60}$$

More interestingly, we can study the evolution of a satellite's intensity by calculating its intensity at time t with respect to its initial intensity

$$\frac{I_{\pm m}(t)}{I_{\pm m}(0)} = \exp\left(-\frac{8m^2\pi^2\tilde{D}}{\Lambda^2}t\right). \tag{2.61}$$

We obtain that the logarithm of the ratio of (normalized and un-normalized) intensities varies linearly with time, and that the linearity constant is a function of the interdiffusion coefficient

$$\ln\left(\frac{I_{\pm m}(t)/I_0(t)}{I_{\pm m}(0)/I_0(0)}\right) = \ln\left(\frac{I_{\pm m}(t)}{I_{\pm m}(0)}\right) = -\frac{8m^2\pi^2\tilde{D}}{\Lambda^2}t. \tag{2.62}$$

Note that the periodicity of the multilayer is either already known, or determined from the XRD profiles from the positions of satellites (Sec. 2.2.3), and m is the order of the satellite under study and is also known. There are some interesting features to this result which appear as a consequence to the approximations made to reach it:

- satellite peak intensities always decay during interdiffusion. This is a consequence of the slope of Eq. 2.62 always being negative (because m, $\tilde{D}$[1] and Λ are all always positive). This results from considering a constant interdiffusion coefficient which leads to a symmetric interdiffusion and evolution of the composition profile until all layers' concentrations become equal to the average concentration. When the system reaches this stationary state, all layers have identical composition and lattice spacing profiles (which are constant average values) and the multilayer is reduced to a homogeneous mono-layer. At this point, satellites disappear and only the main peak corresponding to the average lattice spacing remains, which is in agreement with XRD profiles of mono-layers (i.e. homogeneous systems).

- peak intensities of positive and negative satellites of the same order are equal at all times, $I_{-m}(t) = I_{+m}(t)$, and therefore they both decay in the same way. This is a direct consequence of considering that there are no lattice spacing fluctuations (Eq. 2.54).

As a conclusion of this section, combining Glicksman's solution of Fick's equation with Guinier's theory offers a fast and easy way of calculating interdiffusion coefficients from XRD satellite peak decays. One has to draw the logarithm of satellite intensity ratios as a function of time and calculate the slope. The larger the interdiffusion coefficient, the faster the satellites disappear because the system homogenizes faster. The larger the period of the multilayer, the slower the satellite's decay because atoms have to diffuse for a longer distance in each layer. This is a very simple method to determine $\tilde{D}$, but it is limited to a concentration independent interdiffusion coefficient and to multilayers in which the lattice spacing is constant, which are both too harsh approximations. However, note that these approximations (in particular a constant diffusion coefficient) can be valid for small time intervals during which the system evolves slightly.

---

[1] $\tilde{D}$ is proportional to the thermodynamic factor, which in turn is proportional to the second derivative of free energy (Sec. 2.2.4). $\tilde{D}$ can therefore be negative in a spinodal decomposition regime.

2.2.4.2 Concentration dependent coefficient

Tsakalakos [125] studied this problem in the case of an interdiffusion coefficient that has a quadratic dependence on concentration. He considered the nonlinear diffusion equation

$$\frac{\partial C\left(z,t\right)}{\partial t}=\frac{\partial}{\partial z}\left(\tilde{D}\left(C\right)\frac{\partial C\left(z,t\right)}{\partial z}\right)-2\tilde{K}\frac{\partial^4 C\left(z,t\right)}{\partial z^4}, \tag{2.63}$$

where $\tilde{K}=(2M/N_V)\,\kappa$, with M the atomic mobility, N_V the number of atoms per unit volume, κ a constant termed as the gradient energy coefficient, and $\tilde{D}\left(C\right)$ the interdiffusion coefficient which is expressed as

$$\tilde{D}\left(C\right)=D_0+D_1C+D_2C^2. \tag{2.64}$$

Using a perturbation theory, Tsakalakos obtained the solution to the composition variation as a sum of truncated first and second order Fourier components, whose time-dependent amplitudes are a function of their amplitudes before annealing, the interdiffusion coefficient, and the period of the multilayer. He then deduced the intensities of different order satellites from the square of the amplitude of the same order Fourier component. He finally used a non-linear regression model to calculate the diffusion parameters and the gradient energy coefficient. The problem with Tsakalakos' approach is that it does not provide an analytical solution and requires numerical calculations. The solution is therefore not straightforward, and the model has been used in very few applications. In addition, it requires the interdiffusion coefficient to have a quadratic form, but this remains a better approximation than a concentration independent coefficient. We will see in the next section (Sec. 2.3.2) that interdiffusion coefficients in FeCr alloys are quadratic over limited concentration ranges. Note that in the case of a non dependence of $\tilde{D}$ on concentration, Tsakalakos' model gives correctly the time evolution of the intensity of the 1st order satellite of Eq. 2.62 ($m=\pm1$).

2.3 Fe-Cr alloy

FeCr alloys are widely used in the nuclear industry as the basis of ferritic and ferritic-martensitic steels used for the structures of nuclear and fusion reactors. Additionally, Fe-Cr alloys are good candidates for magnetic sensor devices, as well as for micro and nano-electronics, because of their giant magnetoresistance [128, 129]. However, diffusion properties of Fe-Cr alloys are still not well known at low temperatures and in alloys with high Cr concentrations. The interdiffusion coefficient in Fe/Cr multilayers is concentration dependent and its value in Cr-rich regions cannot be extrapolated from its value in Fe-rich regions. In this section we will present the thermodynamic and kinetic properties of this alloy.

2.3.1 Thermodynamic properties

Phase diagrams are usually built based on thermodynamic properties that are either measured experimentally, either calculated from *ab initio* methods. The Computer Coupling of Phase Diagrams and Thermochemistry method [130], more commonly known as the Calphad method, is the most used numerical method to calculate the phase diagram based on experimental and/or *ab initio* properties.

The Fe-Cr phase diagram calculated with the Calphad method was adjusted on experimental data measured at temperatures above 400°C. The first Fe-Cr phase diagrams calculated with the Calphad method showed a symmetric miscibility gap. However, many studies showed that the miscibility gap shouldn't be symmetric since, at low concentrations of Cr, there is tendency for ordering linked to the magnetic properties of Fe-Cr, and at high concentrations of Cr, there is tendency for phase separation. The parametrization of Calphad was then optimized in two different ways separately by Bonny *et al.* [131] and by Xiong [132] by adjusting the parameters on more recent theoretical and experimental data. Both Bonny *et al.* and Xiong managed to calculate phase diagrams that present a non-symmetric miscibility gap and that are in agreement with each other and with experimental results. Senninger's Monte Carlo model [9, 16], that implements Levesque *et al.*'s pair interaction model, was also in agreement with Bonny's results (Fig. 2.3).

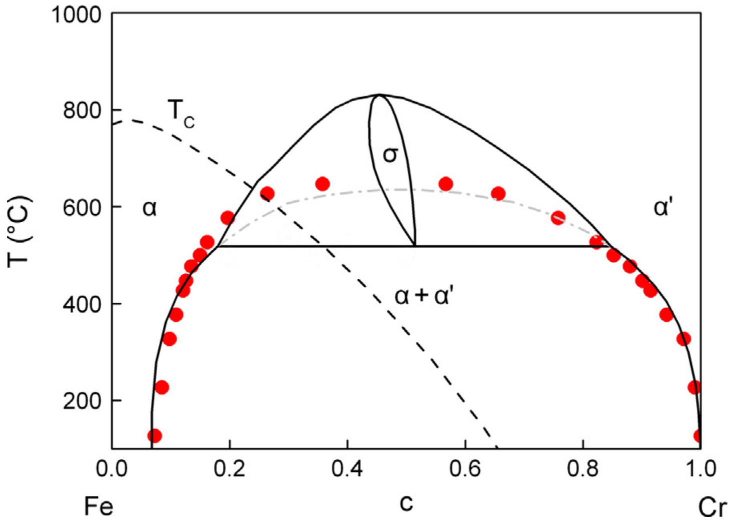

Figure 2.3: Phase diagram of Fe-Cr as calculated by Bonny *et al.* using Calphad [133] (black line) and by Senninger *et al.* using a Monte Carlo simulation [9, 16] (red points). The point-dashed line represents the Curie temperature of the homogeneous solid solution as calculated by Xiong et al. [134].

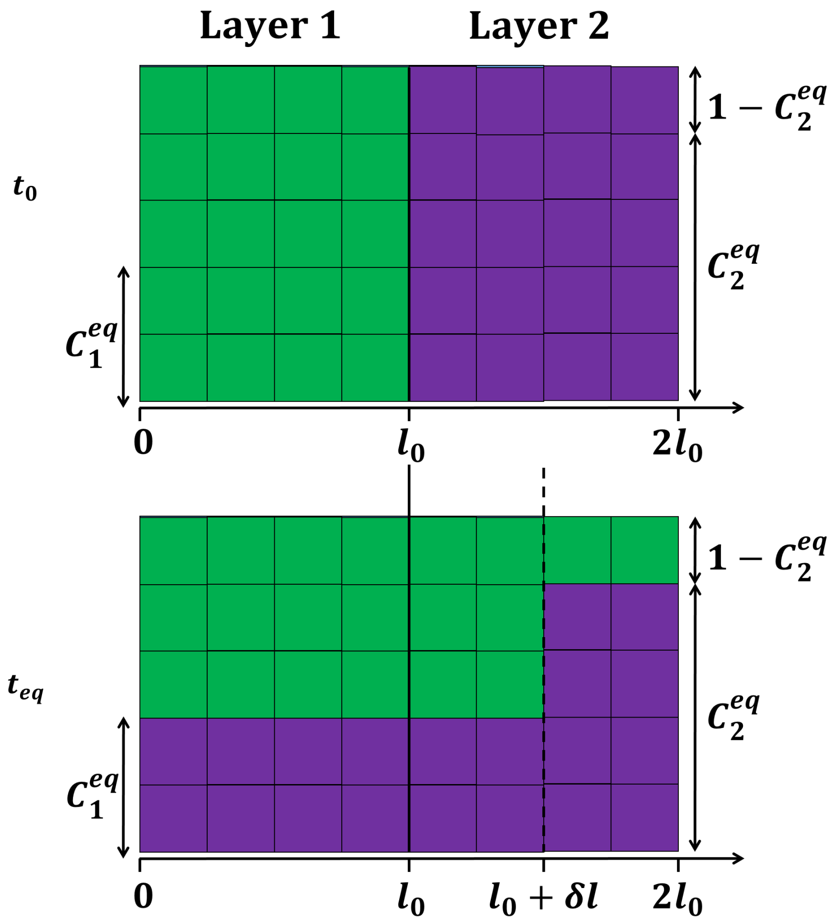

Figure 2.4: Schematic representation of an interface shift in the case of asymmetric solubility limits with $C_1^{eq} > 1 - C_2^{eq}$. Initially at $t = t_0$, both layers have the same thickness l_0. The number of purple (green) squares has to remain the same.

In a Fe/Cr multilayer, the concentration of Cr (respectively Fe) in the Fe-rich layer (respectively Cr-rich layer), will increase until it reaches its solubility limit (if we neglect finite size effects). At 500°C, the equilibrium concentration of Cr in Fe is of 15.0 at. %Cr, and that of Fe in Cr is of 14.8 at. %Cr. If we start with equiatomic layers of Fe and Cr, and if we assume a sharp interface throughout interdiffusion, at equilibrium, the Cr concentration in Fe has to be higher than that of Fe in Cr, which means that the Fe layer will have a lower total number of atoms and it will be thinner than the Cr layer. This can be seen mathematically using a conservation law. We consider two layers with a rectangular profile before annealing at $t = t_0$ (Fig. 2.4). At equilibrium, $t = t_{eq}$, we consider an interface shift from its initial position by δl, such that a positive (negative) δl means an interface shift towards Layer 2 (Layer 1). What is lost in one layer is gained in the other, in a way to keep the total amount of each species constant and equal to its initial value. Let us consider the purple species, which here represents Cr,

$$C_1^{eq}\left(l_0 + \delta l\right) + C_2^{eq}\left(l_0 - \delta l\right) = l_0, \tag{2.65}$$

where l_0 is the initial thickness of each layer, and $l_0 + \delta l$ and $l_0 - \delta l$ are the thicknesses of the Fe-rich (Layer 1) and Cr-rich (Layer 2) layers respectively. C_1^{eq} and C_2^{eq} are the equilibrium concentrations of Cr in the Fe-rich and Cr-rich layer respectively. Since $C_1^{eq} > 1 - C_2^{eq}$, we obtain that $\delta l_0 > 0$ and that the Fe-rich (Cr-rich) layer's thickness increases (decreases) with respect to its initial value.

The asymmetry in equilibrium concentrations is of the order of 0.2 at. %Cr, and the relative difference in thickness will be of the order of 1.3%. Therefore, the asymmetry of the phase diagram is not expected to have a significant influence on the difference between layer thicknesses at equilibrium.

2.3.2 Kinetic properties

Figure 2.5 shows the Fe-Cr interdiffusion coefficient as a function of temperature and composition, measured experimentally and using Monte Carlo simulations with the wave attenuation method [16], for temperatures above 500°C. Figure 2.6 shows the values calculated at 500°C using the same AKMC model. The interdiffusion coefficient has not been calculated below 600°C experimentally, and below 500°C using AKMC simulations. Additionally, there is a lack of experimental data at high concentrations of Cr. Both the experiment and simulation show a strong dependence of the interdiffusion coefficient on temperature, and a dependence on concentration which is mostly observed in the simulations due to the lack of experimental data in the Cr-rich region. At temperatures below 1440°C, the interdiffusion coefficient seems to be parabolic in the Fe-rich region, reaching a maximum value at around 15 at. %Cr, which is the solubility limit in this region. At all temperatures, the interdiffusion coefficient calculated using AKMC is almost 100 times larger in pure Fe than in pure Cr. This diffusion asymmetry leads to interface mobility in multilayers, since when one atomic species diffuses fast in one of the layers and is blocked in the other one, some atoms are forced to accumulate at the interface between the two layers.

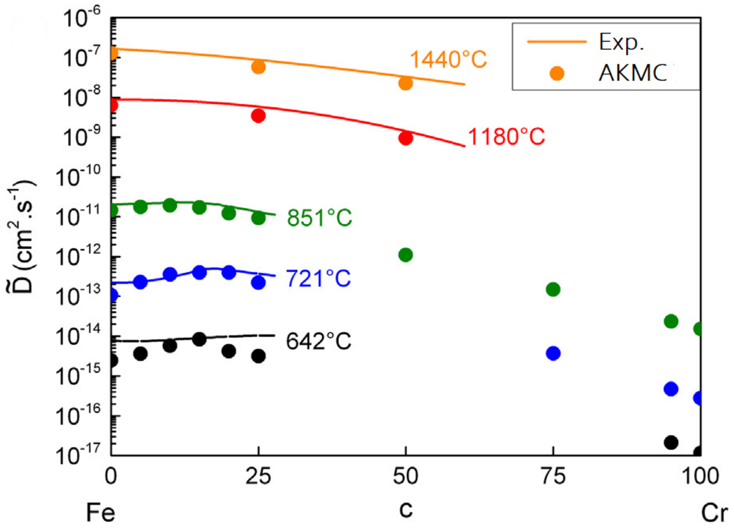

Figure 2.5: Interdiffusion coefficient calculated using AKMC [16] and measured experimentally (at temperatures below 1000°C from [135] and above 1000°C from [67]).

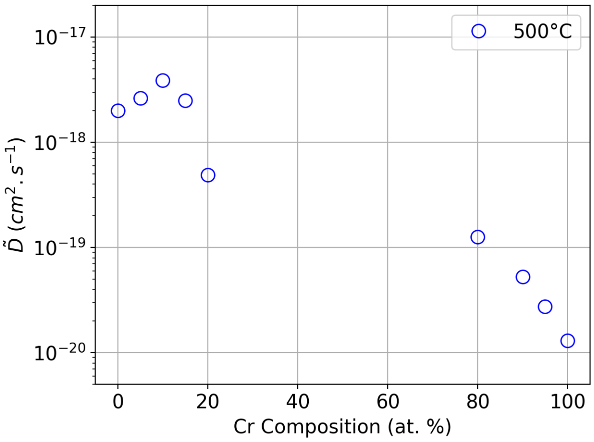

Figure 2.6: Interdiffusion coefficient calculated using AKMC [16] at 500°C.

2.4 Context of the study

Within the framework of Gladice Magnifouet's thesis at the "Institut de physique et de chimie des Matériaux de Strasbourg" (IPCMS) under the supervision of Véronique Pierron-Bohnes, Magnifouet and Pierron-Bohnes prepared nanometric Fe/Cr multilayers by molecular beam epitaxy (MBE). They annealed the multilayers at different temperatures and analyzed the evolution of the X-ray diffraction profile during annealing. The XRD profiles showed the presence of satellite peaks around the main Bragg peak (as expected), and the satellites decayed throughout the annealing. Additionally, samples before and after annealing at 500°C for 4h were sent to our laboratory, the "Service de Recherches de Métallurgie Physique" (SRMP) at CEA. Researchers Maxime Vallet and Estelle Meslin analyzed the concentration profiles and layer thicknesses using Atom Probe Tomography (APT) and Scanning Transmission Electron Microscopy/High-Angle Annular Dark-Field (STEM/HAADF). On the other hand, in 2013 at the SRMP, Oriane Senninger and Frédéric Soisson developed during Senninger's thesis an Atomic Kinetic Monte Carlo (AKMC) model to study diffusion in Fe-Cr alloys. They used an energetic model that is concentration and temperature dependent to better reproduce the behavior of Fe-Cr alloys. Their model was tested in alloys at different concentrations and temperatures (Fig. 2.5). The model reproduces well the Fe-Cr phase diagram (Fig. 2.3) and the simulated interdiffusion coefficients are in agreement with the experimental results in Fe-rich regions. In the Cr-rich part, there is not enough experimental data to compare with. The simulation showed the strong concentration dependency of the interdiffusion coefficient, with a difference between pure Fe and pure Cr of 2 orders of magnitude. The AKMC model was never tested on multilayers to know if it correctly reproduces interdiffusion or not. It is not obvious that the model would work in multilayers because, on one hand, we do not know the validity of the results in Cr-rich layers, and, on the other hand, we do not know if interdiffusion around the interface requires some special treatment. Given the new experimental data that was provided by the experimental teams of IPCMS and SRMP, we wanted to apply the AKMC model to multilayers and compare the simulated concentration profiles with the experimental ones, and we wanted to simulate the XRD profiles during annealing from the AKMC concentration profiles, to calculate interdiffusion coefficients from XRD profiles. Therefore, the aim of this study is to reproduce the experimental results of interdiffusion using

AKMC simulations and a theoretical work on XRD diffraction to better understand the attenuation of XRD satellite peak intensities, and to try and calculate accurate interdiffusion coefficients from a simulated concentration profile.

We will first present in this section the experimental tools that were used by the collaborating teams to elaborate the multilayers and characterize them. We will then present the AKMC model developed by Senninger [9, 16] as well as the code provided by Pierron-Bohnes to simulate XRD profiles from input concentration profiles.

2.4.1 Experimental tools

Fe/Cr multilayers were prepared by molecular beam epitaxy (MBE) to ensure an interface as close as possible to the ideally simulated interface. The multilayer was cut into several pieces, and after verifying using XRD that the growth is coherent in and out of the multilayer plane, each group of samples was annealed under vacuum at a constant temperature for different annealing times: at 500°C for 16h, at 450°C for 540h and at 400°C for 540h. XRD measurements were performed on the samples before and after annealing at the three temperatures to study the evolution of satellite peak positions and intensities. Atom Probe Tomography (APT), Scanning Transmission Electron Microscopy/High-Angle Annular Dark-Field (STEM/HAADF) measurements were performed on the multilayers annealed at 500°C for 4h to study the layer compositions and widths. We will list the experimental tools used by the various experimental teams and what each of these method gives us insight into.

2.4.1.1 Molecular Beam Epitaxy (MBE)

MBE is an advanced epitaxy technique that allows the growth of nanostructured samples at a rate of about one atomic monolayer per second. This makes it possible to control a homogeneous doping of the multilayer and to insure an interface as close as possible to an ideally sharp interface. The slow growth also enables measurements in real time which allows to follow the evolution of the structure during growth. Fe/Cr multilayers were prepared by molecular beam epitaxy (MBE) by Gladice Magnifouet and Véronique Pierron-Bohnes at IPCMS. Five bilayers of Fe/Cr were grown on an MgO/STO(100) substract at room temperature, such that each layer has a thickness of 10nm (Fig. 2.7).

We will therefore use Senninger's AKMC model to simulate Fe/Cr multilayers by initializing the composition profiles to sharp rectangular profiles such that the thickness of each layer is 10nm.

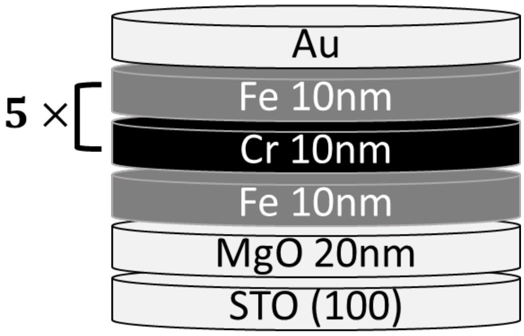

Figure 2.7: Schematic representation of the experimentally grown Fe/Cr multilayers.

2.4.1.2 X-Ray Diffraction (XRD)

XRD is a commonly used characterization technique because it is a non-destructive tool which provides information on numerous properties of the material. It allows us to identify the crystalline phases and the atomic structure of crystals, in a non-destructive manner.

Gladice Magnifouet and Véronique Pierron-Bohnes at IPCMS performed X-ray diffraction on the multilayers before annealing them. XRD profiles showed a main peak surrounded by four satellites, two on each side. A cumulative fit peak and the $\sin^2 \Psi$ method were used to calculate the average lattice parameters parallel and perpendicular to the multilayer growth direction. This was done with respect to the main peak position and the satellite peak positions, and all calculations resulted in the same values of $a_\perp = 2.8628 \pm 2 \times 10^{-4}$Å and $a_\parallel = 2.8896 \pm 5 \times 10^{-4}$Å.

XRD measurements were performed again on samples annealed at 450°C and at 500°C, throughout the annealing process to study the evolution of the microstructure. Absolute values of the diffracted intensities depend on the experimental measurement conditions. For example, the intensity of the incident rays on the sample as well as the adjustment parameters (like the position of the sample with respect to the incident beam) vary between different measurements. Therefore, XRD intensities obtained from different measurements (on different samples annealed at different times) cannot be directly compared. To overcome the dependency on experimental conditions, after each measurement, diffracted intensities are normalized with respect to the maximum measured intensity. This allows for a consistent comparison of relative intensities at different annealing times. Additionally, this makes it easier to compare relative peak intensities with Guinier's theory (Sec. 2.59), since in his theory the intensity of the main peak is predicted to be constant over time.

We will simulate the XRD profile of AKMC simulated concentration profiles before and after annealing, and compare our results to the experimental findings.

2.4.1.3 Atom Probe Tomography (APT)

APT is a high resolution atomic-scale experimental technique to study the three-dimensional chemical composition of a sample. It's a destructive technique which consists in sending an intense and periodic electric field on the surface of a sample to evaporate the atoms one by one in the form of ions, and then detect theses ions and reconstruct the initial position of the atoms based on the position and time of their impact with the detector. APT reconstruction algorithms are based on the assumption that the shape of the emitter during field evaporation is spherical. Evaporation of two alternative metal layers with different evaporation fields produces some local compression effect within the low evaporation field layers [136]. Because of the difference in the evaporation field between Fe and Cr ($E_{Cr} > E_{Fe}$), we have an over-density at the Fe/Cr interface and an under-density at the Cr/Fe interface. This leads to erroneous concentrations at the interfaces. As a consequence, the thicknesses of the layers measured from the composition profile are also wrong. The most reliable data that we can extract from the APT analysis are the compositions at the center of the layers that are less sensitive to reconstruction artifacts. Therefore, in our comparisons, we will use the APT results only to compare the compositions at the center of the layers.

APT measurements were done by Maxime Vallet and Estelle Meslin at SRMP on samples before annealing and after annealing at 500°C for 4h. We will use their results as a reference for comparison with the simulated composition profiles.

2.4.1.4 Scanning Transmission Electron Microscopy/High-Angle Annular Dark-Field (STEM/HAADF)

STEM/HAADF is another high resolution technique to characterize the three-dimensional structure of a sample. The advantage of this technique is that images obtained by it are easy to interpret and do not require post-processing. It consists in sending a beam of electrons at the sample, collecting the electrons scattered from it and forming a contrasting image based on the atomic number of the atoms scattering the electrons. Elements with a higher atomic number appear brighter on the image, allowing direct and easy interpretation of the results. This technique is highly sensitive to the atomic number and allows precise measurements of layer thicknesses in multilayers. The geometry of the detector allows, on one hand, the collection of a bigger number of scattered electrons than what can be done with conventional STEM imagining, which offers higher resolution. On the other hand, it can be coupled with the Electron Energy Loss Spectroscopy (EELS), which allows a chemical characterization of the sample.

STEM/HAADF measurements on the Fe/Cr multilayers were done by Maxime Vallet and Estelle Meslin at SRMP on samples before and after annealing at 500°C for 4h. This provides an accurate tool to measure the thicknesses of layers and allows us to study the accuracy of the simulated layer thicknesses.

2.4.1.5 Summary of experimental tools

The conditions of elaboration of the Fe/Cr multilayers, as well as the annealing conditions in which characterizations were made, are summarized in Table. 2.1. We also cite the most reliable information that each technique gives us so that we know which information is reliable for comparisons with simulations. Combining all these methods allows us to know the compositions at the center of the layers and layer thicknesses at 500°C, and the evolution of the XRD profile at two different temperatures.

	Research team	Experimental conditions	Most reliable information available
MBE	Magnifouet and Pierron-Bohnes (IPCMS)	5 bi-layers of Fe/Cr 10nm each layer	Expected homogeneous layers and sharp interfaces
Annealing	Magnifouet and Pierron-Bohnes (IPCMS)	500°C, 0h - 16h 450°C, 0h - 260h	-
XRD	Magnifouet and Pierron-Bohnes (IPCMS)	500°C, 0h - 16h 450°C, 0h - 260h	XRD peak positions and intensities, lattice parameters
APT	Vallet and Meslin (SRMP)	500°C, 0h and 4h	Compositions at the center of the layers
STEM/HAADF	Vallet and Meslin (SRMP)	500°C, 0h and 4h	Layer thicknesses

Table 2.1: Summary of the work of the experimental research teams, the elaboration and characterization conditions (annealing temperatures and duration), and the most reliable information available from each contribution.

2.4.2 Simulation tools

Fe/Cr multilayers were simulated by us using Senninger *et al.*'s Atomic Kinetic Monte Carlo code developed to study diffusion in FeCr alloys [9,16]. We simulate two Fe/Cr bilayers with periodic boundary conditions and we initialize the profiles to step functions in order to simulate the sharp interfaces. We choose a number of planes that ensures that the thicknesses of each layer is as close as possible to 10nm (Fig. 2.8). The system evolves under constant temperature and we simulate through three different simulations the annealing of multilayers: at 500°C for 274h, at 450°C for 276 days and at 400°C for 6 years. We obtain the time evolution of the concentration profiles and the layer thicknesses. We simulate the XRD profiles using a code where the theory presented in Sec. 2.2.1 is implemented. Using the concentration profiles obtained by the AKMC simulation, the time evolution of the satellite peak positions and intensities are simulated at the different temperatures. In this section, we will present in more detail the AKMC simulation and the XRD code that we used in this study.

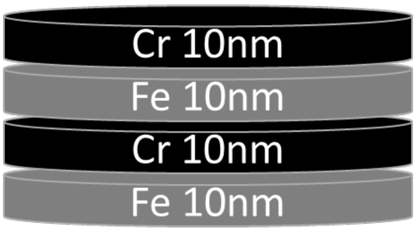

Figure 2.8: Schematic representation of the Fe/Cr multilayers simulated using Senninger's AKMC model [9,16].

2.4.2.1 Atomic Kinetic Monte Carlo simulation

Senninger's AKMC model relies on a DFT-based vacancy diffusion model, is concentration and temperature dependent, and successfully reproduces the phase diagram and high temperature diffusion properties. The code has not been tested in the case of multilayers nor for temperatures below 500°C. The Hamiltonian is reduced to a pair interaction model in which interactions between Fe and Cr are dependent on temperature and on local concentration (up to the second nearest-neighbors) [137]. Magnetic properties are properly reproduced in this model by fitting the decrease of the migration barriers near the ferromagnetic to paramagnetic transition to experimental data, which allowed the model to reproduce the experimental interdiffusion coefficients (Fig. 2.5). The AKMC model uses a residence time algorithm [77] (Sec. 1.5.2.2) and includes a time correction with respect to vacancy concentration [78]. As explained in Sec. 1.5.3, this correction is necessary for the calculated physical time to match the real time.

We use this code to simulate the annealing of two 20nm Fe/Cr bilayers. We simulate the annealing of the multilayers at 500°C for 274h, and at 450°C for 276 days, which correspond to the experimental annealing temperatures but to much longer annealing times. The concentration profiles and layer thicknesses obtained at 500°C after approximately 4h ($\approx$ 3.8h) of annealing are compared with the experimental APT, STEM/HAADF observations. The concentration profiles are also used as input in the XRD code (Sec. 2.4.2.2) to simulate the time evolution of the diffracted profiles from the multilayers.

2.4.2.2 X-Ray Diffraction simulation code

There are several models, usually involving some approximations, to obtain the XRD spectra from AKMC simulations. Pierron-Bohnes's code [138] simulates the X-ray diffraction of FeCr multilayers by calculating the total amplitude of the superposition of the waves scattered from each atomic plane. The code takes as input an average uni-dimensional (along z axis) concentration profile (obtained from AKMC simulations for example) and outputs the diffraction profile. The theory behind this method was presented in Sec. 2.2.1. The diffracted intensity is calculated as the amplitude squared (combining Eq. 2.16 and Eq. 2.15)

$$I\left(2\theta\right) = \left\|\sum_j f\left(j\right) \exp\left(i\frac{4\pi\sin\theta}{\lambda}z_j\right)\right\|^2, \tag{2.66}$$

where $z_j = \sum_{k=0}^{j-1} d_{k,,k+1}$ is the z-position of plane j with respect to the reference plane which is chosen to be the first plane of the multilayer. $f\left(j\right)$ is the average scattering factor (Eq. 2.17), λ is the X-ray wavelength, and θ is the angle between the incident ray and the atomic plane (Fig. 2.2).

The atomic scattering factor of an atom of species α is calculated as a function of θ and λ using Cromer and Mann's fit [139]

$$f_\alpha^0\left(\theta,\lambda\right) = \sum_{i=1}^{4} a_i^\alpha e^{-b_i^\alpha(\sin\theta/\lambda)^2} + c^\alpha, \tag{2.67}$$

where a_i^α, b_i^α and c^α are the Cromer-Mann fitting parameters [139] corresponding to species α and are tabulated in Table 2.2 for Fe and Cr.

The interplanar spacing between planes j and $j+1$ is calculated using a local Vegard's law of the form

$$d_{j,j+1} = \sum_{\alpha} C^{\alpha}_{j,j+1} d_{\alpha}, \tag{2.68}$$

where d_α is the interplanar spacing in the pure α phase, and $C^{\alpha}_{j,j+1} = \left(C_\alpha\left(j\right) + C_\alpha\left(j+1\right)\right)/2$ is the average α concentration between planes (j) and $(j+1)$. The values of the interplanar spacing in pure BCC Cr and pure BCC Fe are taken respectively as $d_{Cr} = 0.14425$ nm and $d_{Fe} = 0.14200$ nm. As we saw throughout Sec. 2.2, the interplanar spacing profile will affect both satellite peak positions and intensities, and it is therefore important to make sure that the model used to simulate it is accurate. Using a Vegard's law assumes an incoherent growth of the multilayers (stress-free) [140], and is justified because loss of coherency is usually observed in multilayers with periods larger than around 4 nm [141], which is our case (our multilayer's period is 20 nm).

	a_1	a_2	a_3	a_4	$b_1(\text{Å}^2)$	b_2 (Å^2)	b_3 (Å^2)	b_4 (Å^2)	c
Fe	11.769	7.357	3.522	2.305	4.761	0.307	15.354	76.881	1.037
Cr	10.641	7.354	3.324	1.492	6.104	0.392	20.263	98.740	1.183

Table 2.2: Cromer-Mann fittings parameters [139] of the scattering factors of Fe and Cr used in the XRD code.

2.4.2.3 Summary of simulation tools

Table 2.3 summarizes the two codes which were used in this study and the input parameters that were used to simulated the Fe/Cr multilayers. We can identify two main approximations which are made with respect to the experimental multilayers. The first one is in the AKMC simulation code which assumes that the multilayers have no dislocations or inclusions. The second one is in the XRD simulation code which assumes that the lattice spacing follows a Vegard's law and neglects local lattice strains.

	Simulation approximations	Simulation parameters	Most reliable information available	Code developers
AKMC	- Residence time algorithm - Concentration and temperature dependent pair interaction model - Magnetic correction - Time correction	2 bi-layers of Fe/Cr; 10nm each layer; 500°C, 0h - 274h; 450°C, 0h - 6623h;	Composition profiles and layer thicknesses	Senninger *et al.* (SRMP) [9, 16]
XRD	- Vegard's law for the lattice spacing - Bragg's law for intensity calculations	$d_{Cr} =$ 0.14425nm; $d_{Fe} =$ 0.14200nm; $f^0_{Cr}(\theta, \lambda)$ and $f^0_{Fe}(\theta, \lambda)$ from Cromer and Mann [139]; 500°C, 0h - 16h; 450°C, 0h - 6623h;	XRD peak positions and intensities	Pierron-Bohnes (IPCMS) [138]

Table 2.3: Summary of the codes we used and the simulation conditions (multilayers, annealing temperatures and duration), and the most reliable information available from each simulation method.

2.5 Identifying XRD peaks of a Fe/Cr multilayer

The aim of this part of the work is to study interdiffusion in Fe/Cr multilayers by analyzing, among other things, XRD peak positions and intensities. We know from Sec. 2.2 that there is a close link between interdiffusion, composition profile, lattice spacing profile and XRD peak positions and intensities, however the link is not clear and depends on the approximations and assumptions of each theory. We also saw in Guinier's theory with several harmonics that there could be several satellites around the main peak, and that each peak's position and intensity depends on different factors. Therefore, the time evolution of each satellite's intensity will differ from the others, and it will be sensitive to different diffusion and composition parameters. Note that Guinier's equations were in Fourier space and a function of the space frequency k. We can re-write these equations as a function of the 2θ angle instead by using the fact that $k = \dfrac{2\pi \sin\theta}{\lambda}$, and make the link with commonly used X-ray profiles. The set of Eq. 2.49, becomes

$$\begin{cases} 2\theta_0 = 2\arcsin\left(\dfrac{n\lambda}{2d_0}\right), & I_0 = \left(\dfrac{2\pi f_0}{d_0}\right)^2, \\ 2\theta_{+m} = 2\arcsin\left(\dfrac{n\lambda}{2d_0} + m\dfrac{\lambda}{2\Lambda}\right), & I_{+m}\left(2\theta_{+m}\right) = \left(\dfrac{2\pi f_0}{d_0}\right)^2 \left(\dfrac{\Lambda\epsilon_m \sin\theta_m}{\lambda} - \dfrac{A_m \Delta f}{2f_0}\right)^2, \\ 2\theta_{-m} = 2\arcsin\left(\dfrac{n\lambda}{2d_0} - m\dfrac{\lambda}{2\Lambda}\right), & I_{-m}\left(2\theta_{-m}\right) = \left(\dfrac{2\pi f_0}{d_0}\right)^2 \left(\dfrac{\Lambda\epsilon_m \sin\theta_{-m}}{\lambda} + \dfrac{A_m \Delta f}{2f_0}\right)^2, \end{cases} \tag{2.69}$$

and $2\theta_m$ is the peak position of satellite m.

According to Bragg's law of diffusion (Eq. 2.20), which makes no assumptions on the composition nor lattice spacing profiles, constructive interference at an angle 2θ results from rays diffracted by planes r and j that are distant by

$$d_{r,j} = \frac{n\lambda}{2\sin\theta}, \tag{2.70}$$

where n is an integer and λ is the X-ray wavelength. The position and intensity of peaks depends on the dominant lattice spacings. The intensity further depends on the scattering factor, and therefore on the atomic species on each plane and the composition profile. All of this shows that, before analyzing XRD profiles, it is important to know what each peak represents by identifying what its position and intensity are sensitive to. This is the aim of this section.

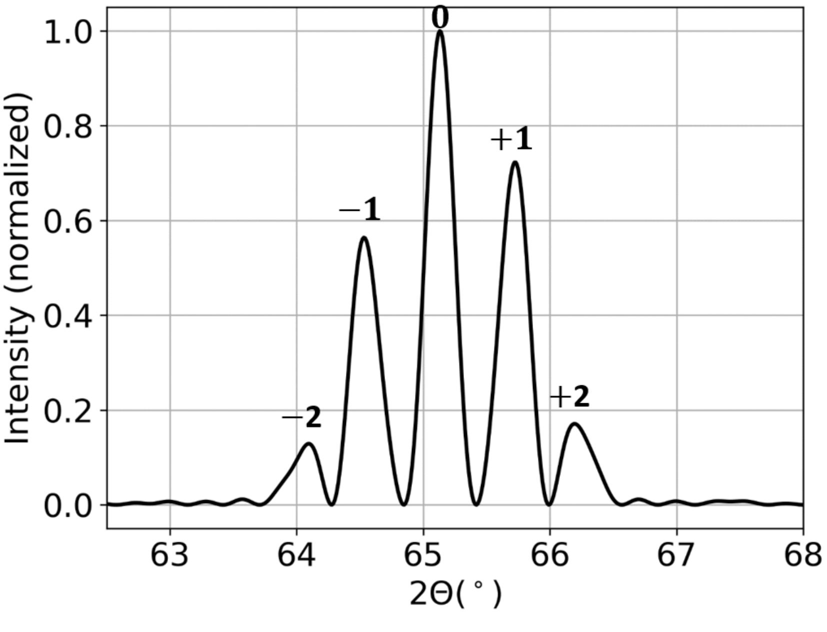

Figure 2.9: Normalized XRD profile simulated using the the XRD simulation code on the initial (rectangular) composition profile of the multilayers before annealing.

Let us consider the multilayers before annealing. The composition profile is rectangular and we expect the lattice spacing profile to also be almost rectangular. This is because we expect the lattice spacing in a pure α layer to be almost equal to the bulk lattice spacing in a pure α crystal. This is especially true far from the interfaces because the short range distribution will be the same as in a free-strain alloy and strains from differences in lattice parameters become negligible. Therefore, $d_{j,j+1} = d_\alpha$ when j and $j+1$ are planes of the α layer, α here being Fe or Cr, and at the interface we consider a Vegard's law like it is implemented in the code. In this case, Vegard's law is a good approximation because we know it should be exact in the pure layers, and as a consequence, the error resulting from this approximation is smaller than when the concentration profile is not rectangular (i.e. after annealing).

We simulate the XRD profile and plot it in Fig. 2.9. As predicted by Guinier's theory with several harmonics, the XRD profile is composed of a main peak surrounded by satellites on both sides. Here, there are 4 satellites, 2 on each side of the main peak. Guinier's theory further predicts that all consecutive peaks are equally spaced, which is not what we observe in the simulated profiles. While first order satellites are indeed equidistant from the main peak by 0.6°, negative (resp. positive) order satellites -1 and -2 (resp. +1 and +2) are distant from each other by 0.43° (resp. 0.46°). Note that Guinier's equations are established in Fourier space and peaks are represented by Dirac functions, whereas here in 2θ space, peaks have a non-null width. Throughout this manuscript, a peak's position is calculated as the position of its maximum intensity. Using Eq. 2.70, we calculate the lattice spacing corresponding to each peak position at $t = 0$h, $d_{r,j}(m)$ with $m \in [0, \pm 1, \pm 2]$, and we tabulate the values in Table 2.4. Note that the 2θ is inversely proportional to the lattice spacing (Eq. 2.70), and higher values of 2θ correspond to lower values of $d_{r,j}$.

- The lattice spacings calculated from the simulation of first order satellites $m = -1$ and $m = +1$ correspond respectively to the input values of the lattice spacing in pure Cr ($d_{Cr} = 0.14425$ nm) and the lattice spacing in pure Fe ($d_{Fe} = 0.14200$ nm) within a 0.04% relative error. This is further confirmed in Fig. 2.10 where first order satellite positions are in agreement with the main peaks of pure Fe and pure Cr layers. Therefore, the peaks of satellites $m = -1$ (respectively $m = +1$) corresponds to a positive interference of rays diffracted from the planes of the Cr layer (respectively Fe layer). Note that, even though the number of constructive waves is the same from both Cr and Fe layers, the intensity diffracted from Fe layers (satellite $+1$) is higher than the intensity diffracted from Cr layers (satellite -1) due to the higher scattering factor of Fe atoms. This asymmetry due to the scattering factor profile (or equivalently the composition profile) is present in Guinier's theory with several harmonics, in which satellite intensities are a function of the composition modulation (Sec. 2.2.3).

- The lattice spacing calculated from the main peak's position corresponds to the average lattice spacing $d_0 = (d_{Cr} + d_{Fe})/2$ within a 0.01% relative error. This means that the average lattice spacing is the most dominant one in the structure, which is intuitive. This is also in agreement with Guinier's theory (Sec. 2.2.2 and Sec. 2.2.3), in which he predicts the main peak's position at $2\theta_0 = 2\arcsin\left(\frac{n\lambda}{2d_0}\right)$, see Eq. 2.69.

- The lattice spacing calculated from second order satellites is harder to identify and it is not clear which part of the multilayers they represent. We know that second order satellites appear when the lattice spacing profile is not perfectly rectangular and that the peak width is very large (and therefore not very noticeable) in the case of only one Fe/Cr bi-layer (Fig. 2.10). Second order satellites must therefore be related to the presence of an interface and to the periodicity of the bi-layer. It is interesting to note that both these satellites are not centered around their peak positions and their intensity distribution has an asymmetric Gaussian form. This means that lattice spacing fluctuations around its main value are not symmetric. Since satellite -2 (respectively +2) is inclined towards higher values of 2θ, there are more planes with negative (positive) lattice spacing fluctuations around its corresponding lattice spacing $d_{r,j}(-2)$ (respectively $d_{r,j}(+2)$).

	-2	-1	0	+1	+2
calculated lattice spacings, in nm	0.145160	0.144296	0.143111	0.141949	0.141074
input lattice spacings, in nm		$d_{Cr} = 0.144250$	$d_0 = 0.143125$	$d_{Fe} = 0.142000$	
absolute value of the relative error		0.03%	0.01%	0.04%	

Table 2.4: Lattice spacings (in nm) calculated from the simulated XRD profiles before annealing using Bragg's law on each peak's position. The X-ray wavelength is $\lambda = 0.154061$ nm and $n = 1$.

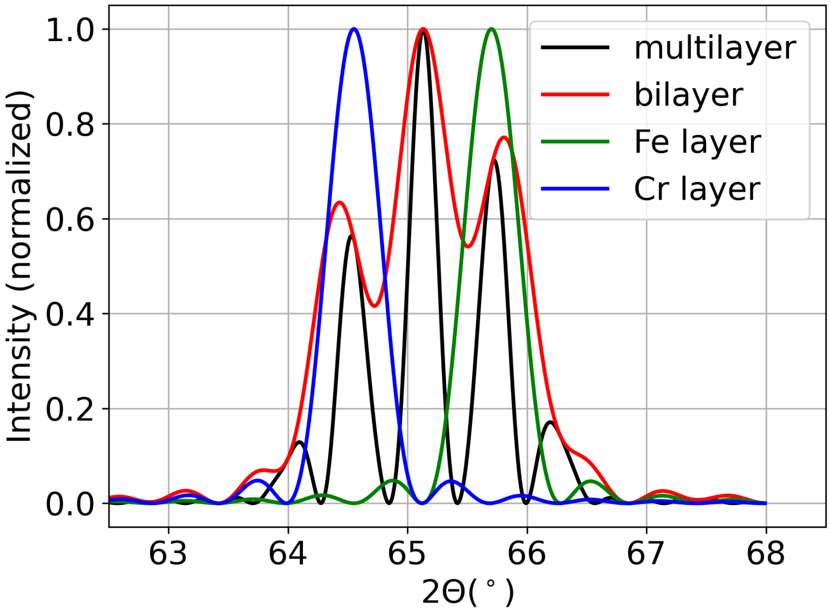

Figure 2.10: Comparison of the XRD profile obtained in the case of a multilayer, one bilayer, a pure Fe layer, and a pure Cr layer. The main XRD peak of the pure Fe layer (resp. Cr layer) is at the same position as satellite +1 (resp. -1) of the multilayer. In the case of one bilayer, second order satellites disappear.

What we can conclude from this study is that each satellite results from rays diffracted from specific planes of the multilayer, and therefore the time evolution of each satellite is mostly related to the evolution of the composition profile (and as a consequence the scattering factor and the lattice spacing profiles) in these particular layers. We conclude the following

- satellite 0: related to the average lattice spacing in the multilayer. Peak position shift related to the decrease of the homogeneity of the multilayer;
- satellite -1: related to the Cr-rich layer. Peak position shift and intensity decay related to the decrease in the homogeneity in the Cr-rich layer due to Fe diffusion, which affects the lattice spacing (less constructive waves) and the scattering factor (increases on average it because $f^0_{Fe}(\theta, \lambda) > f^0_{Cr}(\theta, \lambda)$, $\forall\theta$);
- satellite +1: related to the Fe-rich layer. Peak position shift and intensity decay related to the decrease in the homogeneity in the Fe-rich layer due to Cr diffusion in it, which affects the lattice spacing (less constructive waves) and the scattering factor (decreases on average because $f^0_{Cr}(\theta, \lambda) < f^0_{Fe}(\theta, \lambda)$, $\forall\theta$);
- satellites ±2: related to the periodicity of the multilayer but the relation is not very clear. Peak positions affected by the change in lattice spacing periodicity in the whole multilayer. Peak intensities affected by the in-homogeneity in the composition and lattice spacing profiles.

Since the intensity of first order satellites depends here on the average lattice spacing in a pure layer, the intensity of such satellites will decrease if:

- atoms with a lower scattering factor replace atoms with a higher scattering factor. Here, if Cr atoms replace Fe atoms. In the opposite scenario in which Fe atoms replace Cr atoms, the intensity of the satellite will increase;
- the number of planes belonging to the layer decreases. When the thickness of a layer decreases the diffracted intensity from it will decrease, and the opposite is true when the thickness increases;
- planes have different compositions. When the concentration deviates from its initial value in a fraction of the planes, so does the lattice spacing and only a fraction of the diffracted rays are constructive which decreases the intensity of the satellite.

On the other hand, the position of the main peak will change if the average lattice spacing changes (which is not expected to happen with a linear Vegard's law), and the position of first order satellites will change if the average lattice spacing in their corresponding layer changes.

2.6 Simulation of interdiffusion in Fe/Cr multilayers

In this section, we simulate the concentration profiles using an AKMC simulation (Sec. 2.4.2.1), and we simulate XRD profiles using the XRD simulation code (Sec. 2.4.2.2). We simulate the evolution of two bi-layers of Fe/Cr at 500°C for up to 274h, at 450°C for around 276 days. We analyze the evolution of the composition profile, the microstructure and the XRD peak positions and intensities. From the XRD profiles we study the evolution of the lattice spacing and the periodicity of the multilayer, we identify different kinetic regimes and calculate interdiffusion coefficients. In this section, we will only discuss in detail the results obtained at

500°C because all temperatures lead to the same conclusions. The evolution of the microstructure, the composition profile and the XRD profiles are the same qualitatively, the only difference being that diffusion is slower at lower temperatures. As a consequence, the evolution of the diffusion profile using the AKMC simulation is the most advanced at 500°C and allows us to study with better accuracy the diffusion in the Cr-rich layer, which is the slowest diffusion process in this system.

2.6.1 Concentration profiles

We simulate the annealing of Fe/Cr multilayers using Senninger's AKMC code by studying 2 Fe/Cr bilayers as shown in Fig. 2.8. We simulate the annealing at the constant temperature of 500°C for 274h. Figure 2.11 shows how the simulated concentration profile in one of the bilayers evolves during annealing. The concentration profile is not symmetric between the two different layers. This makes sense because we know that the interdiffusion coefficient is concentration dependent and that Cr diffusion is faster in a pure Fe layer than in a pure Cr layer (Fig. 2.6). At the beginning of annealing, Cr diffuses fast and deep into the Fe-rich layer while Fe atoms diffuse slower in the Cr-rich layer and accumulate in the vicinity of the interface. The interface (if we define it at the inflection point of the concentration profile) shifts towards the Cr-rich layer, which leads to a thickening of the Fe layer and a shrinking of the Cr layer. Equilibrium is reached in the Fe-rich layer after approximately 24h. After that, Cr no longer diffuses in the Fe-rich layer while the Fe atoms that accumulated at the interface start diffusing slowly in the bulk of the Cr layer until equilibrium is almost reached at 274h. During this latter diffusion mechanism, the interface shifts in the opposite direction, towards the Fe-rich layer, and the layers almost go back to their initial thicknesses (minus the broadening of the interface). After equilibrium is reached in both layers, if the interface is sharp, we know that the Fe-rich layer will be slightly thicker than the Cr-rich layer due to the asymmetry in the miscibility gap (discussed in Sec. 2.3.1).

Therefore, at the beginning of annealing, there is diffusion of Cr in the Fe-rich layer accompanied by a diffusion of Fe along the interface and an interface shift. At longer times, and after equilibrium is reached in the Fe-rich layer, there is slow diffusion of Fe in the Cr-rich layer. The two bulk diffusion phenomena happen in two separate times and both of them occur along with interface mobility.

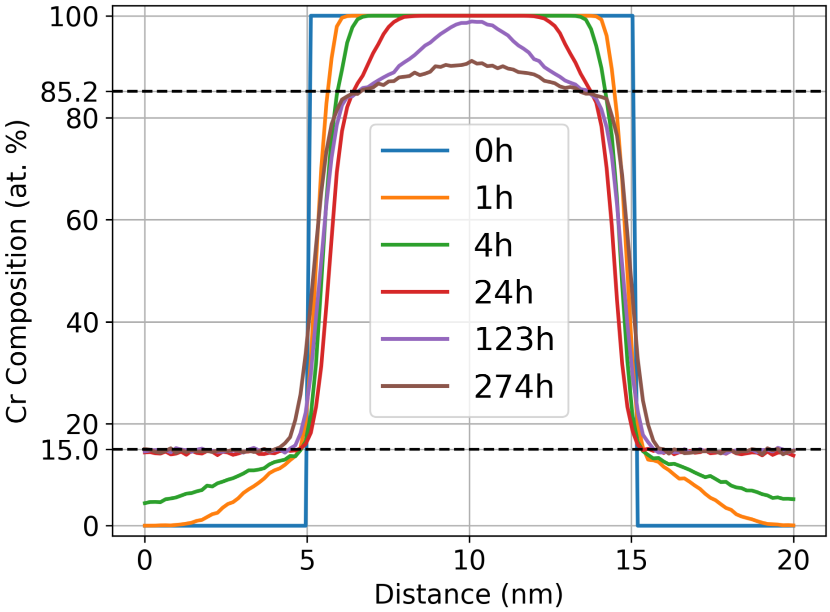

Figure 2.11: Simulated Cr concentration profile before and after annealing at 500°C for 274h. Dashed lines indicate the solubility limits in the Fe-rich (15 at. %Cr) and the Cr-rich (85.2 at. %Cr) layers. At $t = 24$h, equilibrium is reached in the Fe-rich layer, and at 274h, equilibrium is almost is reached in the Cr-rich layer.

2.6.2 Microstructural evolution

Figure 2.11 shows the evolution of the average concentration in the z-direction, which is a direction perpendicular to the multilayer's stacking planes. Each concentration value is an average value over a plane and is not necessarily representative of the local concentration at all points of the plane. We do not know if there is preferential diffusion directions or planes or if diffusion is homogeneous in all directions. OVITO [142] allows us to study the microstructure of the multilayers from the configurations obtained in the AKMC simulation. In Fig. 2.12, we study the evolution of the atomic structure and the local equilibrium concentration at different annealing times. We take a slice perpendicular to the interface planes and of 10 lattice planes of thickness, and we consider, around each Cr atom, a local surrounding made up of its nearest-neighbors within a 3 lattice parameter radius. In the right part of Fig. 2.12, we only draw the Cr atoms whose local surrounding has a concentration equal to one of the two equilibrium concentrations (15 at. %Cr in a Fe phase, and 85.2 at. %Cr in a Cr phase). From the left side of Fig. 2.12, we can know that Cr and Fe diffuse progressively through the interface and that diffusion is homogeneous in each plane, the Cr diffusion being faster. From the right side the figure, we can see that as diffusion progresses plane by plane, so does local equilibrium concentration.

When annealing starts, local equilibrium concentration is immediately established at the interfaces with the Cr-rich layers. Then Cr diffuses fast in the Fe-rich layers and local equilibrium concentration in the Fe-rich layers is established progressively from the interface towards the middle of the layer. The same phenomena is observed when Fe later diffuses in the Cr-rich layers, except that this latter diffusion and equilibrium happen at a slower pace.

When equilibrium is reached in the Fe-rich layer at 24h of annealing, around 21% of the Cr atoms that are in the Fe-rich layer are at local equilibrium and they are distributed in a homogeneous manner in the layer. In the Cr-rich layer, there is only equilibrium concentration at the interfaces and its distribution is also homogeneous.

After 274h of annealing, around 24% of the Cr atoms that are in the Fe-rich layer are at local equilibrium and they are still distributed homogeneously. The number of Cr atoms at equilibrium remained almost the same between 24h and 274h, but their percentage increased because the Fe-rich layer's thickness decreased and the total number of atoms in it decreased. On average, around 14% of Cr atoms are at equilibrium in the Cr-rich layer and are also distributed in a homogeneous manner. The percentage of Cr atoms at equilibrium in the middle plane of the Cr-rich layer is 12% and is slightly lower than the average 14%, which confirms that equilibrium is almost but not yet reached in this layer.

We conclude from this paragraph that Cr and Fe diffuse in a homogeneous way plane by plane from the interface towards the bulk, and by progressively establishing local equilibrium concentration in the planes.

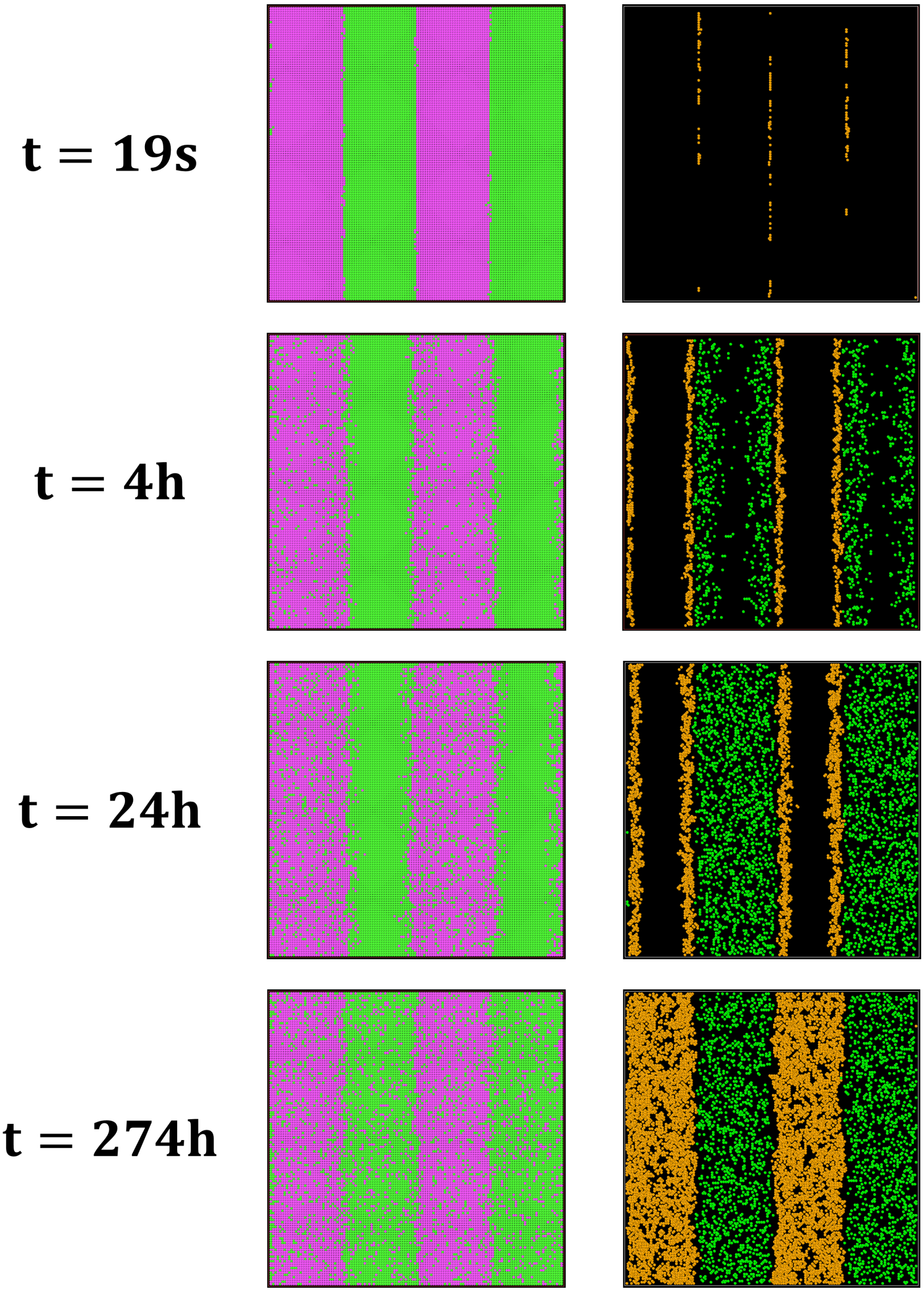

Figure 2.12: Left: distribution of all Fe and Cr atoms in the bi-layer. Fe atoms are represented in purple, while Cr atoms are represented in green; Right: distribution of Cr atoms that are at local equilibrium concentration within a radius of 3 lattice parameters during annealing. Cr atoms at a local equilibrium concentration $C_1^{eq} = 15.0 \pm 0.5$ at. %Cr are drawn in dark green, while Cr atoms at a local equilibrium concentration $C_2^{eq} = 85.2 \pm 0.5$ at. %Cr are drawn in orange.

2.6.3 XRD simulation

We use the concentration profiles obtained in the AKMC simulation (Fig.2.11) as inputs in the XRD simulation code (Sec. 2.4.2.2), to simulate the diffracted profiles before and after annealing. Since experimental XRD profiles should always be normalized with respect to the maximum intensity (Sec. 2.4.1.2), we present simulated profiles in the same way. Normalized satellite intensities decay with annealing in a visible manner, while peak positions shift in a less pronounced way. In this section, we will study in detail the qualitative and quantitative peak position shifts and intensity decays.

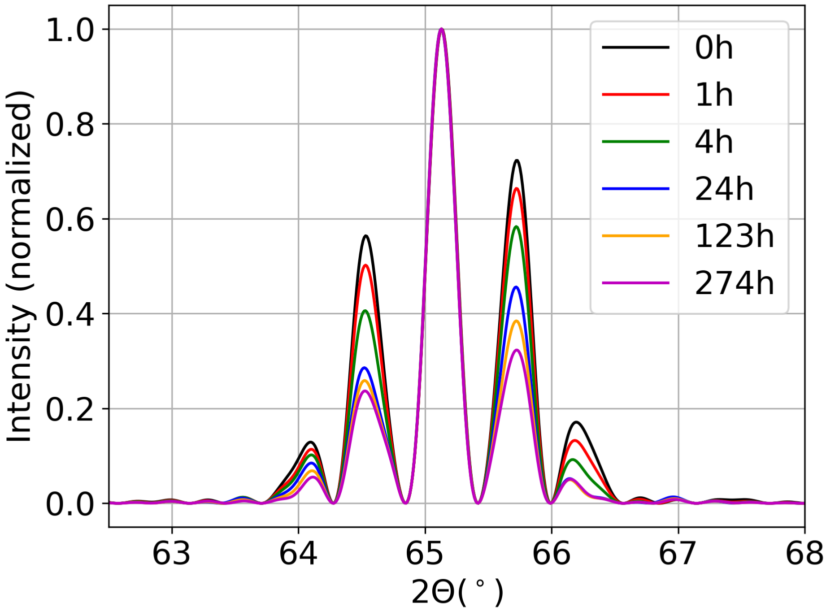

Figure 2.13: Normalized XRD profiles simulated using the AKMC concentration profiles and the XRD simulation code, before and after annealing at 500°C for up to 274h. The intensities at a time t are normalized by the intensity of the main peak at time t, such that the intensity drawn corresponds to $I(t)/I_0(t)$, where $I(t)$ and $I_0(t)$ are respectively the un-normalized intensity and the main peak's intensity, at time t.

2.6.3.1 Satellite peaks decay

The decay of satellite peak intensities with annealing can be observed more clearly by studying the time evolution of the un-normalized intensity of each satellite, $I_{\pm m}(t)$, with respect to its initial intensity, $I_{\pm m}(0)$. In Fig. 2.14 we plot the time evolution of the logarithm function of the intensity ratios. Remember that, if the interdiffusion coefficient does not depend on concentration, the evolution of this function is expected to be linear (Sec. 2.2.4). All satellite intensities exhibit a sharp linear decrease at the beginning of annealing, and until around 4h. At longer annealing times, the evolution of satellites has a slower pace, and is again linear after 32h. Satellites +1 and -2 keep decaying but in a slower manner, satellite -1 decays very slowly and seems to reach a stationary evolution, while the intensity of satellite +2 increases slightly over time. Therefore, there are two regimes in which the decay is linear, the first one between 0 and 4 hours, and the second one between 32 and 274 hours. We know that the FeCr interdiffusion coefficient is concentration dependent (Fig. 2.5), however the linearity of the intensity decay at different time ranges hints at the presence of separate kinetic regimes, such that, in each regime, one interdiffusion coefficient dominates and drives the evolution of the system. We call these regimes respectively A and C. Between regimes A and C, a regime B which is not linear is identified and is sort of a transition regime between the two. The critical times at which regimes A and C begin and end are therefore: 0, 4, 32 and 274 hours.

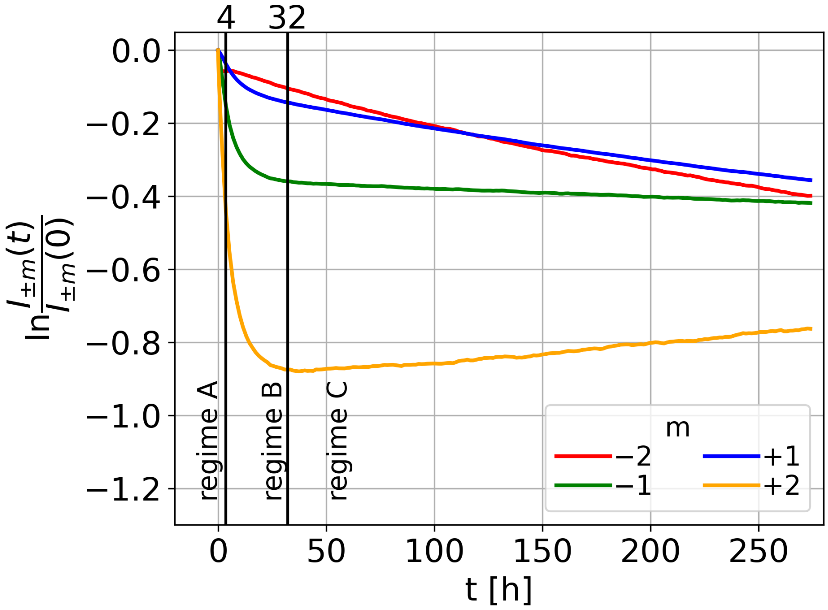

Figure 2.14: XRD satellites intensity decay of AKMC simulated multilayers annealed at 500°C for 274h. The three different kinetic regimes are separated by black vertical lines. The decay is linear in regimes A and C, and non-linear in regime B. Therefore, only regimes A and C could be linearly fit.

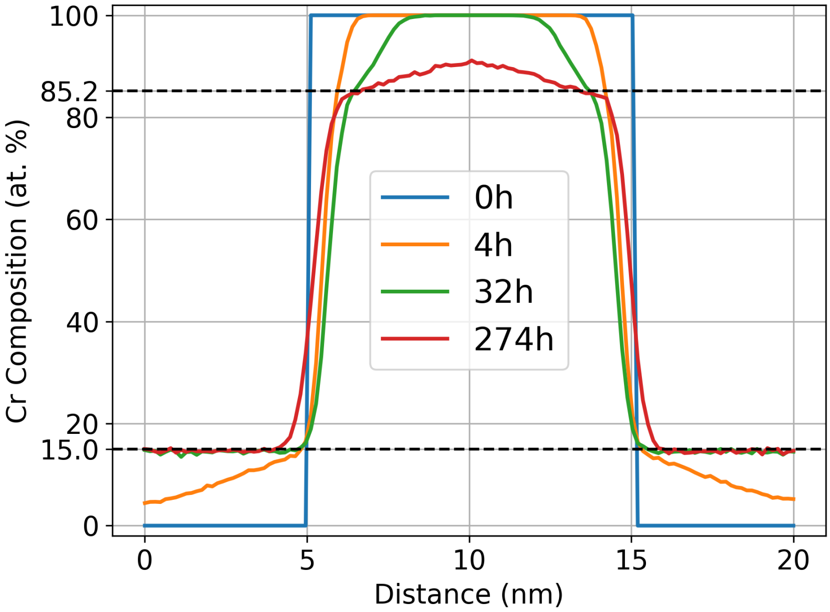

Figure 2.15: Simulated Cr concentration profile at the regime transition times: regime A is between 0h and 4h, regime B is between 4h and 32h, and regime C is between 32h and 274h. Dashed lines indicate the solubility limits in the Fe-rich (15 at. %Cr) and the Cr-rich (85.2 at. %Cr) layers.

Analysis of the composition profile in each regime In order to identify the diffusion mechanisms dominating each kinetic regime, we plot in Fig. 2.15 the composition profiles at these critical times. In regime A, Cr diffuses in the Fe-rich layers and reaches the center of the layer, while Fe accumulates at the interfaces and causes the interfaces to move towards the Cr-rich layers. In regime C, Fe diffuses in the Cr-rich layers and the interfaces move towards the Fe-rich layers. In regime B, a transition between the kinetics of regimes A and C takes place when equilibrium is reached in the Fe-rich layer (which happens at t=24h, see Sec. 2.6.1 and Sec. 2.6.2). Note that the two bulk interdiffusion mechanisms happen in two separate times since Fe does not diffuse in the Cr layer until after equilibrium is reached in the Fe-rich layer. In regime A, there is only bulk diffusion in the Fe-rich layer, while in regime C there is only bulk diffusion in the Cr-rich layer. Therefore, the fast decay of satellite intensities in regime A happens along with a fast interdiffusion in a local environment of low Cr concentration, while the slower decay in regime C takes place in parallel with a slower interdiffusion in a local environment of high Cr concentration. Interface mobility also affects satellite decays and peak positions because it reflects a change of layer thicknesses. Table 2.5 summarizes the kinetic phenomena happening in each regime. Since the evolution of satellites +1 and -1 is related to the evolution of the Fe-rich layer and Cr-rich layer respectively (Sec. 2.5), we can study the absolute intensity of these satellites and their decay rates as a function of the kinetic events listed in Table 2.5.

Regime A	Regime B	Regime C
fast diffusion of Cr in the Fe-rich layer	fast diffusion of Cr in the Fe-rich layer until equilibrium, then slow diffusion of Fe from the interface to the Cr-rich layer	slow diffusion of Fe from the interface to the Cr-rich layer
fast diffusion of Fe from the Fe-rich layer to the interface	fast diffusion of Fe from the Fe-rich layer to the interface until equilibrium, then slow diffusion of Cr from the Cr-rich layer to the interface	slow diffusion of Cr from the Cr-rich layer to the interface
fast Fe accumulation at the interface	fast Fe accumulation at the interface, then slow Fe depletion at the interface	slow Fe depletion at the interface
interface shift towards Cr-rich layers: - thickness of the Fe-rich layer increases - thickness of the Cr-rich layer decreases	interface shift towards Fe-rich layers until equilibrium, then interface shift towards Cr-rich layers: - thickness of the Fe-rich layer decreases then increases - thickness of the Cr-rich layer increases then decreases	interface shift towards Fe-rich layers: - thickness of the Fe-rich layer decreases - thickness of the Cr-rich layer increases

Table 2.5: Comparative summary of the kinetic phenomena happening in regimes A, B and C.

Analysis of peak intensity changes in each regime We know from Table 2.5 how in each regime the composition profile changes in the Fe-rich and Cr-rich layers, and how the interface shift modifies the number of planes of these layers. We can make the following conclusions, which are also summarized in Table 2.6:

- In regime A, in the Fe-rich layer,
  - the thickness of the layer increases. This increases the number of diffracting planes;
  - the concentration gradient increases, and therefore the lattice spacing is not constant between all planes. This lowers the number of diffracted rays in constructive interference;
  - Cr atoms replace Fe atoms. This lowers the scattering factor of these planes.

  Therefore, in regime A, the decay of satellite +1 results from a competition between, on one hand, Cr atoms replacing Fe atoms and the non-homogeneity of the layer, which decrease the diffracted intensity, and, on the other hand, the increase of the Fe-rich layer's thickness, which increases the diffracted intensity.

- In regime A, in the Cr-rich layer,
  - the thickness of the layer decreases. This decreases the number of diffracting planes;
  - the concentration is constant across all planes, and therefore so is the lattice spacing;
  - Fe atoms did not replace Cr atoms. The scattering factor remains the same.

  Therefore, in regime A, the decay of satellite -1 is a consequence of the interface shift which decreases the Cr-rich layer's thickness.

- In regime B, in the Fe-rich layer,
  - the thickness of the layer increases. This increases the number of diffracting planes;
  - the concentration gradient decreases and becomes null, and therefore the lattice spacing is the same between all planes of the layer. This increases the number of rays in constructive interference;
  - Cr atoms replace Fe atoms. This lowers the scattering factor of these planes.

  Therefore, in regime B, the decay of satellite +1 results from a competition between, on one hand, Cr atoms replacing Fe atoms which decreases the diffracted intensity, and, on the other hand, the homogenization of the concentration gradient in the layer and the increase of the Fe-rich layer's thickness, which increases the diffracted intensity.

- In regime B, in the Cr-rich layer,
  - the thickness of the layer decreases. This decreases the number of diffracting planes;
  - the concentration gradient increases, and therefore so does the lattice spacing. This decreases the number of rays in constructive interference;
  - Fe atoms replace Cr atoms. This increases the scattering factor of these planes.

  Therefore, in regime B, the decay of satellite -1 results from a competition between, on one hand, the decrease of the Cr-rich layer's thickness and the increase of the concentration gradient, which decreases the diffracted intensity, and, on the other hand, Fe atoms replacing Cr atoms, which increases the diffracted intensity.

- In regime C, in the Fe-rich layer,
  - the thickness of the layer decreases slightly. This decreases the number of diffracting planes;

  - the concentration is constant across all planes, and therefore so is the lattice spacing;
  - there is no diffusion and atoms remain the same. The scattering factor remains the same.

  Therefore, in regime C, the decay of satellite +1 is a consequence of the interface shift which decreases the Fe-rich layer's thickness.

- In regime C, in the Cr-rich layer,
  - the thickness of the layer increases. This increases the number of diffracting planes;
  - the concentration gradient in the middle of the Cr-rich layer increases until Fe atoms reach the middle plane (after around 124h, see Fig. 2.11), and then the concentration gradient tends towards zero. This lowers the number of rays in constructive interference before 124h, then increases it;
  - Cr atoms are replaced by Fe atoms. This increases the scattering factor of these planes.

  Therefore, during the first 100 hours of regime C, the decay of satellite -1 results from a competition between, on one hand, the concentration gradient in the layer, which decreases the diffracted intensity, and, on the other hand, Fe atoms replacing Cr atoms and the increase of the Cr-rich layer's thickness, which increase the diffracted intensity. After Fe reaches the middle Cr plane in the Cr-rich layer, there are no factors that we can identify that lead to the decay of satellite -1. This is in agreement with the observations of Fig. 2.14.

Table 2.6 summarizes how the peak intensity of satellites ±1 is affected in each regime. Furthermore, this table shows clearly how the evolution of satellite intensities in regime B is at first the same as the evolution in regime A until equilibrium is reached in the Fe-rich layer (around 24h), and then becomes the same as the one in regime C. It is therefore not surprising that the decay is not linear in this regime since there is not one dominating kinetic phenomena but rather a transition between two.

	Regime A	Regime B	Regime C
decay of satellite +1	- Cr diffusion in the Fe-rich layer (Cr atoms replacing Fe atoms, and increased concentration gradient)	- Cr diffusion in the Fe-rich layer (Cr atoms replacing Fe atoms)	- interface shift
increase of satellite +1	- interface shift	- interface shift - Cr diffusion in the Fe-rich layer (homogenization of the concentration gradient)	-
decay of satellite -1	- interface shift	- interface shift - Fe diffusion in the Cr-rich layer (increased concentration gradient)	- Fe diffusion in the Cr-rich layer (increased concentration gradient until Fe reaches the middle of the Cr-rich layer)
increase of satellite -1	-	- interface shift - Fe diffusion in the Cr-rich layer (Fe atoms replacing Cr atoms)	- interface shift - Fe diffusion in the Cr-rich layer (Fe atoms replacing Cr atoms and homogenization of the concentration gradient after Fe reaches the middle of the Cr-rich layer)

Table 2.6: Comparative summary of the reasons behind the increase and decrease of the intensities of satellites ±1 in regimes A, B and C.

Analysis of peak decay rates in each regime After having identified in each regime the factors which increase and decrease a satellite's intensity, now we can better understand the difference in decay rates between different satellites and in different regimes. Interdiffusion in the Fe-rich layer is faster than in the Cr-rich layer due to the asymmetry of the interdiffusion coefficient. Therefore, the diffusion of Cr in the Fe-rich layer and the interface shift caused by it (regime A) alter the concentration and lattice spacing profiles at a faster rate than the interface shift caused by the diffusion of Fe in the Cr-rich layer (regime C). Therefore, the time evolution of all satellites will be faster in regime A. Then we try to understand why the decay of satellite -1 is faster than that of satellite +1 in regime A, and why the opposite is true in regime C:

- We first compare satellite intensity decay rates in regime A. This can be due to the fact that the decay of satellite -1 is caused by interface mobility and there are no factors that favor its increase. In contrast, the decay of satellite +1 resulting from the diffusion of Cr in the Fe-rich layer is opposed to by the interface shift. If we assume that the interface broadening is symmetric, then the interface shift which increases the number of planes in one layer decreases the number of planes in the other layer by an equal amount. Therefore, interface shift decreases the intensity of satellite -1 and increases the intensity of satellite +1 by the same amount. As a consequence, if we add up the decay of both satellites, we should obtain the decay of satellite +1 resulting from only the diffusion of Cr in the Fe-rich layer.

- Then we compare satellite intensity decay rates in regime C. In this regime, the decay of satellite +1 is caused by interface mobility and there are no factors that favor its increase. The decay of satellite -1 results from a competition of several factors and is therefore slower. We expect an intensity increase of satellite +1 after around 124h of annealing, however Fig. 2.14 shows that the intensity reaches a constant value instead. This hints that there are other factors contributing to first order satellite decays that we are not taking into consideration here. We know however, that interface shift contributes to the decrease of the intensity of satellite +1 in the regime.

What we can conclude from this study is that, in regime A, the fast and deep diffusion of Cr in the Fe-rich layer changes in a fast manner the composition and lattice spacing profiles of the Fe-rich layer, keeps the interface sharp and leads to a fast interface mobility due to the accumulation of Fe at the interface instead of diffusing in the Cr-rich layer. This leads to a fast decay of the satellite intensities, especially that of satellite -1 which is caused by the shrinking of the Cr-rich layer's thickness. In regime C, Fe diffuses slowly in the Cr-rich layer and the resulting interface shift is also slow. The evolution of the profiles affecting the XRD satellites is slower than in regime A and leads to a slower decay. Satellite +1 decays faster in regime C due to the interface shift which reduces the Fe-rich layer's thickness. In both regimes, the layer corresponding to the fastest decaying satellite corresponds to the layer whose thickness decreases and in which the composition profile does not change, and the decay of the fastest satellite is therefore directly related to the interface mobility. Ideally, this study should also be conducted for second order satellites. Unfortunately, since it is not clear which planes or layers contribute to the 2$^{\text{nd}}$ order satellite intensities, a similar study cannot be conducted for these satellites at the moment.

2.6.3.2 Interpretation of kinetic regimes

Separating satellite intensity decays into different kinetic regimes in which the decay is linear allows us to use Eq. 2.62 to calculate the interdiffusion coefficient. The use of this equation assumes that the interdiffusion coefficient does not depend on concentration. In our case, we assume that in each regime there is one dominating kinetic phenomena driven by an interdiffusion coefficient which alters the structure of the system in the most noticeable way. The use of Eq. 2.62 further assumes that the lattice spacing is constant in the multilayer which leads to the same intensities of satellites $\pm m$ (see Eq. 2.54). In our case, we know that these satellites do not have the same intensities at any time, not even at $t = 0h$. Since each satellite is diffracted at a different 2θ angle, it is a consequence of X-rays diffracted from planes with different lattice spacings (through the use of Bragg's law, Eq. 2.20). We showed in Sec. 2.5 that, before annealing, peak positions of satellites -1 and +1 correspond to the lattice spacing of the Cr-rich and Fe-rich layer respectively. Annealing will change the composition and lattice spacing profiles of these layers and therefore the intensity and position of these satellites. In general, each satellite stems from constructive interference in some part of the multilayer, and we assume that each of these parts has a constant average lattice spacing, and that we can write Eq. 2.62 for each satellite separately. This makes sense because all our previous analysis showed that each satellite is expected to be more sensitive to a specific interdiffusion coefficient, and because the evolution of the different parts of the multilayers (for example the bulk of the Fe-rich layer and the bulk of the Cr-rich layer) does not happen within the same time scale. Even though there are several approximations behind Eq. 2.62, the linearity of each satellite's decay in each regime suggests that we can use it by assuming that each satellite's decay is linked to a dominant interdiffusion coefficient. This might not give us exact values of interdiffusion coefficients, but could provide us with an order of magnitude for its value.

2.6.3.3 Multilayer period

To calculate the interdiffusion coefficients, we first need to determine the period of the multilayer. Guinier finds that the distance between a satellite m and a main peak is a function of the period of the multilayer (Eq. 2.69), which allows us to calculate this latter property from the XRD profiles as

$$\Lambda = \frac{\pm m\lambda}{2\left(\sin\theta_{\pm m} - \sin\theta_0\right)} = \frac{\pm m d_0 d_{\pm m}}{d_0 - d_{\pm m}}, \tag{2.71}$$

where $\theta_{\pm m}$ corresponds to the peak position of satellite $\pm m$, and $d_{\pm m}$ is the lattice spacing calculated from it using Bragg's law. According to Eq. 2.71, the value of the period is independent of the satellite and all peak positions lead to the same value of Λ. However, this is not the case in our work because peaks are not equally spaced. Remember that for first order satellites, $d_{-1} = d_{Cr}$ and $d_{+1} = d_{Fe}$, and we know that $d_{Cr} - d_0 \neq d_{Fe} - d_0$. Therefore, if we want to use Eq. 2.71, we will not obtain the real period of our multilayer. The positions of each satellite $\pm m$ with respect to the main peak's position will give us a different period $\Lambda_{\pm m}$. $\Lambda_{\pm m}$ can be seen as the period of an ideal multilayer in which the lattice spacing corresponds to $d_{\pm m}$. Additionally, peak positions shift with annealing, and therefore each satellite's period $\Lambda_{\pm m}$ changes over time. This is clearly seen in Fig. 2.16.

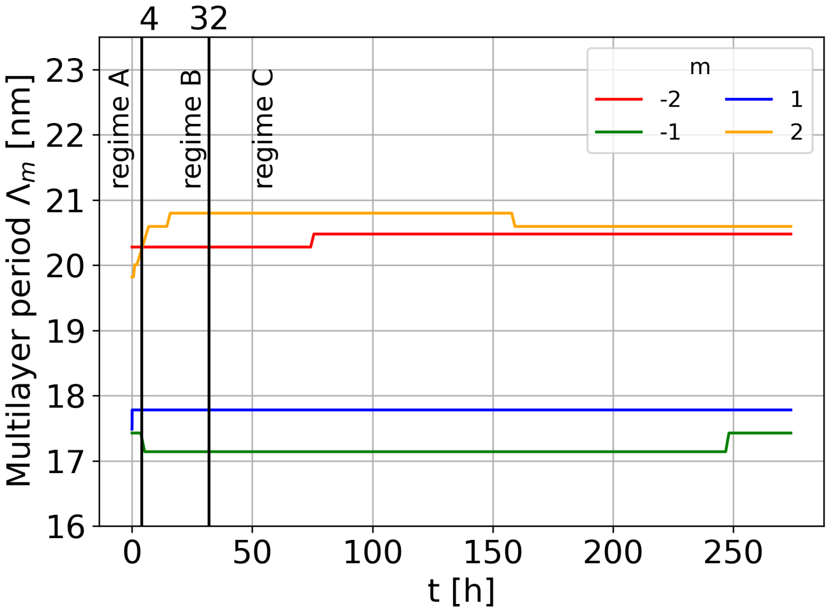

Figure 2.16: Multilayer period $\Lambda_{\pm m}$ calculated from the positions of first and second order satellites with respect to the main peak's position at different annealing times, using Eq. 2.71.

The period related to satellite -1 decreases by 0.286165 nm after around 5h of annealing (beginning of regime B), while the one related to satellite +1 increases by 0.295866 nm at the beginning of annealing (beginning of regime A). The change of periods related to satellites ±1 are therefore similar in absolute value. This result is consistent with our previous observations and how peak positions of satellites -1 and +1 are affected by the lattice spacing in the Cr-rich and Fe-rich layers respectively. Satellite -1 (resp. +1) corresponds to the Cr-rich (resp. Fe-rich) layer whose average lattice spacing decreases (resp. increases) because of the incorporation of Fe (Cr) atoms in it, knowing that $d_{Fe} < d_{Cr}$. This explains why Λ_{-1} decreases, while Λ_{+1} increases. Λ_{-1} increases again towards the end of annealing and it is not very clear why this happens. It could be related to the interface shift which increases the thickness of the Cr-rich layer, but this assumes that the added planes have a higher Cr concentration than the ones in the middle of the Cr-rich layer. Concerning second order satellites, the period of satellite +2 is the one that changes the most. It increases gradually throughout regimes A and B and reaches a stationary value in regime C, before decreasing again towards the end of annealing. This satellite's period changes mainly with the diffusion of Cr in the Fe-rich layer. The period calculated from satellite -2 remains the same until around 80 hours (which is close to when Fe reaches the middle Cr-rich layer) when it increases to a constant value for the rest of annealing. It is interesting that the periods calculated from second order satellites are the closest to the real multilayer period (20 nm), and that they both have similar values at the end of annealing.

For the calculation of the interdiffusion coefficient in each kinetic regime, we will consider the average values of $\Lambda_{\pm m}$ calculated in each kinetic regime. We assume that this average period is the one that is the most representative of the part of the multilayer which affects the evolution of satellite m throughout the corresponding regime. We call Λ_m^R the average period calculated from the position of satellite m during regime R, and we present in Table 2.7 the calculated averages for the different satellites and regimes.

	-2	-1	+1	+2
$\Lambda^{A}_{\pm m}$ (nm)	20.279361	17.427120	17.722187	19.971828
$\Lambda^{C}_{\pm m}$ (nm)	20.442590	17.172402	17.781360	20.702744

Table 2.7: Average multilayer period (in nm) in each kinetic regime $R = \{A, C\}$, calculated from the simulated XRD profiles, using Eq. 2.71 and the peak position of each satellite m with respect to the main peak's position.

2.6.3.4 Interdiffusion coefficients

We calculate in regimes A and C, the interdiffusion coefficients by applying Eq. 2.62 to the normalized intensity decays of each satellite separately. We use the average multilayer period values calculated in Table 2.7. For better readability, we plot the results in Fig. 2.17 as a function of each satellite, and in Fig. 2.18 as a function of concentration, in order to compare with Senninger's results of the concentration dependent interdiffusion coefficient (Fig. 2.6).

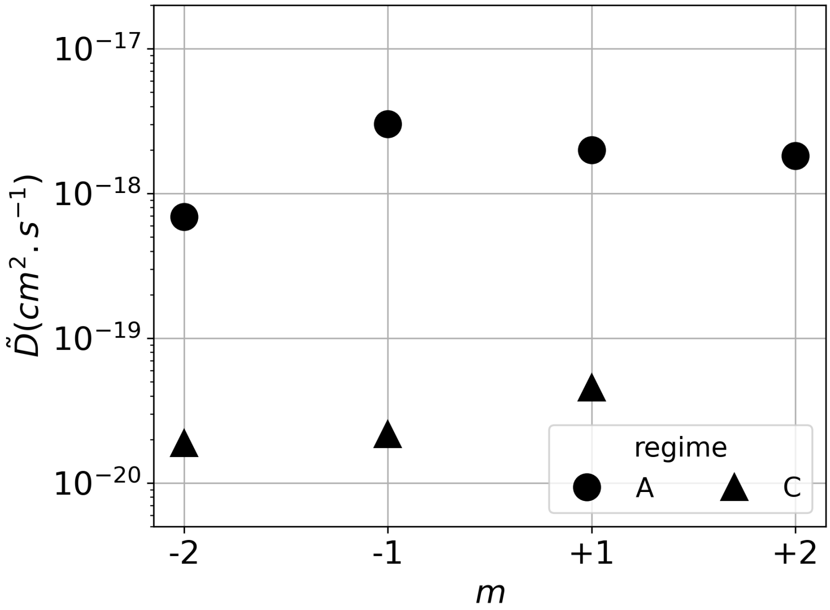

Figure 2.17: Interdiffusion coefficient calculated using Eq. 2.62 from the simulated XRD satellite intensity decays (Fig. 2.17) in the kinetic regimes A and C, and from each satellite decay separately. Note that $\tilde{D}$ could not be calculated from the evolution of satellite +2 in regime C because its intensity does not decrease.

Extracted interdiffusion coefficients are around 10^{-18} cm^2/s in regime A, and between 10^{-20} and $10^{-19}cm^2$/s in regime C. As expected, coefficients in regime A are larger than those in regime C because the evolution of the structure as a consequence of Cr diffusion in the Fe-rich layer is faster than its evolution as a consequence of Fe diffusion in the Cr-rich layer. Additionally, coefficients calculated in regime A are consistent with Senninger's coefficients at low-Cr concentrations, while those calculated in regime C are similar to her coefficients at high-Cr concentrations. Let us examine in more detail the values of the interdiffusion coefficient calculated in each regime:

- Regime A: The values of $\tilde{D}$ extracted from the decay of satellites ±1 and satellite +2 correspond to the values calculated by Senninger for concentrations between 0 and 15% at. Cr, which is the concentration range in the Fe-rich layer during this regime. This is consistent with our previous findings. The interdiffusion coefficient related to satellite -1 is close to the value at 15 at. %Cr, which is the concentration close to the interface with the Fe-rich layer, and its value slightly below the 15 at. %Cr one is consistent with the fact that Cr content inside the Fe-rich layer is below 15 at. %Cr. This further confirms that this satellite is sensitive to the interface shift. Concerning satellite +1, we know that its decay is directly a consequence of Cr diffusing in the Fe-rich layer, and the calculated value of $\tilde{D}$ is coherent with this hypothesis. Satellite -2 gives the smallest value of $\tilde{D}$ and is consistent with the one calculated by Senninger at 20 at. %Cr. This concentration represents the Cr content at the interface and satellite -2 could be related to the diffusion along the interface with the Fe-rich layer or across it.

- Regime C: All satellites yield a value of $\tilde{D}$ consistent with Senninger's coefficients in a range of concentrations between 90 and 100 at. %Cr. The value calculated from the decay of satellite +1 is the highest and close to the value at 90 at. %Cr. This concentration is similar to the concentration near the interface with the Cr-rich layer, and confirms this satellite's sensitivity to interface shift in this regime. We expected satellite -1 to be sensitive to the diffusion of Fe from the interface to the middle of the Cr-rich layer, and this is consistent with a value of the interdiffusion coefficient at a concentration between 95 and 100 at. %Cr.

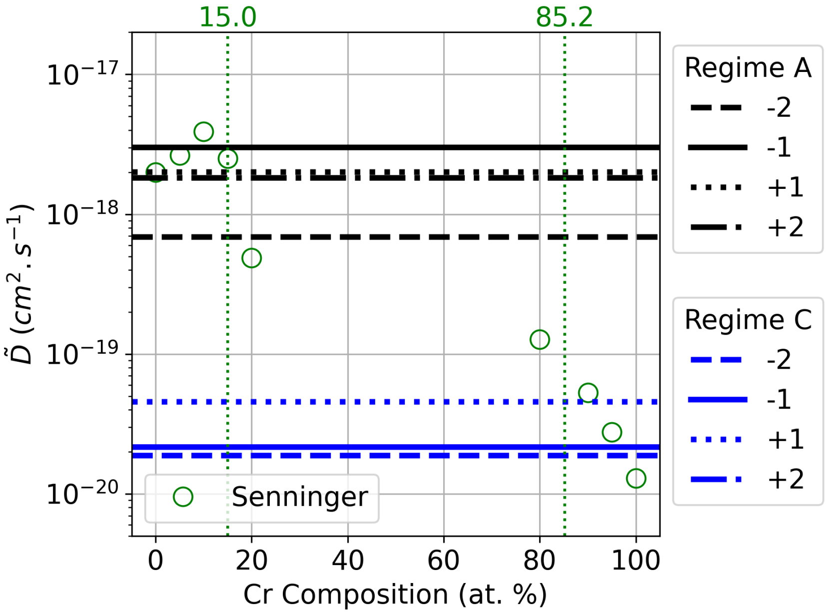

Figure 2.18: Values of the interdiffusion coefficient calculated from each simulated satellite intensity decay, in regimes A and C, for multilayers annealed at 500°C for 274h. The values are compared to the values of the concentration dependent interdiffusion coefficient calculated by Senninger et al. using the wave attenuation method and the same AKMC model [9, 16]. Since our calculated coefficients do not depend on concentration, we draw them as horizontal lines.

We conclude from this section that, in the case of a concentration dependent interdiffusion, we can still split the kinetics of the system into different regimes in which one diffusion mechanism dominates in changing the composition and lattice parameter. Then we can identify, with a good order of magnitude, the value of the interdiffusion coefficient affecting the satellite's decay. This method of calculating interdiffusion coefficients should apply best when diffusion is most asymmetric, because then the different kinetic regimes are well separated. In Fe/Cr multilayers, in the first kinetic regime, we can calculate the interdiffusion coefficient at the interface with the Fe-rich layer (close to the solubility limit) and at a concentration close to 100 at. %Fe. In the second regime, we can calculate the interdiffusion coefficient at the interface with the Cr-rich layer (close to the solubility limit) and at a concentration close to 100 at. %Cr. In theory, this should be applicable to any binary multilayers in which one species diffuses faster than the other, by at least two orders of magnitude. In Table 2.8, we compare the values obtained from satellites ±1 to the values calculated by Senninger at different concentrations. The absolute value of the relative error between these values is less than 31% for all concentration ranges, which is reasonable for an interdiffusion coefficient. This suggests that the method we proposed to calculate interdiffusion coefficients, combining AKMC simulations, XRD simulation based on Bragg's law, linear diffusion theory and Guinier's model, is a powerful tool to calculate concentration dependent interdiffusion coefficients in multilayers. In Table 2.9, we list the calculated interdiffusion coefficients from first order satellite peak decays as a function of the concentration ranges which we think they represent.

In the next section (Sec. 2.7), we will apply the same methodology to experimentally annealed Fe/Cr multilayers and test the validity of our analysis and conclusions. We will calculate interdiffusion coefficients from satellite peak decays at 450°C and 500°C, and compare the values with the simulation results.

500°C			
Senninger		Our simulation	Absolute value of the relative error
at.%Cr	$\tilde{D}$ (cm^2/s)	$\tilde{D}$ (cm^2/s)	
0-15	2.76E-18	2.00E-18	27.4%
15	2.50E-18	3.02E-18	20.9%
90	5.30E-20	4.57E-20	13.7%
90-100	3.12E-20	2.17E-20	30.4%

Table 2.8: Interdiffusion coefficients calculated at 500°C from our simulations and compared to the values obtained by Senninger [9, 16] at different concentrations: the average value at concentrations between 0 and 15 at. %Cr, at the solubility limits (ideally we should compare our calculated value with $\tilde{D}\,(85.2)$ but this value was not calculated by Senninger, so we compare it with $\tilde{D}\,(90)$ instead, and the average value at concentrations between 90-100 at. %Cr (also, ideally, it should be 85.2-100 at. %Cr).

450°C	
at.%Cr	$\tilde{D}$ (cm^2/s)
0-15	7.79E-20
15	1.19E-19
85	1.13E-21
85-100	5.34E-22

Table 2.9: Interdiffusion coefficients at 450°C extracted from our multilayer simulations as a function of the concentration ranges we think they represent.

2.6.4 Conclusion on the simulation results

We conclude from this section that the combination of an AKMC simulation with an XRD simulation which produces diffraction profiles based on the AKMC composition profiles, is a powerful tool to extract composition-dependent interdiffusion coefficients in multilayers. The analytical theory behind the work was based on several assumptions which were not satisfied in the case of Fe/Cr multilayers. We managed to overcome this by properly dividing the evolution of the kinetics into several regimes, by identifying the time scales in which XRD satellite intensity decay is linear and by carefully analyzing the evolution of composition profiles. We identified that in each regime there is a main part of the multilayer (a set of planes or a layer) whose structure is the most affected by interdiffusion. This variation reflected in the decay of satellite intensities which allowed us to determine an interdiffusion coefficient at the average concentration in this part of the multilayer. In the first kinetic regime, which is the fastest, the diffusion of Cr in the Fe-rich layer changes the composition profile in that layer and allowed us to calculate interdiffusion coefficients at low Cr concentrations. During the second kinetic regime, the diffusion of Fe in the Cr-rich layer changed its composition and allowed us to calculate interdiffusion coefficients at high Cr concentrations. Additionally, we identified satellites sensitive to diffusion in the bulk part of the layers and satellites sensitive to diffusion near the interfaces, and therefore calculate coefficients in a Cr-rich layer, Fe-rich layer, and at concentrations near the solubility limits. In both regimes, the calculated coefficients were in agreement with Senninger's calculations [16].

2.7 Comparison of simulation and experiment results

In this section, we will compare experimental and simulation interdiffusion results. Experimentally, multilayers were annealed at 500°C for 16h and at 450°C for 260h, and XRD measurements were done throughout annealing at both these temperatures. Additionally, samples annealed at 500°C for 4h were analyzed using APT and STEM/HAADF. Therefore, we will compare the composition profiles and the layer thicknesses before and after annealing at 500°C for 4h, and we will compare XRD profiles at both temperatures, 450°C and 500°C. A comparative table at the end of this section (Table 2.11) summarizes these different comparison points.

2.7.1 Concentration profiles

We compare the Cr concentration profiles obtained by AKMC to the profiles obtained by APT before and after annealing at 500°C for 4h. The simulated and experimental profiles shown respectively in yellow and red in Fig. 2.19, are qualitatively and quantitatively in agreement, before and after annealing. In both simulation and experiment, Cr diffuses into the bulk of the Fe layer and reaches its center, while Fe diffuses more slowly into the Cr-rich layer, mainly close to the interface and without reaching the center of the Cr layer. The average values of Cr atomic fraction in the middle of the Cr-rich and Fe-rich layers are also in agreement between AKMC and experiment. The average of Cr atomic fraction (averaged over 5 different layers in the experiment, and 2 different layers in the simulation) in the middle plane of the Fe-rich layer and Cr-rich layer is measured to be 4.2 at. %Cr and 99.9 at. %Cr respectively by APT, and 4.7 at. %Cr and 100.0 at. %Cr respectively by AKMC. The average of Cr atomic fraction over the different layers and over 2.5 nm in the middle of the Fe-rich and Cr-rich layer is measured to be 4.5 at. %Cr and 99.9 at. %Cr respectively, by APT, and 5.0 at. %Cr and 100.0 at. %Cr respectively, by AKMC. We conclude that the asymmetry of the annealed profile and the resulting Cr composition in the center of the Fe-rich layers are in good agreement between AKMC and APT. Remember that, due to reconstruction artifacts, APT is not reliable around interfaces and leads to erroneous layer widths (Sec. 2.4.1.3). Therefore, layer thicknesses are studied experimentally using STEM/HAADF and the comparison is done in the next paragraph (Sec. 2.7.2).

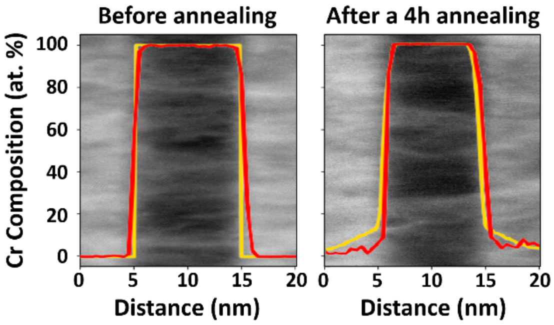

Figure 2.19: Cr concentration profiles in a Fe/Cr bilayer before (left) and after (right) annealing at 500°C for 4h measured by APT (red) and simulated by AKMC (yellow). The background image shows the Fe (light) and Cr (dark) layers obtained by STEM/HAADF.

2.7.2 Layer thicknesses

Figure 2.19 shows the simulated concentration profiles on a STEM/HAADF background. The layer thicknesses are in qualitative and quantitative agreement before and after annealing. Figure 2.20 shows more clearly how the simulated layer thicknesses change after a 4h annealing. Before annealing, the average values of Fe and Cr layer thicknesses measured by STEM/HAADF over the 3 middle layers are 9.6 nm ±0.3 nm and 9.3 nm ±0.3 nm respectively. After annealing, the thickness of the Fe-rich layer increases by relatively 5.8%, in the experiment, and by relatively 4.7%, in the AKMC. The thickness of the Cr-rich layer decreases by relatively 4.6%, in the experiment, and by relatively 4.7% in the AKMC. While the decrease of the thickness of the Cr layer is in agreement between AKMC and experiment, the relative increase of the Fe-rich layer is in less good agreement. This could be due to the fact that the simulations are done at constant volume as a consequence of using Vegard's law for the lattice parameter . This is why, in the simulation, the relative increase of one layer (here the Fe-rich layer) is exactly equal to the relative decrease of the other layer (here the Cr-rich layer), which is not the case in the experiment.

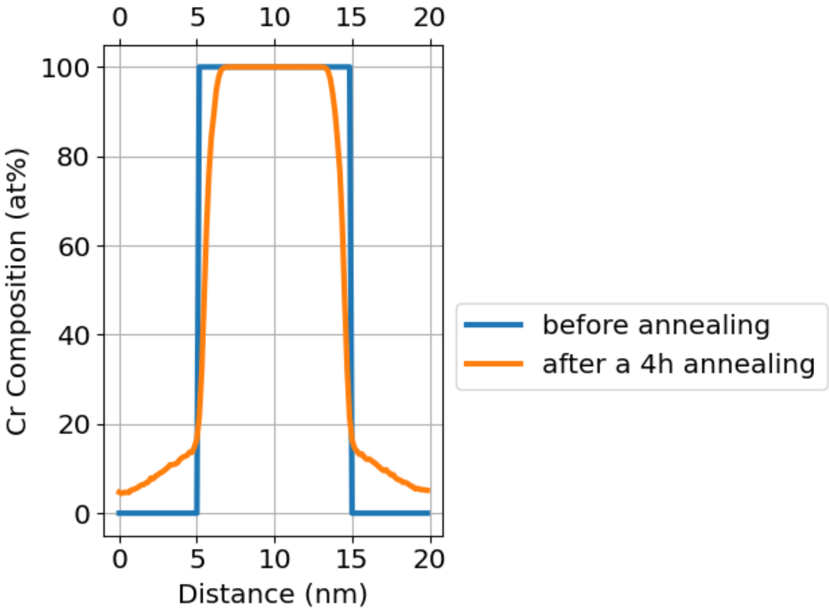

Figure 2.20: Cr concentration profile in the AKMC simulation of a Fe/Cr bilayer before and after annealing the multilayer at 500°C for 4h.

2.7.3 Microstructure

APT results showed that the annealed multilayer samples contain Fe-rich inclusions and oxides around dislocation lines traversing the Cr layers in various directions. The composition of these inclusions and oxides is not homogeneous and differs from one inclusion to the other. An example of an inclusion is shown in Figure 2.21, in comparison with the simulated layers. Since the simulation is missing these inclusions, this could lead to discrepancies between the experimental and simulated results. The chemical composition of the inclusion is shown in two directions in Fig. 2.22. The concentration of the inclusion ranges between 50 and 72 at. %Fe in one direction, and between 40 and 75 at. %Fe in another direction. These inclusions do not seem to affect the planar concentration profile in a noticeable way, since the concentrations in the middle of the Cr-rich layer remain almost equal to 100 at. %Cr (Sec. 2.7.1) and show no presence of Fe in this layer. Note that, according to Fig. 2.19, these inclusions do not seem to affect the compositions in the middle of the Cr-rich layer.

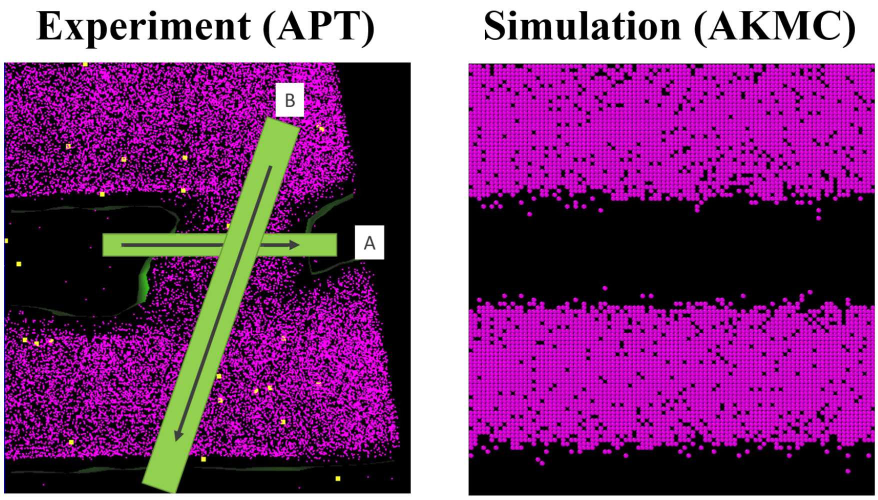

Figure 2.21: Fe inclusion (purple) traversing the Cr-rich layer (black) observed using APT (left) in the sample annealed at 500°C for 4h. The simulation (right) does not include any inclusions. The chemical compositions of the inclusion in the A and B directions are shown in Fig. 2.22.

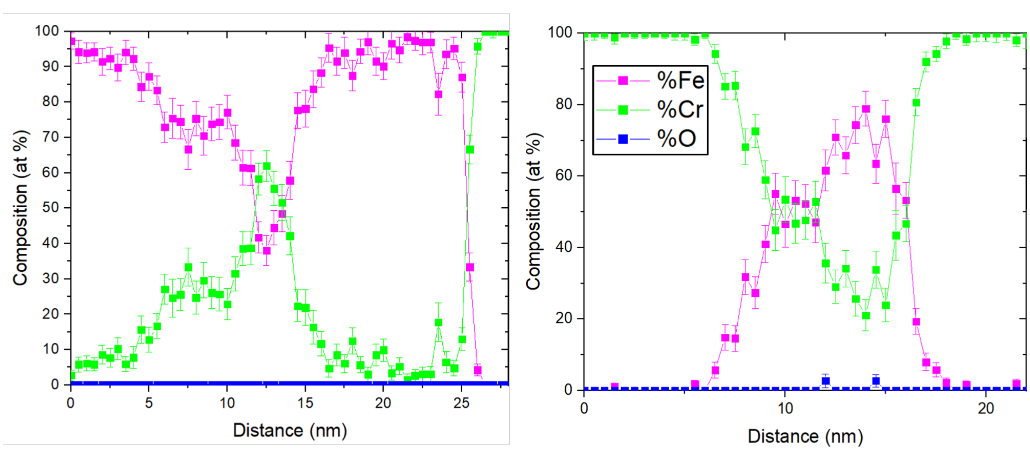

Figure 2.22: The chemical composition of the Fe inclusion (Fig. 2.21) in the A direction (left) and in the B direction (right).

2.7.4 XRD profiles

In this section, we compare the experimental and simulated XRD profiles. We focus on comparing the time evolution of peak positions and intensities. In Fig. 2.23, we show the profiles before annealing and after annealing at 500°C for 4h and for 16h. Note that we cannot compare absolute values of intensities, and in both experiment and simulation, the intensities are normalized with respect to the main peak's intensity (discussed in Sec. 2.4.1.2). In both experiment and simulation, the XRD profiles present a main Bragg peak at around $2\theta = 65°$ and four satellite peaks, two on each side of the main peak.

Before annealing, the intensities and positions of the peaks are in good agreement between the experiment and simulation. Table 2.10 shows that the lattice spacings calculated from the experimental and simulated satellite peak positions are all below a 0.1% relative error. This verifies that the input conditions in the AKMC code (number of planes) and in the XRD simulation code (lattice spacings

	-2	-1	0	+1	+2
experimental $d_{r,j}(m)$, in nm	0.145220	0.144216	0.143228	0.142083	0.141055
simulated $d_{r,j}(m)$, in nm	0.145160	0.144296	0.143111	0.141949	0.141074
absolute value of relative error	0.04%	0.06%	0.08%	0.09%	0.01%

Table 2.10: Lattice spacings (in nm) calculated from the experimental and simulated XRD profiles before annealing by using Bragg's law on each peak's position, and the absolute value of the relative errors between them. The X-ray wavelength is $\lambda = 0.154061$ nm and $n = 1$.

and scattering factors of the pure elements, and Vegard's law) are consistent with the experiment before annealing. This confirms again the APT analysis which showed that before annealing, the multilayers have almost the same composition.

After annealing, peak positions shift and satellite intensities decay. These two changes are more pronounced in the experimental profiles, in which satellites decay faster after 4h of annealing, and all peaks shift positions in a more visible way. In particular, 2^{nd} order satellites almost disappear in the experiment after 4h of annealing, while this is not the case in the simulation even after 16h of annealing. The main peak's position also shifts towards lower values of 2θ in a sharp way after 4h of annealing in the experiment, while it remains constant throughout annealing in the simulation. In the following, we will analyze the evolution of the positions and intensities in closer details, and study what causes the discrepancies between experiment and simulated XRD profiles.

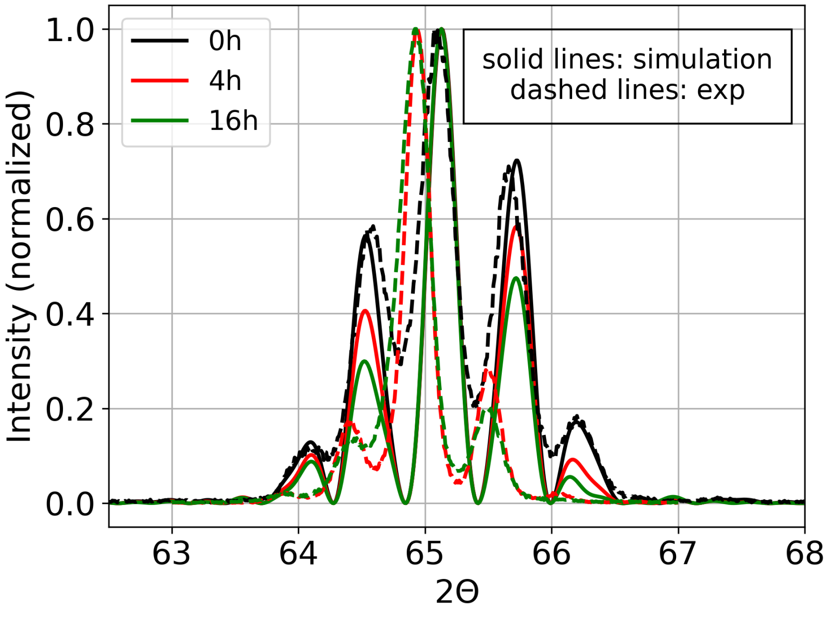

Figure 2.23: Experimental (dashed lines) and simulated (solid lines) XRD profiles, before (black) and after annealing at 500°C for 4h (red) and for 16h (green). The intensity at a time t is normalized by the intensity of the main peak at time t, such that the intensity drawn corresponds to $I(t)/I_0(t)$.

2.7.4.1 Satellite intensity decay

The decay of satellite peak intensities with annealing can be observed more clearly by studying the time evolution of the intensity of each satellite, $I_{\pm m}(t)$, with respect to its initial intensity, $I_{\pm m}(0)$. In Fig. 2.24 we plot the time evolution of the logarithm of normalized intensity ratios of the experimental and simulated profiles at 500°C. Remember that if the interdiffusion coefficient does not depend on concentration, the evolution of this function is linear (Sec. 2.2.4). Qualitatively, all satellites exhibit the same behavior: a sharp linear decrease at the beginning of annealing, followed by a slower linear decrease at longer annealing times. A difference can be seen in the behavior of satellite -2, whose intensity remains almost the same in the simulation but decays fast in the experiment (this can also be seen in the XRD profiles of Fig. 2.23). Quantitatively, the intensity decay of all satellites is faster in the experiment, especially at short times. Since intensity decay is linked to interdiffusion, this hints to a faster diffusion in the experiment, especially at the beginning of annealing. The transition between the two linear slopes is around 4h in the experiment as well as in the simulation, however; we do not know if the two regimes observed experimentally are the same two regimes that are observed in the simulation. We therefore separate the experimental time evolution in regime 1 and regime 2. Note that we know, from the study done in Sec. 2.6, that the evolution of the simulated multilayers between 4 and 32h is not linear but rather a transition between the two kinetic regimes A and C. However, it seems from the plot in Fig. 2.24 that regime B can also be decomposed into linear kinetic regimes, at least between 4 and 16h. We will call the regime between 4 and 16 hours regime B'. We draw in Fig. 2.25 the simulated concentration profiles at 0, 4 and 16 hours to better visualize how the concentration profile evolves in regimes A and B'. After reaching the center of the Fe-rich layer, Cr continues to diffuse in the Fe-rich layer. At 16h, equilibrium is almost reached in this layer, but not quite (this actually happens at 24h, see Sec. 2.7.1). Fe on the other hand keeps accumulating at the interface and this asymmetry leads to interface mobility towards the Cr-rich layer. If regime B is a transitional regime between A and C, we can clearly see that regime B' is the part of it which is a continuation of regime A. Therefore, it is dominated by almost the same kinetics driving regime A, in which bulk diffusion mainly occurs in the Fe-rich layer. It is therefore not surprising that the evolution of satellites in B' is linear. The evolution of the composition field in B' is slower than in A because the Cr concentration gradient is smaller and interdiffusion in the Fe-rich layer decreases with the Cr concentration.

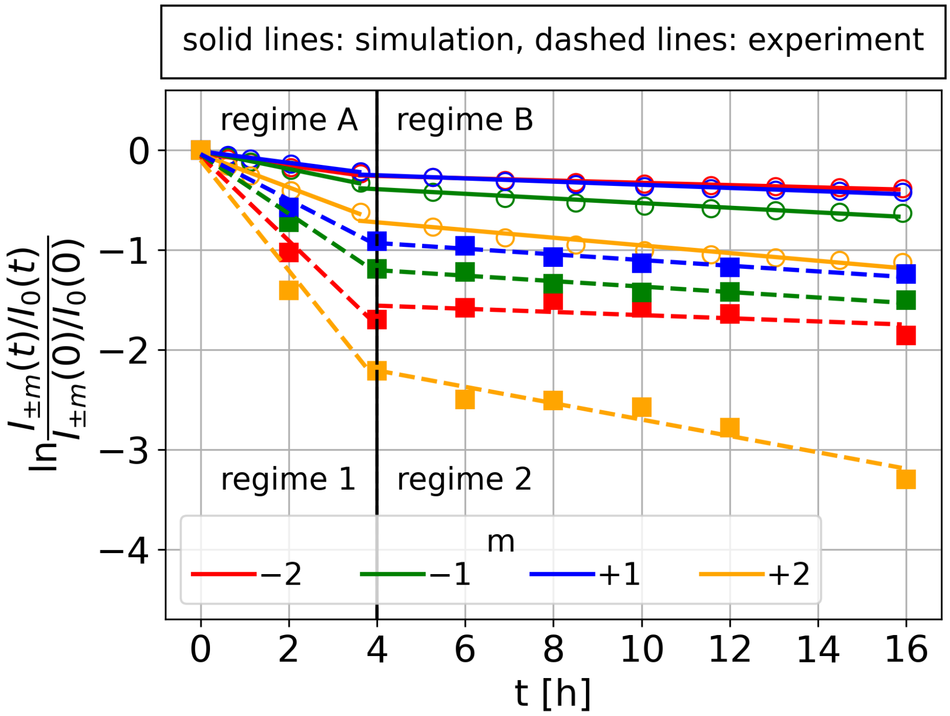

Figure 2.24: Time evolution of the decay of satellite intensity ratios during annealing at 500°C for around 16h, in the experiment (filled squares) and simulation (empty circles). Dashed and filled lines represent the linear fits of experimental and simulated data respectively. Each satellite's decay requires two linear fits which we attribute to two different kinetic regimes. We call the two experimental regimes "regime 1" and "regime 2", and we separate them with a black vertical line at 4h. The simulated regimes are "regime A" and "regime B'" and they are separated as well at 4h. The average decay slope of regime 1 is 13 times bigger than that of regime A, while in regime 2 it is 4 times bigger than that of regime B'.

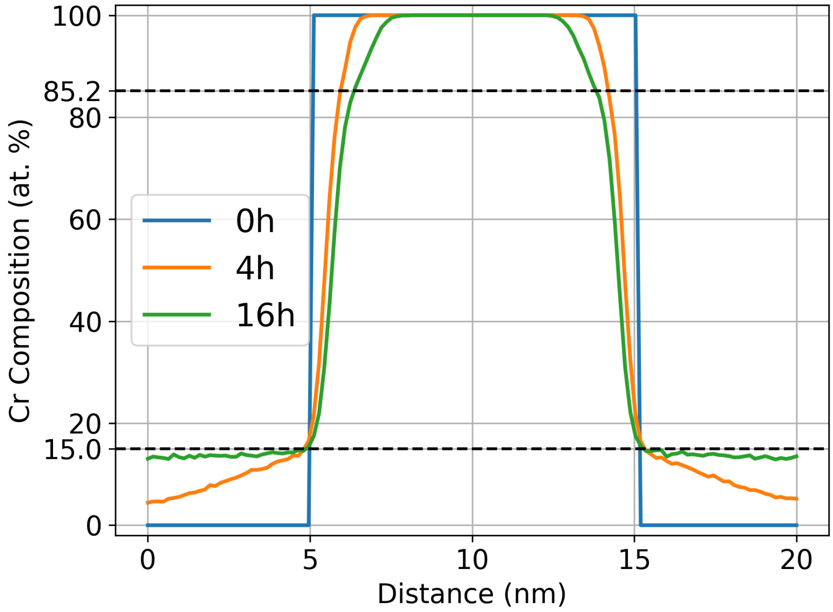

Figure 2.25: Simulated concentration profiles in regimes A and B' at 500°C.

We found the same results and conclusions in the case of multilayers annealed at 400°C and at 450°C. We plot the decay of the satellite intensities at 450°C in Fig. 2.26. At this temperatures, the experimental and simulated kinetic regimes (1 and 2, and A and B') are separated at around $t = 85$h instead of 4h. What is interesting at 400°C and at 450°C is that, between 0 and 4h, a very sharp decay is observed only in the experimentally annealed multilayers. This decay is even faster than the one observed in regime 1. Fig. 2.27 is a zoomed-in version of Fig. 2.26 and better shows that there is a different kinetic regime that cannot be considered part of regime 1. This suggests the presence of a fast diffusion that is missing from the simulation. It is not clear if at 500°C this regime does not exist, if it is happening along regime 1 and we were unable to separate the two, or if annealing times were not short enough to observe it. If it occurs at the same time as regime 1, it could explain why XRD satellites decay faster in the experiment when APT and STEM/HAADF showed composition profiles and layer thicknesses similar to the simulated one. On the other hand, at a temperature higher than 450°C, this fast decay might occur at a time earlier than 4h, and it was simply not measured at 500°C. Moreover, the different regimes have been well identified in the simulation, so the question is: what is happening during the early and very fast regime?

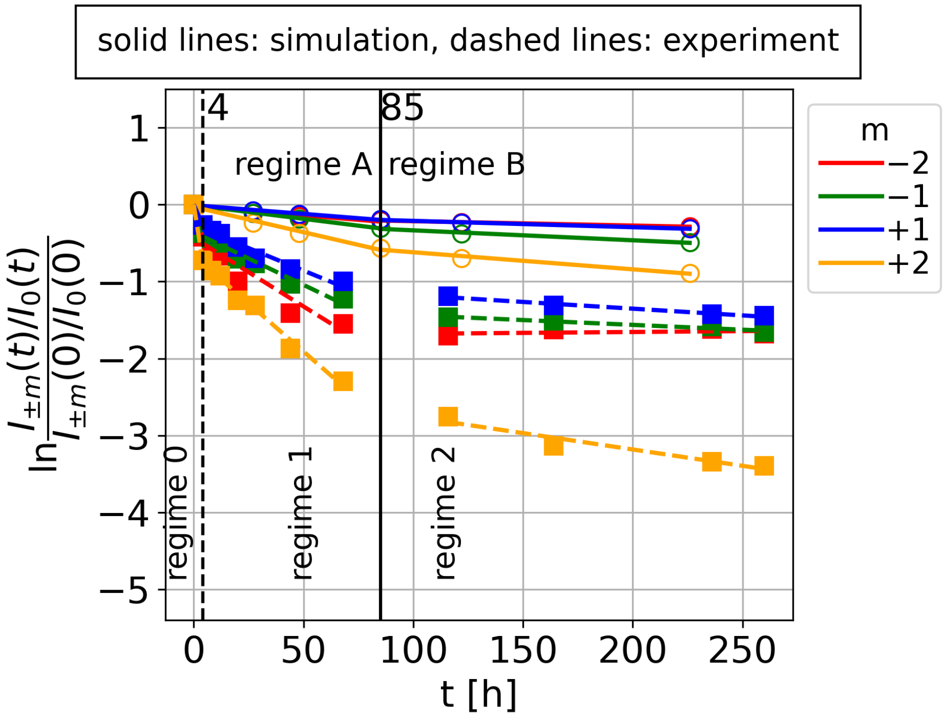

Figure 2.26: Time evolution of the decay of satellite intensity ratios during annealing at 450°C for around 260h, in the experiment (filled squares) and simulation (empty circles). Dashed and filled lines represent the linear fits of experimental and simulated data respectively. Each satellite's decay requires two linear fits which we attribute to two different kinetic regimes. We call the three experimental regimes "regime 0", "regime 1" and "regime 2", and we separate them with a dashed black vertical line at 4h and 85h. The two simulated regimes are "regime A" and "regime B'" and are separated at 85h. Fig. 2.27 shows a magnified version of regime 0.

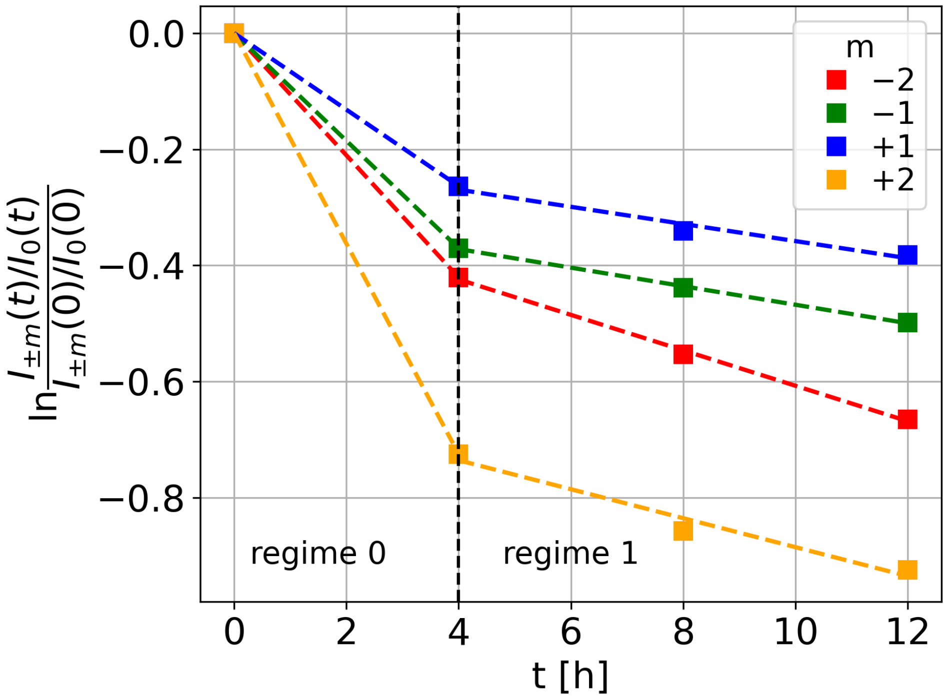

Figure 2.27: Sharp decay of the experimental satellite intensities in regime 0.

2.7.4.2 Lattice parameter

Véronique Pierron-Bohnes used the $\sin^2 \Psi$ method [126] to calculate in-plane and perpendicular lattice parameters during the annealing of the multilayers at 500°C, and deduced the average volume lattice parameter. The results are plotted in Fig. 2.28. The perpendicular (parallel) lattice spacing increases (decreases) throughout regime 1. In regime 2, the lattice parameters vary only at the beginning of the regime and then seem to reach a constant value close to the average volume lattice parameter. This suggests that the system was strained at the beginning of annealing and relaxes throughout regime 1. The strain originates from lattice mismatch during the growth of the multilayer. When a layer is grown on another layer with a different in-plane lattice parameter, the system is forced to relax in the perpendicular direction by varying the perpendicular lattice parameter in a way to compensate for the change in the in-plane parameter. The system relaxes with annealing as atoms diffuse and the lattice mismatch is reduced. Fig. 2.28 shows that relaxation happens mainly during regime 1, and that the system reaches a relaxed state at the early stage of regime 2. In our simulations, deformations and elastic properties are not taken into account, neither in the AKMC simulation, nor in the XRD simulation code. These results show that there is residual strain and possibly a partial coherency growth of the multilayers, which means that Vegard's law should not be used to simulate the interplanar lattice spacing [140]. This needs further investigation and will be discussed in more detail in the perspectives (Sec. 3.11). XRD peak positions and intensities are directly linked to the perpendicular lattice spacing, and this could explain why experimental satellites decay faster, especially in regime 1.

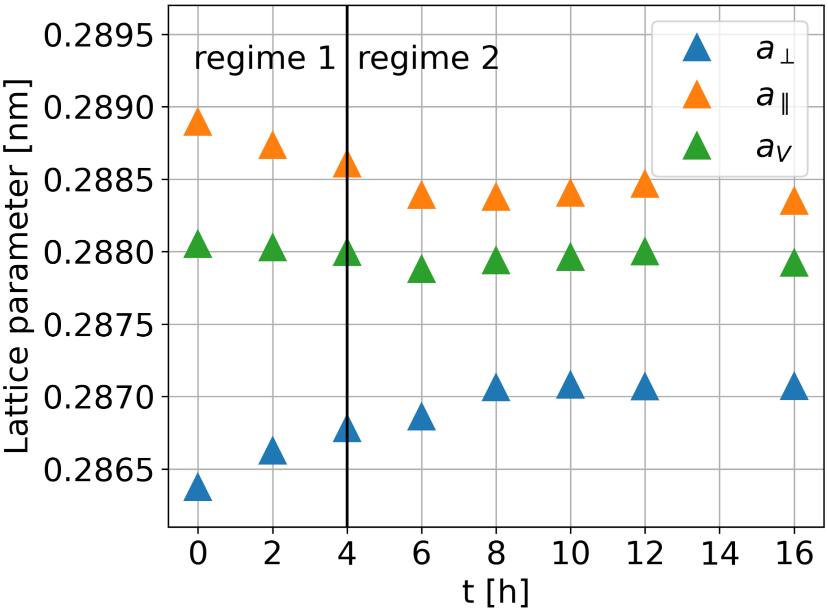

Figure 2.28: Time evolution of the parallel ($a_\parallel$), perpendicular ($a_\perp$) and average volume (a_V) lattice parameters, calculated by Véronique Pierron-Bohnes [138] using the $\sin^2\Psi$ method from the experimental XRD profiles of multilayers annealed at 500°C. The black vertical line separates the two kinetic regimes observed in the experiment (1 and 2).

The perpendicular lattice parameter can also be calculated from each satellite peak position in the simulation and experiment. The lattice spacing can be calculated using Eq. 2.70, and the perpendicular lattice parameter is deduced (the lattice parameter is the double of the lattice spacing in the BCC structure). Note that a shift of peak positions towards lower (higher) angles is related to an increasing (decreasing) lattice parameter. The time evolution of the lattice parameter calculated this way is plotted in Fig. 2.29. The lattice parameter variation is negligible in the simulation for all satellites. In the experiment, all lattice spacings increase in regime 1 and seem to fluctuate around a constant value in regime 2 (as expected from Fig. 2.28). Strain relaxations increase the perpendicular lattice spacing of the layers with higher lattice spacing (here Cr) because it is the layer whose in-plane lattice parameter decreases. Therefore, the increase in the lattice parameter of satellite -1 is a consequence of this relaxation. On the other hand, throughout regime 1, Cr diffuses in the Fe-rich layer, which leads to an increase of its in-plane and perpendicular lattice parameters (because $d_{Cr} > d_{Fe}$). The increase in the lattice parameter of satellite +1 is not necessarily linked to relaxations, but rather to an increase in the lattice spacing of the Fe-rich layer due to Cr diffusion in it. However, in this case, it is surprising that the simulated peak position of satellite +1 does not reflect this increase. Even with a linear Vegard law, there should be an increase of $C_1^{eq} + (1 - C_1^{eq})\, a_{Cr}/a_{Fe} = 6.75 \times 10^{-3}$ nm in the lattice spacing of the Fe-rich layer, which is not observed here. Overall, experimental values are higher and this is in agreement with strain relaxations of experimental multilayers, which are missing from the simulations.

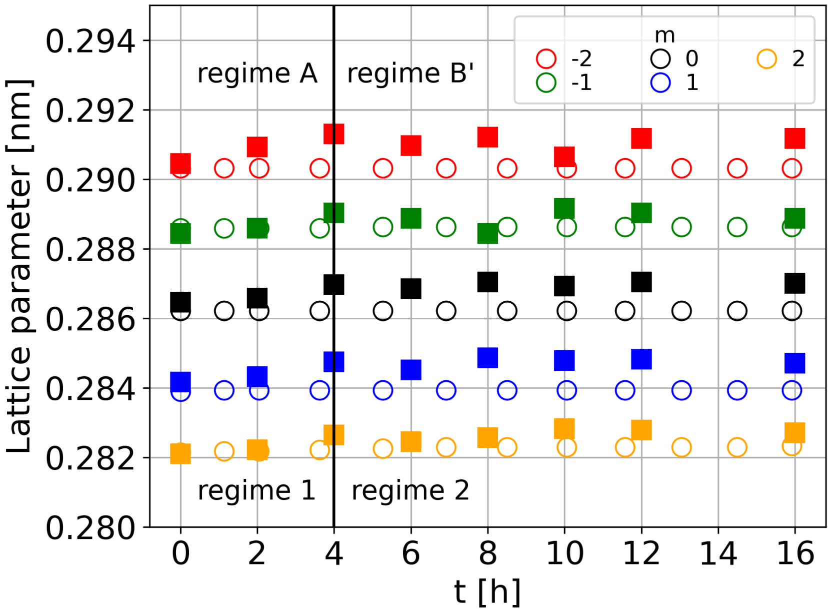

Figure 2.29: Time evolution of the lattice parameter calculated from experimental (full squares) and simulated (open circles) satellite peak positions of XRD profiles of multilayers annealed at 500°C for up to 16h. The values are calculated for 1st and 2nd order satellites, $m = \{\pm 1, \pm 2\}$. The black vertical line separates the two kinetic regimes in the experiment (1 and 2) and simulation (A and B').

2.7.4.3 Multilayer period

In order to calculate interdiffusion coefficients, we need to calculate the average period related to each satellite's position in each regime. The procedure was explained in detail in Sec. 2.6.3.3. Figure 2.30 shows the evolution of the average period Λ_m at 500°C between the first and second kinetic regimes, in the experiment and simulation. There is a large deviation between experimental and simulated values. The experimental periods are higher than the simulation ones for all satellites except ±2 in the first regimes and +2 in the second regimes. In the experiment, periods of first order satellites vary slightly between regimes 1 and 2, while the variation is more apparent in the case of periods of second order satellites which both increase in regime 2. This is a consequence of satellites ±1 and the main peak shifting by the same amount which keeps the distance between ±1 peaks and the main peak constant. This can be a consequence of the Cr-rich and Fe-rich layers both expanding by the same amount.

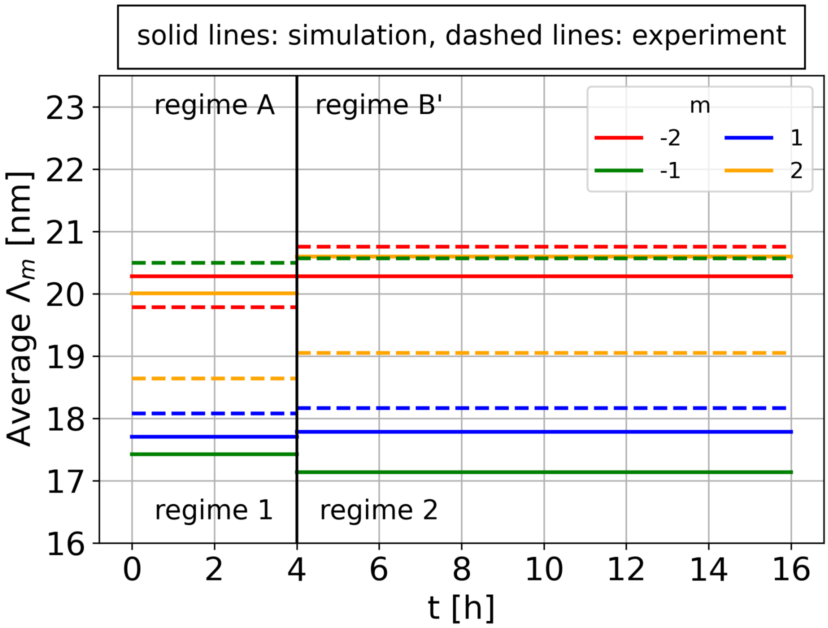

Figure 2.30: Average period Λ_m of multilayers annealed at 500°C, in the experiment (dashed lines) and simulation (solid lines). The values are calculated using Eq. 2.71 for 1^{st} and 2^{nd} order satellites, $m = \{\pm 1, \pm 2\}$ and averaged in each kinetic regime. The black vertical line separates the two kinetic regimes in the experiment (1 and 2) and simulation (A and B').

2.7.4.4 Interdiffusion coefficients calculation

Using the values of the multilayer periods obtained in the previous paragraph (Sec. 2.7.4.3), we calculate the interdiffusion coefficients which dominate in each regime and which are responsible for the decay of each satellite (Eq. 2.62). The results obtained at 450°C and at 500°C are plotted respectively in Fig. 2.32 and in Fig 2.31, as a function of the different satellites. At both temperatures and in all kinetic regimes except regime C, we obtain the same qualitative variation of $\tilde{D}$ as a function of satellites m. Values calculated in regimes 1 and A are in good agreement, and so are the values calculated in regimes 2 and B'. The experiment shows slightly faster kinetics, especially in regime 1. On other hand, values calculated in regimes 0 and C are respectively the highest and lowest, and do not seem to match with any other regime's kinetics. This suggests that the simulation is missing a fast regime at the beginning of annealing at 450°C, while the experiment cannot be performed for long enough to reach regime C.

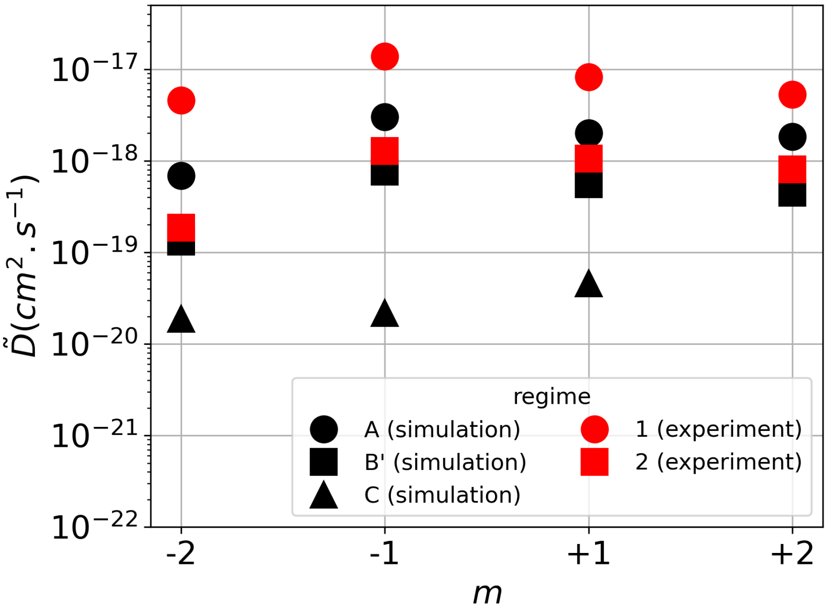

Figure 2.31: Values of the interdiffusion coefficient calculated from the experimental (regimes 1 and 2) and simulated (regimes A, B' and C) XRD intensity decays of each satellite separately using Eq. 2.62, after annealing at 500°C.

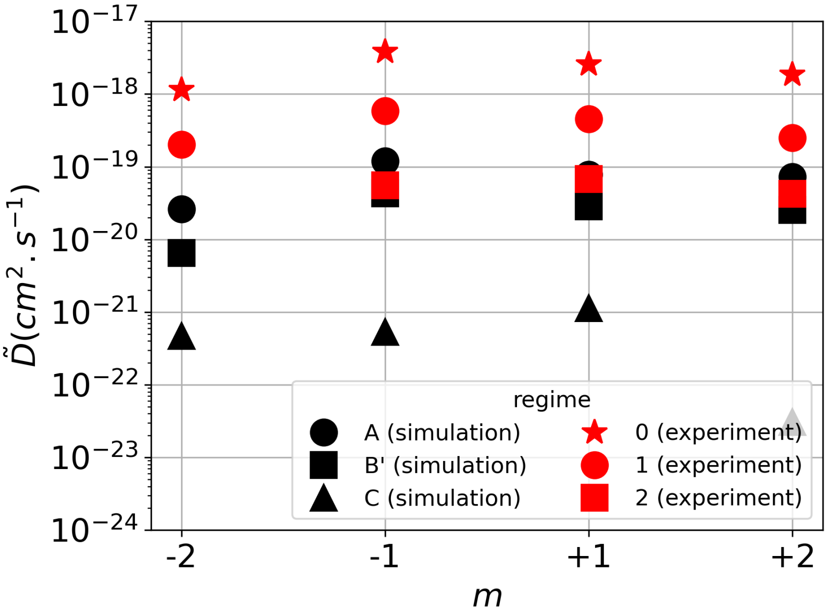

Figure 2.32: Values of the interdiffusion coefficient calculated from the experimental (regimes 0, 1 and 2) and simulated (regimes A, B' and C) XRD intensity decays of each satellite separately using Eq. 2.62, after annealing at 450°C.

In Fig. 2.33 and Fig. 2.34, we compare the results at 500°C, in the first and second regimes respectively, to Senninger's values. Figure 2.33 shows that, while simulated coefficients in the first regime are all around Senninger's values at high Cr concentrations, the experimental values are all slightly higher. This figure allows us to extract reliable experimental values of $\tilde{D}(C)$ around the solubility limit. In the second regime, the experimental and simulated coefficients are between Senninger's values at the solubility limits (between $\tilde{D}(15)$ and $\tilde{D}(80)$). In the region inside the miscibility gap, the system should separate in two phases, one rich in Cr and the other one rich in Fe, and it is hard to define interdiffusion coefficients in this region because the measurement would be accompanied by an evolving microstructure due to phase separation. If we assume that $\tilde{D}$ decreases linearly from $\tilde{D}\,(15)$ to $\tilde{D}\,(80)$, then the values of $\tilde{D}$ calculated in regimes 2 and B' corresponds to the interdiffusion coefficient at concentrations between 15 and 80 at. %Cr. This is consistent with our initial hypothesis that regime B is a transition between regimes A and C.

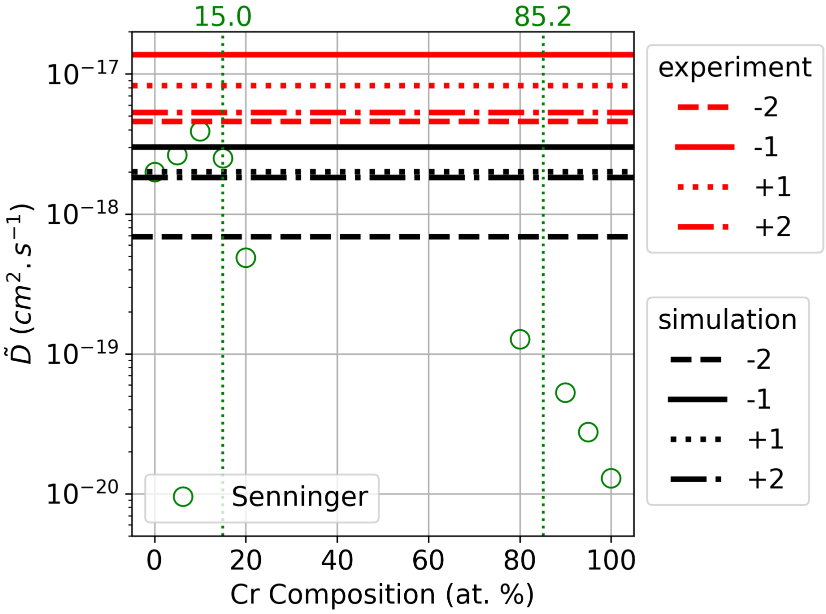

Figure 2.33: Interdiffusion coefficients calculated in the first kinetic regimes, from the experimental (regime 1) and simulated (regime A) XRD satellite intensity decays after annealing at 500°C. The values are compared to the values of the concentration dependent interdiffusion coefficient calculated by Senninger et al. using the wave attenuation method with the same AKMC model [9, 16].

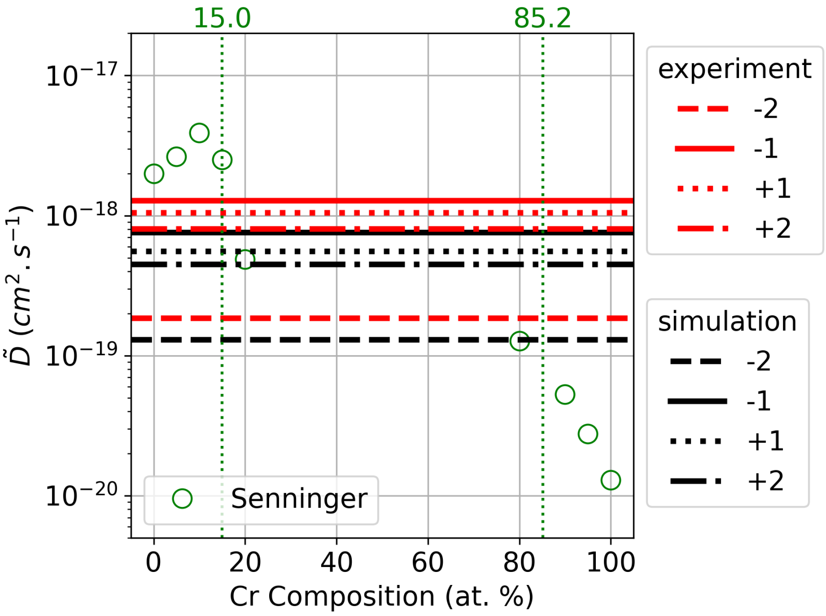

Figure 2.34: Interdiffusion coefficients calculated in the second kinetic regimes, from the experimental (regime 2) and simulated (regime B') XRD satellite intensity decays after annealing at 500°C. The values are compared to the values of the concentration dependent interdiffusion coefficient calculated by Senninger et al. using the wave attenuation method with the same AKMC model [9,16].

2.7.5 Comparative summary

Table 2.11 summarizes the most important points of comparison between the simulation and the experiment after 4h of annealing at 500°C. APT and STEM/HAADF comparisons showed that the kinetics of interdiffusion are qualitatively and quantitatively well reproduced by the AKMC model. APT even suggests that the experiment is slightly slower than the simulation because the concentration of Cr in the Fe-rich layer does not increase as fast as it does in the simulation, while XRD comparisons hinted at a faster interdiffusion in the experiment. After 4h of annealing at 500°C, simulated Cr composition in the center of the Fe-rich layers as well as the simulated layer thicknesses are in good agreement with the experiment, while XRD measurements show that experimental satellites decay faster than the simulation. This overall slow satellite intensity decay in the simulation is also observed when annealing at 450°C. An additional fast decay is observed at the very early stages of experimental annealing at 450°C. This fast decay, in what we call regime 0, is not reproduced in the simulation and is not observed experimentally at 500°C. The slow decay at late annealing times, in the simulated regime C, is not observed experimentally because experimental annealing times were much shorter than the simulations.

		Experiment	Simulation	Absolute value of the relative error
Cr concentration in the middle plane of the Cr-rich layer		99.9 at. %Cr	100 at. %Cr	0.1%
Cr concentration in the middle plane of the Fe-rich layer		4.2 at. %Cr	4.7 at. %Cr	10.6%
Cr concentration over 2.5nm in the middle of the Cr-rich layer		99.9 at. %Cr	100 at. %Cr	0.1%
Cr concentration over 2.5nm in the middle of the Fe-rich layer		4.5 at. %Cr	5 at. %Cr	10%
Thickness increase of the Fe-rich layer		5.8 %	4.7 %	23.4%
Thickness decrease of the Cr-rich layer		4.6 %	4.7 %	2.1%
Defects		Fe-rich inclusions and oxides around dislocation lines traversing the Cr-rich layers	No defects	-
Satellite peak intensities (normalized)	-2	0.183	0.102	44.3%
	-1	0.305	0.406	33.1%
	+1	0.401	0.583	45.3%
	+2	0.110	0.092	15.9%
Satellite peak positions	-2	63.86	64.10	0.8%
	-1	64.42	64.53	0.2%
	0	64.94	65.13	0.3%
	+1	65.51	65.72	0.3%
	+2	66.06	66.17	0.2%

Table 2.11: Comparative summary of the experimental and simulated results after a 4h annealing at 500°C.

It seems that the overall kinetics is comparable between AKMC and experiment, and that the physical time calculated by the AKMC matches the experimental one. Despite the apparent faster experimental interdiffusion, calculated values of the interdiffusion coefficient show a satisfying agreement between regimes 1 and 2 of the experiment and regimes A and B' of the simulation for all satellites. These regimes correspond to the fast diffusion of Cr in the Fe-rich layer until equilibrium is reached, and to the accumulation of Fe atoms at the interface leading to an interface mobility. At 450°C and 500°C, interdiffusion coefficients are less than an order of magnitude different, and the relative errors decrease with annealing times. This can be better understood by combining all our previous analysis. Remember that each satellite stems from interference in some part of the multilayer, and is therefore sensitive to that part's lattice spacing profile and interdiffusion coefficient. An increase in the perpendicular lattice spacing leads at the same time to an increase in the multilayer period and to a faster XRD peak decays. In the experiment, the perpendicular lattice spacing increases to relax strains resulting from lattice mismatch at the interfaces (especially at the interface between Fe and the substrate). The simulation misses to reproduce lattice relaxation because, on one hand, the AKMC simulation is at a constant volume, and on the other hand, a linear Vegard law was used to calculate the perpendicular lattice spacing as a function of concentration only, without taking into account the material's elastic properties as a function of Fe and Cr distribution in the sample. Strains are more important when annealing starts and relax over time through diffusion, until the system becomes unstrained. Pierron-Bohnes calculations (Fig. 2.28) and our calculations based on satellite peak positions (Fig 2.29) confirm that the perpendicular lattice spacing increases throughout regime 1 and reaches a constant value at the early stages of regime 2. This justifies on one hand, why the experiment is slightly faster, and on the other hand, why the deviations of experimental and simulated results are more important in regime 1.

The sharp peak decay at the beginning of annealing in the experiment's regime 0 also seems to result from simulating a perfect system which does not exactly describe the experimental system. APT showed that the samples annealed at 500°C contain oxides and Fe inclusions in the Cr-rich layers around dislocation lines, which are all missing from the simulation. The agreement between the simulated and experimental profiles tends to show that these defects do not affect interdiffusion in the Fe-rich layers nor at the interfaces. We think that, when annealing starts, misfit dislocations originating from the Fe/substrate interface and which were formed to relax the lattice mismatch strain, become diffusion shortcuts for Fe in the Cr layers. This leads to a fast diffusion of Fe along these dislocations and the formation of Fe inclusions around them. This reduces the periodicity of the multilayer and disrupts the interplanar spacing profile. The effect of these inclusions could be negligible on the average planar composition profile but important on the lattice spacing profile. If characteristic time for diffusion along dislocations is small with respect to the characteristic time for microstructure evolution, the effects of this diffusion would be mainly seen on the XRD profiles at the very early stages of annealing, and become negligible over time. This would explain the agreement between composition profiles at 500°C, and the sharp peak decays in the experiment at the beginning of annealing at 450°C.

Finally, we can summarize the kinetic regimes in the following:

- Regime 0: only observed experimentally at 450°C and at the very early stages of annealing (first 4h). We think it is dominated by Fe's fast diffusion along dislocation lines in the Cr-rich layers. Characterized by the sharpest satellite intensity decays and the highest calculated interdiffusion coefficients.

- Regime 1/A: observed in the experiment and simulation at 450°C and 500°C within the same time scales. Simulated and experimental profiles at 500°C show that it is dominated by Cr's diffusion from the Cr-rich layer to the middle layers of the Fe-rich layer and an interface shift towards the Cr rich layers. Allowed us to calculate interdiffusion coefficients at high Fe concentrations in agreement with Senninger's wave attenuation method calculations.
- Regime B: observed in the simulation at 450°C and 500°C. Represents the transition between Cr's diffusion in the Fe-rich layer and Fe's diffusion in the Cr-rich layer which happens when equilibrium is reached in the Fe-rich layer. Satellite decays are not linear and reflect the presence of several competing interdiffusion coefficients.
- Regime 2/B': observed in the experiment and simulation at 450°C and 500°C within the same time scales. This regime is a linear part of regime B in which kinetics are mainly driven by Cr's diffusion in the Fe-rich layer until equilibrium. This regime's kinetics are slower than regime 1/A because the Cr concentration gradient decreases in the Fe-rich layer and the interdiffusion coefficient decreases when the Cr concentration becomes greater than 10 at. %Cr in the Fe-rich layer. The extracted interdiffusion coefficients correspond to the average value of $\tilde{D}$ at the solubility limits.
- Regime C: observed only in the simulation, at time scales beyond the experimental annealing times. The evolution of the structure is dominated by Fe's slow diffusion from the interface to the Cr-rich layer. Characterized by the slowest intensity decays. The calculated interdiffusion coefficients agree with Senninger's values at high Cr concentrations.

2.7.6 Challenges in comparing AKMC and experiment

Besides the fact that our AKMC simulations do not include dislocation lines and lattice elasticity, which are present in real life and have a non-negligible effect on interdiffusion, this work made us ask ourselves a lot of questions related to the general way AKMC simulations are made, and to what extent they can be compared to experiments. Even though AKMC simulations show good agreement with experiment in many cases of interdiffusion, a lot of subtleties exist that are rarely addressed or questioned.

One of these things is the way equilibrium vacancy concentration is treated in AKMC simulations. In real alloys, the equilibrium vacancy concentration depends on the vacancy formation energy and therefore on the local concentration. This means that the equilibrium concentration changes in space and time. It is often assumed that local equilibrium is established fast enough for vacancies to be treated as conservative species whose equilibrium concentration is fixed. Vacancy sources and sinks create and absorb vacancies in a way to keep their concentration equal to the equilibrium one. Kirkendall's interdiffusion experiment ([61–63] and Sec. 1.3.2) showed that when an α species is diffusing faster than a β species, there is a net flux of vacancies that compensates the flux difference between α and β. This net flux increases the concentration of vacancies in one region and decreases it in another, and regulating the vacancy concentration can only be done via the presence of vacancy sources and sinks. Sites and planes can disappear and appear as a consequence leading to a mobility of the lattice itself, in addition to the fluxes of atoms on this lattice. The number of vacancies in the simulation box is fixed and the vacancy concentration is ensured to be equal to the equilibrium one through the time correction explained in Sec. 1.5.3. However, this correction does not affect the trajectory of the vacancy, and only affects the time scale associated with a given portion of the trajectory. This correction comes as a post-processing step after the vacancy-atom exchanges have happened and after the composition profile has been modified. In the AKMC simulation, there is nothing that simulates a net flux of vacancies, and sites and planes are fixed and cannot disappear or appear. There is also no proper simulation of sources and sinks of vacancies, since in the simulation box a vacancy can only jump from one site to a neighboring site, and in no way can it disappear in one layer and appear in another. Periodic boundary conditions might be considered as an approximation to sources and sinks since they make a vacancy disappear from one extreme side of the box and appear on the other extreme, but it is not necessarily a good approximation and its effect on vacancy migration decreases as the simulation box size increases. This condition rather adds a layer of ambiguity to the way vacancies diffuse in the simulation box. Imagine a vacancy at a plane X that diffuses towards the left side of the box until it reaches plane L. In reality, the only way for the vacancy to go back to plane X is to make a U-turn and diffuse back in the opposite direction, by passing through the same planes in the reverse order. In the AKMC simulation however, a vacancy that reaches plane L can jump to the left and get teleported to the right side of the box, to plane R. Then the vacancy can keep diffusing to the left and reach the X plane from the right side. Sources and sinks are related to defect positions and to interdiffusion, and there is no reason for them to be only at the extremities of the box. All this calls into question the interdiffusion coefficient that we calculate from the simulation and how it can be compared with experimental measurements. Since the lattice in the simulation does not move, we may be calculating an intrinsic diffusion coefficient rather than an interdiffusion coefficient (Sec. 1.2.2.3). While there is one interdiffusion coefficient that characterizes both species, each one has its own intrinsic coefficient. If we are computing an intrinsic diffusion coefficient, the question is: which one are we computing? Since the kinetics do not represent what is really happening in the experiment, this also brings into question whether or not we can really compare interdiffusion coefficients calculated using AKMC to the experimental ones.

2.8 Conclusions of chapter 2

We presented in this chapter the basics of X-ray diffraction and some important analytical models that make the link between satellite peak positions and intensities on one hand, and composition profiles, lattice spacing profiles, and interdiffusion coefficients on the other hand. We used a combination of Fick's law and Guinier's theory to calculate interdiffusion coefficients from satellite peak intensity decays. This combined theory assumes a constant interdiffusion coefficient and no lattice parameter fluctuations. We overcame these constraints by first separating the time evolution of our system into several kinetic regimes and then by treating each satellite separately. To identify the kinetic regimes, we had to find the time ranges in which the decay of satellites is linear and during which there is an interdiffusion coefficient which dominates in altering the system's structure. Because each satellite stems from interferences in some part of the system, we were able to identify these parts based on each satellite's position (at least ±1 satellites, while for satellites ±2 it is still not so clear). A theory based on a constant interdiffusion coefficient and a constant lattice spacing can therefore be used to calculate concentration dependent interdiffusion coefficients.

We applied this methodology to experimental and simulated XRD profiles of Fe/Cr multilayers. The overall kinetics were in agreement between simulation and experiment. We showed that if the regimes are well identified and if it is well understood what each satellite is sensitive to, concentration dependent interdiffusion coefficients can be calculated. Since there are no analytical models which allow the calculation of concentration dependent interdiffusion coefficients from XRD profiles, our work provides a good and simple workaround. We were able to calculate, with satisfying accuracy with Senninger's work, interdiffusion coefficients at 500°C in Fe-rich and Cr-rich environments, at the interfaces and at concentrations close to the solubility limits. We were also able to provide these coefficient values at 450°C.

2.9 Perspectives of chapter 2

To wrap up this work and get a complete analysis of results, additional work can be done, from both the simulation and experimental sides. On the theoretical side as well, additional work can be done to improve the existing theories. Our simulations are mainly missing to take into account dislocations and elasticity.

On the simulation side, we should find ways to take into account dislocations, lattice relaxations, and the non-conservative nature of vacancy diffusion.

- We can account for the dislocation diffusion shortcuts and the Fe-rich inclusions by introducing dislocation lines in the AKMC simulation box where atoms would diffuse faster. In practice, we can do this by adding for example a connected lines in the Cr-rich layer in a way to form a bridge between the two adjacent Fe-rich layers and by either imposing a faster interdiffusion at this line, or by initializing it with Fe atoms. This can be done arbitrarily to see its qualitative effect on interdiffusion, or even more realistically based on experimental measures of the size of these defects. This study will allow us to test the validity of our analysis on the link between fast diffusion along dislocations and the sharp decay of satellites at the beginning of annealing. This could also explain the overall faster experimental kinetics which are less important at long annealing times. In all cases, this will be interesting to study the effect of dislocations at the early and long stages of interdiffusion.

- Furthermore, as mentioned above in the discussion, the vacancy diffusion mechanism related to its non-conservative nature is not taken into account properly in the AKMC simulation. This can be properly modeled by explicitly adding sites and/or planes that act as sources and sinks of vacancies. For example, misfit dislocations can act as such. We have to also account for the fact that when vacancies get eliminated and created, sites and/or planes can disappear or appear in different layers.

- Throughout our work, we have demonstrated the importance of the lattice spacing on both satellite peak positions and intensities, and it is therefore important to reproduce it as accurately as possible in the simulation. The noticeable difference between experimental and simulated satellite peak positions suggests that the simulations are missing to properly reproduce the interplanar spacing, and could be due to the fact that stress is neglected. We need to study the elastic properties of the multilayers in more detail to see how they affect the lattice spacing. Since it is not clear whether or not the multilayers were grown in a coherent way or not, and since it is more likely to have partial coherency than one of the two extremes (no coherency and perfect coherency), we need to calculate the strain in our multilayers. There are several models which allow for such calculations. This will add a correction to Vegard's linear law [140], and can potentially lead to a perpendicular lattice spacing closer to the experimental one.

- Finally, on the theoretical side, this work can be completed by studying the mobility of the interface in more details. This will be further discussed in the general perspectives as it requires extensive work and can consist a research project on its own.

On the experimental side, we need a more complete set of data to compare with.

- One of our theories is that the diffusion of Fe in the Cr-rich layer is not observed experimentally (besides the diffusion along dislocation lines). This can be confirmed by analyzing with the APT at least one of the annealed samples at the end of the experimental annealing times.
- Additionally, one can anneal the samples at 500°C for longer times and perform XRD measurements on them. It is probably not possible to observe regime C in the experiment at temperatures below 500°C because annealing times are unrealistically long at lower temperatures. At 500°C however, annealing the samples for 20 more hours allows us to reach regime C, and any longer annealing will allow us to observe the eventual slow diffusion of Fe in the Cr-rich layer. This would allow us to extract experimental interdiffusion coefficients in the Cr-rich region, and validate our simulation results.
- Samples annealed at 450°C can rather be analyzed at shorter annealing times using APT and STEM/HAADF. Since at 450°C we observe an additional kinetic regime, it will be interesting to see the experimental profiles at the beginning of each kinetic regime and how they compare to the simulated profiles.

All these simulation improvements and additional experimental annealings and characterizations will allow us see how dislocations and inclusions affect interdiffusion throughout the annealing process, and the effect of the lattice parameter and relaxations on peak positions and intensities.

On the theoretical side, the link between concentration and lattice profiles and XRD satellite peak positions and intensities has not been made in the general case. There is also no model to calculate concentration dependent interdiffusion coefficients from XRD profiles. The difficulty in developing such models lies in the fact that we cannot establish a general analytical function which describes the interdiffusion coefficient of any alloy. Tsakalakos considered a quadratic function to describe the interdiffusion coefficient and developed a model to calculate it from satellite intensity decays. However, the solution he provided required an iterative calculation and was not used in applications. Therefore, considering a polynomial function of high order to describe $\tilde{D}\left(C\right)$ does not necessarily allow us to express it as a function of satellite intensities. Improving the model of Tsakalakos or working on another mathematical form of the interdiffusion coefficient seems to be a far-from-reach perspective at the moment.

Another way to calculate interdiffusion coefficients is to use atomic-scale analytical models developed to study diffusion in concentrated alloys. We presented in the first chapter (Sec. 1) the most important models an showed their limitations and the need for a general diffusion model for concentrated alloys. In the next chapter, we will tackle the diffusion problem within a more general framework and from a different perspective. We will present the development of an analytical model to compute diffusion coefficients in any concentrated alloy, and not just in the case of FeCr alloys. Instead of relying on XRD profiles and interdiffusion in multilayers, we will solve a general diffusion problem in a concentrated alloy, by studying the thermodynamics and kinetics of the system to calculate the transport coefficients matrix. From that, we can fit analytical laws of interdiffusion variation as a function of local concentration, and maybe improve on Tsakalakos' work.

Chapter 3

Extending SCMF-d and KineCluE to concentrated alloys

3.1 Introduction to chapter 3

Many materials of interest are concentrated alloys, and yet, as seen in chapter 1, there is no general model to compute the full Onsager matrix in these alloys. The exact expression of transport coefficients as a function of atomic jump frequencies is out of reach due to the vastness and complexity of the configuration space. A standard analytical approach consists in replacing each atom by average or mean-field atoms. Using a mean-field approach in a random alloy, Manning, followed by others, managed to properly take into account kinetic correlations in the case of vacancy diffusion. Despite its simplicity, Manning's model remains limited to Bragg-Williams alloys. In the general case of an interacting alloy with short-range order, a mean-field simplification becomes too crude and prevents treating kinetic correlations properly. The only models that allowed for the computation of the full transport coefficients matrix in interacting alloys are the PPM [143] and the SCMF-o [22]. These two methods consisted key milestones in studying diffusion in concentrated interacting alloys and showed great potential in many applications. Despite their great results, both these methods were mostly applied in specific simple cases only due to their mathematical complexity, and a general analytical solution was hard to obtain. Among these methods, the SCMF-o allowed for greater flexibility and control over the thermodynamic and kinetic approximations. This made it less complex than the PPM and allowed for its use in a wider range of applications. In this chapter, we present a new atomic-scale model to study diffusion in concentrated alloys and we show its application to the case of a random alloy and an interacting alloy within a thermodynamic pair approximation. Our formalism is based on an extension of the SCMF-o and our approach is intermediary between an exact solution and a mean-field approximation.

First in section 3.2, we will present the work of T. Schuler *et al.* on the reformulation and implementation of the SCMF-o theory in an open-source code called "KineCluE", which allowed for the study of diffusion in dilute alloys [18]. We will show how, in the framework of this PhD, we managed to extend both the theoretical framework (Sec. 3.3) and the KineCluE code (Sec. 3.4) to the case of concentrated alloys. In our case, the convergence of kinetic correlations required a large computational effort, therefore, we decide to introduce a sampling scheme. In sections 3.5 and 3.6, we present our original sampling scheme and analyze the accuracy of the sampling procedure. In Sec. 3.7, we propose an energetic model to calculate mean-field interactions, in order to apply our theory to the case of an interacting alloy. In Sec. 3.8 we analyze our code's computational performance by studying the convergence of correlation factors. In Sec. 3.9, we compare our model's results to the literature in the case of a non-interacting alloy, and to our own AKMC simulations in the case of an interacting alloy. We finally conclude with the most important results and analysis in Sec. 3.10, and offer our perspectives accordingly in Sec. 3.11.

3.2 SCMF-d and KineCluE in the case of dilute alloys

The SCMF-o theory, presented in the first chapter in Sec. 1.7.4, has the advantage of reproducing the full Onsager matrix in the case of concentrated alloys. However, it is very system specific and it is hard to generalize analytically for the case of any crystal structure, any jump mechanism, any defects or any number of components. In 2020, Schuler *et al.* [18] reformulated it and implemented it in an open-source code that they called "KineCluE" in order to automate it and allow it to be more accessible. We will call, in this thesis, their new theoretical formalism the "SCMF-d". The SCMF-d is based on the same general assumptions and hypotheses as the SCMF-o, but treats the effective Hamiltonian and effective interactions in a different way. The new treatment comes with a different set of assumptions which allow the computation of transport coefficients in the case of dilute alloys only, and the aim of this thesis is to extend it to concentrated alloys. In this section we will discuss the theoretical framework of, the SCMF-d and outline the main differences with the original SCMF-o method. We will also present the way they implemented it in KineCluE and the general functioning of the code. It is important to detail this section since our work is directly based on it, rather than on the original SCMF-o.

3.2.1 Kinetic cluster expansion method

Cluster expansions (CE) have been extensively used to divide a configuration function into cluster functions and calculate thermodynamic properties as a function of the cluster functions [115]. Based on CE, the SCMF-d makes the assumption that the system is sufficiently dilute to divide it into independent clusters of finite size (Fig. 3.1). This relies on the hypothesis that each cluster is surrounded by a homogeneous medium and is able to reach local equilibrium before it interacts with the other clusters. Each cluster is characterized by a kinetic radius within which equilibrium cluster properties are calculated exactly, and beyond which the cluster is considered to be dissociated, i.e. cluster components are assumed to not interact with each other anymore. The limitation of this approach is therefore that it is limited to dilute systems.

KineCluE allows the study of each cluster c separately and the computation of equilibrium cluster properties (transport coefficients, partition function, mobility, ...). The total transport coefficient of the system, $L_{\alpha\beta}$, can then be calculated by the user in a post-processing step as the sum over all cluster transport coefficients, $L^{eq}_{\alpha\beta}(c)$, calculated using KineCluE, each weighted by the concentration of the corresponding cluster $[c]$

$$L_{\alpha\beta} = \sum_{c} [c] \, L^{eq}_{\alpha\beta} (c) \, . \tag{3.1}$$

Here, while the cluster transport coefficients are equilibrium quantities, the cluster concentrations $[c]$ can be out-of-equilibrium quantities, which allows for the computation of the total transport coefficients in out-of-equilibrium systems. For example, cluster concentrations can be calculated at equilibrium using a low-temperature expansion (LTE) formalism [144], or out-of-equilibrium using a cluster dynamics simulation.

Concerning the choice of the kinetic radius, on one hand, it has to be small enough to preserve the dilute hypothesis that clusters are sufficiently far from from each other to not interact. On another hand, the kinetic radius has to be big enough to include enough trajectories with a high thermodynamic weight for cluster properties to converge. It was found that the kinetic radius should be the smallest value for which the product $Z(\alpha\beta) \, L_{\alpha\beta}(\alpha\beta)$ converges, where $Z(\alpha\beta)$ and $L_{\alpha\beta}(\alpha\beta)$ are respectively the partition function and the off-diagonal transport coefficient of an $\alpha\beta$ pair cluster. KineCluE includes an option that allows the user to calculate this product for several values of the kinetic radius until $Z(\alpha\beta) \, L_{\alpha\beta}(\alpha\beta)$ converges (within a desired value). Additionally, numerical applications showed that in several cases, a relatively small kinetic radius - around 3 lattice parameters - is enough for this product to converge [18].

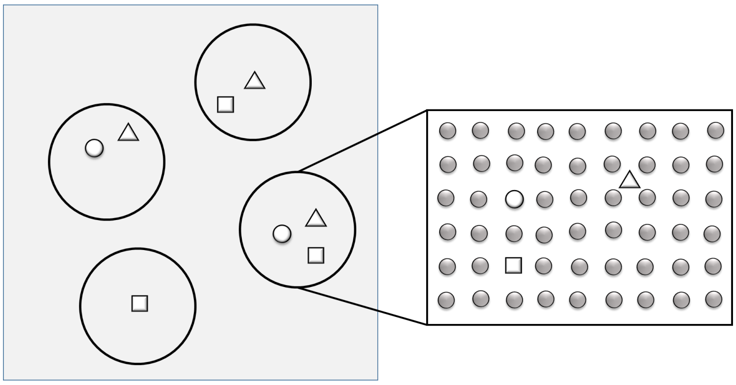

Figure 3.1: Schematic representation of a cluster decomposition in a homogeneous gray matrix.

3.2.2 Theoretical background of the SCMF-d

The SCMF-o in its original form studies a system in a stationary state close to a homogeneous equilibrium and considers a stationary and homogeneous driving force (chemical potential gradients) that drives the system out-of-equilibrium. The out-of-equilibrium system is described by a distribution function written as a function of the equilibrium distribution and a correction term that contains the deviation from equilibrium. The time evolution of the system is described by means of a master equation and the microscopic detailed balance is supposed to be satisfied. To calculate the flux or the Onsager transport coefficients, effective interactions that appear in the correction term of the distribution function need to first be calculated. All these assumptions and approximations are maintained in the new formulation of the SCMF-d, and the main difference will appear in the way of calculating the effective interactions, which will require making different assumptions. Therefore, even though the SCMF-o directly studies the whole system and computes the total transport coefficients, while the SCMF-d aims to first study independent clusters and calculates cluster transport coefficients, the spirit behind this new formalism is based on the original SCMF-o, and the theory remains almost the same up to the point of calculating the effective interactions.

Cluster distribution function

In the SCMF-o formalism, a configuration n represents one configuration of the whole system, while in the SCMF-d formalism n represents a configuration of the cluster c under study. A configuration n is divided into a specific configuration of cluster components, c_n, and a uniform environment surrounding them, such that $n = c_n \cup \bar{c}_n^A$, where $\bar{c}_n$ represents all sites outsides of cluster component sites (all sites that are not occupied by any of the cluster components), and the suffix A designs the atomic species which occupies all these sites. Remember that cluster components are assumed to be in a homogeneous matrix, and therefore all sites of $\bar{c}_n$ have to be occupied by the same atomic species, which in this case we arbitrarily chose it to be species A.

In both formalisms, the out-of-equilibrium probability, P_n, of a configuration n is considered to be a deviation from the equilibrium probability, P_n^0, such that $P_n = P_n^0 \delta P_n$. δP_n represents the deviation from the equilibrium probability and has the same mathematical form as P_n^0 (Eq. 1.116). The time evolution of the distribution function is described by a master equation of the form of Eq. 1.122, which, using the microscopic detailed balance (Eq. 1.125) reduces to Eq. 1.130. In both formalisms, the probability distribution is a function of an effective Hamiltonian h_n, but each one defines it differently. In SCMF-o, h_n has the same mathematical form as the thermodynamic Hamiltonian and is written as a sum over N-body effective interactions $\nu_{i,j,\ldots}^{\alpha,\beta,\cdots}$, which represent the deviation from equilibrium of the N-body thermodynamic interactions (Eq. 1.121). In SCMF-d, the expression is simplified by assigning to each configuration n, associated with a specific configuration of the cluster, an effective interaction ν_n, and the effective Hamiltonian of n is simply written as the effective interaction of configuration n

$$h_n = \nu_n. \tag{3.2}$$

The effective Hamiltonian is therefore simply reduced to the effective interaction in SCMF-d. The deviation from equilibrium is therefore

$$\delta P_n = \exp\left(-\frac{\nu_n - \sum_{i,\alpha} n_i^\alpha \delta\mu_i^\alpha - \delta\Omega}{k_B T}\right). \tag{3.3}$$

Note that this new way of defining effective interactions allows us to talk about cluster configurations n and effective interactions ν_n interchangeably.

Cluster transport coefficients

The flux of atoms of species β between sites i and j in a cluster c, is calculated using the continuity equation per site, in the same way as Eq. 1.126. This leads to the same microscopic flux equation (Eq. 1.127), with the difference being that the microscopic flux here represents the flux associated to cluster c and not in the entire system

$$J_{i\to j}^{\beta}\left(c\right)=\sum_{n}P_{n}^{0}n_{i}^{\beta}m_{j}^{\beta}W_{nm}\left(\frac{h_{m}-h_{n}}{k_{B}T}-\sum_{\alpha}\vec{d}_{nm}^{\alpha}\frac{\vec{\nabla}\mu_{\alpha}}{k_{B}T}\right). \tag{3.4}$$

In SCMF-d, the effective Hamiltonian difference is equivalent to an effective interactions difference, and the flux equation is therefore

$$J_{i\to j}^{\beta}\left(c\right)=\sum_{n}P_{n}^{0}n_{i}^{\beta}m_{j}^{\beta}W_{nm}\left(\frac{\nu_{m}-\nu_{n}}{k_{B}T}-\sum_{\alpha}\vec{d}_{nm}^{\alpha}\frac{\vec{\nabla}\mu_{\alpha}}{k_{B}T}\right). \tag{3.5}$$

Also in SCMF-d, the flux can be expressed as an average over the equilibrium distribution function

$$J_{i\to j}^{\beta}\left(c\right)=\left\langle n_{i}^{\beta}m_{j}^{\beta}W_{nm}\left(\frac{\nu_{m}-\nu_{n}}{k_{B}T}-\sum_{\alpha}\vec{d}_{nm}^{\alpha}\frac{\vec{\nabla}\mu_{\alpha}}{k_{B}T}\right)\right\rangle. \tag{3.6}$$

In SCMF-d, the macroscopic flux is calculated along a direction $\vec{e}_d$ as the average over all sites of the system of the microscopic flux along the same direction, weighted by the jump distance along $\vec{e}_d$

$$\begin{aligned}
J_{d}^{\beta}\left(c\right)&=\frac{1}{V}\sum_{i}n_{i}^{\beta}\sum_{j\in\theta_{i+}^{\beta}}d_{ij}^{\beta d}J_{i\to j}^{\beta}\left(c\right) && (3.7)\\
&=\frac{1}{V}\sum_{i}\sum_{j\in\theta_{i+}^{\beta}}d_{ij}^{\beta d}\sum_{n}n_{i}^{\beta}m_{j}^{\beta}P_{n}^{0}W_{nm}\left(\frac{\nu_{m}-\nu_{n}}{k_{B}T}-\sum_{\alpha}\vec{d}_{nm}^{\alpha}\frac{\vec{\nabla}\mu_{\alpha}}{k_{B}T}\right) && (3.8)\\
&=\frac{1}{V}\sum_{i}\sum_{j\in\theta_{i+}^{\beta}}d_{ij}^{\beta d}\left\langle n_{i}^{\beta}m_{j}^{\beta}W_{nm}\left(\frac{\nu_{m}-\nu_{n}}{k_{B}T}-\sum_{\alpha}\vec{d}_{nm}^{\alpha}\frac{\vec{\nabla}\mu_{\alpha}}{k_{B}T}\right)\right\rangle, && (3.9)
\end{aligned}$$

where V is the volume of the system, and $d_{ij}^{\beta d}$ is the jump distance of an atom of species β between sites i and j along the direction $\vec{e}_d$. The ensemble θ_{i+}^{β} represents the ensemble of β jumps from i to j such that the jumping distance $d_{ij}^{\beta d}$ is positive. Taking only positive distances ensures that a jump and its reverse jump are not contributing twice to the flux calculation. If one were to sum over all sites and all jumps of the system, a jump's contribution would be counted twice and the flux expression would need to be divided by two

$$J_{d}^{\beta}\left(c\right)=\frac{1}{2V}\sum_{i}n_{i}^{\beta}\sum_{j}d_{ij}^{\beta d}J_{i\to j}^{\beta}\left(c\right), \tag{3.10}$$

because $d_{ij}^{\beta d}J_{i\to j}^{\beta}=d_{ji}^{\beta d}J_{j\to i}^{\beta}$. To extract cluster transport coefficients from the above equation, the flux needs to be expressed as a linear function of the chemical potential gradients (Onsager's Eq. 1.2). In SCMF-o, the effective interactions were found to be a linear function of the chemical potential gradient (CPG). The next paragraph will show that in SCMF-d, the effective interactions can also be expressed as a linear function of the CPG.

Effective interactions To calculate the effective interactions as a linear function of the chemical potential gradients, the SCMF-o applied the stationnarity principle to the different moments of the distribution function. The maximum size of interactions n_ν is chosen based on the desired level of approximation, and all N-body effective interactions with $N \leq n_\nu$ are studied, while all others are considered to be null. The n_σ effective interactions are calculated from the stationnarity of each N-moment of the out-of-equilibrium distribution function (Eq. 1.147). In SCMF-d, the effective interaction ν_n is calculated by applying the stationnarity principle directly to the out-of-equilibrium distribution function of configuration n, since in this case each cluster configuration n corresponds to an effective interaction ν_n

$$\frac{dP_n}{dt} = 0. \tag{3.11}$$

Substituting dP_n/dt with its expression (Eq. 1.130) and replacing h_n with ν_n in the above equation gives

$$\forall n, \ \sum_m P_n^0 W_{nm} \left(\nu_n - \nu_m\right) = \sum_m P_n^0 W_{nm} \sum_\alpha \vec{d}_{nm}^\alpha \vec{\nabla} \mu_\alpha. \tag{3.12}$$

Equation 3.12 is written for each cluster configuration n (or equivalently effective interaction ν_n), which gives a system of coupled linear equations whose unknowns are the effective interactions. Solving this system of equations gives the effective interactions as linear functions of the chemical potential gradients

$$\nu_n = \sum_\alpha \nu_n^\alpha \nabla \mu_\alpha, \tag{3.13}$$

where ν_n^α are calculated. Since the chemical potential gradients of different species are independent of each other, the stationnarity equation can be re-written for each species α independently

$$\forall n \ \forall \alpha \ , \sum_m P_n^0 W_{nm} \left(\nu_m^\alpha - \nu_n^\alpha\right) = \sum_m P_n^0 W_{nm} d_{nm}^{\alpha\mu}, \tag{3.14}$$

where $d_{nm}^{\alpha\mu} = \vec{d}_{nm}^\alpha \vec{e}_\mu$ is the projection of the distance vector along the direction of the CPG, $\vec{e}_\mu$. Once the ν_n^α are calculated from the system of equations formed by Eq. 3.14, the effective interactions are re-injected in the flux expression (Eq. 3.9).

Back to cluster transport coefficients Once the effective interactions are calculated, the flux becomes a linear function of the CPG

$$J_d^\beta\left(c\right) = -\sum_\alpha \frac{1}{V} \sum_i \sum_{j \in \theta_{i+}^\beta} d_{ij}^{\beta d} \sum_n n_i^\beta m_j^\beta P_n^0 W_{nm} \left(\nu_n^\alpha - \nu_m^\alpha + d_{nm}^{\alpha\mu}\right) \frac{\nabla \mu_\alpha}{k_B T}, \tag{3.15}$$

and the cluster transport coefficients along a direction $\vec{e}_d$ can be identified using the Onsager equation (Eq. 1.2)

$$L_{\beta\alpha}^d\left(c\right) = \frac{1}{V} \sum_i \sum_{j \in \theta_{i+}^\beta} d_{ij}^{\beta d} \sum_n n_i^\beta m_j^\beta P_n^0 W_{nm} \left(\nu_n^\alpha - \nu_m^\alpha + d_{nm}^{\alpha\mu}\right). \tag{3.16}$$

The transport coefficients can be further expressed as an average over the equilibrium distribution function

$$L^d_{\beta\alpha}(c) = \frac{1}{V}\sum_i \sum_{j\in\theta^\beta_{i+}} d^{\beta d}_{ij} \left\langle n^\beta_i m^\beta_j W_{nm}\left(\nu^\alpha_n - \nu^\alpha_m + d^{\alpha\mu}_{nm}\right)\right\rangle . \tag{3.17}$$

3.2.3 Symmetry operations

A system of N_{conf} equations has to be solved to calculate the effective interactions, N_{conf} being the total number of cluster configurations. Even in dilute alloys,N_{conf} can become a big number depending on the number of cluster components and the kinetic radius they can diffuse in. Symmetry operations can be used to reduce the number of equations. There are two types of symmetry operations that we can use: crystal symmetry operations which preserve the crystal lattice, and CPG symmetry operations which are crystal symmetry operations that additionally preserve the direction of the CPG. Configurations that are symmetric with respect to the crystal have the same equilibrium probability P^0_n, and are therefore thermodynamically equivalent. Let N_{thconf} be the number of configurations that are thermodynamically equivalent. However, these configurations do not necessarily have the same out-of-equilibrium distribution. Remember that δP_n and ν_n appear due to a driving force and represent deviations from equilibrium. All configurations which are symmetric with respect to the CPG direction will be influenced by the driving force in the same way and will have the same δP_n and ν_n. These configurations have the same out-of-equilibrium probability and are therefore kinetically equivalent. Kinetically equivalent configurations will have effective interactions with the same magnitude and their corresponding stationnarity equations (Eq. 3.14) will be the same. This reduces the number of equations in the system and the number of effective interactions to calculate from N_{conf} to N_{inter}, N_{inter} being the number of symmetry unique effective interactions. Note that configurations that are kinetically equivalent are necessarily thermodynamically equivalent, but the opposite is not necessarily true.

3.2.4 Classes of effective interactions

It is convenient to group CPG symmetric effective interactions in classes, such that effective interactions that have the same magnitude, $\|\nu_n\| = \nu_\sigma$, belong all to the same class $\sigma = \{\nu_n; \|\nu_n\| = \nu_\sigma\} = \{\nu^\alpha_n; \|\nu^\alpha_n\| = \nu^\alpha_\sigma \ \forall\alpha\}$. Each effective interaction ν_n can further be characterized by an occupation number n_σ which represents the class it belongs to, such that n_σ equals ± 1 if $\nu_n \in \sigma$, and 0 otherwise. In each class, a representative effective interaction ν^{ref}_σ can be arbitrarily chosen so that its n_σ is equal to one, and for the remaining interactions in σ, $n_\sigma = 1$ if the symmetry operation that transforms it into ν^{ref}_σ preserves the CPG vector, and $n_\sigma = -1$ if the symmetry operation inverses the CPG vector (Fig. 3.2). Note that as a consequence to this, a configuration that is symmetric to itself with respect to the direction of the CPG has a null effective interaction. This makes sense because the distribution function of such configuration will not be affected by the CPG. The effective interactions are therefore re-written as

$$\nu_n = \sum_\sigma n_\sigma \nu_\sigma , \tag{3.18}$$

and

$$\nu_n^\alpha = \sum_\sigma n_\sigma \nu_\sigma^\alpha. \tag{3.19}$$

Note that there is only one non-zero term in the sums. Effective interactions belonging to the same class will have effective interactions with the same magnitude and their corresponding stationnarity equation (Eq. 3.14) will be the same. The advantage of grouping effective interactions in symmetry unique classes is that it reduces the number of equations to solve and the number of effective interactions to calculate from N_{conf} to N_{inter}, N_{inter} being the number of effective interactions classes.

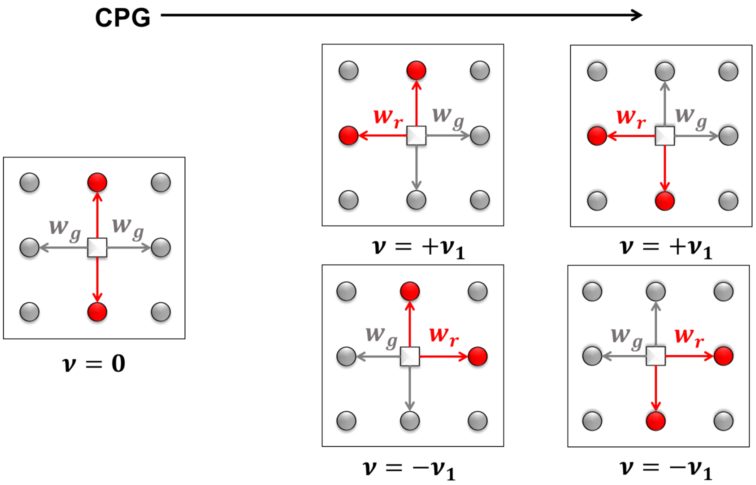

Figure 3.2: Schematic representation of two effective interactions. On the left, a configuration is symmetric to itself with respect to the CPG direction. The jump frequency of the vacancy (white square) in the positive and negative directions of the CPG are equal (w_g). This configuration is not affected by the presence of the CPG and it therefore has a null effective interaction. On the right, a class of 4 configurations which are symmetry equivalents with respect to the CPG direction. None of these configurations is symmetric to itself with respect to the CPG direction, and note that a vacancy jump frequency in the positive direction of the CPG is different from the vacancy jump frequency in the negative direction of the CPG ($w_G \neq w_R$). These configurations have non-null effective interactions equal to $\pm\nu_1$, depending on whether a symmetry operation that allows us to obtain them from the first configuration (top left) keeps the CPG vector or inverts it.

3.2.5 Matrix notations

The stationnarity and flux equations can be more conveniently re-written in matrix format.

Vector of effective interactions

The stationnarity equation 3.14 is re-written in matrix notation as

$$T\nu = M\mu, \tag{3.20}$$

where ν is a vector of length N_{inter} whose components are the values of the effective interactions of each class $\nu_\sigma/(k_BT)$, and μ is a vector of length $N_{species}$ whose components are the chemical potential gradients of each species $\nabla\mu_\alpha/\left(k_BT\right)$, $N_{species}$

being the total number of species. T is a matrix of size $N_{inter} \times N_{inter}$ whose components are

$$T_{\sigma_0\sigma} = n_{\sigma_0} \sum_m P_n^0 W_{nm} \left(m_\sigma - n_\sigma\right) \tag{3.21}$$

and M is a matrix of size $N_{inter} \times N_{species}$ whose components are

$$M_{\sigma_0\alpha} = n_{\sigma_0} \sum_m P_n^0 W_{nm} d_{nm}^{\alpha\mu}. \tag{3.22}$$

The effective interactions vector is calculated by inverting the T matrix and solving the system of N_{inter} equations of N_{inter} unknowns

$$\nu = T^{-1} M \mu. \tag{3.23}$$

Note that microscopic detailed balance (Eq. 1.125) can be used to express the components of T and M as equilibrium averages

$$T_{\sigma_0\sigma} = \left\langle n_{\sigma_0} W_{mn} \left(m_\sigma - n_\sigma\right)\right\rangle, \tag{3.24}$$

and

$$M_{\sigma_0\alpha} = \left\langle n_{\sigma_0} W_{mn} d_{nm}^{\alpha\mu}\right\rangle. \tag{3.25}$$

Tensor of cluster transport coefficients

The flux equation (Eq. 3.9) can be written as a function of the ν and μ vectors

$$J_d^\beta\left(c\right) = -\frac{1}{V}\left(\Lambda_0^d \mu - \Lambda^d \nu\right), \tag{3.26}$$

where Λ_0^d is a matrix of size $N_{species} \times N_{species}$ whose components are

$$\Lambda_{0,\beta\alpha}^d = \sum_i \sum_{j \in \theta_{i+}^\beta} d_{ij}^{\beta d} \left\langle n_i^\beta m_j^\beta \sum_m W_{nm} d_{nm}^{\alpha\mu} \right\rangle, \tag{3.27}$$

and Λ^d is a matrix of size $N_{species} \times N_{inter}$ whose components are

$$\Lambda_{\beta\sigma}^d = \sum_i \sum_{j \in \theta_{i+}^\beta} d_{ij}^{\beta d} \left\langle n_i^\beta m_j^\beta \sum_m W_{nm} \left(n_\sigma^\alpha - m_\sigma^\alpha\right) \right\rangle. \tag{3.28}$$

Replacing the effective interaction vector in Eq. 3.26 with its calculated value from Eq. 3.23, allows us to express the flux as a function of the μ vector

$$J_d^\beta\left(c\right) = -\frac{1}{V}\left(\Lambda_0^d - \Lambda^d T^{-1} M\right)\mu, \tag{3.29}$$

and the cluster transport coefficients are identified as

$$L_{\beta\alpha}^d\left(c\right) = \frac{1}{V}\left(\Lambda_0^d - \Lambda^d T^{-1} M\right)_{\beta\alpha}. \tag{3.30}$$

Schuler *et al.* [18] showed that if the matrix Λ is calculated along the CPG direction (i.e. if $\vec{e}_d = \vec{e}_\mu$), it can be expressed as a function of the M matrix, such that their components are linked via

$$N_\sigma M_{\sigma\alpha} = \Lambda_{\alpha\sigma}^\mu, \tag{3.31}$$

where N_σ is the number of effective interactions belonging to class σ. The matrices can be linked through a diagonal matrix N of size $N_{inter} \times N_{inter}$ and whose components are N_σ

$$NM = (\Lambda^\mu)^t . \tag{3.32}$$

Here, the t exponent denotes the transpose of the matrix. Each N_σ can be calculated by applying symmetry operations that preserve the CPG direction to one of the configurations in σ and counting the number of unique symmetry equivalent configurations, and this is simpler and faster than calculating the M matrix. The transport coefficient components can then be calculated along the CPG direction as a function of three matrices only $\tilde{T}$, Λ and Λ_0

$$\begin{aligned} L^\mu_{\beta\alpha}(c) &= \frac{1}{V}\left[\Lambda^\mu_0 - \Lambda^\mu (NT)^{-1} NM\right]_{\beta\alpha} \\ &= \frac{1}{V}\left[\Lambda^\mu_0 - \Lambda^\mu \tilde{T}^{-1} (\Lambda^\mu)^t\right]_{\beta\alpha}, \end{aligned} \tag{3.33}$$

where $\tilde{T} = NT$. Note that as long as microscopic detailed balance holds, $\tilde{T}$ is a symmetric positive definite matrix. Furthermore, $\tilde{T}$ is a sparse matrix because, in the general case, the number of configurations in the system is large, however, from one configuration (ν_{σ_0}) there are few accessible configurations (ν_σ), and therefore most components of a line or column will be null.

3.2.6 Finite number of configurations

The dilute alloy approximation allows us to ensure a finite number of cluster configurations to study. This is done by using the system's invariance by translation and by setting a kinetic radius beyond which the cluster dissociates.

System volume and invariance by translation

To calculate the sums which appear in the flux and stationnarity equations (Eq. 3.9 and 3.14), it is necessary to sum over all possible configurations n of the cluster system which has a total volume V, and to sum over all configurations m accessible from n. In practice, even if the cluster components are surrounded by a homogeneous medium, the number of possible configurations in a volume of interest V can still be large depending on the size of V, which could lead to a large number of elements in the sums and make the system of equations harder to solve. However, the homogeneity around cluster components makes it possible to use invariance by translation and to work in a smaller volume. A primitive cell can be chosen to represent the system where a translated version of all configurations with different relative positions of the components can be built. The volume V that appears in the equations represents then the volume of the primitive cell and not of the whole system, and jumps are studied only from configurations belonging to this volume. This represents a small but very important change to the stationnarity equation by reducing a large sum to a much smaller one

$$L^d_{\beta\alpha}(c) = \frac{1}{V}\sum_i \sum_{j\in\theta^\beta_{i+}} d^{\beta d}_{ij} \sum_{n\in V} n^\beta_i m^\beta_j P^0_n W_{nm}\left(\nu^\alpha_n - \nu^\alpha_m + d^{\alpha\mu}_{nm}\right). \tag{3.34}$$

Note that here, from a configuration n in V, accessible configurations m are not necessarily in the primitive cell volume and can be translated versions of a configuration belonging to the primitive cell.

Associated and dissociated configurations

As mentioned in Sec. 3.2.1, each cluster is characterized by a kinetic radius beyond which the cluster dissociates and can associate with other clusters. The kinetic radius represents the cut-off radius for effective interactions. Dissociated configurations are configurations in which one or more cluster component is found at a distance greater than the kinetic radius from all other components (Fig. 3.3). In this case, there is no linking path between cluster components whose branches are shorter than the kinetic range. Cluster components are assumed to no longer interact with each other, and jumps from dissociated configurations are not studied. Connected (or associated) configurations are configurations in which all cluster components are found to be within the kinetic radius, and jumps from these configurations are studied. A jump that transforms a connected configuration to a dissociated configuration is a dissociated jump, while the inverse jump is an associated jump. All trajectories within the kinetic radius are to be explored. In the formalism, all sums over initial configurations (sums over n) are sums over associated configurations. Configurations that are accessible (m) from an associated configuration can be both associated or dissociated, however once a dissociated configuration is found, its corresponding kinetic trajectory is not further explored. This happens naturally since the sum over initial configurations n does not include dissociated configurations.

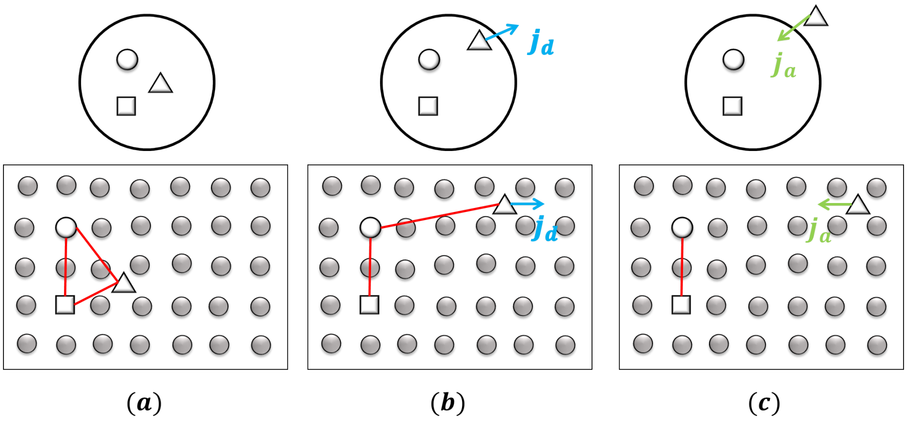

(*a*) (*b*) (*c*)

Figure 3.3: Examples of associated configurations (a and b) and a dissociated configuration (c) in the case of a kinetic radius of 4 lattice parameters. A jump from an associated configuration to a dissociated configuration is a dissociated jump j_d, and the inverse jump is an associated jump j_a.

3.2.7 Implementation of the SCMF-d in KineCluE

This new formalism of the SCMF, SCMF-d, was implemented in an open-source code named KineCluE in order to make the calculation of cluster transport coefficients more accessible and user-friendly. The aim of the code is to calculate $L^{\mu}_{\beta\alpha}(c)$ using Eq. 3.33, which requires the computation of the three matrices $\tilde{T}$, Λ and Λ_0. The code also outputs the partition function of the cluster, which can be used later by the user to calculate cluster concentrations and deduce the total transport coefficients. The code is split in two parts. The first part is an analytical part in which the code looks for all possible cluster configurations within a user-defined kinetic radius, makes all the links between the configurations by finding the jump frequencies between them, and then constructs and outputs the symbolic matrices needed to compute the transport coefficients. The second part is a numerical part in which the code uses numerical energy values input by the user to fill the symbolic matrices and outputs the numerical values of the transport coefficients. The way the code is split in an analytical and numerical part allows to compute transport coefficients as a function of temperature and strain in the most efficient way, by running the analytical part once for each crystal structure and atomic jump model, and by running the numerical part several times for different values of interactions, temperature and strain.

The user input, code output and organigram of both the analytical and numerical parts are summarized in the following.

3.2.7.1 Analytical part

User input The code requires information on the crystal, cluster components and atomic jump model. The mandatory user input required to run the analytical part of the code consists in:

- Kinetic radius.
- Lattice vectors and basis atoms to construct the crystal.
- Cluster components species and lattice sites they can occupy.
- Symmetry unique jump mechanisms.

Running the code with these information only allows the study of the transport coefficients in a crystal with no deformations in which the driving force is along the first user defined lattice vector. Additional user input can be provided, for example, to:

- Apply a deformation to the crystal.
- Change the default direction of the CPG.
- Compute transport coefficients in a direction normal to the CPG.
- Run a convergence study of the transport coefficients as a function of the kinetic radius to find the optimal kinetic radius.

Organigram Figure 3.4 shows the main steps of the analytical part of the code which consist in reading the user input, exploring the configuration space and finding the jump frequencies that connect the configurations, computing the symbolic matrices and finally outputting and saving the necessary objects to run the numerical part of the code.

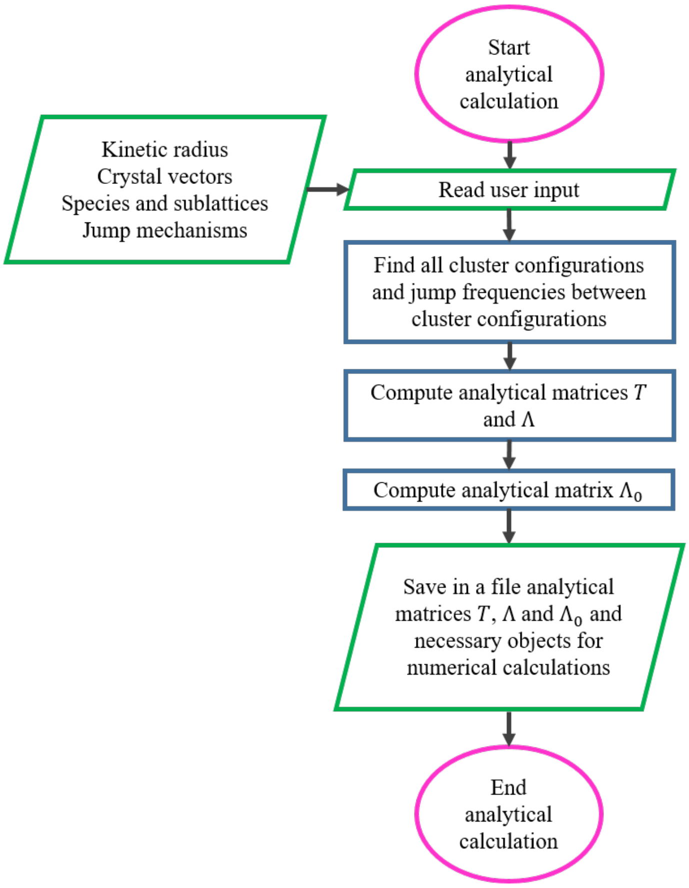

Figure 3.4: Organigram of the analytical part of KineCluE, in the case of a dilute alloy.

Configuration space exploration Finding all cluster configurations and jump frequencies that link them is a crucial step of the analytical part of the code. This step is computationally demanding and it is therefore important to do it in an optimized way. Figure 3.5 shows how the code finds all cluster configurations in an efficient way. The code starts with an initial associated configuration of the cluster components and uses the provided jump mechanisms to find all the configurations that are accessible from it. The code then picks the next available configuration that is associated and that hasn't been studied before and does the same until all configurations whose components satisfy the kinetic radius condition are found. This allows the code to also find all jump frequencies that link configurations through jump mechanisms. While exploring the configuration space, the code applies symmetry operations (which conserve the crystal and the CPG direction) to reduce the number of configurations and speed up the exploration. The code studies symmetry unique configurations instead of studying all configurations, and finds all accessible configurations from each symmetry unique configuration, which reduces the code's computational time and memory needs.

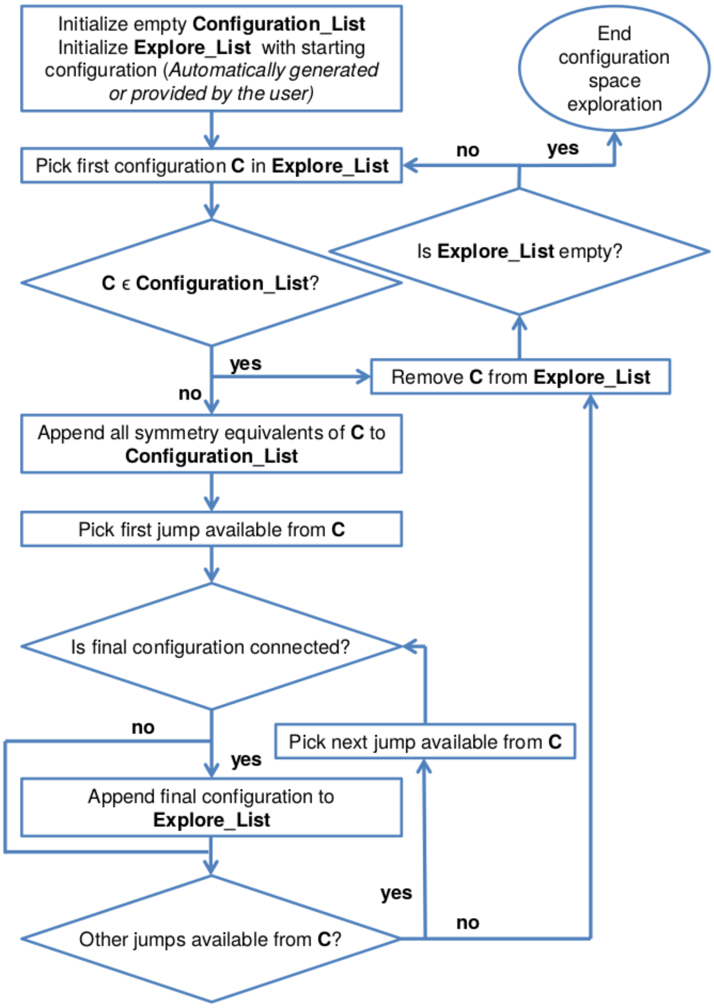

Figure 3.5: Organigram of the full configuration space exploration in KineCluE, in the case of a dilute alloy [18].

Output The analytical part of the code outputs and mainly saves the following objects:

- Thermodynamically unique configurations (symmetry unique configurations with respect to the crystal symmetry).
- Kinetically unique configurations (one configuration of each effective interaction class).
- Thermodynamically unique jump frequencies (associated to symmetry unique saddle-point configurations).
- Symbolic matrices $\tilde{T}$, Λ and Λ_0.
- Symbolic partition function Z.

3.2.7.2 Numerical part

User input The numerical part of the code requires information to perform a numerical application to the matrices. The mandatory user input has to contain:

- Configuration binding energies.
- Saddle-point binding energies.
- Temperature(s) at which to calculate the transport coefficients.

Note that there are several ways for the energies to be given. The user can either provide these energies directly, or provide enough information for the code to calculate them using an interaction model. The user can also ask the code to assign random values to them. In the next section, we will present briefly some information related to the calculation of these binding energies, and for more detailed information, one can refer to the KineCluE documentation file.

In this numerical part as well, the user can provide additional information, for example, to:

- Compute mobility coefficients, exchange coefficients, drag ratios, correlation factors and uncorrelated contributions.
- Compute transport coefficients in a strained crystal.
- Compute transport coefficients in a direction normal to the CPG.
- Change the default numerical precision.
- Perform a sensitivity study of the transport coefficients to identify the most relevant jump frequencies.
- Run a convergence study of the transport coefficients as a function of the kinetic radius to find the optimal kinetic radius.

Organigram The flowchart of the numerical part of the code is presented in Fig. 3.6. The main steps are to load the saved objects, to read the user input and to apply numerical values to the matrices in order to output the desired numerical quantities.

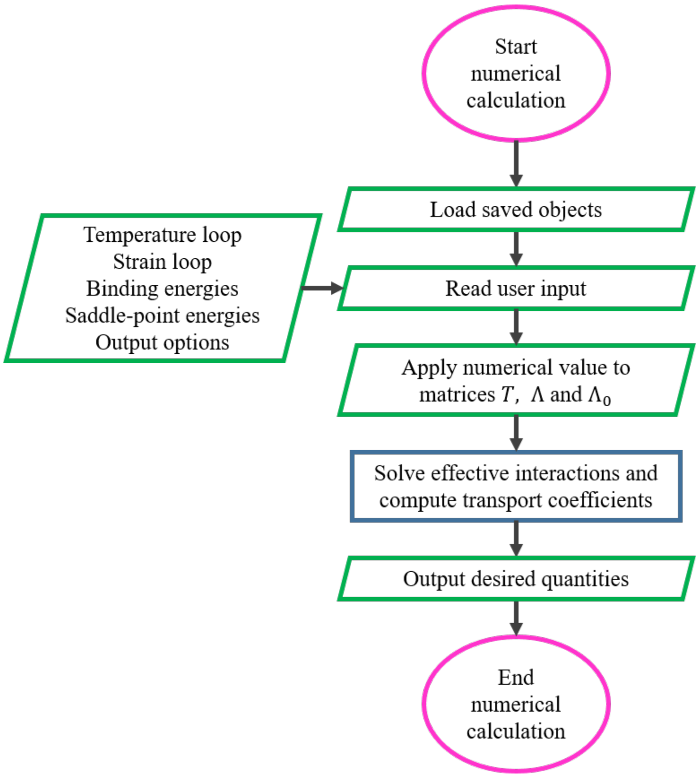

Figure 3.6: Organigram of the numerical part of KineCluE, in the case of a dilute alloy.

Output The numerical part of the code outputs by default the numerical:

- Tensor of the transport coefficients along the CPG direction.
- Partition function.

Based on the user input, the code can additionally output the numerical:

- Mobility coefficients, exchange coefficients, drag ratios, correlation factors and uncorrelated contributions.
- Tensor of the transport coefficients in a direction normal to the CPG.

3.2.8 Energy calculations

In the previous section (Sec. 3.2.7), we said that in order to run the numerical part of the code the user needs to provide configuration binding energies and saddle-point energies. The user needs to either directly provide these values, or provide sufficient information for the code to calculate them. Configuration energies appear in the equilibrium probabilities while saddle-point energies appear in the jump frequency. Remember that a configuration n is split into a cluster configuration c_n and a a homogeneous matrix of pure A atoms surrounding it. Let us introduce some notations. Let $P^0\left(c_n, \bar{c}_n^A\right) \equiv P_n^0$ and $E\left(c_n, \bar{c}_n^A\right)$ be respectively the equilibrium distribution function and the energy of a configuration n. A saddle-point configuration is a configuration in which the cluster components are in a saddle-point position between two stable configurations. The 'SP' index is then added to the energy notation so that $E_{SP}\left(c_{nm}, \bar{c}^{A}_{nm}\right)$ represents the energy of a saddle-point configuration between the stable configurations n and m. The equilibrium distribution function of a configuration n is a function of its energy and the partition function (see Eq. 1.116 of the SCMF-o), such that

$$P^{0}\left(c_n, \bar{c}^{A}_{n}\right) = \frac{1}{Z}\exp\left(-\frac{E\left(c_n, \bar{c}^{A}_{n}\right)}{k_B T}\right), \tag{3.35}$$

where Z is the partition function of the cluster system defined as

$$Z = \sum_{c_n \in V} \exp\left(-\frac{E\left(c_n, \bar{c}^{A}_{n}\right)}{k_B T}\right). \tag{3.36}$$

The jump frequency between a configuration n and m is a function of the energy difference between the saddle-point energy and the stable configuration energy

$$W^{ij}_{nm} \equiv \Gamma^{ij}_{nm}\exp\left(-\frac{E_{SP}\left(c_{nm}, \bar{c}^{A}_{nm}\right) - E\left(c_n, \bar{c}^{A}_{n}\right)}{k_B T}\right), \tag{3.37}$$

where Γ^{ij}_{nm} is the attempt frequency. The energy of any configuration n is defined as

$$E\left(c_n, \bar{c}^{A}_{n}\right) = H\left(c_n, \bar{c}^{A}_{n}\right) - \mu\left(c_n, \bar{c}^{A}_{n}\right), \tag{3.38}$$

where $H\left(c_n, \bar{c}^{A}_{n}\right)$ is the Hamiltonian of configuration n, and $\mu\left(c_n, \bar{c}^{A}_{n}\right)$ is the chemical potential of n. Note that the stationnarity equation and the transport coefficients equation depend on the product $P^{0}_{n}W^{ij}_{nm}$ which is a function of saddle-point energies and the partition function

$$P^{0}_{n}W^{ij}_{nm} = \frac{1}{Z}\Gamma^{ij}_{nm}\exp\left(-\frac{E_{SP}\left(c_{nm}, \bar{c}^{A}_{nm}\right)}{k_B T}\right). \tag{3.39}$$

We can re-write the stationnarity equation

$$\forall n\ \forall \alpha,\ \sum_{m}\Gamma^{ij}_{nm}\exp\left(-\frac{E_{SP}\left(c_{nm}, \bar{c}^{A}_{nm}\right)}{k_B T}\right)\left(\nu^{\alpha}_{m} - \nu^{\alpha}_{n}\right) = \sum_{m}\Gamma^{ij}_{nm}\exp\left(-\frac{E_{SP}\left(c_{nm}, \bar{c}^{A}_{nm}\right)}{k_B T}\right) d^{\alpha\mu}_{nm}, \tag{3.40}$$

and the transport coefficient

$$L^{d}_{\beta\alpha}(c) = \frac{1}{VZ}\sum_{i}\sum_{j\in\theta^{\beta}_{i+}} d^{\beta d}_{ij}\sum_{n\in V} n^{\beta}_{i} m^{\beta}_{j}\Gamma^{ij}_{nm}\exp\left(-\frac{E_{SP}\left(c_{nm}, \bar{c}^{A}_{nm}\right)}{k_B T}\right)\left(\nu^{\alpha}_{n} - \nu^{\alpha}_{m} + d^{\alpha\mu}_{nm}\right), \tag{3.41}$$

explicitly as a function of the energies. Notice that the $1/Z$ factor gets simplified on both sides of the stationnarity equation, and therefore the effective interactions depend only on saddle-point energies and not on stable configuration energies. This is interesting to note because, on one hand, it makes sense that the energy of the configuration in which the system is should not affect its kinetic transition to the next state, and it is rather the competition between different saddle-point energies that dictate the transition. On the other hand, this means that two systems with completely different landscapes of configuration energies will have the same kinetic behavior if they have the same distribution of saddle-point energies. Stable configuration energies will only affect the value of the transport coefficients, but not the kinetic trajectories of the system.

Equations 3.40 and 3.41 are a function of absolute values of energies which in practice cannot be calculated. We can calculate energy differences and therefore we need to introduce a reference energy, E_{ref}, with respect to which we calculate $E\left(c_n, \bar{c}_n^A\right)$ and $E_{SP}\left(c_{nm}, \bar{c}_{nm}^A\right)$. We can multiply both sides of Eq. 3.40 with an exponential involving the energy of a reference configuration. We call this exponential

$$\kappa = \exp\left(-\frac{E_{ref}}{k_B T}\right). \tag{3.42}$$

We further multiply and divide by κ both Eq. 3.41 and the partition function. The stationnarity equation and the transport coefficient equation become

$$\forall n\ \forall \alpha\ , \sum_m \Gamma_{nm}^{ij} \exp\left(\frac{E_{SP}^b\left(c_{nm}, \bar{c}_{nm}^A\right)}{k_B T}\right)\left(\nu_m^\alpha - \nu_n^\alpha\right) = \sum_m \Gamma_{nm}^{ij} \exp\left(\frac{E_{SP}^b\left(c_{nm}, \bar{c}_{nm}^A\right)}{k_B T}\right) d_{nm}^{\alpha\mu}, \tag{3.43}$$

and

$$L_{\beta\alpha}^d(c) = \frac{1}{VZ}\sum_i \sum_{j\in\theta_{i+}^\beta} d_{ij}^{\beta d} \sum_{n\in V} n_i^\beta m_j^\beta \Gamma_{nm}^{ij} \exp\left(\frac{E_{SP}^b\left(c_{nm}, \bar{c}_{nm}^A\right)}{k_B T}\right)\left(\nu_n^\alpha - \nu_m^\alpha + d_{nm}^{\alpha\mu}\right), \tag{3.44}$$

where

$$Z = \sum_{c_n\in V} \exp\left(\frac{E^b\left(c_n, \bar{c}_n^A\right)}{k_B T}\right). \tag{3.45}$$

$E_{SP}^b\left(c_{nm}, \bar{c}_{nm}^A\right) = E_{ref} - E_{SP}\left(c_{nm}, \bar{c}_{nm}^A\right)$ is the binding energy at the saddle-point, and $E^b\left(c_n, \bar{c}_n^A\right) = E_{ref} - E\left(c_n, \bar{c}_n^A\right)$ is the binding energy of configuration n. The change of sign is just a matter of convention, and here a positive binding energy means attraction. The choice of the reference energy is left for the user and should not affect the calculations, as long as all energies are calculated with respect to it. The most obvious choice is to choose it as the energy of the configuration in which all cluster components are isolated in a pure A matrix. The energy difference represents the binding energy of cluster components in each configuration and can be calculated using standard approaches like Density Function Theory (DFT) or a theoretical interaction model.

3.3 Extending the SCMF-d to concentrated alloys

When dividing the system into cluster, the SCMF-d makes the assumption that the system can be divided into independent clusters that do not interact with each other. Within the dilute approximation, each cluster is in a homogeneous matrix. The number of possible configurations of each cluster is a finite number equal to the number of possible ways cluster components can occupy the sites of a primitive cell volume within a defined kinetic radius. As a consequence the number of effective interactions was also finite and the system of stationnarity equations could be solved to calculate them (Eq. 3.14). However, in a concentrated alloy, clusters can be found surrounded by different types of atoms depending on their location in the matrix, and the medium around cluster components is heterogeneous. Invariance by translation can no longer be used since the occupation of sites is not the same everywhere in the crystal. The number of cluster configurations becomes infinite, and, as a consequence, we cannot solve the SCMF-d equations exactly. We also showed that replacing all sites around the cluster by a homogeneous mean-field is a strict approximation that disables us from properly treating correlations. A mean-field approximation can be made to replace the heterogeneous matrix by an average homogeneous matrix. In this case, the SCMF-d formalism can be used by considering the bulk species to have properties that are the average of those of the species consisting the concentrated alloy. However, this approximation disables us from properly treating the diffusion problem in concentrated alloys: short-range order, kinetic coupling between the alloy species and kinetic correlations related to the chemical nature of species are all not taken into account. Furthermore, we cannot study diffusion properties related to specific chemical species since these quantities will be calculated for the average bulk species and not for each chemical species separately. For example, in a binary AB alloy, a mean-field approximation which replaces all A and all B atoms by an average atom M, prevents us from calculating collecting transport coefficients of atoms of species A since they no longer exist in the system, and we can instead calculate transport coefficients related to M atoms. Even though the SCMF-d is globally based on the SCMF-o, it differs from it in the way it decomposes the system into clusters and in the way it calculates effective interactions. This new formulation simplifies the original theory, and the implementation of SCMF-d in the KineCluE code made it further simpler and faster to use. In light of this new progress of the SCMF theory, the aim of this thesis is to extend the SCMF-d to concentrated alloys and implement the extension in the KineCluE code, in order to compute the full Onsager matrix in a concentrated alloy in a general and automated way. In this section, we will present the theoretical formalism of extending the SCMF-d equations to concentrated alloys, and in the next section (Sec. 3.4), we will show its implementation in KineCluE and the general functioning of the code.

3.3.1 Theoretical development of SCMF-c

Our model

The equations derived in SCMF-d do not explicitly take into account the homogeneity of the system. The dilute approximations simplify the problem when summing over the different configurations and finding all configurations that are accessible from each one of them. The derived equations remain therefore valid for a concentrated alloy. The system of stationnarity equations to calculate effective interactions (Eq. 3.14) , the flux equation (Eq. 3.9) and the transport coefficients equation (Eq. 3.16) can all be used.

To calculate the flux and cluster transport coefficients, we first need to calculate the unknown effective interactions. We start from the stationnarity equation of SCMF-d (Eq. 3.14), in which we re-organize the terms as follows just for convenience

$$\forall n \ \forall \alpha \ , \sum_{m} P_n^0 W_{nm} \nu_n^{\alpha} = \sum_{m} P_n^0 W_{nm} \left(\nu_m^{\alpha} - d_{nm}^{\alpha\mu} \right). \tag{3.46}$$

Remind that here, the system under study is a cluster c, and that n represents one cluster configuration of the system such that all atomic positions are occupied by well defined atoms up to infinity. This equation is valid for the case of any concentrated alloy, given that we treat all possible configurations and jump frequencies.

However, as discussed in the introduction of this section, Eq. 3.46 represents an infinite set of equations with an infinite sum in each, and the equations cannot be established nor solved in an exact manner. We also discussed that replacing all sites around the cluster components by a homogeneous mean-field is too crude of an approximation which prevents us from properly treating correlations. The aim of our model, as shown in Fig. 3.7, is to provide an intermediate approach between the exact solution and a mean-field approximation. Around each cluster component, we consider a local environment in which we treat the problem exactly by considering well identified atomic species occupying these lattice sites. Outside of this environment and far from the cluster components, we consider a mean-field. Our approach relies therefore on a mean-field approximation, but studies exactly big clusters which do not only include the species whose diffusion is being followed, but also their near surroundings. The advantage of this approach is that we are precise locally around the diffusing species, which is where it matters most, and further away we consider a mean-field which restores translational invariance since a cluster and its local environment are in a homogeneous system. The definition of the mean-field and mean-field atoms is not required so far and it will be defined naturally later on as we develop the formalism. Note that, depending on the positions of cluster components, and for a fixed environment radius, the geometry of the environment will be different. Therefore, the number of environment sites changes from one cluster configuration to the other. Also, the type of chemical species occupying the environment sites can change from one configuration to the other. The varying number of species in each environment leads us to naturally develop our formalism within the grand canonical ensemble.

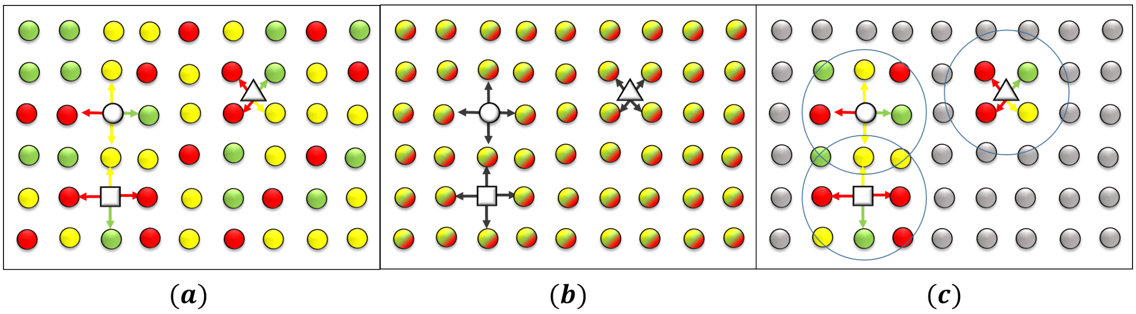

Figure 3.7: Schematic representation of a 2D-square ternary concentrated alloy. Left: exact representation. Diffusing species (white) are surrounded by a heterogeneous medium (green, red and yellow circles). Jump frequencies depend on the diffusing species, on the species with which it is exchanging and on their surroundings; Middle: mean-field approximation. Diffusing species (white) are surrounded by a homogeneous medium (tricolor circles) in which the properties of the mean-field species are the average of those constituting the alloy. Jump frequencies only depend on the diffusing species; Right: our model. Diffusing species (white) are surrounded by a local environment radius in which the species are well-defined (green, red and yellow circles), which in turn is embedded in a mean-field (gray circles) whose properties are not necessarily average properties. Jump frequencies depend on the diffusing species, on the species with which it is exchanging and on their local surrounding.

Effective interactions

In the case of a dilute alloy, a configuration n consisted in a cluster configuration c_n surrounded by a homogeneous matrix $\bar{c}_n^A$, which we arbitrarily chose to be a pure A matrix; $n = c_n \cup \bar{c}_n^A$. In the case of a concentrated alloy, we split the configuration n into a cluster configuration c_n, a cluster environment e_n (i.e. local environment around cluster components) and sites outside of the environment $\bar{e}_n$ (sites that do not belong to the cluster c_n nor the environment e_n); $n = c_n \cup e_n \cup \bar{e}_n$ (Fig. 3.8). Note that, in the case of a dilute alloy, e_n and $\bar{e}_n$ are both occupied by the same species A. Equation 3.46 is rewritten by showing the explicit dependency of P_n^0, W_{nm}, and ν_n^α on the components of n

$$\begin{aligned}\forall n\ \forall\alpha\ ,&\sum_m P^0\left(c_n,e_n,\bar{e}_n\right) W\left(c_n,e_n,\bar{e}_n,c_m,e_m,\bar{e}_m\right)\nu^\alpha\left(c_n,e_n,\bar{e}_n\right)\\ =&\sum_m P^0\left(c_n,e_n,\bar{e}_n\right) W\left(c_n,e_n,\bar{e}_n,c_m,e_m,\bar{e}_m\right)\left[\nu^\alpha\left(c_m,e_m,\bar{e}_m\right)-d_{nm}^{\alpha\mu}\right]. \qquad (3.47)\end{aligned}$$

The equilibrium probability can be written explicitly as a function of exponential energies and the partition function

$$P^0\left(c_n,e_n,\bar{e}_n\right)=\frac{1}{Z}\exp\left(-\frac{E\left(c_n,e_n,\bar{e}_n\right)}{k_BT}\right), \qquad (3.48)$$

where the energy contains the Hamiltonian and the chemical potentials $E\left(c_n,e_n,\bar{e}_n\right) = H\left(c_n,e_n,\bar{e}_n\right) - \sum_{i,\alpha} n_i^\alpha \mu_\alpha$. Moreover, the sum over all other configurations m can be replaced by a sum over jumps j available from configuration n. The jump frequency is also calculated as a function of the energy difference between the saddle-point energy and the stable configuration energy. Let c_{nj} be the saddle-point cluster configuration. In our case, the saddle-point energy depends on the union of the environments of initial and final cluster configurations. Let e_{nj} be this union of environments and $\bar{e}_{nj}$ the sites outside of it. We introduce the notation C_n^j to describe all the sites which do not belong to the environment of the initial configuration, e_n, but belong to the environment of the final configuration, e_m, such that $e_{nj} = e_n \cup C_n^j$. We call C_n^j the complement of e_n available from jump j. Note that, for any jump j, $\bar{e}_n = C_n^j \cup \bar{e}_{nj}$. The jump frequency from configuration n to configuration m can be expressed as (Fig. 1.5)

$$W_{nm}=W_j\left(c_n,e_{nj},\bar{e}_{nj}\right)=\Gamma_j\exp\left(-\frac{E_{SP}\left(c_{nj},e_n,C_n^j,\bar{e}_{nj}\right)-E\left(c_n,e_n,\bar{e}_n\right)}{k_BT}\right), \qquad (3.49)$$

where Γ_j is the attempt frequency associated with jump j. We make the following assumptions:

- the effective interactions only depend on cluster configuration and cluster environment, $\nu_n^\alpha \equiv \nu^\alpha\left(c_n,e_n,\bar{e}_n\right) \approx \nu^\alpha\left(c_n,e_n\right)$, and not on sites beyond e_n;

- the cluster configuration c_n only interacts with sites belonging to the environment, and therefore not with sites of $\bar{e}_n$, $E_{c_n,\bar{e}_n} = 0$;

- the saddle-point cluster configuration c_{nj} only interacts with the union of sites belonging to the environment of the initial and final configuration e_{nj}, $E_{c_{nj},\bar{e}_{nj}} = 0$;

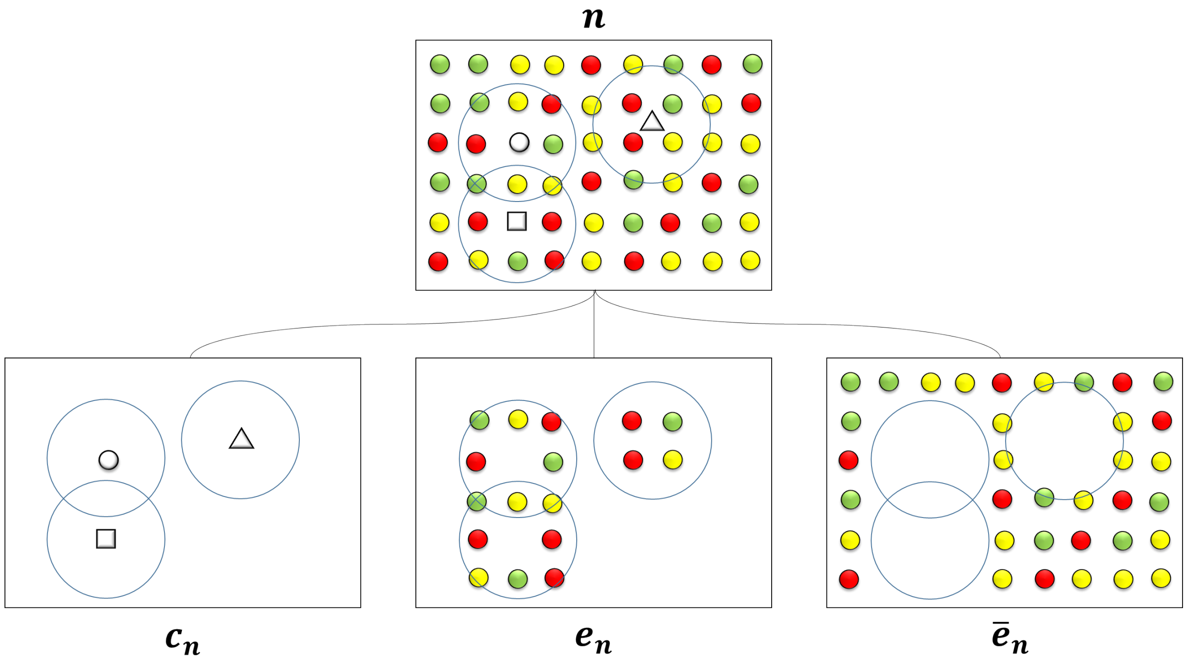

Figure 3.8: Schematic representation of the decomposition of a configuration n in the case of a ternary alloy into a cluster configuration c_n (containing three cluster components drawn in white), a cluster environment e_n (i.e. local environment around cluster components) and sites outside of the environment $\bar{e}_n$ (sites that do not belong to the cluster c_n nor the environment e_n). Chemical species of the ternary alloy are drawn in colored circles.

Let us now focus on the left-hand side of the stationnarity equation (Eq. 3.47), which we will call $S^l_{n\alpha}$

$$\begin{aligned}\forall n,\ \forall \alpha,\ S^l_{n\alpha} &= \nu^\alpha\left(c_n, e_n\right) \sum_j P^0\left(c_n, e_n, \bar{e}_n\right) W_j\left(c_n, e_{nj}, \bar{e}_{nj}\right) \\ &= \nu^\alpha\left(c_n, e_n\right) \sum_j \frac{1}{Z} \exp\left(-\frac{E\left(c_n, e_n, \bar{e}_n\right)}{k_B T}\right) \Gamma_j \exp\left(-\frac{E_{SP}\left(c_{nj}, e_n, C^j_n, \bar{e}_{nj}\right) - E\left(c_n, e_n, \bar{e}_n\right)}{k_B T}\right) \\ &= \nu^\alpha\left(c_n, e_n\right) \frac{1}{Z} \sum_j \Gamma_j \exp\left(-\frac{E_{SP}\left(c_{nj}, e_n, C^j_n, \bar{e}_{nj}\right)}{k_B T}\right). \qquad (3.50)\end{aligned}$$

The last line shows that, since the effective interaction $\nu^\alpha\left(c_n, e_n\right)$ does not depend on $\bar{e}_n$, for a given c_n and e_n, the same equation can be written for the different occupations of the complement C^j_n and the outside sites $\bar{e}_{nj}$ (since $\bar{e}_n = C^j_n \cup \bar{e}_{nj}$), with $\nu^\alpha\left(c_n, e_n\right)$ being a common factor. Configurations with the same c_n and e_n also have the same jump mechanisms j, and we can therefore sum both sides of the equation over all possible occupations of C^j_n and $\bar{e}_{nj}$

$$\forall c_n,\ \forall e_n,\ \forall \alpha,\ \mathfrak{S}^{\mathfrak{l}}_{n\alpha} \equiv \sum_{C^j_n} \sum_{\bar{e}_{nj}} S^l_{n\alpha} = \nu^\alpha\left(c_n, e_n\right) \frac{1}{Z} \sum_j \Gamma_j \sum_{C^j_n} \sum_{\bar{e}_{nj}} \exp\left(-\frac{E_{SP}\left(c_{nj}, e_n, C^j_n, \bar{e}_{nj}\right)}{k_B T}\right). \qquad (3.51)$$

Effective interactions are treated in the same way as in the SCMF-d, the difference being that they now depend on a cluster configuration and an environment around it, instead of just depending on a cluster configuration. In this case as well, effective interactions can be divided into classes such that each class contains effective interactions that have the same magnitude. There are two main difficulties in calculating this equation in an exact manner and they are due to the large number of cluster-environment configurations (c_n, e_n), and on the large number of environments $\bar{e}_{nj}$ for each (c_n, e_n). The first one arises when the size of the environment e_n and the number of different chemical species in the alloy lead to a large number of possible (c_n, e_n) configurations, and hence to a large number of effective interactions (in Chapter 1 we discuss several times how the number of configurations scales exponentially with the number of different species and sites, and how it can become too large to handle even in systems that seem small). The second problem lies in calculating the sum over all possible occupations of $\bar{e}_{nj}$. This would require us to explicitly set a size for our system in order to know the number of sites in $\bar{e}_{nj}$, since there is no translational invariance. Then, we would have to enumerate all possible occupations of these sites, knowing that the size of $\bar{e}_{nj}$ needs to be big enough to ensure that clusters are isolated and do not interact with each other. The number of configurations with the same (c_n, e_n, C_n^j) and different $\bar{e}_{nj}$ is equal to the number of ways we can arrange the different species of the alloy on the different sites of $\bar{e}_{nj}$, and is therefore equal to

$$\Omega_{\bar{e}_{nj}} = \left(N_{spec}\right)^{N_{\bar{e}_{nj}}}, \tag{3.52}$$

N_{spec} being the number of chemical species, and $N_{\bar{e}_{nj}}$the number of sites in $\bar{e}_{nj}$. We arbitrarily choose to write this sum as

$$\sum_{\bar{e}_{nj}} \exp\left(-\frac{E_{SP}\left(c_{nj}, e_n, C_n^j, \bar{e}_{nj}\right)}{k_B T}\right) = \Omega_{\bar{e}_{nj}} \exp\left(-\frac{E_{SP}\left(c_{nj}, e_n, C_n^j, \bar{e}_{nj}^M\right)}{k_B T}\right), \tag{3.53}$$

where M represents mean-field atoms whose properties are not defined yet, and the upper index M on $\bar{e}_{nj}$ means that all of its sites are occupied by mean-field atoms. Therefore, $E_{SP}\left(c_{nj}, e_n, C_n^j, \bar{e}_{nj}^M\right)$ represents the energy of a saddle-point cluster configuration c_{nj}, surrounded by a jump frequency environment $e_{nj} = e_n \cup C_n^j$, which in turn is embedded in a homogeneous mean-field M. Equation 3.53 represents our mean-field definition. Since we do not know the number of sites in $\bar{e}_{nj}$, and since we do not want to explicitly specify a size of the system, we write $\Omega_{\bar{e}_{nj}} = \Omega_e/\Omega_{e_{nj}}$, where $e = e_{nj} \cup \bar{e}_{nj}$ represents the entire environment lattice sites, i.e. all the sites that can be occupied the chemical species. We do not know the size of e, but as will be shown in a bit, Ω_e is a common factor that can be simplified, unlike $\Omega_{\bar{e}_{nj}}$. $\mathfrak{S}_{n\alpha}^l$ becomes

$$\forall c_n,\ \forall e_n,\ \forall \alpha,\ \mathfrak{S}_{n\alpha}^l = \nu^\alpha\left(c_n, e_n\right) \frac{1}{Z} \Omega_e \sum_j \Gamma_j \frac{1}{\Omega_{e_{nj}}} \sum_{C_n^j} \exp\left(-\frac{E_{SP}\left(c_{nj}, e_n, C_n^j, \bar{e}_{nj}^M\right)}{k_B T}\right). \tag{3.54}$$

So far, no approximations were made on how to calculate the mean-field or an energy involving mean-field atoms, and we only made a change in writing the sum over $\bar{e}_{nj}$ as a function of a mean-field energy. The same calculation can be carried out for the right-hand side of the stationnarity equation (Eq. 3.47)

$$\forall c_n,\ \forall e_n,\ \forall \alpha,\ \mathfrak{S}^r_{n\alpha} = \frac{1}{Z}\Omega_e \sum_j \Gamma_j \frac{1}{\Omega_{e_{nj}}} \sum_{C_n^j} \exp\left(-\frac{E_{SP}\left(c_{nj}, e_n, C_n^j, \bar{e}^M_{nj}\right)}{k_B T}\right)\left[\nu^\alpha\left(c_{n+j}, e_{n+j}\right) - d_j^{\alpha\mu}\right], \tag{3.55}$$

where $\nu^\alpha\left(c_{n+j}, e_{n+j}\right)$ represents the effective interaction of the configuration accessible from n via a jump j (originally written as ν^α_m), and $d_j^{\alpha\mu}$ is the total displacement distance of atoms of species α after a jump j from configuration n (originally written as $d^{\alpha\mu}_{nm}$). The system of coupled linear equations that we need to solve to obtain the effective interactions is

$$\forall c_n,\ \forall e_n,\ \forall \alpha,\ \nu^\alpha\left(c_n, e_n\right) \sum_j \Gamma_j \frac{1}{\Omega_{e_{nj}}} \sum_{C_n^j} \exp\left(-\frac{E_{SP}\left(c_{nj}, e_n, C_n^j, \bar{e}^M_{nj}\right)}{k_B T}\right)$$
$$= \sum_j \Gamma_j \frac{1}{\Omega_{e_{nj}}} \sum_{C_n^j} \exp\left(-\frac{E_{SP}\left(c_{nj}, e_n, C_n^j, \bar{e}^M_{nj}\right)}{k_B T}\right)\left[\nu^\alpha\left(c_{n+j}, e_{n+j}\right) - d_j^{\alpha\mu}\right]. \tag{3.56}$$

Note that Ω_e is simplified on both sides of the equations. Just like in SCMF-d, the saddle-point energy that appears in the equations is an absolute energy, and we multiply both sides of the equation by some exponential involving the energy of a reference configuration with respect to which we can calculate the saddle-point energy. We call this exponential κ, and$-E_{SP}\left(c_{nj}, e_n, C_n^j, \bar{e}^M_{nj}\right)$ is turned to $E^b_{SP}\left(c_{nj}, e_n, C_n^j, \bar{e}^M_{nj}\right)$, the binding energy at the saddle-point. We keep the same sign convention for the binding energy, such that a positive binding energy means attraction.

$$\forall c_n,\ \forall e_n,\ \forall \alpha,\ \nu^\alpha\left(c_n, e_n\right) \sum_j \Gamma_j \frac{1}{\Omega_{e_{nj}}} \sum_{C_n^j} \exp\left(\frac{E^b_{SP}\left(c_{nj}, e_n, C_n^j, \bar{e}^M_{nj}\right)}{k_B T}\right)$$
$$= \sum_j \Gamma_j \frac{1}{\Omega_{e_{nj}}} \sum_{C_n^j} \exp\left(\frac{E^b_{SP}\left(c_{nj}, e_n, C_n^j, \bar{e}^M_{nj}\right)}{k_B T}\right)\left[\nu^\alpha\left(c_{n+j}, e_{n+j}\right) - d_j^{\alpha\mu}\right]. \tag{3.57}$$

To solve this system of equations, we need to first calculate the mean-field saddle-point binding energies. We already explained the difficulty in calculating these terms exactly because of the sum in Eq. 3.53. Therefore, we need to find another way of calculating them, or approximating them, and this will be the main topic of Section 3.5. Once we know the values of these binding energies, we can calculate the effective interactions from Eq. 3.57. These effective interactions are then used to calculate the cluster transport coefficients.

Cluster transport coefficients

We need to establish the expressions of the cluster transport coefficients in the case of a concentrated alloy. Equation 3.16 of SCMF-d which gives the transport coefficients is also valid in the general case of a cluster. We make few notation adjustments which make the expression more convenient to use in the treatment of concentrated alloys. The respective sums over all sites in the cluster system i and all accessible sites j with a positive displacement vector between them is instead written as a sum over all jumps j that are possible from a configuration n, and the expression is divided by a factor 2 since a jump and its reverse jump are counted twice (see Eq. 3.10). Lastly, the displacement distance $d_{ij}^{\beta d}$ is replaced by the notation $d_j^{\beta d}$, and the cluster transport coefficient becomes

$$L_{\beta\alpha}^{d}\left(c\right)=\frac{1}{2V}\sum_{n\in V}\sum_{j}d_j^{\beta d}P_n^0W_{nm}\left(\nu_n^{\alpha}-\nu_m^{\alpha}+d_j^{\alpha\mu}\right). \tag{3.58}$$

Note that here and in the following, we will write ν_n^{α} instead of $\nu^{\alpha}\left(c_n,e_n\right)$ to simplify notations, but keep in mind that an effective interaction ν_n only depends on c_n and e_n, and not on $\bar{e}_n$. By analogy with the way we treated the stationnarity equation, a configuration m accessible from n via a jump j is represented by the symbols $(n+j)$, the probability of being in a configuration n and transition into a configuration m is calculated as a function of a saddle-point energy

$$P_n^0W_{nm}=\frac{1}{Z}\Gamma_j\exp\left(-\frac{E_{SP}\left(c_{nj},e_n,C_n^j,\bar{e}_{nj}\right)}{k_BT}\right), \tag{3.59}$$

and the sum over n is divided into a sum over its components $(c_n,e_n,\bar{e}_n)$, which for a jump j is equivalent to $(c_n,e_n,C_n^j,\bar{e}_{nj})$,

$$L_{\beta\alpha}^{d}\left(c\right)=\frac{1}{2VZ}\sum_{c_n\in V}\sum_{e_n}\sum_{j}d_j^{\beta d}\Gamma_j\sum_{C_n^j}\sum_{\bar{e}_{nj}}\exp\left(-\frac{E_{SP}\left(c_{nj},e_n,C_n^j,\bar{e}_{nj}\right)}{k_BT}\right)\left(\nu_n^{\alpha}-\nu_{n+j}^{\alpha}+d_j^{\alpha\mu}\right). \tag{3.60}$$

Using the mean-field definition (Eq. 3.53), the transport coefficient becomes a function of a mean-field saddle-point energy

$$L_{\beta\alpha}^{d}\left(c\right)=\frac{1}{2VZ}\sum_{c_n\in V}\sum_{e_n}\sum_{j}d_j^{\beta d}\Gamma_j\sum_{C_n^j}\Omega_{\bar{e}_{nj}}\exp\left(-\frac{E_{SP}\left(c_{nj},e_n,C_n^j,\bar{e}_{nj}^M\right)}{k_BT}\right)\left(\nu_n^{\alpha}-\nu_{n+j}^{\alpha}+d_j^{\alpha\mu}\right). \tag{3.61}$$

Here again, we need to transform the absolute energy into a binding energy, so we multiply and divide Eq. 3.61 by the energy exponential of a reference configuration, which we call κ. We also replace $\Omega_{\bar{e}_{nj}}$ by $\Omega_e/\Omega_{e_{nj}}$

$$L_{\beta\alpha}^{d}\left(c\right)=\frac{\Omega_e}{2\kappa VZ}\sum_{c_n\in V}\sum_{e_n}\sum_{j}d_j^{\beta d}\Gamma_j\frac{1}{\Omega_{e_{nj}}}\sum_{C_n^j}\exp\left(\frac{E_{SP}^b\left(c_{nj},e_n,C_n^j,\bar{e}_{nj}^M\right)}{k_BT}\right)\left(\nu_n^{\alpha}-\nu_{n+j}^{\alpha}+d_j^{\alpha\mu}\right). \tag{3.62}$$

Just like in SCMF-d, we can use matrix notations for convenience, and we can calculate the components of the transport coefficients tensor as

$$L_{\beta\alpha}^{d}\left(c\right)=\frac{1}{V}\left[\Lambda_0^d-\Lambda^dT^{-1}M\right]_{\beta\alpha}, \tag{3.63}$$

where, Λ_0^d is an $N_{species}\times N_{species}$ matrix whose components are

$$\Lambda_{0,\beta\alpha}^{d}=\frac{\Omega_e}{2\kappa Z}\sum_{c_n\in V}\sum_{e_n}\sum_{j}d_j^{\beta d}\Gamma_j\frac{1}{\Omega_{e_{nj}}}\sum_{C_n^j}\exp\left(\frac{E_{SP}^b\left(c_{nj},e_n,C_n^j,\bar{e}_{nj}^M\right)}{k_BT}\right)d_j^{\alpha\mu}, \tag{3.64}$$

Λ^d is an $N_{species}\times N_{inter}$ matrix whose components are

$$\Lambda_{\beta\alpha}^{d}=\frac{\Omega_e}{2\kappa Z}\sum_{c_n\in V}\sum_{e_n}\sum_{j}\left(n_{\sigma}^{\alpha}-m_{\sigma}^{\alpha}\right)d_j^{\beta d}\Gamma_j\frac{1}{\Omega_{e_{nj}}}\sum_{C_n^j}\exp\left(\frac{E_{SP}^b\left(c_{nj},e_n,C_n^j,\bar{e}_{nj}^M\right)}{k_BT}\right), \tag{3.65}$$

T is an $N_{inter} \times N_{inter}$ matrix whose components are

$$T_{\sigma_0\sigma} = n_{\sigma_0} \sum_j \Gamma_j \left(m_\sigma - n_\sigma\right) \frac{1}{\Omega_{e_{nj}}} \sum_{C_n^j} \exp\left(\frac{E_{SP}^b\left(c_{nj}, e_n, C_n^j, \bar{e}_{nj}^M\right)}{k_B T}\right), \tag{3.66}$$

and M is an $N_{inter} \times N_{species}$ matrix whose components are

$$M_{\sigma_0\alpha} = \sum_j \Gamma_j \frac{1}{\Omega_{e_{nj}}} \sum_{C_n^j} \exp\left(\frac{E_{SP}^b\left(c_{nj}, e_n, C_n^j, \bar{e}_{nj}^M\right)}{k_B T}\right) d_j^{\alpha\mu}. \tag{3.67}$$

Remember that Λ_0^d and $\Lambda^d T^{-1} M$ represent respectively the un-correlated and the correlated part of $L_{\beta\alpha}^d$. Furthermore, in case the diffusion direction is taken to be the CPG direction ($\vec{e}_d = \vec{e}_\mu$), the expression of the transport coefficient is further simplified such that we only need to calculate three of these matrices

$$L_{\beta\alpha}^d\left(c\right) = \frac{1}{V}\left[\Lambda_0^\mu - \Lambda^\mu \tilde{T}^{-1}\left(\Lambda^\mu\right)^t\right]_{\beta\alpha}, \tag{3.68}$$

where $\tilde{T} = NT$, with N a diagonal matrix whose components are the number of effective interactions in each class.

Cluster partition function

The partition function of the system can be calculated

$$Z = \sum_{n\in V} P^0\left(c_n, e_n, \bar{e}_n\right) \tag{3.69}$$

$$= \sum_{c_n\in V} \sum_{e_n} \sum_{\bar{e}_n} \exp\left(-\frac{E\left(c_n, e_n, \bar{e}_n\right)}{k_B T}\right). \tag{3.70}$$

The difficulty in calculating the partition function exactly is of the same spirit as the problem encountered in the above equations. The number of configurations n depends mainly on the number of configurations $\bar{e}_n$ for each cluster-environment configuration, because of its relatively big size. We use the same mean-field approximation used for saddle-point energies, but this time we apply it to stable configurations

$$\sum_{\bar{e}_n} \exp\left(-\frac{E\left(c_n, e_n, \bar{e}_n\right)}{k_B T}\right) = \Omega_{\bar{e}_n} \exp\left(-\frac{E\left(c_n, e_n, \bar{e}_n^M\right)}{k_B T}\right). \tag{3.71}$$

$\Omega_{\bar{e}_n}$ is the number of ways we can arrange species on the sites of $\bar{e}_n$, and $E\left(c_n, e_n, \bar{e}_n^M\right)$ represents the energy of a cluster-environment configuration embedded in a homogeneous mean-field whose properties are still undetermined. Since e represents the set of all environment sites, it can also be written as $e = e_n \cup \bar{e}_n$, and therefore $\Omega_{\bar{e}_n} = \Omega_e / \Omega_{e_n}$. The partition function becomes a function of a mean-field energy

$$Z = \Omega_e \sum_{c_n\in V} \frac{1}{\Omega_{e_n}} \sum_{e_n} \exp\left(-\frac{E\left(c_n, e_n, \bar{e}_n^M\right)}{k_B T}\right), \tag{3.72}$$

which is then expressed as a function of a mean-field binding energy for convenience

$$Z = \frac{\Omega_e}{\kappa} \sum_{c_n\in V} \frac{1}{\Omega_{e_n}} \sum_{e_n} \exp\left(\frac{E^b\left(c_n, e_n, \bar{e}_n^M\right)}{k_B T}\right). \tag{3.73}$$

Note that κ and Ω_e get simplified when substituting the partition function (Eq. 3.73) in the transport coefficient expression (Eq. 3.62). The choice of the reference configuration and its energy do not affect the calculations, and only provides a reference with respect to which all energies (stable configuration energies and saddle-point energies) are calculated. The size of the system also does not appear explicitly and does not affect the calculations.

Correlation factors

In the following sections, we will be interested in calculating correlation factors of cluster components, therefore it is useful to quickly show its expression in the SCMF-c. Remember that the correlation factor represents the ratio of the real diffusion coefficient over the diffusion coefficient that we would obtain in case there were no correlations (see Sec. 3.3.1). In our formalism, the full transport coefficient is given by Eq. 3.68 and the uncorrelated part is given by Λ_0^μ/V. Therefore, once the three matrices are computed, the correlation factor of a species β can be calculated from

$$f_{\beta\beta}^{(\beta)} = \frac{L_{\beta\beta}^{\mu}}{\left[\Lambda_0^\mu\right]_{\beta\beta}/\left(V\right)} = 1 - \left[\frac{\Lambda^\mu \tilde{T}^{-1}\left(\Lambda^\mu\right)^t}{\Lambda_0^\mu}\right]_{\beta\beta}. \tag{3.74}$$

3.3.2 Theoretical differences between SCMF-d and SCMF-c

In SCMF-c, the three main equations are the stationnarity equation,

$$\forall c_n,\ \forall e_n,\ \forall \alpha,\ \nu^\alpha\left(c_n, e_n\right) \sum_j \Gamma_j \frac{1}{\Omega_{e_{nj}}} \sum_{C_n^j} \exp\left(\frac{E_{SP}^b\left(c_{nj}, e_n, C_n^j, \bar{e}_{nj}^M\right)}{k_B T}\right) \tag{3.75}$$

$$= \sum_j \Gamma_j \frac{1}{\Omega_{e_{nj}}} \sum_{C_n^j} \exp\left(\frac{E_{SP}^b\left(c_{nj}, e_n, C_n^j, \bar{e}_{nj}^M\right)}{k_B T}\right) \left[\nu^\alpha\left(c_{n+j}, e_{n+j}\right) - d_j^{\alpha\mu}\right], \tag{3.76}$$

the transport coefficients,

$$L_{\beta\alpha}^d\left(c\right) = \frac{\Omega_e}{2\kappa V Z} \sum_{c_n \in V} \sum_{e_n} \sum_j d_j^{\beta d} \Gamma_j \frac{1}{\Omega_{e_{nj}}} \sum_{C_n^j} \exp\left(\frac{E_{SP}^b\left(c_{nj}, e_n, C_n^j, \bar{e}_{nj}^M\right)}{k_B T}\right) \left[\nu^\alpha\left(c_n, e_n\right) - \nu^\alpha\left(c_{n+j}, e_{n+j}\right) + d_j^{\alpha\mu}\right], \tag{3.77}$$

and the partition function,

$$Z = \frac{\Omega_e}{\kappa} \sum_{c_n \in V} \frac{1}{\Omega_{e_n}} \sum_{e_n} \exp\left(\frac{E^b\left(c_n, e_n, \bar{e}_n^M\right)}{k_B T}\right). \tag{3.78}$$

Terms colored in red represent the deviation of the SCMF-c equations from those of the SCMF-d. The key differences are summarized in Table 3.1. In a dilute alloy, for any cluster configuration c_n there is no environment $e_n = \emptyset$, and there is one exterior $\bar{e}_n = \bar{e}_n^A$. Note that since there are no environments around cluster configurations, $\bar{e}_n = \bar{c}_n$, and therefore for any configuration we have $\bar{e}_n = \bar{e}_n^A = \bar{c}_n^A$. For each jump j, there are no complements or jump frequency environments, and there is one exterior of pure A atoms, so that for all j, $C_n^j = \emptyset$, $e_{nj} = \emptyset$ and

$\bar{e}_{nj} = \bar{e}^A_{nj} = \bar{c}^A_{nj}$. The number of possible configurations of $\bar{e}_{nj}$ is therefore $\Omega_{e_{nj}} = 1$. Using all this in the stationnarity equation (Eq. 3.76), it reduces as expected to its dilute form

$$\forall c_n,\ \forall \alpha,\ \nu^\alpha(c_n) \sum_j \Gamma_j \exp\left(\frac{E^b_{SP}\left(c_{nj}, \bar{c}^A_{nj}\right)}{k_B T}\right) \tag{3.79}$$

$$= \sum_j \Gamma_j \exp\left(\frac{E^b_{SP}\left(c_{nj}, \bar{c}^A_{nj}\right)}{k_B T}\right) \left[\nu^\alpha(c_{n+j}) - d^{\alpha\mu}_j\right]. \tag{3.80}$$

This is also the case for transport coefficients (Eq. 3.77)

$$L^d_{\beta\alpha}(c) = \frac{1}{2\kappa V Z} \sum_{c_n \in V} \sum_j d^{\beta d}_j \Gamma_j \exp\left(\frac{E^b_{SP}\left(c_{nj}, \bar{c}^A_{nj}\right)}{k_B T}\right) \left[\nu^\alpha(c_n) - \nu^\alpha(c_{n+j}) + d^{\alpha\mu}_j\right], \tag{3.81}$$

and for the partition function (Eq. 3.78)

$$Z = \frac{1}{\kappa} \sum_{c_n \in V} \exp\left(\frac{E^b\left(c_n, \bar{c}^A_n\right)}{k_B T}\right). \tag{3.82}$$

Note that the binding-energy which is a function of a mean-field (Eq. 3.71) can be calculated exactly in the case of a dilute alloy since the sum over $\bar{e}_n$ reduces to one element

$$\exp\left(\frac{E^b\left(c_n, e_n, \bar{e}^M_n\right)}{k_B T}\right) = \frac{1}{\Omega_{\bar{e}_n}} \sum_{\bar{e}_n} \exp\left(\frac{E^b\left(c_n, e_n, \bar{e}_n\right)}{k_B T}\right) = \exp\left(\frac{E^b\left(c_n, \bar{c}^A_n\right)}{k_B T}\right). \tag{3.83}$$

	SCMF-d	SCMF-c
Stable configuration n	cluster + cluster exterior pure A $c_n \cup \bar{c}^A_n \equiv c_n \cup e^A_n \cup \bar{e}^A_n$	cluster + environment + environment exterior pure M $c_n \cup e_n \cup \bar{e}^M_n$
Saddle-point configuration nj	jump cluster + jump cluster exterior pure A $c_{nj} \cup \bar{c}^A_{nj} \equiv$ $c_{nj} \cup e^A_n \cup C^{j,A}_n \cup \bar{e}^A_{nj}$	jump cluster + jump environment $(e_n \cup C^j_n)$ + jump environment exterior pure M $c_{nj} \cup e_n \cup C^j_n \cup \bar{e}^M_{nj}$
Effective interaction ν^α_n	function of c_n	function of c_n and e_n
Number of possible occupations of environments (e, e_n, and e_{nj})	1 1 1	Ω_e Ω_{e_n} $\Omega_{e_{nj}}$
Configuration binding energy E^b_n	$E^b\left(c_n, e^A_n, \bar{e}^A_n\right)$	$k_B T \ln\left[\frac{1}{\Omega_{\bar{e}_n}} \sum_{\bar{e}_n} \exp\left(\frac{E^b(c_n, e_n, \bar{e}_n)}{k_B T}\right)\right]$
Saddle-point binding energy E^b_{nj}	$E^b\left(c_{nj}, e^A_n, C^{j,A}_n, \bar{e}^A_{nj}\right)$	$k_B T \ln\left[\frac{1}{\Omega_{\bar{e}_{nj}}} \sum_{\bar{e}_{nj}} \exp\left(\frac{E^b\left(c_{nj}, e_n, C^j_n, \bar{e}_{nj}\right)}{k_B T}\right)\right]$

Table 3.1: Summary of the main differences between SCMF-c and SCMF-d.

3.4 Extending KineCluE to concentrated alloys

The theoretical development of SCMF-c was implemented in the KineCluE code to extend it to the computation of transport coefficients in concentrated alloys. To study dilute alloys, the code assumes a homogeneous medium around the cluster components, and to study concentrated alloys, the code creates the required local environments around user-chosen defects and assumes a homogeneous mean-field around them. The implementation of the formalism was done in a way to preserve as much of the original organigram as possible, and to include the special treatment of concentrated alloys only when needed, particularly the management of environments and the mean-field homogeneous medium. For the study of a dilute alloy, the user input, the organigram and the output remain the same as presented in Sec. 3.2.7. For the study of a concentrated alloy, additional user input is required to the original one, and the output of the code is now also concentration dependent.

In the case of concentrated alloys, the main difference is the presence of local environments with different species in them around cluster components. This directly increases the number of configurations and effective interactions, and therefore the size of the matrices that need to be calculated. Particularly, this increases the size of the $\tilde{T}$ matrix ($N_{inter} \times N_{inter}$) which needs to be inverted. It is therefore important to find the optimal balance between what to calculate once, store in memory and use several times (memory consuming but time friendly), and between what to calculate several times (memory friendly but time consuming).

The main question was to find if it is better to construct symbolic matrices, store them and then apply numerical values to them, or if it is better to directly construct the numerical matrices. As discussed in 3.2.7 when exploring the configurations, symmetry operations help reduce the size of the configuration space. In the case of cluster configurations, the number of components is usually small enough to obtain several symmetry equivalent configurations and reduce the size of the configuration space. Adding environment sites with different species occupying them reduces the number of symmetry equivalent configurations and therefore doesn't reduce by much the size of the configuration space. Reducing the number of cluster-environment configurations through symmetry operations comes mainly from symmetry equivalent cluster components positions. It is therefore more interesting to apply symmetry operations on cluster components alone first, reduce the number of cluster configurations, construct environments around symmetry unique cluster configurations, then apply symmetry operations on the reduced number of cluster-environment configurations.

In practice, we cannot enumerate all environments around cluster configurations, and we need to introduce a sampling scheme that reduces their number. The most efficient sampling is a concentration based sampling (this will be further discussed in Sec. 3.5). Ideally, we want to calculate transport coefficients as a function of concentration and we don't want to repeat the analytical calculation from zero for the same crystal structure, jump mechanism and environment structure, every time we change the concentration of species. This means that it is more efficient to construct only once the environments around symmetry unique cluster configurations and around symmetry unique jump frequencies, and, in a second step, to fill the environments with species based on a sampling scheme, to identify symmetry unique cluster-environment configurations and effective interactions, and to directly construct numerical matrices. We can no longer build the complete symbolic matrices in the analytical part of the code, and we will need to directly construct the numerical matrices. This is an added argument to fill environments in the numerical part of the code, since the size of the matrices can become large, symbolic calculations can be slow, and it can become computationally demanding to save these objects and to apply numerical values to them. enumeration of cluster-environment configurations and effective interactions has to be done in the numerical part of the code.

Based on the symmetry and sampling arguments given in the previous two paragraphs, grouping cluster-environment configurations in thermodynamically equivalent classes and kinetically equivalent classes has to be done in two separate steps and divided between the analytical and numerical parts. In the first step in the analytical part of the code, we work with cluster components alone as if they were surrounded by a homogeneous matrix, and we group them in effective interaction classes of cluster components. This is equivalent to what the code already did in the case of dilute alloys. In the second step, once the concentration is known, environments are built around representatives of these previously identified classes, symmetry operations are applied to them again, and they are split accordingly into cluster-environment classes that are thermodynamically equivalent and kinetically equivalent.

In this section we will highlight the most important additional algorithmic features and functionalities, as well as the required user input to study a concentrated alloy, in both the analytical and numerical parts of the code.

3.4.1 Analytical part

Additional user input The analytical part of the code creates environments around symmetry unique defects, jump mechanisms, cluster configurations and jump frequencies. For the creation of such environments, the necessary additional user input consists of:

- Environment radius (the maximum distance between the cluster component and the sites of the environment):
- Lattice sites that can be occupied by the environment species:
- Cluster components whose local environment is to be explored.

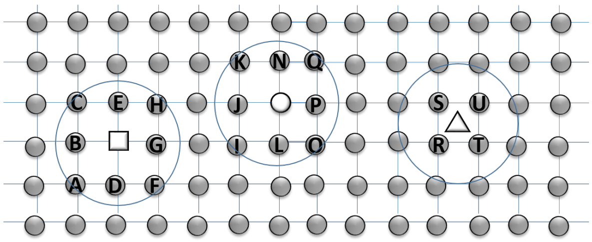

(a) Scheme of local environment (blue circles) around isolated cluster components (white square, circle and triangle). The environment radius is 1.5 lattice parameters and the environment sites are substitutional lattice sites. Each letter denotes a unique environment site (not the occupation of it).

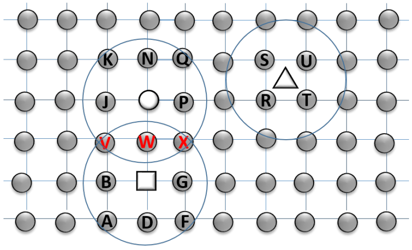

(b) Scheme of local environment around a cluster configuration n. The environment of a configuration is the combination of the environments around the isolated cluster. Environment sites that overlap (red letters) are identified and considered to be only one unique site (only one species can occupy each of these sites).

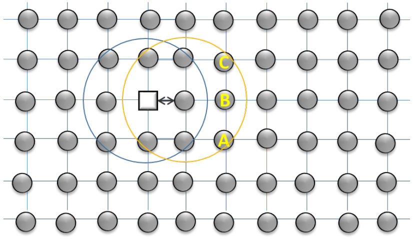

(c) Scheme of local environment around a jump mechanism j (white square exchange with a nearest neighbor atom). We define a jump mechanism environment as the collection of sites that are around the final cluster component configuration (within the yellow circle) and that do not overlap with the sites around the initial cluster component configuration (within the blue circle). This definition is useful to construct the environments around jump frequencies.

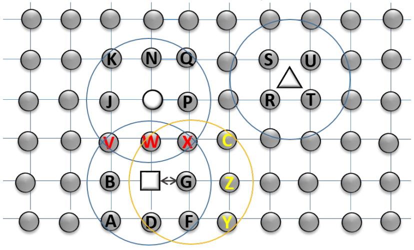

(d) Scheme of local environment around a jump frequency that links configurations n and m via a jump mechanism j. The jump frequency environment is the combination of the environment around the initial cluster components configuration (within the blue circles) and the environment around the corresponding jump mechanism (yellow letters).

Figure 3.9: Schemes of local environment construction around isolated cluster components, a cluster configuration, a jump mechanism and a jump frequency. Note that environments are constructed only around symmetry unique objects to reduce computational time and memory, and symmetry operations are used to determine environments around symmetry equivalent objects when needed.

Organigram Figure 3.10 shows the main steps of the analytical part of the code. The first part is common for studying both dilute and concentrated alloys and consists in finding all cluster configurations and jump frequencies and reducing their numbers by grouping them using symmetry operations. In the case of a concentrated alloy, the code then uses the additional input to create local environments around isolated cluster components and around jump mechanisms, and combines them to create a local environment around each symmetry unique cluster configuration and around each symmetry unique cluster jump frequency. Figure 3.9 shows how the code creates these environments and combines them while dealing with overlapping sites. In the case of a dilute alloy, the code instead computes the symbolic matrices and stores them.

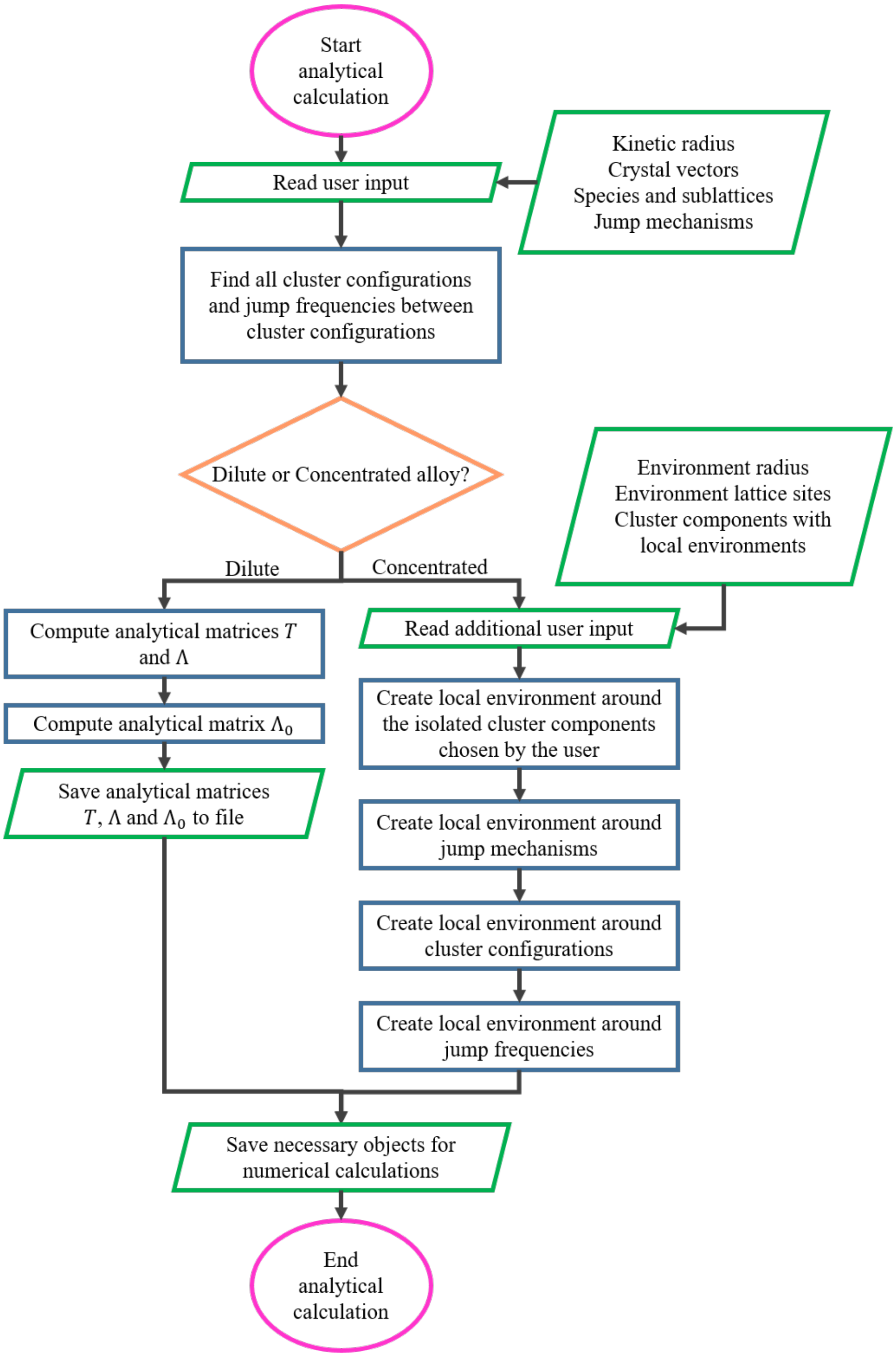

Figure 3.10: New organigram of the analytical part of KineCluE.

Output The analytical part of the code outputs and saves mainly the following objects:

- Thermodynamically unique cluster configurations;
- Thermodynamically unique cluster jump frequencies;
- Environment objects around configurations and jump frequencies.

Note that in this case, the symbolic matrices are no longer needed and the numerical matrices are calculated directly in the numerical part since the exact cluster-environment configurations and effective interactions cannot be determined until the environment species are given and the environment occupations are explored.

3.4.2 Numerical part

Additional user input The numerical part of the code consists mainly on filling the environment sites with species, grouping cluster-configurations in symmetry unique groups and effective interaction classes by the use of symmetry operations, and finally computing the numerical matrices and the transport coefficients. For this, the mandatory numerical user input should contain:

- Environment species;
- Average concentrations and local concentration fluctuations of each species.

Additionally, as will be shown in the next Section 3.5, it is recommended to use a sampling scheme to reduce the configuration space. The user has to provide information on the sampling scheme and set a maximum number of effective interaction classes, N_{inter}, to explore, which is equivalent to setting the maximum size of the $\tilde{T}$ $(N_{inter} \times N_{inter})$ and Λ $(N_{species} \times N_{inter})$ matrices. Note that the code samples the configurations on-the-fly while finding them, and the way it is implemented and how it reduces the number of configurations efficiently are discussed in more detail in the Sec. 3.5.

Organigram Figure 3.11 shows the main flowchart of the numerical part of the code which, for the case of a concentrated alloy, consists in exploring the full or sampled configuration space, finding the jump frequencies that link the configurations and directly computing the numerical matrices. Note that the code remains unchanged when studying a dilute alloy.

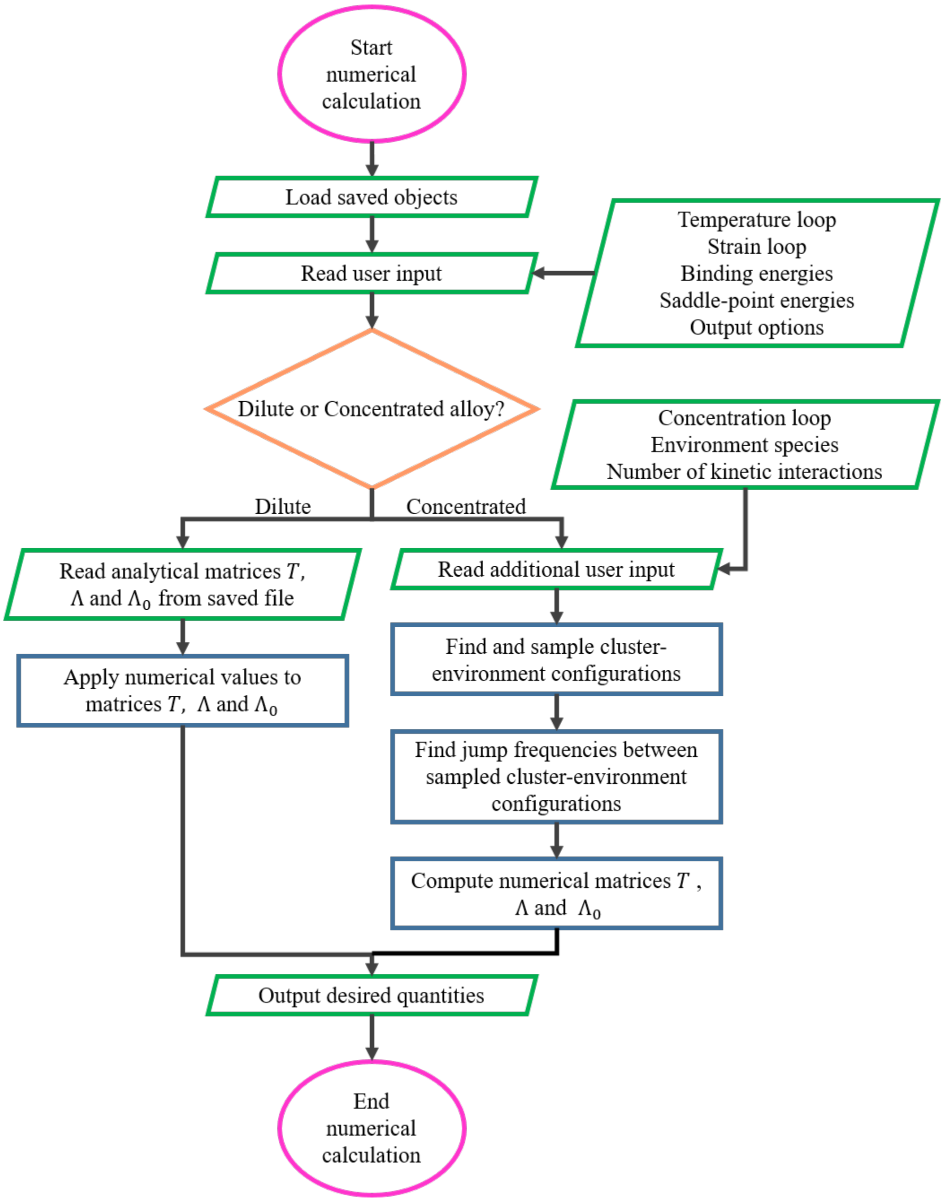

Figure 3.11: New organigram of the numerical part of KineCluE.

Output The numerical part of the code outputs the same properties as in the case of a dilute alloy except that they are concentration dependent. By default the code outputs the concentration dependent:

- Tensor of the transport coefficients along the CPG direction;
- Partition function.

Additionally the code can output the concentrated dependent:

- Mobility coefficients, exchange coefficients, drag ratios, correlation factors and uncorrelated contributions;
- Tensor of the transport coefficients in a direction normal to the CPG.

3.5 Sampling the configuration space: general sampling organigram

As has been discussed multiple times in this manuscript so far, the main difficulty when studying concentrated alloys is the number of configurations and jump frequencies that scales with the size of the system and the number of species in it. In the SCMF-d and SCMF-c theories, the number of effective interaction classes is also a limiting factor because the size of the linear system to solve increases with the number of effective interaction classes. In SCMF-c, instead of studying precisely all the possible occupations of the sites of the system, under our assumptions, the problem reduces to the study of a finite number of local environments sites surrounding the diffusing species, which reduces drastically the size of the relevant configuration space. Yet, if environments have radii up to only the 2^{nd} or 3^{rd} nearest neighbors (nn), the number of environment sites is still big enough to make the problem too large to be solved. Imagine the simplest case of diffusion of one vacancy in a simple cubic structure, and let us suppose the local environment around the vacancy has a radius of $a_0\sqrt{3}$, a_0 being the lattice parameter (Fig. 3.12). Such environment consists in considering the nearest-neighbor sites around the vacancy up to its 3^{rd} nn, which makes a total of 26 sites to fill. For binary alloys, there are more than 67 million configurations to explore, and for ternary alloys, the number of possible configurations is more than a trillion! Computational time and memory are limiting factors when it comes to enumerating such a big number of configurations while finding all jumps that connect them. Even though computational time can become a limiting factor, we will show in Sec. 3.23 that the main computational limitation of the code in its current state is its memory requirements. Memory scales with the number of cluster-environment configurations and in particular with the number of effective interactions. On one hand, the code requires enough memory to save necessary information and objects related to each configuration and effective interaction. More importantly on the other hand, as shown in Sec. 3.3.1, the sizes of the $\tilde{T}$ and Λ matrices are respectively $N_{inter} \times N_{inter}$ and $N_{spec} \times N_{inter}$, where N_{inter} is the number of effective interaction classes. Even though the $\tilde{T}$ matrix is in general sparse, and even though we use mathematical tools that are optimized for sparse matrices, like the Cholesky decomposition [145], storing and inverting an $N_{inter} \times N_{inter}$ matrix becomes a limiting factor as the size and number of species of the environment increase. It is therefore crucial to implement a sampling scheme that reduces the number of configurations and effective interaction classes. Our goal is to compute transport coefficients using only a fraction of the effective interactions, in order to reproduce the results of the full configuration space with as few configurations as possible. In order to get accurate results, the sampling scheme has to be able to identify the configurations and trajectories with the most important thermodynamic and/or kinetic weights and which have the most important effect on the calculated values of transport coefficients.

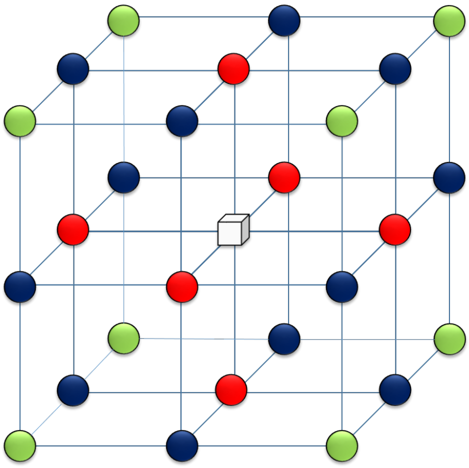

Figure 3.12: Schematic representation of a simple cubic structure in which a vacancy is surrounded by an environment with a $a_0\sqrt{3}$ radius, a_0 being the lattice parameter. The 26 environment sites represent the vacancy's nearest neighbors (nn) up to the 3^{rd} nn. The vacancy is represented by a white cube, its 1^{st} nn by red spheres, its 2^{nd} nn by blue spheres and its 3^{rd} nn by green spheres.

Remember that, in our formalism, a configuration n is defined by its cluster configuration and the local environment surrounding it, and all remaining sites constitute a homogeneous mean-field. A cluster-environment configuration in the concentrated case can be treated in the same way as a cluster configuration in the case of a dilute alloy. The first difference is that a cluster-environment is bigger than a cluster alone, with more species and sites to consider, which increases the number of configurations. The second main difference is that the homogeneous bulk around the configuration in the concentrated case is a mean-field and affects the calculations, while in the dilute case it is a reference system which has no effect on the calculations. Even though the environment is local around cluster components, and its size increases exponentially the extent of the configuration space, we still need to consider a big enough environment radius for a better representation of the real system and to properly take into account interactions and kinetic correlations. This implies that we cannot enumerate and calculate the energies of all the configurations, and we need to sample the cluster-environment configurations. Since these configurations are used to study the kinetics of the system, they need to be connected among each other, and therefore we need to insure that the sampled configurations form a connected sub-space of the original configuration space. Additionally, each time a configuration is found, all its symmetry equivalent configurations are automatically accounted for. The reason behind this is that, on one hand, symmetry equivalent configurations are thermodynamically equivalent and it is necessary to include them all to properly account for the symmetry of kinetic trajectories. On the other hand, it is not very computationally expensive to add them since some of them will also be kinetically equivalent, and most importantly we only need to explore the trajectory from one of them (the trajectories from the others being symmetrically equivalent).

We present here the general way the sampling algorithm works, and in the next section we will discuss in detail the different schemes that we tested. Here, we need to distinguish between three different lists of configurations

- **Kirep_List** contains configurations that have a non-null kinetic interaction and that were explored, i.e. all jumps from these configurations were considered. An equation of the form of Eq. 3.57 will be written for each of these configurations, and the size of the system to be solved will depend on the number of configurations in this list. The maximum size of this list is set by the user.

- **Found_List** contains configurations that were found but not necessarily explored. This includes both associated and dissociated configurations, and configurations with a null or non-null kinetic interactions.
- **To_Explore_List** contains non-dissociated configurations which were found and are waiting to be explored.

The steps of the algorithm are

1. Initialize empty **Kirep_List**;
2. Pick a random cluster configuration c_i;
3. Apply a **sampling scheme** to the environment of c_i and get one environment occupation e_i, such that $(c_i \cup e_i)$ has a non-null effective interaction;
4. Initialize **To_Explore_List** with $(c_i \cup e_i)$;
5. Initialize **Found_List** with $(c_i \cup e_i)$ and its symmetry equivalents;
6. Apply a **sampling scheme** to cluster-environment configurations in **To_Explore_List** and select one $(c_n \cup e_n)$ from the list;
7. Add (c_n, e_n) and its kinetic equivalents to **Kirep_List**;
8. Loop over jumps available from $(c_n \cup e_n)$
    (a) Find final cluster configuration c_m and identify its environment sites e_m;
    (b) Identify the species that occupy the sites that are in common between e_n and e_m;
    (c) Apply a **sampling scheme** to the environment of c_m and get one environment occupation e_m, while properly managing the sites that are in common between e_n and e_m;
    (d) Add $(c_m \cup e_m)$ and its symmetry equivalents to **Found_List**, if it was not there already;
    (e) Add $(c_m \cup e_m)$ to **To_Explore_List** if its c_m is not a dissociated cluster configuration, if its kinetic interaction is not null, and if it was not already in the list;
9. Is the number of effective interaction classes in **Kirep_List** equal to the desired number?
    (a) yes: end configuration space sampling;
    (b) no: continue to next step;
10. Remove (c_n, e_n) from **To_Explore_List**;
11. Is **To_Explore_List** empty?

   (a) yes: end configuration space sampling;
   (b) no: go back to step 6;

We need to use a sampling scheme at steps 3, 6, and 8(c). Ideally, we want the sampling scheme to give us in the end the sub-space of cluster-environment configurations that is the most representative of the full configuration space. At the same time, we want the sampling algorithm to be computationally optimized since we are applying it several times. We need it to be fast and to not waste time by computing things that will not be used later on by the algorithm. The sampling scheme at steps 3 and 8(c) needs to sample environments and fill environment sites to create new configurations, while the one at step 6 needs to select one configuration among existing cluster-environment configurations. The filling of environment sites can be done at random or based on concentration, and will be further discussed in Sec. 3.5.2.

The sampling scheme at steps 3 and 8(c) is used to find one occupation of the environment sites among all the possible occupations. If at these steps the code enumerates all possible occupations, calculates the energy of all associated cluster-environment configurations and then picks only one of them, we can see that a lot of computational time will be lost on enumerating and calculating the energies of configurations which will not be used. Ideally, we want to instead pick an occupation among all the possible ones without enumerating them.

On the other hand, for the sampling that happens at step 6, we already have a list of well identified cluster-environment configurations and we want to pick one of them. Additionally, these configurations will be part of the configuration space, even if we do not explore the possible jumps from them. This means that the energies of these configurations are needed and we will need to calculate them at some point. For this reason, in step 6, we decide to use a pseudo residence-time algorithm to pick a configuration to explore among the ones in **To_Explore_List** based on its energy.

The coupling of the pseudo residence-time algorithm which picks a configuration based on its energy with another sampling scheme that picks a configuration based on concentration, has the power to construct a sub-space in which concentration distribution and thermodynamic interactions both play a role in the selection of configurations.

3.5.1 Sampling configurations: the pseudo residence-time algorithm

This sampling step consists in selecting one configuration from a list of previously identified configurations. This list represents a subspace of the configuration space, and we use the pseudo-residence time algorithm to select one of the configurations based on thermodynamic weights. The pseudo residence-time algorithm that we implemented works in a similar way to the residence-time algorithm discussed in Sec. 1.5.2.2. In the residence-time algorithm, the probability of picking a transition is proportional to its frequency. Here, the probability of picking a configuration is proportional to its equilibrium probability. The main steps of the algorithm are:

1. Calculate the sum of all un-normalized configuration probabilities,

$$\mathfrak{Z} = \sum_{n=1}^{N_{conf}} p_n = \sum_{n=1}^{N_{conf}} \exp\left[-E_n/\left(k_B T\right)\right], \tag{3.84}$$

   where $\mathfrak{Z}$ represents the partition function of a subspace of the phase space;

2. Pick a random number between 0 and 1, $r_n \in [0, 1]$;

3. Form the list of all configurations and pick the k-th configuration whose probability satisfies

$$\sum_{n=1}^{k-1} p_n \leq r_n \mathfrak{Z} \leq \sum_{n=1}^{k} p_n. \tag{3.85}$$

The probability of picking a configuration is therefore proportional to its probability, as shown in Figure 3.13. Additionally, using this algorithm guarantees that at every time step a configuration is chosen, as opposed to using a Metropolis algorithm for example. We chose to apply this algorithm to stable configuration energies, but one can also apply it to saddle-point configuration energies. While configuration energies and saddle-point energies are linked, from a configuration n, the jump with the highest probability does not necessarily lead to the configuration with the highest probability among the accessible ones. We showed in Sec. 3.2.8 that it is in fact saddle-point energies which drive the kinetics of the system. The subspace built based on the lowest saddle-point energies will therefore contain the most probable trajectories. While a good representation of kinetic trajectories is important for a good description of the diffusion phenomena and kinetic correlations, so is a good representation of the thermodynamics of the configuration space. Here, we choose to apply the pseudo residence-time algorithm to configuration energies because it is easier to implement and less computationally demanding. It would be interesting to conduct a study to analyze the effect of this choice on the results.

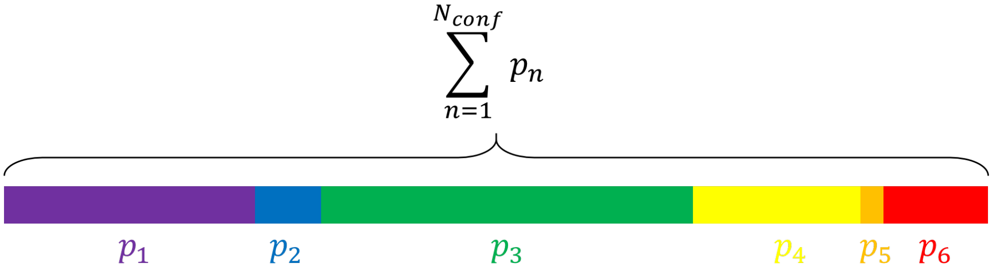

Figure 3.13: Scheme that shows how the pseudo residence-time algorithm works in the case of a number of configurations $N_{conf} = 6$. The pseudo residence-time algorithm is equivalent to stacking the configuration probabilities such that the length of a probability is proportional to its value p_n, and to randomly set a point on the line and pick the configuration on which the point falls. This guarantees that the probability of picking a configuration n is proportional to its length, which is proportional to its probability p_n. Note the similarities with the residence-time algorithm presented in Chapter 1 in Sec. 1.5.2.2, where the difference between the two is only in replacing transition probabilities with configuration probabilities.

In an Atomic Kinetic Monte Carlo (AKMC) simulation, we explore the configuration space in a linear manner by following a specific kinetic trajectory. In the sampling scheme of KineCluE, we construct little by little trajectories in all directions, and at each stage of the sampling algorithm, the construction starts from any of the previously visited points, and not necessarily from the last one. Once the configuration subspace is built, we generate all the possible trajectories within it and solve the problem of effective interactions in an exact way inside this subspace.

3.5.2 Sampling environments

As discussed in Sec. 3.5, we need a sampling scheme to fill the sites of an environment around a cluster configuration, without having to enumerate all the possible occupations of these sites. Therefore, this sampling does not depend on the energy of the cluster configuration. Nonetheless, the choice of how to fill environment sites is important because it is the cluster-environment configurations built from these environments which will constitute the basis from which the pseudo residence-time algorithm will pick the most probable configurations. The pseudo residence-time algorithm makes sense only if the configurations among which it chooses one are relevant, and these configurations are generated by the environment sampling scheme.

We suggest two environment sampling schemes. The first one is the “random” sampling which consists in filling environment sites in a completely random way. The second one is the “reservoir” sampling which consists in filling environment sites from an outside reservoir of atomic species. In the next section (Sec. 3.6), we will discuss in detail these two schemes, and highlight the advantages and disadvantages of each.

3.6 Sampling the configuration space: choice of the environment sampling scheme

In order to study the random sampling scheme and the reservoir sampling scheme, we apply both of them to the case of a mono-vacancy diffusion in a binary random alloy AB with a 2D-square structure. Since filling environment sites does not depend on their energies, we choose to study the case of a random alloy in which there are no thermodynamic interactions between atoms and in which all configurations have the same equilibrium probability. The system consists of a cluster of one vacancy, and the local environment radius around it is $2a_0$, a_0 being the lattice parameter (Figure 3.14). The environment includes 12 sites up to the 3^{nd} nearest-neighbors (nn) of the vacancy. Since the cluster contains only one vacancy, there is no use of a kinetic radius (see Sec. 3.2.6). We consider that the vacancy (V) diffuses via vacancy-environment ($V-A$ and $V-B$) exchanges, where w_A (resp. w_B) is the vacancy-A (resp. vacancy-B) exchange frequency. The vacancy jump frequency ratio w_A/w_B is taken equal to 5. The size of the configuration space of this system (4096 cluster-environment configurations and 1008 cluster-environment kinetic interaction classes) is on one hand big enough to be interesting and to include a variety of configurations, and on the other hand not too big to be able to perform a full exploration and use its results as a reference. We test the random sampling and the reservoir sampling by creating with each one of them a configuration subspace containing only a fraction of the effective interactions, and we calculate the values of the vacancy correlation factor and compare it to the value obtained when considering the full configuration space.

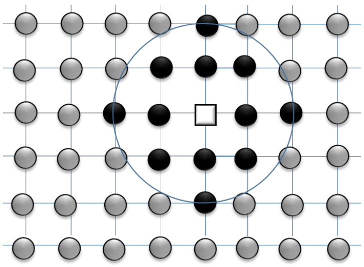

Figure 3.14: Representation of the system used to study and optimize the environment sampling schemes: a vacancy (white square) in a 2D-square random alloy with an environment radius of 2 lattice parameters. Sites belonging to the environment are colored in black, and sites outside of the environment are colored in gray. In the case of a binary alloy, each black site can be occupied by either an A or a B atom, while all gray sites are occupied by mean-field atoms.

3.6.1 Properties of interest

Before we study the sampling schemes, let us define the properties that we will be calculating and using to judge a sampling's performance.

3.6.1.1 Sampled percentage

We need to reduce the number of effective interaction classes in the system. Based on the available computational power, we can usually know the maximum size of the linear system that can be solved and therefore the biggest number of effective interactions that can be considered (in our case it was around 50000 for a calculation on a personal laptop). A sampling's accuracy will depend on the number of sampled interactions, but more importantly on the percentage of interactions that are sampled. A sampled space of 500 effective interaction classes out of 600 is more representative of the full configuration space than a sample of 500 interactions out of 6000. We define η as the percentage of sampled effective interaction classes, such that

$$\eta = \frac{N_{inter}^{scs}}{N_{inter}^{fcs}} \times 100\ [\%]\,, \tag{3.86}$$

where N_{inter}^{scs} and N_{inter}^{fcs} represent the number of effective interaction classes in the sampled configuration space (scs) and the full configuration space (fcs) respectively. Note that, practically, we cannot always know the value of N_{inter}^{fcs}, as calculating it requires us to explore the full configuration space and to find CPG symmetry equivalent configurations in order to group them in effective interaction classes. What we can know is the total number of possible configurations, which requires us to explore cluster configurations only (not cluster-environment configurations) and can be directly calculated from the number of environment sites in each cluster configuration (which depends on the geometry of the configuration) and the number of components in the system. The total number of configurations in the system is higher than the number of effective interaction classes, but it can give us an order of magnitude. In all cases, we know that in realistic applications, the value of η will be much lower than 1%.

3.6.1.2 Relative error

Ideally, we want the properties (transport coefficients, correlation factors, etc...) calculated using a sampled configuration space to be as close as possible to the values we would calculate if we were to consider the full configuration space. The accuracy of a property ϕ calculated using a sampled system is therefore given by the relative error

$$\zeta\left(\phi\right)=\frac{\left|\phi^{scs}-\phi^{fcs}\right|}{\phi^{fcs}}, \tag{3.87}$$

where ϕ^{scs} and ϕ^{fcs} are respectively the values of ϕ calculated using a sampled configuration space (scs) and the full configuration space (fcs). In order to calculate this relative error, we need to work with systems in which the number of effective interaction classes is small enough for a full configuration space exploration to be feasible.

3.6.1.3 Distribution functions

Local concentration distribution In an alloy, the local concentration can differ from the average concentration in the alloy. The local concentration distribution represents the number of configurations at different local concentrations. We define the normalized local concentration distribution of A as the ratio of the number of sampled configurations at a concentration X_A with respect to the total number of configurations at the same concentration X_A that can be found in the full configuration space

$$C_d\left(X_A\right)=\frac{N^{scs}\left(X_A\right)}{N^{fcs}\left(X_A\right)}, \tag{3.88}$$

where $N^{scs}\left(X_A\right)$ and $N^{fcs}\left(X_A\right)$ represent respectively the number of configurations in the sampled configuration space in which the concentration of A equals X_A, and the number of configurations in the full configuration space in which the concentration of A equals X_A. This allows us to know how many of the available configurations at a given concentration the code managed to find. A ratio $C_d\left(X_A\right)$ of 1 means that the sample includes all the possible configurations at X_A, and a ratio of 0 means that the sample does not include any configurations at X_A. Ideally, if the targeted average alloy concentration of A is say 0.1, we want most of the configurations that have a local concentration of A of 0.1 to be found and included in the sample, and most of the configurations with a concentration far from 0.1 to be less included because they have a lower thermodynamic weight and therefore will probably not affect much the numerical result. Therefore, we want the distribution $C_d^A\left(X_A\right)$ to be centered around the average A concentration with a value close to 1.

Probability distribution It is important to some extent that the local concentration be centered around the average concentration, but it is much more important that the sampled probability distribution reproduces the full configuration space probability distribution. It is physically less accurate to have the local concentration sharply centered around the average concentration while the proportion of configuration probabilities is not maintained. Since diffusion is based on the probability of being in a certain configuration and transitioning into another, if the probabilities of the configurations remain the same, the diffusion problem that we are solving also remains the same. In other words, even if the un-normalized probability of a configuration varies because of the sampling, it is important to keep the normalized probability distribution as close as possible to the expected one. We denote the probability distribution of configurations in which the concentration of A equals X_A as

$$P\left(X_A\right)=\frac{1}{Z}\sum_{X=X_A}\exp\left(-\frac{E\left(X\right)}{k_BT}\right), \tag{3.89}$$

where the sum runs over all configurations with a concentration X_A, $E\left(X\right)$ is the generalized energy of a configuration which contains its internal energy and the chemical potentials, and Z is the partition function of the system in the same thermodynamic ensemble. Because of the finite size of the environments, local concentration values are discrete. Remember that here, we are working with a vacancy diffusion in a random alloy. This implies that there is only one cluster configuration and that the number of environment sites is the same in all cluster-environment configurations (here equal to 12, see Fig. 3.14). As a consequence, configurations in which the concentration equals X_A will have the same number of A atoms. In a random alloy, the energy of a configuration depends only on the number of elements of each species (their chemical potential) and not on the way they are arranged on the sites because thermodynamic interactions are null. All configurations in which the number of A equals N_A (i.e. the concentration of A equals X_A) will therefore have the same energy, which allows us to re-write Eq. 3.89 as

$$P\left(X_A\right)=\frac{1}{Z}g_{X_A}\exp\left(-\frac{E\left(X_A\right)}{k_BT}\right), \tag{3.90}$$

and

$$Z=\sum_{X_A}g_{X_A}\exp\left(-\frac{E\left(X_A\right)}{k_BT}\right) \tag{3.91}$$

where $g_{X_A}$is the degeneracy number of a configuration in which the concentration of A is X_A. In the sampled system $g_{X_A}=N^{scs}\left(X_A\right)$, and in the full configuration space $g_{X_A}=N^{fcs}\left(X_A\right)$.

In the next paragraph, we sample 50% of the configuration space using separately the random sampling and the reservoir sampling, and we calculate the vacancy correlation factor and the relative error with respect to the one calculated using the full configuration space. At each concentration, we run the code with the corresponding sampling method 20 separate times and average the result. We show in each case the correlation factor calculated from the separate runs as well as its average value, the relative error, the local concentration distribution and the probability distribution of the sampled configurations.

3.6.2 Random sampling scheme

3.6.2.1 Basics of the random sampling

In a random sampling scheme, the probability that a species α occupies any site i is independent of the species and site; $\forall i$, $\forall\alpha$, $p=1/N_{spec}$, N_{spec} being the number of species. The probability to fill an environment e of N_{sites} sites with N_α, N_β, ... atoms of species α, β, ... depends only on the number of species and the number of sites in the environment, $\sum_{i,\alpha}\left(p\right)^{n_i^\alpha}=\left(1/N_{spec}\right)^{N_{sites}}$. The number of species is fixed in the system, while the number of environment sites can differ from one environment to another based on its geometry. In our example, all environments have the same number of sites $N_{sites} = 12$, and therefore all environments have the same probability to be obtained using a random filling, $p = (1/2)^{12}$, independently on their local concentrations. This sampling is equivalent to having an equiatomic alloy and filling sites with atomic species based on their average concentration.

3.6.2.2 Local concentration and probability distributions

The left part of Fig. 3.15 shows the local concentration distribution of the sampled system averaged over the 20 separate runs of the code. The distribution is almost symmetric and centered around 0.5. Configurations with concentrations ranging between 3/12 and 9/12 are chosen with the same ratio (around 0.9) while configurations with the largest deviation from 0.5 (pure A and pure B configurations) are chosen with a smaller ratio of around 0.3. The concentration distribution is therefore not constant and the sampled configurations are not completely random, contrary to what we would expect. This is in part due to effective interactions and in part due to symmetry operations. Pure A and pure B configurations have a null effective interaction, and therefore, regardless on whether or not a pure configuration is found, the code still needs to find N^{scs}_{inter} effective interaction classes which have concentrations between 1/12 and 11/12 inclusive. Therefore, our sampling procedure will favor configurations with non-null effective interactions, which here are configurations with local concentrations far from 0/12 and 12/12. Symmetry equivalent configurations additionally contribute to a non-constant concentration distribution. When a configuration is found, all its symmetry equivalents are automatically added to the sampled configuration space (see steps 5 and 7(d) of the general sampling algorithm in Sec. 3.5). For example, there are 12 configurations with an $X_A = 1/12$, but only 3 symmetry unique ones (configurations in which the distance between the A atom and the vacancy are equal are equivalent by symmetry). It is therefore sufficient to find 3 symmetry unique configurations in order to add all 12 of them to the sampled configuration space. Configurations with a higher number of symmetry equivalents will therefore be faster to find than configurations with no equivalents. All of this biases the concentration distribution by favoring configurations at concentrations that can give rise to non-null effective interactions and configurations with a higher number of symmetry equivalent configurations.

The probability distribution of the sampled configurations (right part of Fig. 3.15) is almost exact when $X_A = 0.5$ and less accurate as the concentration deviates from 0.5. The probability distribution slightly deviates from the exact one at a local concentration of $3/12 = 0.25$ and of $9/12 = 0.75$, but the main deviations occur when the A alloy concentration is 0.1 and 0.9, where the peak values are overestimated by around 65% and 92% respectively. This confirms that the random sampling produces a sampled configuration space representative of an equiatomic alloy.

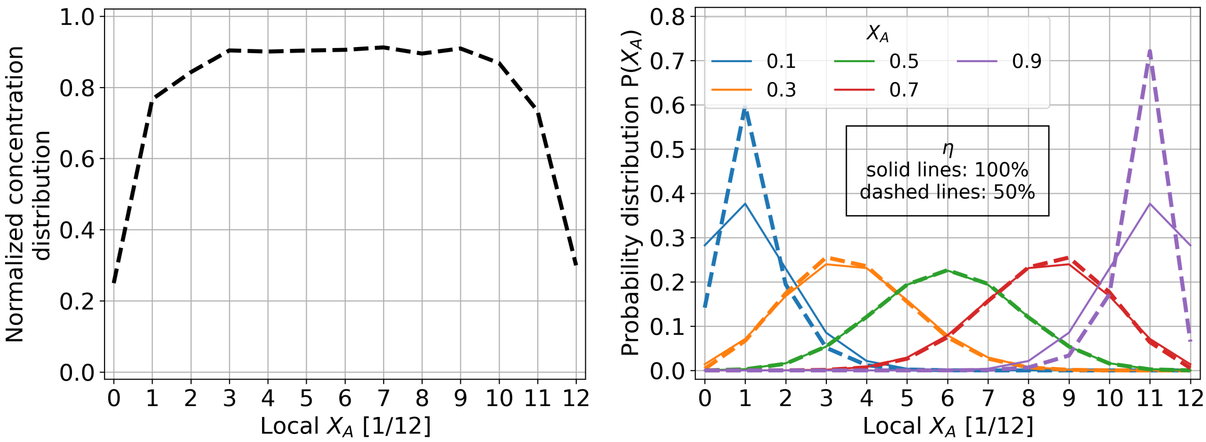

Figure 3.15: Normalized concentration distribution (left) and average probability distribution (right) in the case of a random sampling. These values are averaged over 20 separate runs of the code. Here, the x-axis represents the local concentration of A in the different configurations. Note that the random sampling is independent from the average alloy concentration. The number of environment sites in all configurations is 12, and local concentrations are equal to $x/12$, where x is an integer between 0 and 12.

3.6.2.3 Accuracy of the vacancy correlation factor

Figure 3.16 shows the vacancy correlation factor calculated after sampling half the effective interaction classes with a random sampling, along with the relative error with respect to the reference value. The correlation factor is well reproduced for concentrations ranging between 0.3 and 0.7, where the relative error ranges from 0.90% to 5.09%. The values obtained from the different runs of the code are centered when the concentration is 0.5 and more scattered the further away the concentration deviates from 0.5. Especially at a concentration of 0.1, the relative error varies from around 0% to 78%, making it indispensable to average over several runs to obtain a reliable result. However, even when averaging over 20 different samples, the relative error remains above 20%. Also, there is nothing which guarantees that averaging the results over multiple runs would converge towards the expected result. This confirms that the accuracy of a sampling depends on how well the probability distribution is reproduced.

It is interesting to note that at $X_A = 0.9$ the calculated values from the different runs are less scattered than at $X_A = 0.1$, and that on average the correlation factor calculated at $X_A = 0.9$ is more accurate than the one calculated at $X_A = 0.1$, even though the probability distribution of the former is less accurate. This shows that the probability distribution is not the only factor which affects the accuracy of a sampled correlation factor. The same is observed between $X_A = 0.7$ and $X_A = 0.3$, even though their probability distribution functions are calculated as accurately. The asymmetry of the jump frequency ratio creates an asymmetry of the correlation factor, and it seems that the random sampling is more accurate when the system is less correlated (higher values of f_V). The more correlated a system is, the more important the kinetic weight of trajectories is, and sampling the configuration space based on only the thermodynamic weights of configurations becomes less accurate.

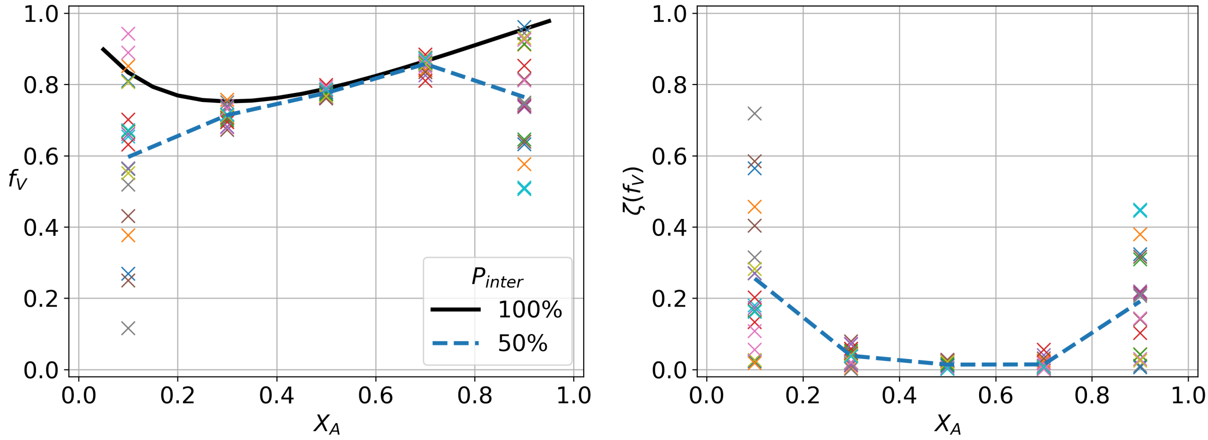

Figure 3.16: Vacancy correlation factor f_V (left) and absolute value of the relative error $\zeta\left(f_V\right)$ (right) as a function of concentration. The solid line represents the reference value of the correlation factor calculated when the full configuration space is explored. Symbols with different colors correspond to 20 separate runs of the code when 50% of the effective interactions are sampled using the random sampling, and the dashed line represents the average values. Note that the jump frequency ratio is $w_A/w_B = 5$.

3.6.2.4 Conclusion on the random sampling

The random sampling has the advantage and disadvantage of being concentration independent. This makes it time efficient because it can be performed only once and the same sampled configurations can be used at different concentrations of the alloy. However, this subspace is only representative of an equiatomic alloy and is not accurate in the general case of a concentrated alloy. This is why we implemented instead a concentration dependent sampling. This reservoir sampling will be the topic of the next paragraph.

3.6.3 Reservoir sampling scheme

3.6.3.1 Defining the reservoir

In the reservoir sampling, we consider the reservoir to be a box of a certain size filled with species such that the concentration of each α species in the box is equal to its average alloy concentration. In practice, the concentration of a species α in the reservoir, X_α^{res}, is not necessarily exactly equal to the desired composition X_α due to the finite size of the box. The exact concentration of α in the reservoir is then

$$X_\alpha^{res} = \frac{N_{res}^\alpha}{N_{res}} = \frac{f_r\left(N_{res}X_\alpha\right)}{\sum_\alpha f_r\left(N_{res}X_\alpha\right)}, \tag{3.92}$$

where N_{res}^α and N_{res} are respectively the number of atoms of species α in the reservoir and the total number of reservoir sites. $f_r\left(x\right)$ is a function which rounds a real number x to an integer, to make sure there is not a fractional number of atoms. When $N_{res}X_\alpha$ is not an integer, the reservoir composition will be close to, but not exactly equal to, the average alloy composition. Note that here, $f_r\left(x\right)$ is a general rounding function that can be chosen to round up to the closest integer, round down to the closest integer, round to the nearest integer where halves get rounded either up or down, etc... In our code, we choose it to be a ceiling function,

$f_r(x) = \min\{n \in \mathbb{Z} | n \geq x\}$, such that it rounds up a real number x to the nearest integer greater or equal to x.

From this reservoir, we pick species to fill the environment sites one after the other. Some questions can be raised regarding the way we pick and fill sites with species, and regarding when to reset the reservoir. The choice of the size of the reservoir and the evolution of the reservoir's size and concentrations (which are linked) with the filling are not obvious as each choice implies a different approximation regarding the concentration distribution of environments.

3.6.3.2 Global versus local reservoir

One possibility is to have one global reservoir from which we fill all environment sites of the system, while another possibility is to have different local reservoirs which fill different sets of environment sites. The global reservoir affects the concentration of all environment sites of the system, while the local reservoirs affect directly the concentration in a specific set of environment sites, which indirectly affects the global concentration of all environment sites. Both approaches can guarantee a global concentration close or equal to the average concentration, but the latter approach has the additional advantage of controlling local compositions and their fluctuations from the average composition. For this reason, we chose to use local reservoirs. This required us to further identify the set of environment sites to fill with the same reservoir. This step is important because it is the composition of this set of sites which can be controlled. Figure 3.17 shows three different examples of what a set of environment sites can be:

1. environment sites around one cluster configuration; e_n.
2. environment sites around one jump frequency configuration; $e_n \cup C_n^j$, for a jump j available from $c_n \cup e_n$.
3. environment sites around one cluster configuration and all its jump complements; $e_n \cup (\cup_j C_n^j)$. We call this set of sites the total jump environment of a configuration n.

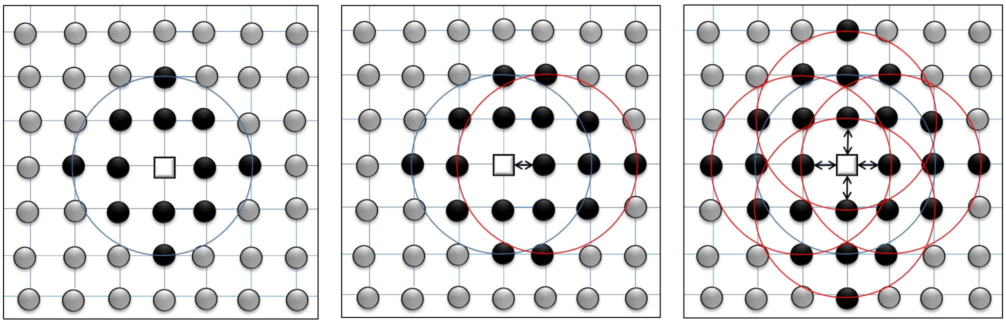

Figure 3.17: Three examples of sets of environment sites around a vacancy (white square) that we can choose to fill with the same reservoir. Left: environment sites around one cluster configuration; e_n. Middle: environment sites around one jump frequency configuration; $e_n \cup C_n^j$, for a jump j available from $c_n \cup e_n$. Right: environment sites around one cluster configuration and all its jump complements; $e_n \cup (\cup_j C_n^j)$. Sites belonging to each set are colored in black, the blue circle represents the environment radius around the cluster configuration c_n, and the red circle(s) represent(s) the environment radius around the vacancy's position in the accessible configuration(s).

We choose the third option because we think that it allows to have more concentration fluctuations at the level of the cluster configurations but to keep at the same time a bigger local environment around the diffusing cluster at the average concentration. This way, the total jump environment is at the average composition, and the environment around a final cluster configuration will depend on the environment around the initial cluster environment. For example, in an equiatomic binary alloy AB, if the environment around a cluster configuration is mainly composed of A atoms, we expect its surrounding to have more B atoms than A to compensate, which implies that the environment around the accessible configurations is mainly composed of B atoms instead of being at equiatomic composition. In this case, a vacancy surrounded by a pure A environment will transition to configurations that have more B atoms than A, and vice-versa. With this option, even when using the smallest possible reservoir, cluster environment compositions can fluctuate while keeping the local cluster and the total jump environment at the average composition. Note that these fluctuations exist in an alloy and should be taken into account as there is nothing that requires us to have an average composition around the cluster components. In addition, our aim from sampling the configuration space is to find the most important trajectories which are not necessarily exclusively built from configurations having a nominal composition.

In theory, the union of all complement sites includes overlapping sites just once. In practice, it is not straightforward to deal with overlapping sites and their occupancy. The way our code works, when looping over jumps separately (see step 7 in the flowchart presented in Sec. 3.5), overlapping sites are not easy to identify and are therefore treated separately. This means that, for a jump j_1, all its complement sites, $C_n^{j_1}$, are filled independently of the occupation of the other complements corresponding to the other jumps, $\cup_{j \neq j_1} C_n^j$. This implies that overlapping sites are filled as many times as they overlap, and the same site can be filled by different species. This introduces a small error to our target set of sites, and the set that we are actually treating is in fact $e_n \cup (\cup_j C_n^j)$. In the general case, the number of overlapping sites is expected to be small compared to the total number of sites, and sites usually overlap between a few number of accessible configurations. This is especially true when the transition does not involve all cluster components because this usually increases the number of sites in e_n, and hence the total number of sites that are not overlapping. Figure 3.18 shows how geometry affects the number of overlapping sites. For example, in the case of a vacancy with an environment of $2a_0$ radius around it, there are 8 out of 24 sites that overlap between two final configurations, while in the case of an environment radius of $1.5a_0$, there would be no overlap among the 20 sites. While the number of overlapping sites is not always negligible, we think that this will not introduce additional errors to our calculations. Not treating overlapping sites exhaustively can create a slight bias in the dynamics of the system but it will not create an additional source of errors since there are already other aspects of our model and sampling procedure which are expected to have a similar effect.

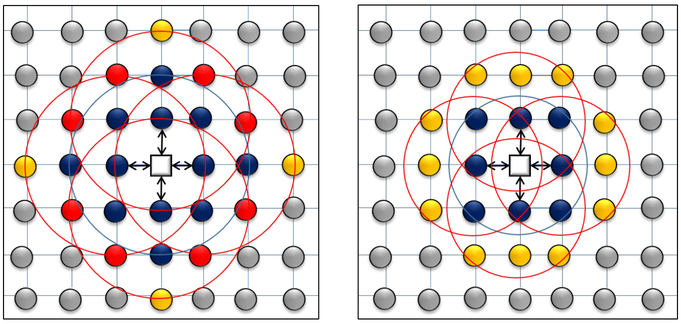

Figure 3.18: Representation of the set of environment sites around one cluster configuration and all its jump complements; $e_n \cup (\cup C_n^j)$. The blue circle represents the environment radius ($EnRa$) around the initial vacancy position, and the red circles represent the environment radius around the final vacancy position in the accessible configurations. The left figure represents the case of $EnRa = 2a_0$ and the right figure represents the case of $EnRa = 1.5a_0$, a_0 being the lattice parameter. Sites belonging to the environment of the initial cluster configuration are colored in blue. Sites that belong exclusively to final cluster configurations and that overlap are colored in red, while those that do not overlap are colored in orange.

3.6.3.3 Reservoir size and concentration

We can impose a varying concentration of species in the reservoir by drawing species from it without replacement. Then the probability to draw a species α from the reservoir after k draws depends on the previous $k-1$ draws. This probability can be calculated as

$$P_{i_k}^{\alpha} = \frac{N_{res_k}^{\alpha}}{N_{res} - (k-1)}, \tag{3.93}$$

where $N_{res_k}^{\alpha}$ is the number of α atoms in the reservoir after $k-1$ draws from it. During the first draw, the probability to pick a species α is equal to its average concentration in the reservoir, and after k draws this probability increases or decreases based on how many times it has been drawn with respect to the other species. In case the size of the reservoir is exactly equal to the number of environment sites to be filled with it, this constrains the concentration of α in the set of environment sites to be exactly equal to its average concentration X_{res}^{α}. The bigger the size of the reservoir with respect to the sites it is filling, the more the local concentration may fluctuate from its average value. In the case of an infinitely big reservoir with respect to the environment sites ($N_{res} \gg (k-1)$ and $N_{res_k}^{\alpha} \approx N_{res}^{\alpha}$), this type of filling becomes equivalent to drawing species with replacement (i.e. keeping the reservoir always at the nominal concentration),

$$P_{i_k}^{\alpha} \approx \frac{N_{res}^{\alpha}}{N_{res}} = X_{\alpha}^{res}. \tag{3.94}$$

In this case, the probability to draw an atom of species α from the reservoir after k draws depends only on its initial reservoir concentration X_{α}^{res}. In all cases, it is the ratio between the size of the reservoir N_{res}, and the size of the set of environments to fill around a configuration n, $N_{e_n \cup \left(\cup_j C_n^j\right)}$, which affects the probabilities of picking species and the local concentrations. We define the reservoir size ratio independently of the size of the jump environment around n, such that

$$\forall n,\ R_{res} = \frac{N_{res}}{N_{e_n \cup \left(\cup_j C_n^j\right)}}. \tag{3.95}$$

In the following, we will analyze the local concentration distribution, the probability distribution and the vacancy correlation factor obtained when sampling using the reservoir sampling with $R_{res} = 2$ and $R_{res} = \infty$, i.e. using respectively Eq. 3.93 and Eq. 3.94 for the filling probabilities.

3.6.3.4 Local concentration and probability distributions

The local concentration distribution and probability distribution are shown in Fig. 3.19. For both $R_{res} = 2$ and $R_{res} = \infty$, the concentration distribution is centered around the average concentration, and its maximum value is found at the local concentration closest to the average one for all concentrations. The probability distribution is almost exactly well reproduced for average concentrations of 0.1 and 0.9, and it is slightly overestimated for other concentrations. Small differences can be seen between the two reservoir size ratios. When $R_{res} = \infty$, the concentration distribution peaks are wider than when $R_{res} = 2$, which is due to larger fluctuations of the local concentration. Concentration distribution peaks have the same value for both size factors except when the alloy's A composition is 0.5. This is due to the large number of configurations with 6 A atoms and 6 B atoms compared to the other compositions (binomial law). At the other compositions, the number of configurations with a local composition close to the average one is small enough so that all of them are found regardless of the reservoir's size. As a consequence ,when $R_{res} = 2$, the probability distribution is slightly overestimated at $X_A = 0.5$. Note that, at this concentration, the reservoir sampling with $R_{res} = \infty$ becomes equivalent to the random sampling, which produces a sampled configuration space of an equiatomic alloy with high accuracy.

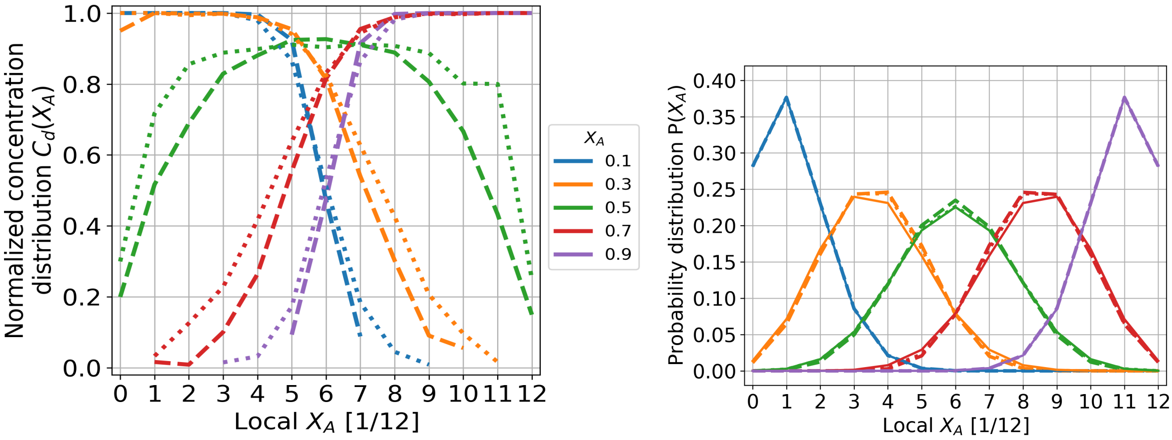

Figure 3.19: Normalized concentration distribution (left) and average probability distribution (right) in the case of a reservoir sampling of 50% of the effective interaction classes, with $R_{res} = 2$ (dashed lines) and $R_{res} = \infty$ (dotted lines), as compared to the reference values of the full configuration space (solid lines). These values are averaged over 20 separate runs of the code. Here, the x-axis represents the local concentration of A in the different configurations.

3.6.3.5 Accuracy of the vacancy correlation factor

Figure 3.20 shows that the vacancy correlation factor calculated using a reservoir sampling is in very good agreement with the reference value at all concentrations and regardless of the reservoir size ratio. In both cases, the average relative error is of 1.4%, with its highest value being at $X_A = 0.3$ and its lowest one at $X_A = 0.7$, which is due the asymmetry of the jump frequency ratio (discussed in Sec. 3.6.2). The values of the correlation factor calculated from separate runs are centered around the average value with very low scattering. When the average concentration of A is 0.1 and 0.9, there is a negligible scattering of the data and the correlation factor is very well reproduced. This is because at these compositions, the sampling scheme finds all configurations with a local composition equal to the average one and the probability distribution is very well reproduced.

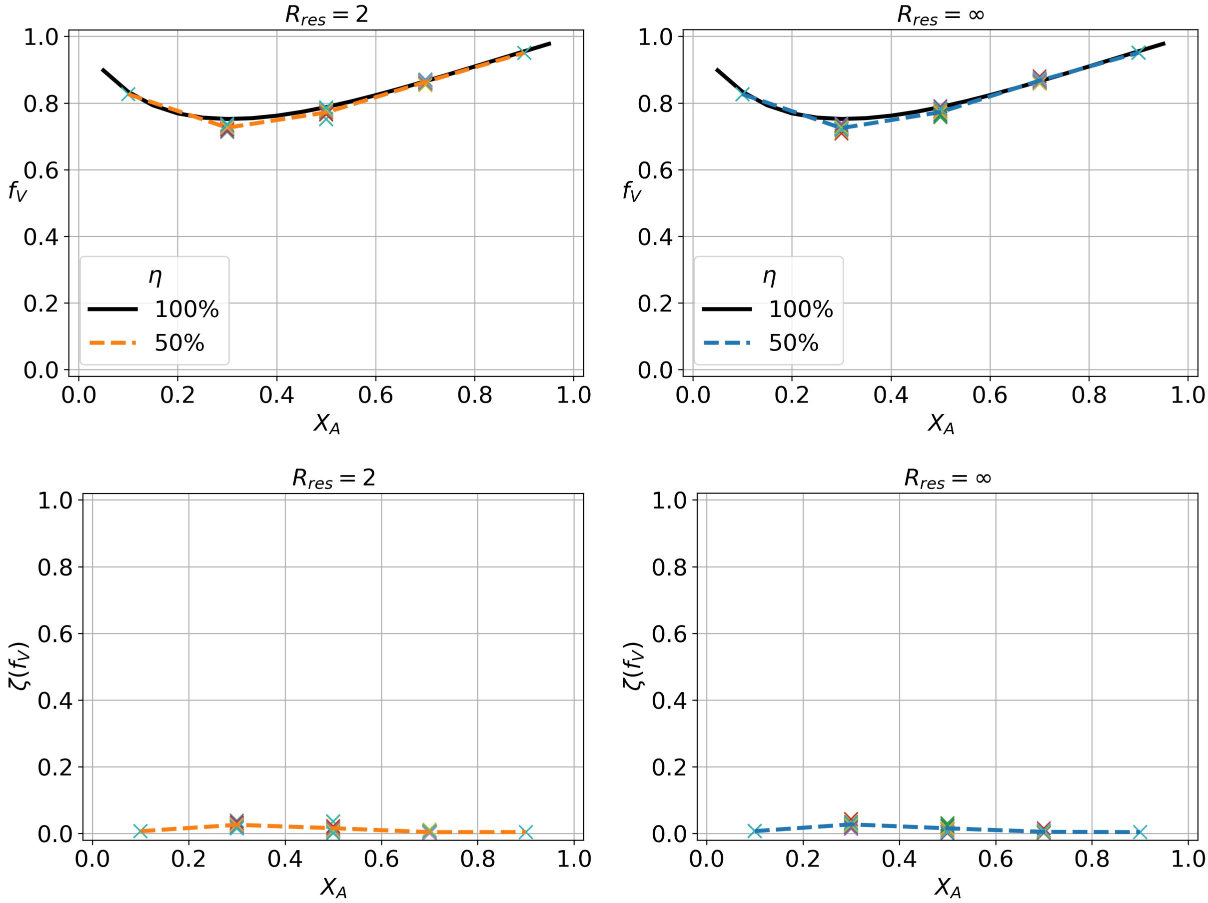

Figure 3.20: Vacancy correlation factor f_V (top) and absolute value of the relative error $\zeta(f_V)$ (bottom) as a function of concentration. The solid line represents the reference value of the correlation factor calculated when the full configuration space is explored. Symbols with different colors correspond to 20 separate runs of the code when 50% of the effective interaction classes are sampled using the reservoir sampling with $R_{res} = 2$ (left) and $R_{res} = \infty$ (right). Dashed lines represent the average values. Note that the jump frequency ratio is $w_A/w_B = 5$.

In order to study multicomponent alloys beyond the binary limit, and to study clusters containing several types of defects, the configuration space will be too large and will require us to sample very low percentages of it. We complete this study by further decreasing the size of the sample, in order to study the accuracy of the sampling scheme in more realistic conditions. Figure 3.21 shows the accuracy of the reservoir sampling with a size factor of 2 for sampled percentages ranging between 5 and 50%. For $\eta = 5\%$, the correlation factor is well reproduced with a relative error below 0.13 at all concentrations. Regardless of the sampled percentage, the correlation factor is always underestimated, and the relative error is the highest at the concentration corresponding to the most correlated system. As discussed in Sec. 3.6.2, this can be due to the fact that some trajectories with high kinetic weight are not included when sampling configurations based on their thermodynamic weights. A sampling based on saddle-point energies instead of stable configuration energies might be more accurate in high correlated systems.

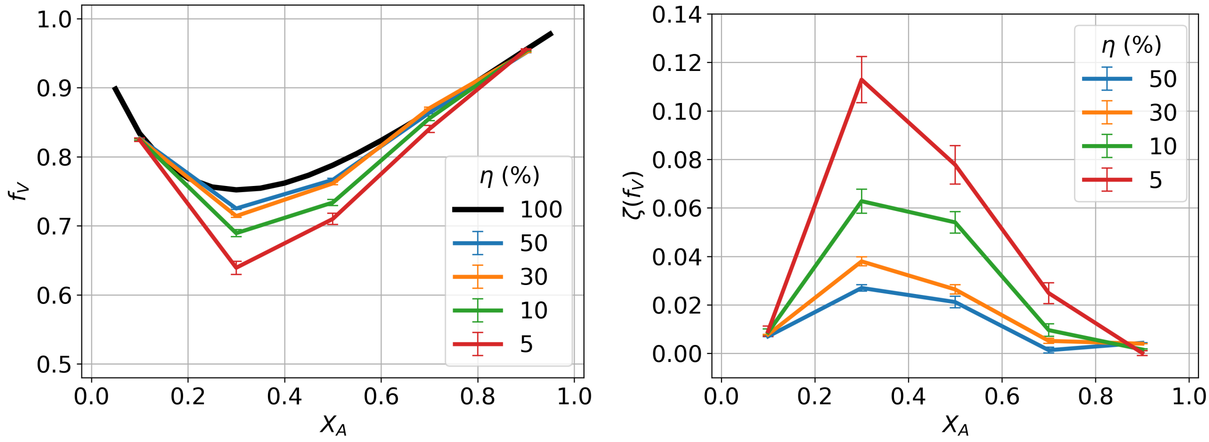

Figure 3.21: Vacancy correlation factor f_V (left) and absolute value of the relative error $\zeta(f_V)$ (right) as a function of concentration. The solid line represents the reference value of the correlation factor calculated when the full configuration space is explored. Lines with different colors correspond to different percentages of the sampled effective interaction classes. These values were obtained by averaging the result over 20 separate runs of the code, and using the reservoir sampling with $R_{res} = 2$. Note that the jump frequency ratio is $w_A/w_B = 5$.

3.6.3.6 Conclusion on the reservoir sampling

With the reservoir sampling with two different reservoir size ratios, we were able to reproduce with high accuracy the vacancy correlation factor at all concentrations. This is a direct consequence of the good agreement between the probability distributions of the sampled configuration space and the full configuration space.

The choice of the set of environment sites to fill with the same reservoir, the evolution of the size of the reservoir and whether we draw species from it with or without replacement all affect the sampled configuration space's concentration and probability distributions, and eventually the accuracy of the calculated transport coefficients. These choices are important because they affect the way we choose to impose a local equilibrium condition on the system. Drawing species from a reservoir with replacement or in the case of an infinitely big reservoir, all environment sites of the system will be filled based on the average composition of species, which is equivalent to imposing a concentration equilibrium condition per site of the system. In case we draw species from the reservoir without replacement the equilibrium is imposed on the set of environment sites that are being filled with the reservoir before we reset it or change it. We can also think of a more sophisticated approach in which trajectories instead of configuration or total jump environments follow the average composition. To keep things simple for the sake of efficiency, we chose to use a local reservoir sampling to fill the sites of the total jump environment around cluster components. We found that this was enough in the case of a random alloy to calculate vacancy correlation factors with high accuracy at all concentrations. The size of the reservoir affects the local concentrations of the sampled configurations, such that the bigger the size of the reservoir the more composition fluctuations are allowed. We expect the effect of the reservoir size to become more apparent when a lower percentage of the configuration space is sampled, because when fewer configurations are selected, the concentration distribution sampled by a small reservoir will be more centered around the average composition. This can be verified in a future study. We found in the several examples that we tested that a reservoir size ratio between 2 and 5 represents a good compromise between not allowing any local fluctuations and allowing some of them.

3.7 Energy model

We cannot calculate absolute values of energies, and we always need a reference with respect to which we calculate all energies. This is why we introduced binding energies in Sec. 3.2.8 and Sec. 3.3 by multiplying all absolute energies by the factor κ (Eq. 3.42). We did not, however, explicit the choice of the reference configuration, nor did we provide a way to calculate binding energies that are a function of mean-field atoms. We only know that we cannot calculate these energies exactly in the case of a concentrated alloy, because it involves an infinite number of configurations (Eq. 3.53). In this section, we will provide an approximate method of calculating mean-field related energies.

3.7.1 Binding energies

We choose our reference configuration to be one in which cluster components are isolated from each other, and surrounded by a buffer environment that we choose as a pure A environment, and which in turn is embedded in a mean-field. Let $(x, e_x, \bar{e}_x)$ represent a configuration of one isolated cluster component x, surrounded by a local environment e_x, which is embedded in $\bar{e}_x$. Let $(X, e_X, \bar{e}_X)$ represent a configuration in which all cluster components are isolated ($X = \cup_x x$), each surrounded by an environment e_x such that e_X is the union of all these environments, $e_X = \cup_x e_x$, and in which e_X is surrounded by $\bar{e}_X = \overline{\cup_x e_x}$. The reference configuration is therefore represented by $\left(X, e_X^A, \bar{e}_X^M\right)$, and

$$\kappa = \exp\left(-\frac{E\left(X, e_X^A, \bar{e}_X^M\right)}{k_B T}\right). \tag{3.96}$$

A mean-field binding energy of the form $E^b\left(c_n, e_n, \bar{e}_n^M\right)$, is therefore calculated as

$$E^b\left(c_n, e_n, \bar{e}_n^M\right) = E\left(X, e_X^A, \bar{e}_X^M\right) - E\left(c_n, e_n, \bar{e}_n^M\right). \tag{3.97}$$

Note that here c_n and e_n can represent any configuration of the cluster and any environment around it, including a saddle-point cluster configuration (c_{nj}) and a jump frequency environment (e_{nj}). We write the binding energy of (c_n, e_n) in a mean-field as a function of the binding energy of (c_n, e_n) in a homogeneous A matrix

$$E^b\left(c_n, e_n, \bar{e}_n^M\right) = E^b\left(c_n, e_n, \bar{e}_n^A\right) - \left[E\left(X, e_X^A, \bar{e}_X^A\right) - E\left(c_n, e_n, \bar{e}_n^A\right)\right] + \left[E\left(X, e_X^A, \bar{e}_X^M\right) - E\left(c_n, e_n, \bar{e}_n^M\right)\right], \tag{3.98}$$

where

$$E^b\left(c_n, e_n, \bar{e}_n^A\right) = E\left(X, e_X^A, \bar{e}_X^A\right) - E\left(c_n, e_n, \bar{e}_n^A\right). \tag{3.99}$$

Note that we simply added and subtracted Eq. 3.99 to Eq. 3.97. In a grand canonical ensemble (GCE), the generalized energy is written as a function of a cohesive energy term and a chemical potential term (Sec. 1.4). For any configuration γ which can be split into γ_1 and γ_2 such that $\gamma = \gamma_1 \cup \gamma_2$, we can write

$$\begin{cases} E\left(\gamma\right) = E\left(\gamma_1\right) + E\left(\gamma_2\right) + h_{\gamma_1\gamma_2}, \\ E\left(\gamma\right) = H\left(\gamma\right) - \mu\left(\gamma\right), \\ H\left(\gamma\right) = H\left(\gamma_1\right) + H\left(\gamma_2\right) + h_{\gamma_1\gamma_2}. \end{cases} \tag{3.100}$$

$H\left(\gamma\right)$ is the cohesive energy of γ, $\mu\left(\gamma\right)$ is the chemical potential of γ, and $h_{\gamma_1\gamma_2}$ is the interaction energy between γ_1 and γ_2. To calculate transport coefficients of the cluster under study, the number and type of cluster components remains the same in all configurations of the system. We are working with a fixed number of cluster components and varying number of chemical species in the environment (leading to a varying number of mean-field atoms). Note that, initially in the case of dilute alloys, KineCluE was developed in the canonical ensemble because it is the most natural one for dilute alloys. In concentrated alloys, the varying number of atoms in each environment naturally leads to a grand canonical formulation for the calculation of transport coefficients. The binding energy of (c_n, e_n) embedded in pure A becomes

$$E^b\left(c_n, e_n, \bar{e}_n^A\right) = H^b\left(c_n, e_n, \bar{e}_n^A\right) - \mu\left(X, e_X^A, \bar{e}_X^A\right) + \mu\left(c_n, e_n, \bar{e}_n^A\right), \tag{3.101}$$

where $H^b\left(c_n, e_n, \bar{e}_n^A\right) = H\left(X, e_X^A, \bar{e}_X^A\right) - H\left(c_n, e_n, \bar{e}_n^A\right)$. The chemical potential difference can be calculated as

$$\mu\left(c_n, e_n, \bar{e}_n^A\right) - \mu\left(X, e_X^A, \bar{e}_X^A\right) = \left(\sum_x N_x \mu_x + \sum_\alpha N_\alpha^{e_n} \mu_\alpha + N_{\bar{e}_n} \mu_A\right) - \left(\sum_x N_x \mu_x + N_{e_X} \mu_A + N_{\bar{e}_X} \mu_A\right), \tag{3.102}$$

where N_e is the number of sites in e, N_α^e is the number of atoms of species α in e, and μ_α is the chemical potential of species α. Note how most of the terms in Eq. 3.102 will get simplified because the number of each type of cluster component is the same in both these configurations, and because most sites of the system are occupied by A atoms. Therefore, the chemical potential difference comes solely from the sites of e_n which are not occupied by A atoms,

$$\mu\left(c_n, e_n, \bar{e}_n^A\right) - \mu\left(X, e_X^A, \bar{e}_X^A\right) = \sum_\alpha N_\alpha^{e_n} \mu_\alpha - N_{e_n} \mu_A = \sum_\alpha N_\alpha^{e_n} \mu_{\alpha A}, \tag{3.103}$$

with $\mu_{\alpha A} = \mu_\alpha - \mu_A$. There are calculation methods to calculate the chemical potentials $\mu_{\alpha A}$, such as the Cluster Variation Method (CVM) [104], the Low Temperature Expansion (LTE) [144] or Widom's integration scheme [146]. There are methods as well to calculate $H^b\left(c_n, e_n, \bar{e}_n^A\right)$, like Density Functional Theory (DFT), Semi-Empirical potentials (SE), or a pair interaction model. Therefore, there exist methods that allow the calculation of the binding energy of (c_n, e_n) in pure A

$$E^b\left(c_n, e_n, \bar{e}_n^A\right) = H^b\left(c_n, e_n, \bar{e}_n^A\right) + \sum_{\alpha} N_{\alpha}^{e_n} \mu_{\alpha A}. \tag{3.104}$$

We need to calculate the remaining terms of Eq. 3.98, which we call ΔE^b,

$$\Delta E^b = E\left(c_n, e_n, \bar{e}_n^A\right) - E\left(c_n, e_n, \bar{e}_n^M\right) + E\left(X, e_X^A, \bar{e}_X^M\right) - E\left(X, e_X^A, \bar{e}_X^A\right). \tag{3.105}$$

Using the definition in Eq. 3.100, the above equation becomes

$$\begin{aligned}\Delta E^b = {} & \left[E\left(c_n, e_n\right) + E\left(\bar{e}_n^A\right) + h_{e_n \bar{e}_n^A}\right] - \left[E\left(c_n, e_n\right) + E\left(\bar{e}_n^M\right) + h_{e_n \bar{e}_n^M}\right] && (3.106)\\ & + \left[E\left(X, e_X^A\right) + E\left(\bar{e}_X^M\right) + h_{e_X^A \bar{e}_X^M}\right] - \left[E\left(X, e_X^A\right) + E\left(\bar{e}_X^A\right) + h_{e_x^A \bar{e}_X^A}\right]. && (3.107)\end{aligned}$$

Remember that, in our model, cluster components only interact with the environment around them, and all $h_{c_n \bar{e}_n}$ interactions are null (this was our assumption at the beginning of the SCMF-c formalism). ΔE^b gets simplified

$$\Delta E^b = \left[E\left(\bar{e}_n^A\right) - E\left(\bar{e}_n^M\right) + E\left(\bar{e}_X^M\right) - E\left(\bar{e}_X^A\right)\right] + \left[h_{e_n \bar{e}_n^A} - h_{e_n \bar{e}_n^M} + h_{e_X^A \bar{e}_X^M} - h_{e_x^A \bar{e}_X^A}\right]. \tag{3.108}$$

Let ΔE_1^b represent the energy term of the first bracket. An energy of the form $E\left(\bar{e}_m^\alpha\right)$ represents the energy of a homogeneous system in which all sites $\bar{e}_m$ are occupied by species α. This energy term lacks the interactions with the exterior (where the exterior of $\bar{e}_m$ is e_m) for it to become an energy of a complete homogeneous system in which there are no edge effects. We assume that the interaction energy of a site with other sites is split equally among them, such that the energy per site includes half the total interaction energy of this site with all other sites. We can add and substract these interactions to the first bracket so that it becomes

$$\begin{aligned}\Delta E_1^b & = \left[\tilde{E}\left(\bar{e}_n^A\right) - \tilde{E}\left(\bar{e}_n^M\right) + \tilde{E}\left(\bar{e}_X^M\right) - \tilde{E}\left(\bar{e}_X^A\right)\right] - \frac{1}{2}\left(h_{e_n^A \bar{e}_n^A} - h_{e_n^M \bar{e}_n^M} + h_{e_X^M \bar{e}_X^M} - h_{e_X^A \bar{e}_X^A}\right) && (3.109)\\ & = \left(N_{\bar{e}_X} - N_{\bar{e}_n}\right)\left(E_M - E_A\right) - \frac{1}{2}\left(h_{e_n^A \bar{e}_n^A} - h_{e_n^M \bar{e}_n^M} + h_{e_X^M \bar{e}_X^M} - h_{e_X^A \bar{e}_X^A}\right), && (3.110)\end{aligned}$$

where $\tilde{E}\left(\bar{e}_m^\alpha\right)=\mathrm{E}(\bar{e}_m^\alpha) + \frac{1}{2} h_{e_m^\alpha \bar{e}_m^\alpha} = N_{\bar{e}_m} E_\alpha$ represents the energy of a complete homogeneous system of $\bar{e}_m$ in which all $N_{\bar{e}_m}$ sites are occupied by α and have the same energy per site. The factor 1/2 comes from the fact that we assumed that an interaction $h_{e_m^\alpha \bar{e}_m^\alpha}$ is split in equally between the energy of sites e_m^α, $\tilde{E}\left(e_m^\alpha\right)$, and the energy of sites $\bar{e}_m^\alpha$, $\tilde{E}\left(\bar{e}_m^\alpha\right)$. The energy per atom α in this system is E_α. Equation 3.108 becomes

$$\Delta E^b = \left(N_{\bar{e}_X} - N_{\bar{e}_n}\right)\left(E_M - E_A\right) + \delta h, \tag{3.111}$$

where

$$\delta h = h_{e_n \bar{e}_n^A} - h_{e_n \bar{e}_n^M} + h_{e_X^A \bar{e}_X^M} - h_{e_x^A \bar{e}_X^A} - \frac{1}{2}\left(h_{e_n^A \bar{e}_n^A} - h_{e_n^M \bar{e}_n^M} + h_{e_X^M \bar{e}_X^M} - h_{e_X^A \bar{e}_X^A}\right), \tag{3.112}$$

contains all interaction energies. Note that ΔE^b represents the energy it takes to replace mean-field atoms with A atoms in an exterior $\bar{e}_X$ surrounded by A atoms

(e_X^A), and the energy it takes to replace A atoms with mean-field atoms in an exterior $\bar{e}_n^M$ surrounded by a specific occupation of e_n. To calculate $N_{\bar{e}_X}$ and $N_{\bar{e}_n}$ we need to know the total size of the system. We do not want our calculations to depend on the size of the system. Therefore, without loss of generality, we write $N_{\bar{e}_X} = N_e - N_{e_X}$ and $N_{\bar{e}_n} = N_e - N_{e_n}$, where N_e is the total number of sites in the system. N_e gets simplified in Eq. 3.111,

$$\Delta E^b = \left(N_{e_n} - N_{e_X}\right)\left(E_M - E_A\right) + \delta h, \tag{3.113}$$

and we are left with the quantities N_{e_X} and N_{e_n}, which are finite quantities that we can determine. In Eq. 3.113, we are able to calculate

- $E_A = E_A^{coh} - \mu_A$, where E_A^{coh} is the cohesion energy of A, and μ_A can be calculated (CVM, LTE, Widom, ...);
- the interaction energies: $h_{e_X^A \bar{e}_X^A}$, $h_{e_n^A \bar{e}_n^A}$ and $h_{e_n \bar{e}_n^A}$, knowing the geometry of the environment e_n and having an interaction model between atoms.

However, we do not have a method to calculate quantities that are a function of mean-field atoms

- The energy per site of a mean-field atom, $E_M = H_M - \mu_M$;
- the interaction energies with mean-field atoms $h_{e_X^A \bar{e}_X^M}$, $h_{e_n \bar{e}_n^M}$, $h_{e_X^M \bar{e}_X^M}$ and $h_{e_n^M \bar{e}_n^M}$.

In the next section (Sec. 3.7.2), we will discuss how to calculate these quantities.

3.7.2 Mean-field energetic properties

Up until this point, we have made two mean-field definitions that have the same mathematical form (Eq. 3.53 and Eq. 3.71). By defining the mean-field in the same way for different sets of sites (e_n and e_{nj} generally do not have the same size), and for any occupation of e_n and e_{nj}, we have assumed that the mean-field definition is valid for any environment e and for any occupation of e. Therefore, the mean-field definition and the quantities related to the mean-field do not depend on the size of e (and equivalently do not depend on the size of $\bar{e}$). The general mean-field definition can be written

$$\forall \mathrm{e}\ , \exp\left(-\frac{E\left(e, \bar{e}^M\right)}{k_B T}\right) = \frac{1}{\Omega_{\bar{e}}} \sum_{\bar{e}} \exp\left(-\frac{E\left(e, \bar{e}\right)}{k_B T}\right). \tag{3.114}$$

3.7.2.1 Energy of a mean-field atom

We can apply the general mean-field definition to the whole system by considering that $e = \emptyset$,

$$\forall \mathrm{e}\ , \exp\left(-\frac{E\left(\bar{e}^M\right)}{k_B T}\right) = \frac{1}{\Omega_{\bar{e}}} \sum_{\bar{e}} \exp\left(-\frac{E\left(\bar{e}\right)}{k_B T}\right). \tag{3.115}$$

$E\left(\bar{e}^M\right)$ represents the energy of a homogeneous system of pure M atoms, and can therefore be written as a function of the mean-field energy per site, $E\left(\bar{e}^M\right) = N_{\bar{e}} E_M$. On the other hand,

$$Z_{\bar{e}}^{GCE} = \sum_{\bar{e}} \exp\left(-\frac{E\left(\bar{e}\right)}{k_B T}\right) = \exp\left(-\frac{A}{k_B T}\right), \tag{3.116}$$

is the grand canonical partition function of the system of $\bar{e}_n$. The grand potential for a system in the GCE (Sec. 1.4) is $A_{\bar{e}} = -k_B T \ln Z_{\bar{e}}^{GCE} = -PV_{\bar{e}}$, where P and $V_{\bar{e}}$ are respectively the pressure and total volume of the system. The volume of the system is equal to the total number of sites in the system, $N_{\bar{e}}$, times the atomic volume, Ω_{at}; $V_{\bar{e}} = N_{\bar{e}}\Omega_{at}$. The number of possible configuration of $\bar{e}$ is equal to the number of ways we can arrange the N_{spec} on the $N_{\bar{e}}$ sites; $\Omega_{\bar{e}} = (N_{species})^{N\bar{e}}$. With all these substitutions, Eq. 3.115 becomes

$$\forall \mathrm{e}\ , \exp\left(-\frac{N_{\bar{e}}E_M}{k_B T}\right) = (N_{spec})^{-N\bar{e}} \exp\left(\frac{PN_{\bar{e}}\Omega_{at}}{k_B T}\right), \tag{3.117}$$

which gives the energy of a mean-field atom by applying a logarithm function on both sides of the above equation

$$E_M = k_B T \ln (N_{spec}) - P\Omega_{at}. \tag{3.118}$$

The order of magnitude of $k_B T \ln (N_{spec})$ is of 0.03 eV in a binary alloy at 500°C. For $P\Omega_{at}$ to be of the same order of magnitude, the pressure needs to be of the order of 1 GPa, which is only encountered in extremely high pressure applications. Therefore, the product $P\Omega_{at}$ is very small compared to $k_B T \ln (N_{spec})$ and we can neglect it. Therefore, we obtain a mean-field energy which is only a function of temperature and of the number of chemical species in the alloy.

3.7.2.2 Mean-field interaction energies

We need to calculate interaction energies between mean-field atoms ($h_{e_X^M \bar{e}_X^M}$ and $h_{e_n^M \bar{e}_n^M}$), and between mean-field atoms and the alloy's chemical species ($h_{e_X^A \bar{e}_X^M}$ and $h_{e_n \bar{e}_n^M}$, where the sites of e_n can be occupied by any combination of species).

ϵ_{MM} interactions between M and M Let us consider a canonical ensemble which has the same concentration and chemical potential as the previously studied system of $\bar{e}$. Our mean-field definition applied within the CE is

$$\forall \mathrm{e}\ , \exp\left(-\frac{H\left(\bar{e}^M\right)}{k_B T}\right) = \frac{1}{\Omega_{\bar{e}}^C} \sum_{\bar{e}} \exp\left(-\frac{H\left(\bar{e}\right)}{k_B T}\right), \tag{3.119}$$

where the generalized energies do not depend on chemical potentials. Note that the number of possible configuration of $\bar{e}$ is different in the canonical system, and can be calculated from

$$\ln \Omega_{\bar{e}}^{CE} = -N \sum_{\alpha} X_\alpha \ln X_\alpha, \tag{3.120}$$

where X_α is the concentration of species α. The canonical partition function is

$$Z_{\bar{e}}^{CE} = \sum_{\bar{e}} \exp\left(-\frac{H\left(\bar{e}\right)}{k_B T}\right) = \exp\left(-\frac{G}{k_B T}\right), \tag{3.121}$$

where the Gibbs free energy is $G = \sum_\alpha N_\alpha^{\bar{e}} \mu_\alpha = N_{\bar{e}} \sum_\alpha X_\alpha \mu_\alpha$ (Sec. 1.4). Equation 3.119 becomes

$$\forall \mathrm{e}\ , \exp\left(-\frac{N_{\bar{e}}H_M}{k_B T}\right) = \exp\left(N_{\bar{e}} \sum_{\alpha} X_\alpha \ln X_\alpha\right) \exp\left(-\frac{N_{\bar{e}} \sum_\alpha X_\alpha \mu_\alpha}{k_B T}\right), \tag{3.122}$$

where

$$H\left(\bar{e}^M\right) = N_{\bar{e}} H_M = N_{\bar{e}} \sum_{\alpha} X_\alpha \left(\mu_\alpha - k_B T \ln X_\alpha\right). \tag{3.123}$$

The mean-field interaction is a function of species concentrations, their chemical potential and temperature. Note that $k_B T \ln X_\alpha$ is the chemical potential of α in a random alloy, and H_M is therefore an average of the chemical potential deviation from its random alloy value. An interaction model can be used to express H_M as a function of $h_{e^M \bar{e}^M}$ and deduce the latter needed interaction. Assuming that interactions within the mean-field can be reduced to nearest-neighbors pair interactions, we can calculate the interaction between two mean-field atoms as $\epsilon_{MM} = \dfrac{2}{z} H_M$, where z is the coordination number of the crystal. Note that combining Eq. 3.100, Eq. 3.118 and Eq. 3.123, gives us the chemical potential of a mean-field atom

$$\mu_M = \sum_{\alpha} X_\alpha \left[\mu_\alpha - k_B T \ln\left(X_\alpha N_{spec}\right)\right]. \tag{3.124}$$

It is interesting to note that, in an equiatomic system (e.g. high entropy alloys), $X_\alpha = 1/N_{spec}$, and μ_M becomes an arithmetic average of the chemical potentials of the alloy's atomic species, $\mu_M = \sum_\alpha X_\alpha \mu_\alpha$.

$\epsilon_{\alpha M}$ interactions between α and M We apply the mean-field definition to a system containing only one atom of species α that is fixed. All sites other than the one occupied by α are averaged using Eq. 3.71

$$\sum_{\bar{\alpha}} \exp\left(-\frac{E(\alpha) + E(\bar{\alpha}) + h_{\alpha\bar{\alpha}}}{k_B T}\right) = \Omega_{\bar{\alpha}} \exp\left(-\frac{E(\alpha) + E\left(\bar{\alpha}^M\right) + h_{\alpha\bar{\alpha}^M}}{k_B T}\right). \tag{3.125}$$

We are interested in calculating the interactions between α and M

$$\exp\left(-\frac{h_{\alpha\bar{\alpha}^M}}{k_B T}\right) = \frac{1}{\Omega_{\bar{\alpha}}} \sum_{\bar{\alpha}} \frac{\exp\left(-\dfrac{E(\bar{\alpha}) + h_{\alpha\bar{\alpha}}}{k_B T}\right)}{\exp\left(-\dfrac{E\left(\bar{\alpha}^M\right)}{k_B T}\right)}. \tag{3.126}$$

Instead of calculating the infinite sum over all possible occupations of $\bar{\alpha}$, we divide $\bar{\alpha}$ into a local finite-sized environment b around the α atom and the exterior of b; $\bar{\alpha} = b \cup \bar{b}$. We assume that thermodynamic interactions are limited within the b environment and therefore that α only interacts with species belonging to environment b; $\epsilon_{\alpha\bar{b}} = 0$. We can make this assumption since interactions are usually short-ranged. The introduction of environment b is important because it allows us to sample a finite-sized system b instead of an infinite system $\bar{\alpha}$. Equation 3.126

becomes

$$
\begin{aligned}
\exp\left(-\frac{h_{\alpha b^M}}{k_BT}\right) &= \frac{1}{\Omega_b\Omega_{\bar{b}}}\frac{\sum_b \exp\left(-\frac{E\left(b\right)+h_{\alpha b}}{k_BT}\right)\sum_{\bar{b}}\exp\left(-\frac{E\left(\bar{b}\right)+h_{b\bar{b}}}{k_BT}\right)}{\exp\left(-\frac{E\left(b^M\right)+E\left(\bar{b}^M\right)+h_{b^M\bar{b}^M}}{k_BT}\right)} \\
&= \frac{1}{\Omega_b\Omega_{\bar{b}}}\frac{\sum_b \exp\left(-\frac{E\left(b\right)+h_{\alpha b}}{k_BT}\right)\Omega_{\bar{b}}\exp\left(-\frac{E\left(\bar{b}^M\right)+h_{b\bar{b}^M}}{k_BT}\right)}{\exp\left(-\frac{E\left(b^M\right)+E\left(\bar{b}^M\right)+h_{b^M\bar{b}^M}}{k_BT}\right)} \\
&= \frac{1}{\Omega_b}\frac{\sum_b \exp\left(-\frac{E\left(b\right)+h_{\alpha b}+h_{b\bar{b}^M}}{k_BT}\right)}{\exp\left(-\frac{E\left(b^M\right)+h_{b^M\bar{b}^M}}{k_BT}\right)} \\
&= \frac{\sum_b \exp\left(-\frac{E\left(b\right)+h_{\alpha b}+h_{b\bar{b}^M}}{k_BT}\right)}{\sum_b \exp\left(-\frac{E\left(b\right)+h_{b\bar{b}^M}}{k_BT}\right)}. \qquad (3.127)
\end{aligned}
$$

The mean-field definition is used between lines 1 and 2 to replace the sum over $\bar{b}$ by a mean-field expression, and between the last two lines to express the mean-field exponential as a function of a sum over b. Note that now we only have sums over b. The size of environment b has to be big enough to include enough thermodynamic interactions between α and its surrounding, and small enough to be able to calculate the sums in Eq. 3.127. We assume that interactions with the mean-field are reduced to first nearest-neighbors interactions;

$$
\begin{cases}
h_{\alpha b^M} = z\epsilon_{\alpha M} \\
h_{b\bar{b}^M} = -k_BT\ln\left(\prod_\gamma \xi_\gamma m_{b^\gamma\bar{b}^M}\right),
\end{cases} \qquad (3.128)
$$

where

$$
\xi_\gamma = \exp\left(-\frac{\epsilon_{\gamma M}}{k_BT}\right), \qquad (3.129)
$$

and $m_{b^\gamma\bar{b}^M}$ is the number of bonds between atoms of species γ in b and $\bar{b}$. This number depends on the geometry of the system and of the chosen b environment. Equation 3.127 becomes a polynomial equation

$$
\sum_b \exp\left(-\frac{E\left(b\right)}{k_BT}\right)\left[\exp\left(-\frac{h_{\alpha b}}{k_BT}\right)-\left(\xi_\alpha\right)^z\right]\prod_\gamma \xi_\gamma m_{b^\gamma\bar{b}^M} = 0. \qquad (3.130)
$$

We can write Eq. 3.130 for all the possible α species separately and obtain a system of N_{spec} coupled equations with N_{spec} unknowns. We can solve this system of equations and obtain all the N_{spec} unknown interactions ξ_γ.

3.7.3 Conclusion on energy calculations

To conclude, we proposed in this section a method to calculate a configuration's binding energy which is a function of the mean-field. These energies are needed for the calculation of effective interactions and transport coefficients. We assume that all interactions with a mean-field atom are limited to first nearest-neighbors pair interactions, and that thermodynamic interactions between an atomic species are limited to a finite range. We finally obtain the binding energy of a configuration n

$$E^b\left(c_n, e_n, \bar{e}_n^M\right) = H^b\left(c_n, e_n, \bar{e}_n^A\right) + \sum_\alpha N_\alpha^{e_n} \mu_{\alpha A} + \left(N_{e_n} - N_{e_X}\right)\left[k_B T \ln\left(N_{spec}\right) - E_A^{coh} + \mu_A\right] + \delta h, \tag{3.131}$$

with

$$\delta h = N_{e_X} \epsilon_{AM} - \sum_\alpha N_\alpha^{e_n} \epsilon_{\alpha M} + \frac{1}{2}\left(N_{e_n} - N_{e_X}\right)\epsilon_{MM} + h_{e_n \bar{e}_n^A} - \frac{1}{2} h_{e_X^A \bar{e}_X^A} - \frac{1}{2} h_{e_n^A \bar{e}_n^A}. \tag{3.132}$$

In Eq. 3.131 and Eq. 3.132, we are able to calculate all the terms

- the total number of species, N_{spec};
- the number of species in an environment, $N_\alpha^{e_n}$;
- the number of sites in an environment, N_{e_X} and N_{e_n};
- the chemical potential of species μ_α, and subsequently $\mu_{\alpha A}$;
- the cohesion energy of A, E_A^{coh};
- the interaction energies $h_{e_X^A \bar{e}_X^A}$, $h_{e_n^A \bar{e}_n^A}$ and $h_{e_n \bar{e}_n^A}$;
- the $M-M$ interaction energies, $\epsilon_{MM} = \frac{2}{z}\sum_\alpha X_\alpha\left(\mu_\alpha - k_B T \ln X_\alpha\right)$, with μ_α and X_α known for all species α;
- the $\alpha - M$ interaction energies, $\epsilon_{\alpha M}$, calculated for each α by solving the system of equations formed by Eq. 3.130.

3.7.4 Calculating the mean-field binding energy in special cases

In this section, we will calculate the configuration binding energies in the case of a concentrated random alloy and in the case of a binary interacting alloy with interactions described by a pair interaction model. These two types of alloys will be the ones used in our applications to test the validity of our model and code. The random alloy has been the most widely used type of alloys to study the validity of a diffusion model in a concentrated alloy, and there are several literature works with which we can compare our results. Additionally, in the case of a random alloy, we can calculate exactly the mean-field energy and compare it to the value calculated using our model. The interacting binary alloy provides on the other hand a model which depends on thermodynamic interactions and will be more sensitive to the accuracy of our energy model.

3.7.4.1 Case of a concentrated random alloy

In the case of a concentrated alloy with N_{spec} species, all thermodynamic interactions are null and we can calculate exactly the generalized energies as a function of the mean-field (Eq. 3.71). The energy of a configuration is only a function of the chemical potentials and the sum reduces to

$$\begin{aligned}
\exp\left(\frac{E^b\left(c_n, e_n, \bar{e}_n^M\right)}{k_B T}\right)\Bigg|_{RA}^{exact} &= \frac{1}{\Omega_{\bar{e}_n}} \sum_{\bar{e}_n} \exp\left(\frac{E^b\left(c_n, e_n, \bar{e}_n\right)}{k_B T}\right) && (3.133)\\
&= \frac{1}{\Omega_{\bar{e}_n}} \sum_{\bar{e}_n} \exp\left(\frac{\sum_\alpha N_\alpha^e \mu_{\alpha A}}{k_B T}\right) && (3.134)\\
&= \frac{1}{\Omega_{\bar{e}_n}} \exp\left(\frac{\sum_\alpha N_\alpha^{e_n} \mu_{\alpha A}}{k_B T}\right) \sum_{\bar{e}_n} \prod_\alpha \exp\left(\frac{\mu_{\alpha A}}{k_B T}\right)^{N_\alpha^{\bar{e}_n}} && (3.135)\\
&= \frac{1}{\Omega_{\bar{e}_n}} \exp\left(\frac{\sum_\alpha N_\alpha^{e_n} \mu_{\alpha A}}{k_B T}\right) \left(\sum_\alpha \exp\left(\frac{\mu_{\alpha A}}{k_B T}\right)\right)^{N_{\bar{e}_n}}, && (3.136)
\end{aligned}$$

where the last line is obtained using Newton's multinomial law. Additionally in a random alloy, we can prove that $\exp\left(\frac{\mu_{\alpha A}}{k_B T}\right) = \frac{X_\alpha}{X_A}$, where X_α is the concentration of species α We write the number of occupancy $\Omega_{\bar{e}_n} = \left(N_{spec}\right)^{N_{\bar{e}_n}}$, and knowing that $\sum_\alpha X_\alpha = 1$, we obtain the exact value of the configuration energy in the case of a random alloy

$$\exp\left(\frac{E^b\left(c_n, e_n \bar{e}_n^M\right)}{k_B T}\right)\Bigg|_{RA}^{exact} = \exp\left(\sum_\alpha N_\alpha^{e_n} \ln\left(X_\alpha / X_A\right)\right) \left(X_A N_{spec}\right)^{-N_{\bar{e}_n}}. \qquad (3.137)$$

Let us now calculate this energy using the approximated equations that we obtained in this section (Eq. 3.131 and Eq. 3.132), and compare the approximated values to the exact ones. We have:

- the total number of species, N_{spec};
- the number of species in an environment, $N_\alpha^{e_n}$;
- the number of sites in an environment, N_{e_X} and N_{e_n};
- the chemical potential of species $\mu_\alpha = k_B T \ln X_\alpha$, and subsequently $\mu_{\alpha A} = k_B T \ln\left(X_\alpha / X_A\right)$;
- the cohesion energy of A, $E_A^{coh} = 0$, because all $A - A$ interactions are null;
- the interaction energies $h_{e_X^A \bar{e}_X^A}$, $h_{e_n^A \bar{e}_n^A}$ and $h_{e_n \bar{e}_n^A}$ are all null;
- the $M - M$ interaction energies, $\epsilon_{MM} = \frac{2}{z} \sum_\alpha X_\alpha \left(\mu_\alpha - k_B T \ln X_\alpha\right) = 0$, since $\mu_\alpha = k_B T \ln X_\alpha$;
- the $\alpha - M$ interaction energies, $\epsilon_{\alpha M} = 0$, $\forall \alpha$, calculated from Eq. 3.130.

In this case, the binding energy of a configuration is a function of the total number of species in the alloy, their average concentrations, the number of environment sites in the configuration, and the number of different species occupying these sites

$$E^b\left(c_n, e_n, \bar{e}_n^M\right) = k_B T \sum_\alpha N_\alpha^{e_n} \ln\left(X_\alpha / X_A\right) + \left(N_{e_n} - N_{e_X}\right) k_B T \ln\left(X_A N_{spec}\right). \tag{3.138}$$

Using $N_{e_n} = N_e - N_{\bar{e}_n}$, the exponential of this energy becomes equivalent to Eq. 3.137 up to a constant

$$\left.\exp\left(\frac{E^b\left(c_n, e_n \bar{e}_n^M\right)}{k_B T}\right)\right|_{RA}^{\text{our model}} = \left.\exp\left(\frac{E^b\left(c_n, e_n \bar{e}_n^M\right)}{k_B T}\right)\right|_{RA}^{exact} \left(X_A N_{spec}\right)^{\left(N_e - N_{e_X}\right)}. \tag{3.139}$$

However, this constant,

$$\left(X_A N_{spec}\right)^{\left(N_e - N_{e_X}\right)}, \tag{3.140}$$

is independent of the configuration n, and shifts all energies of the system by the same amount. In practice, since all energies are normalized by the partition function, which is a sum of energies, this constant will always get simplified, and therefore the normalized probabilities calculated with our energy model are equal to the exact probabilities in the case of a concentrated random alloy.

$$\left.\frac{\exp\left(\frac{E^b\left(c_n, e_n \bar{e}_n^M\right)}{k_B T}\right)}{Z}\right|_{RA}^{\text{our model}} = \left.\frac{\exp\left(\frac{E^b\left(c_n, e_n \bar{e}_n^M\right)}{k_B T}\right)}{Z}\right|_{RA}^{exact}. \tag{3.141}$$

and

$$P_n|_{RA}^{\text{our model}} = P_n|_{RA}^{exact}. \tag{3.142}$$

3.7.4.2 Case of a binary alloy within a pair interaction model

Let us now consider a 2D-square structure ($z = 4$) of a binary alloy AB in which interactions are limited to first nearest-neighbors pair interactions. We define the ordering energy of the alloy as

$$W = \epsilon_{AA} + \epsilon_{BB} - 2\epsilon_{AB}, \tag{3.143}$$

such that, when W is positive, the alloy has an ordering tendency, and when W is negative, the alloy has a clustering tendency. We assume that all interactions in the system are null except for the $A - B$ interactions, such that there is no energy asymmetry between A and B atoms, and A and B atoms do not interact with cluster components unless they are A or B tracer atoms.

- the total number of species, $N_{spec} = 2$;
- the number of species in an environment, $N_A^{e_n}$ and $N_B^{e_n}$;
- the number of sites in an environment, N_{e_X} and N_{e_n};

- the chemical potential of species is calculated within the pair approximation of the CVM [104]

$$\mu_A = \left(1 - \frac{z}{2}\right) k_B T \ln X_A - \frac{z}{2} k_B T \ln \left(1 + \frac{K^2}{2X_A} L\right), \tag{3.144}$$

  and

$$\mu_{BA} = -zW + k_B T \ln \left(\frac{1 - X_A}{X_A}\right) + z k_B T \ln \left(\frac{1}{2\left(1 - X_A\right)} L\right), \tag{3.145}$$

  where

$$L = \sqrt{\left(2X_A - 1\right)^2 + \frac{4X_A\left(1 - X_A\right)}{K^2}} - 2X_A + 1, \tag{3.146}$$

  and

$$K = \exp\left(-\frac{\epsilon_{AB}}{k_B T}\right) = \exp\left(\frac{W}{2k_B T}\right). \tag{3.147}$$

- the cohesion energy of A, $E_A^{coh} = 0$, because all $A - A$ interactions are null;

- the interaction energies $h_{e_X^A \bar{e}_X^A}$ and $h_{e_n^A \bar{e}_n^A}$ are null, and $h_{e_n \bar{e}_n^A} = m_{e_n^B \bar{e}_n^A} \epsilon_{AB}$, where $m_{e_n^B \bar{e}_n^A}$ represents the number of B atoms in e_n interacting with the A atoms of $\bar{e}_n$ and depends on the crystal structure, the geometry of e_n and the distribution of B atoms in it;

- the $M - M$ interaction energies,

$$\epsilon_{MM} = \frac{2}{z}\left[X_A\left(\mu_A - k_B T \ln X_A\right) + \left(1 - X_A\right)\left(\mu_B - k_B T \ln\left(1 - X_A\right)\right)\right]; \tag{3.148}$$

- the $\alpha - M$ interaction energies, $\epsilon_{\alpha M} = -k_B T \ln\left(\zeta_\alpha\right)$ calculated by numerically solving the polynomial equation obtained from Eq. 3.130

$$\sum_{n_B=0}^{z} \binom{z}{n_B} \left[\exp\left(\frac{\mu_{BA}}{k_B T}\right)\left(\frac{\xi_B}{\xi_A}\right)^{z-1}\right]^{n_B} \left[K^{z-n_B} - \left(\frac{\xi_B}{\xi_A}\right)^{z} K^{n_B}\right] = 0. \tag{3.149}$$

  Figure 3.22 shows examples of the calculated interactions ϵ_{AM} and ϵ_{BM} as a function of the alloy's A concentration, for values of the ordering energy normalized by $k_B T$ equal to ±0.5 and ±1.96. ϵ_{AM} and ϵ_{BM} are symmetric and equal to $\epsilon_{AB}/2$ when the alloy has an equiatomic composition. When the alloy is rich in A, ϵ_{AM} tends towards 0 as we would expect since ϵ_{AA} interactions will be more important than ϵ_{AB} interactions. The opposite is also true and ϵ_{AM} tends towards ϵ_{BM} when the alloy is rich in B. We can see from these graphs that the interactions with the mean-field calculated with our energetic model are not equivalent to a Bragg-Williams (BW) point approximation which would be written as

$$\epsilon_{\alpha M} = \sum_{\beta} X_\beta \epsilon_{\alpha\beta}, \tag{3.150}$$

  and in which interactions $\epsilon_{\alpha M}$ vary linearly with the concentration between 0 and ϵ_{AB}. This is the case in our model only when the ordering energy is low, because in this case the alloy is close to a random alloy and the effect of the surrounding atoms of any site is negligible, which is consistent with the point approximation in which the site occupation depends only on the average compositions. However, the BW approximation is not valid in the general case of an interacting alloy, and our model's mean-field interactions deviate from the linear approximation with the increasing ordering energy.

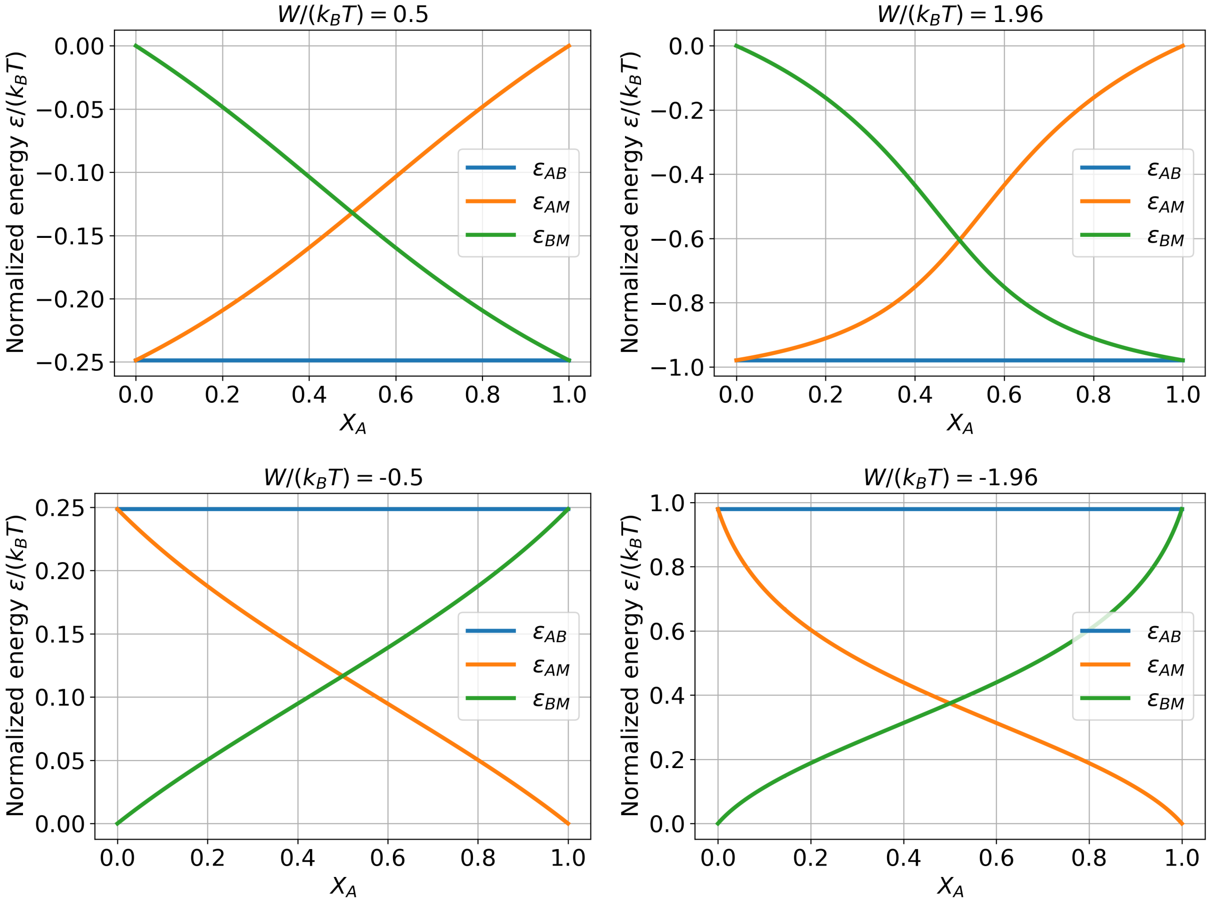

Figure 3.22: Interaction energies between environment species and the mean-field as a function of concentration for different values of the ordering energy normalized by k_BT. These values are calculated numerically by solving Eq. 3.149. Positive (negative) values of W correspond to an alloy with a tendency to ordering (clustering).

3.8 Code's general performance

In this section, we will analyze how the code's computational time and memory scales with the kinetic and environment radii, and how fast correlation factors converge with these increasing radii.

3.8.1 Computational time and memory as a function of KiRa and EnRa

KineCluE's computational time and memory are mostly affected by the number of configurations and effective interaction classes in the system. The number of cluster components, the kinetic radius and the environment radius all increase the number of configurations in the system. Here, we will calculate the transport coefficients in the case of a vacancy-tracer diffusion in a binary alloy with a 2D-square structure and a BCC structure, as a function of the kinetic and the environment radii by fixing one of them and varying the other. In most cases, the environment radius is considered to be null (no environment) around the tracer atom and non-null around the vacancy. Even though this is less realistic to describe a concentrated alloy based on our model, it provides the possibility to further increase the environment radius and to better study the computational performance of the code as a function of the increasing radii. In each case, we determine the number of effective interaction classes (which is also the size of the $\tilde{T}$ matrix, and which represents the needed computational memory) and the computational time required to compute transport coefficients, and we plot these results in Fig. 3.23.

The number of effective interactions and the computational time vary in the same way as a function of the radii in all the tested systems. In all systems, computational load increases with both KiRa and EnRa. The increase is in particular fast with the increasing EnRa. The increase in computational time is of no issue here since all the tested systems required less than 3 hours of calculations on one processor of our laboratory's calculation cluster (Intel® Xeon® Gold 6132 CPU (2.60 GHz)). The size of the $\tilde{T}$ matrix was however a limiting factor here. While the increase in KiRa (at small EnRa values) did not cause computational problems, tests could not be carried out for EnRa values higher than 2 lattice parameters in the 2D-square structure and higher than 1 lattice parameter in the BCC structure, even when KiRa was fixed to the smallest possible value of 1 a_0. We were unable to perform calculations in systems with more than around 10^5 effective interaction classes because the code fills up all the RAM memory of our workstation. This limits local environments to 3rd nearest-neighbors in a 2D structure and to 2nd nearest-neighbors in a BCC structure, knowing that in both these cases, the environment is around only one cluster component. This also forces us to have either a big KiRa or a big EnRa, and not both at the same time, leading us to truncate either kinetic trajectories or local cluster surroundings, and in most cases the approximation has to be done on the size of the environments. Bigger clusters in which more than one component is surrounded by an environment and multicomponent alloys with more than two elements become impossible to treat without a sampling scheme.

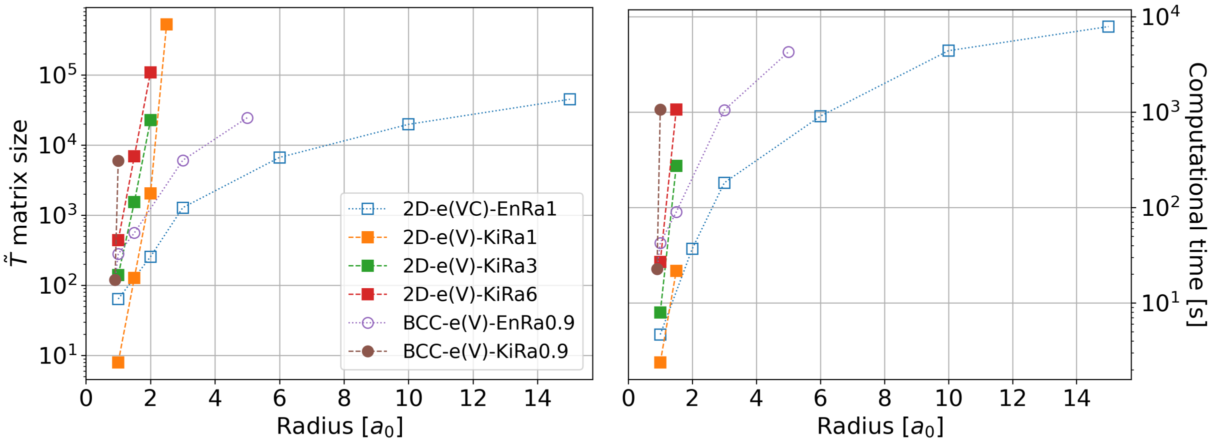

Figure 3.23: Size of the $\tilde{T}$ matrix (left) and computational time (left) as a function of KiRa and EnRa in the case of a vacancy-tracer diffusion in a binary alloy. Closed symbols and dashed lines indicate that KiRa is fixed in this system while EnRa is increased. Open symbols and dotted lines indicate that EnRa is fixed in this system and KiRa is increased. Labels are written in the form $S - e(\alpha) - R$, where S represents the structure (2D-square or BCC), α represents the cluster components around which a local environment is built (V for vacancy and C for tracer), and R represents the fixed radius (kinetic or environment) and its value. These calculations were run on one processor of our laboratory's calculation cluster Gatsby: Intel® Xeon® Gold 6132 CPU (2.60 GHz).

3.8.2 Convergence of correlation factors

If we treat the full configuration space, we know that in the limit of an infinite kinetic radius, all kinetic trajectories are taken into account, and that in the limit of an infinite environment radius, all sites of the system are treated exactly. The previous paragraph showed how computational load increases with both these radii, and that the increase with EnRa is much faster than the increase with KiRa and that EnRa cannot be increased beyond very few lattice parameters because of computational memory limitations. It is important to know the order of magnitude of KiRa and EnRa at which calculations are well converged in order to assess the computational requirements of a converged result.

3.8.2.1 Convergence as a function of KiRa

We study the convergence of tracer and vacancy correlation factors as a function of the kinetic radius in the case of a vacancy-tracer cluster diffusing in an interacting binary alloy AB (Sec. 3.7.4.2) with a 2D-square structure. We fix the environment radius around both cluster components to 1 lattice parameter and we calculate the tracer (Fig. 3.24) and the vacancy (Fig. 3.25) correlation factors for different kinetic radii going from 1 a_0 to 15 a_0, where a_0 is the lattice parameter. We do this study for an average A concentration going from 0.1 to 0.9, and for normalized ordering energies going from -1.96 to +1.96. A well converged calculation (relative error below 5%) does not always occur at the same kinetic radius. Here, it differs between the tracer correlation factor and the vacancy correlation factor, and it changes according to the ordering energy. However, in all cases, the values of the correlation factor converge after a few lattice parameters, and for a kinetic radius of 6 lattice parameters, the relative error is less than 5% at all concentrations and for all ordering energies. For a kinetic radius of 6 a_0 and an environment radius of 1 a_0, the size of the system is still small enough for the full configuration space to be explored (less than 10^4), and the calculation time is less than 20 minutes per point. Therefore, for small environment radii, converged results with respect to the kinetic radius can be obtained with no computational limitations. It is important to have converged results not only for accuracy, but because in some cases it also affects the qualitative evolution of the correlation factor as a function of concentration or ordering energy. For example, in the case of the vacancy correlation factor with $W/k_BT = 1.96$ (Fig. 3.25), when KiRa=1 a_0, the system is found to be the most correlated when the average A composition is of 0.5, while after convergence the opposite is found. Another interesting thing to note here is that, with a small kinetic radius, the values of the correlation factors are almost always overestimated. This is equivalent to underestimating correlation effects and is consistent with the fact that the bigger the kinetic radius the more correlated trajectories are taken into account. After a big enough kinetic radius, all correlated trajectories with an important weight are considered and the correlation factor values converge. These results are in agreement with the observations made in the case of a dilute alloy [18], except that the value of the converged kinetic radius is higher in concentrated alloys ($6a_0$ instead of the $3a_0$ obtained in the case of dilute alloys). This means that, in a concentrated alloy, the kinetic weight of trajectories does not decrease with the length of the trajectory as fast as it does in a dilute alloy. This makes sense because, when the surrounding of diffusing species varies in space as they diffuse, longer kinetic trajectories need to be considered to find all the ones with an important weight which do not randomize the relative positions of species and to properly treat kinetic correlations.

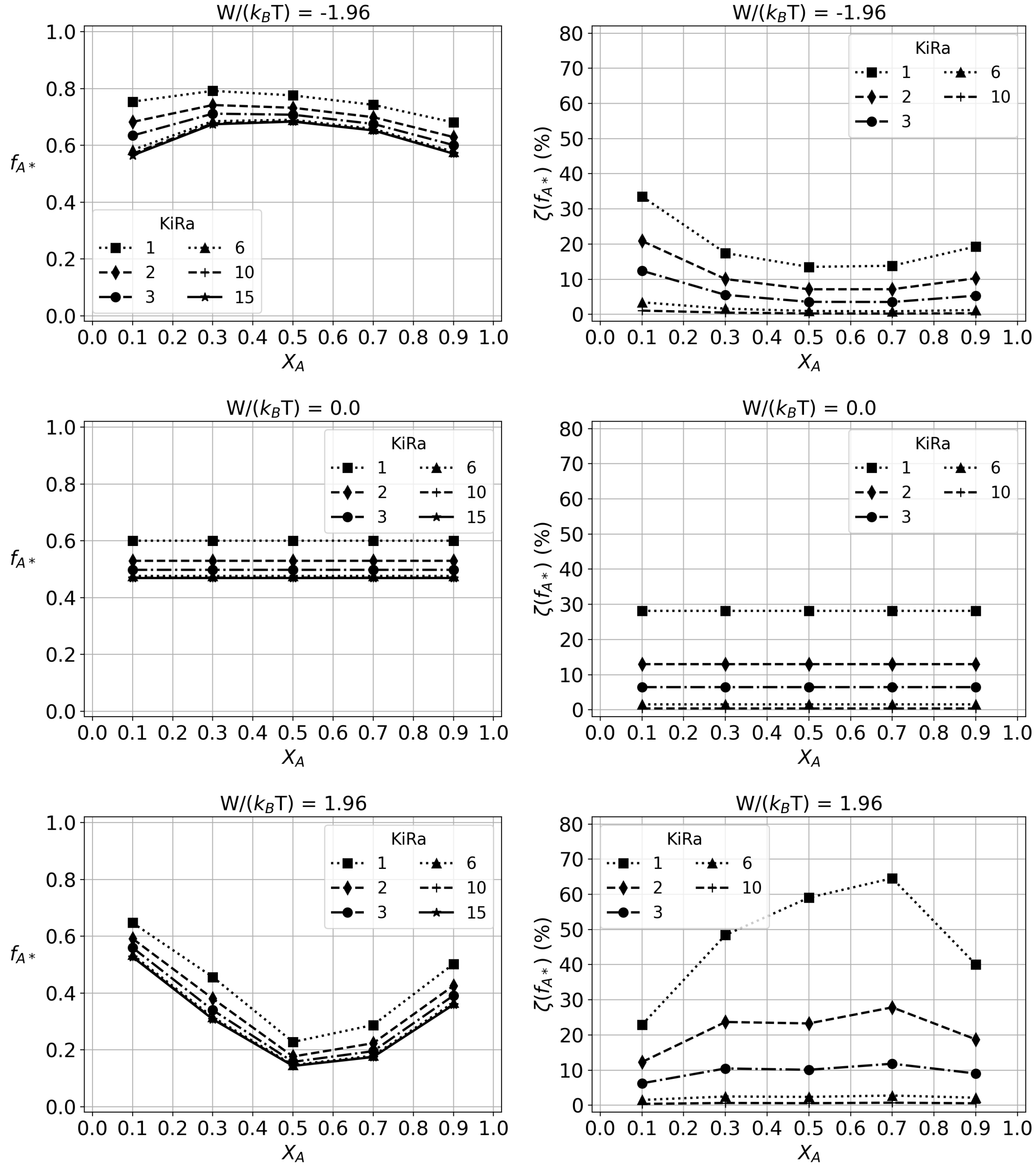

Figure 3.24: Convergence of the tracer correlation factor with increasing KiRa (units of a_0), as a function of concentration, for different values of ordering energies normalized by k_BT, in the case of a tracer-vacancy diffusion in a 2D-square binary alloy with EnRa $= 1\,a_0$. The relative error is calculated by taking as a reference the value of the correlation factor obtained when KiRa $= 15\,a_0$.

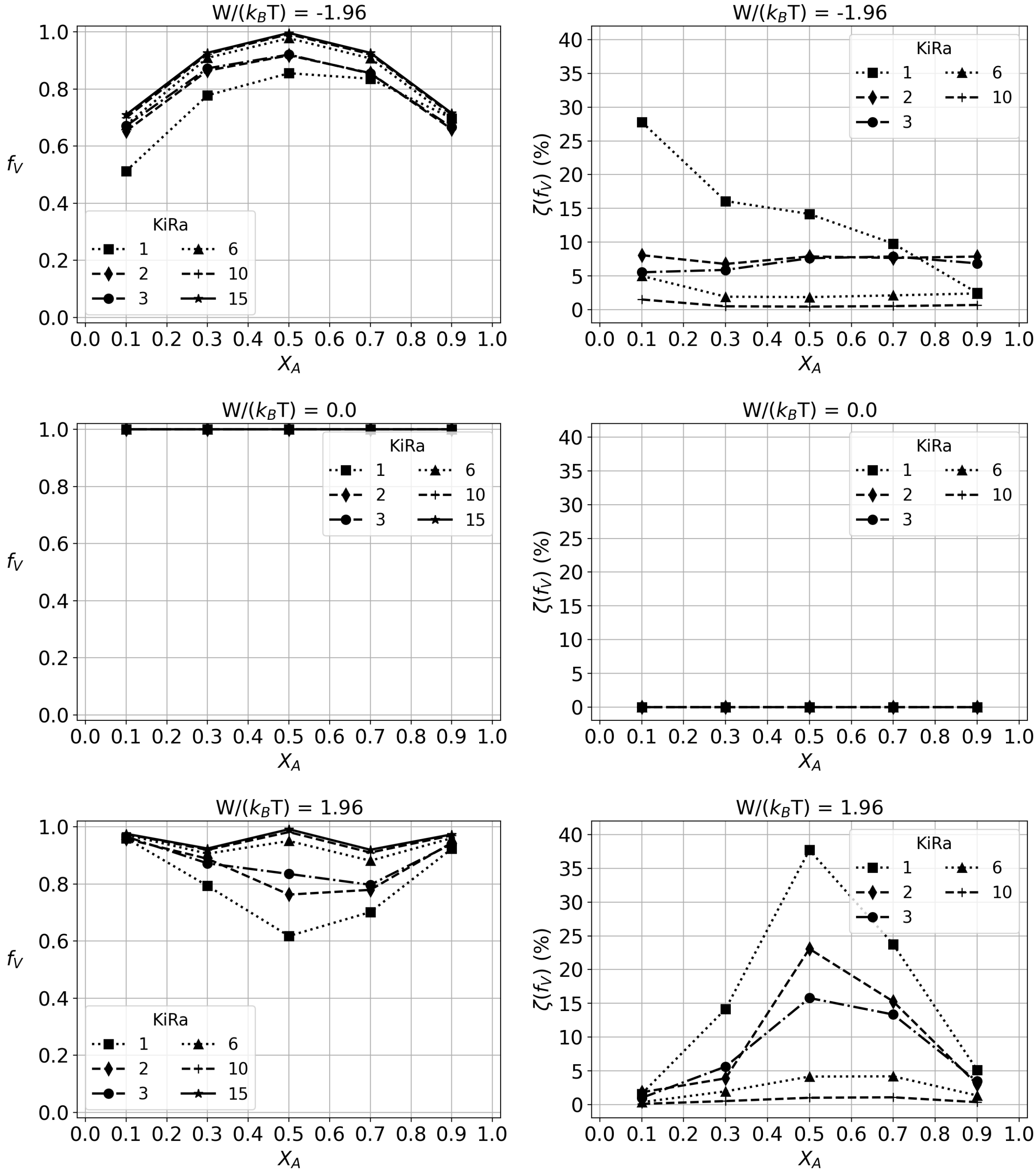

Figure 3.25: Convergence of the vacancy correlation factor with increasing KiRa (units of a_0), as a function of concentration, for different values of ordering energies normalized by $k_B T$, in the case of a tracer-vacancy diffusion in a 2D-square binary alloy with EnRa $= 1\,a_0$.. The relative error is calculated by taking as a reference the value of the correlation factor obtained when $KiRa = 15\,a_0$.

3.8.2.2 Convergence as a function of EnRa

Due to computational memory limitations, we studied the smallest possible system, a cluster of one vacancy diffusing in a binary alloy with a 2D-square structure, and we increased the environment radius from $1a_0$ to $2a_0$. We calculate the mono-vacancy correlation factor at different concentrations and for different values of the normalized ordering energy. While the results shift in the same direction with increasing EnRa, the relative error between EnRa=$1.5a_0$ and EnRa=$2a_0$ remains high in most cases and the results are not fully converged yet. It is therefore necessary to increase the environment radius beyond 2 lattice parameters, and hence the importance of the sampling scheme.

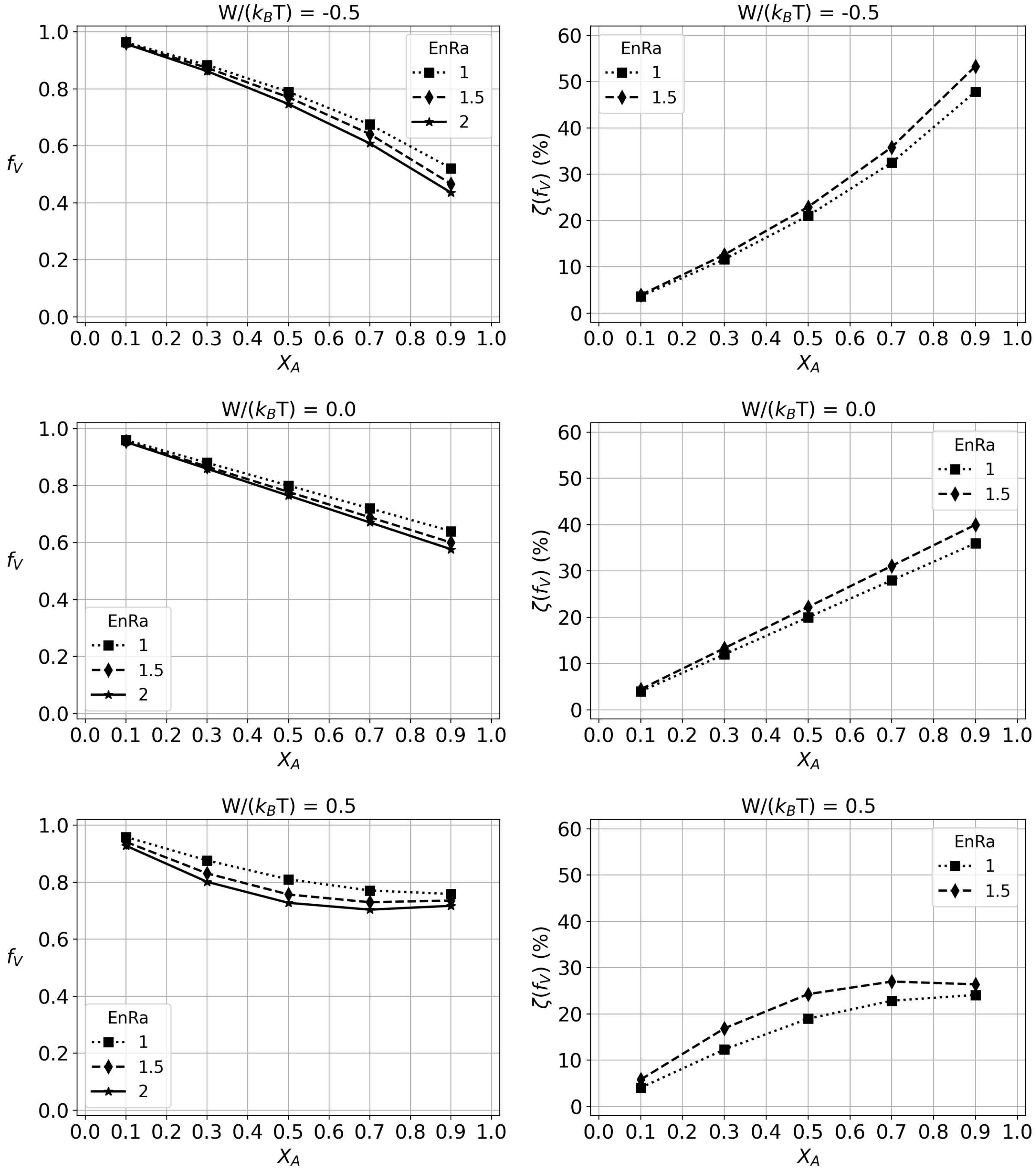

Figure 3.26: Convergence of the vacancy correlation factor with increasing EnRa (units of a_0), as a function of concentration, for different values of ordering energies normalized by k_BT, in the case of a mono-vacancy diffusion in a 2D-square binary alloy. The relative error is calculated by taking as a reference the value of the correlation factor obtained when EnRa=$2a_0$.

3.8.3 Computational performance of sampling

As discussed previously, computational time and memory are mostly affected by the number of configurations and effective interaction classes. In our case, sampling the configuration space should in theory reduce the needed memory to run the calculations because it reduces the number of configurations and the size of the $\tilde{T}$ matrix. As a consequence, sampling also reduces the time needed to invert the $\tilde{T}$ matrix and solve the system of Eq. 3.23. However, it also introduces a new part of the code which is responsible for filling the environment sites with species and choosing which cluster-environment configurations to keep. Remember that when sampling, for each (initial or final) cluster-environment configuration, we need to determine the number of sites in the reservoir based on the number of environment sites to fill, fill the reservoir with species based on their average concentrations, and draw one species from it to fill one of the environment sites until all sites are filled. At a later step, a pseudo residence-time algorithm chooses among the found configurations which ones to keep based on their thermodynamic weights. Additionally, since the sampled configurations differ from one run of the code to another, we are usually required to run the code several times to average the results of the different runs and get a reliable result. All of this requires additional computation time, which in some cases compensates for the time saved by the code when solving a smaller system of equations. This is especially true when the size of the sample is big compared to the size of the full configuration space, as is seen in Fig. 3.27 for the case of $\eta = 10\%$. Here, we sampled the configuration space at a specific percentage η and we calculated the vacancy-tracer transport coefficients from 20 separate runs, and we plot in Fig. 3.27 the time required to run the sampling scheme 20 times as compared to running it once in the case of a full configuration space exploration. For smaller samples, regardless of the ordering energy and kinetic radius, sampling the configuration space saves computational time. Even though computational time is not a limitation, it is good to know that sampling the configuration space will not increase the time needed to compute transport coefficients. Additionally, the more computational time is saved when sampling, the higher the number of calculations that we can run, which leads to averaging over a bigger number of runs and possibly having a more reliable result. In most realistic cases, the size of the sample will be smaller than 1% and sampling the system will therefore save both computational memory and time.

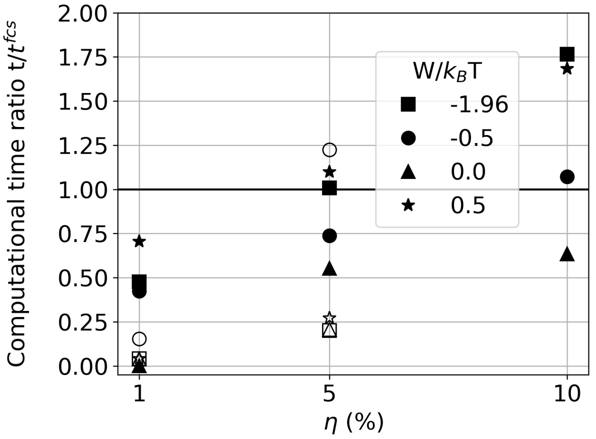

Figure 3.27: Computational time t required to sample the configuration space and calculate transport coefficients 20 times in the case of a vacancy-tracer cluster diffusing in a 2D-square structure of a binary alloy AB, with respect to the computational time t^{fcs} required to calculate the same transport coefficient in the case of a full configuration space exploration. These measurements are plotted as a function of the percentages of sampled effective interactions (η), for different values of the normalized ordering energy, and in the case of KiRa=$3a_0$ (full symbols) and KiRa=$6a_0$ (empty symbols). In all cases, EnRa is limited to 1st nearest-neighbors around cluster components. The solid horizontal line represents the values obtained in the case of a full configuration space exploration. The values are averaged over the range of concentrations, and the error bars are smaller than the markers and therefore not drawn. All these calculations were performed on a standard personal computer: Intel® Core™ i3-8130U CPU (2.20 GHz).

3.9 Comparison of KineCluE's correlation factors with other methods

3.9.1 Case of a random binary alloy

We calculate the tracer correlation factor in a random binary alloy AB (Sec. 3.7.4.1) with a BCC structure in the case of a vacancy jump frequency ratio w_A/w_B of 5 and of 10^4. We consider a local environment which includes the first nearest-neighbors only (EnRa = $a_0\sqrt{3}/2$) around the vacancy, and no local environments around the tracer, and we explore the full configuration space. The kinetic radius is set to 5 lattice parameters which was enough to obtain converged values at this environment radius. The results are shown in Fig. 3.28 in comparison with Manning's RA model ([19, 20] and Sec. 1.7.1), Kikuchi's PPM ([46] and Sec. 1.7.3), and Mishin's Monte Carlo simulations [29]. In the case of a low jump frequency ratio, our results are in very good agreement with the literature results in the full range of concentrations. In the case of a high jump frequency ratio, our model fails to reproduce the percolation curve at low concentrations and to predict a percolation concentration threshold. Our model is more accurate than the PPM at all concentrations, and when the concentration of the fast diffusing species (A) is higher than 0.5, our results are close to Manning's. However, all of these models do not reproduce the Monte Carlo results accurately. It is interesting to note the similarity in our curve and the PPM's curve, which both increase linearly and do not predict a percolation concentration threshold. Kikuchi identified that the PPM's problem was averaging over ensembles while a time average is required to follow the movement of one particular species during diffusion ([47] and Sec. 1.7.3). This is because long range order is necessary to know if an infinitely connected cluster exists in the system or not. The probability of such an event is either 0 or 1, and as long as the concentration of the fast species is below the percolation threshold, this probability is null and so is the diffusion and correlation factors. In our case, this probability is never null because it is calculated based on the short range order established only around the vacancy (no environments around the tracer). Therefore, the size of the environments and trajectories needs to be big enough for this probability to converge towards 0. In the case of a 2D-square structure with an environment around both cluster components and which includes first nearest-neighbors, our model predicts a percolation threshold at $X_A = 0.1$ (Fig. 3.29). Even though the predicted threshold is smaller than the one found by Manning and by our Monte Carlo simulations, nevertheless, it shows that percolation can be studied using our model by further increasing the environment radius and properly applying a sampling scheme. It is interesting to note that our model predicts a null correlation factor only at low concentrations of the fast diffusing species, and that our model is overall more accurate at low and high concentrations of A, regardless of how correlated the system is. This can be related to the fact that, at these concentrations, the local concentration and probability distributions are more centered around the average concentrations (see the probability distribution in Sec. 3.6.3.4). In this case, the concentration distribution of bigger environments and the kinetic probabilities of trajectories converge faster to their exact values than when all configurations have similar probabilities. This leads to a better description of kinetic correlations. Here this also leads to a faster convergence of the probability of having an infinitely connected cluster to 0 at low concentrations, and to 1 at high concentrations.

Overall, our model's result in the case of a random alloy is satisfying in the case of a small jump frequency ratio, and promising in the case of a high jump frequency ratio. Additionally, as was shown in Sec. 3.23, obtaining these results is not computationally demanding. In the case of the 2D-square structure, it was actually faster to calculate the correlation factors with KineCluE than with the Monte Carlo simulations. Long range order cannot be reproduced without increasing the environment radius beyond the first nearest-neighbors, and therefore cannot be done without resorting to sampling the configuration space. This will be especially necessary in the case of concentrated alloys with compositions around 0.5 because they will require larger environment and kinetic radii for a good description of kinetic trajectories and correlations.

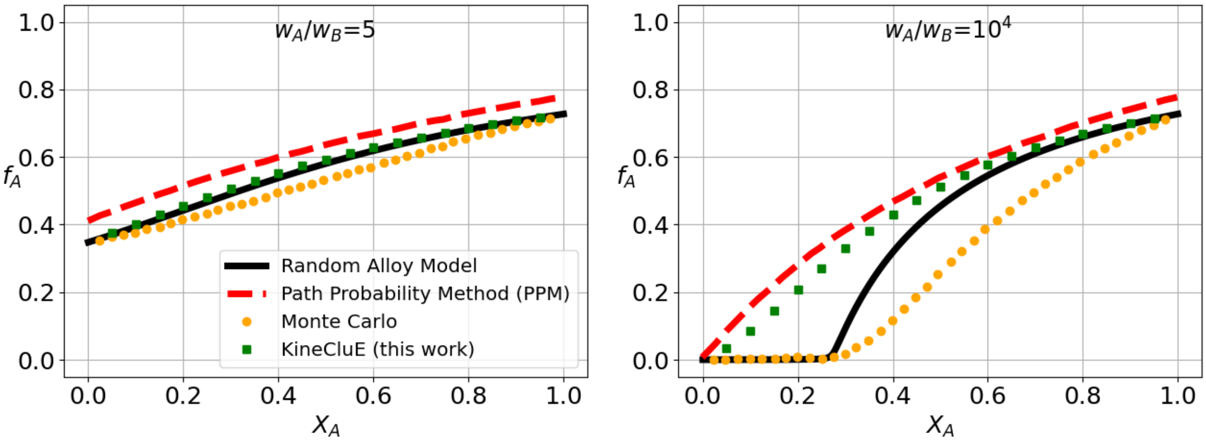

Figure 3.28: Tracer correlation factor f_A in a BCC binary random alloy, in the case of a low jump frequency ratio of 5 (left) and a high jump frequency ratio of 10^4 (right), calculated using KineCluE (this work) and compared with results from the literature: Manning's RA model [19,20], Kikuchi's PPM [46], and Monte Carlo simulations [29]. Note that the Monte Carlo results are the most accurate ones.

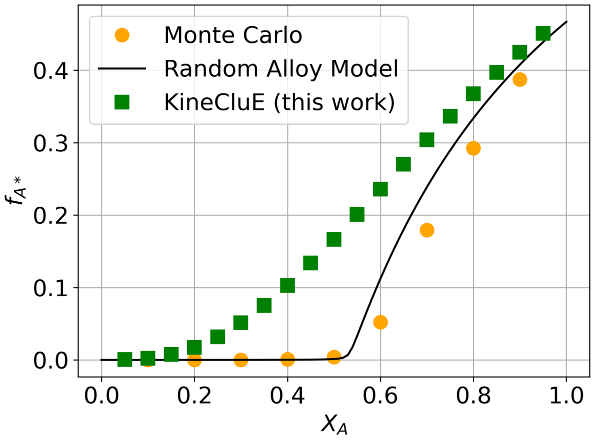

Figure 3.29: Tracer correlation factor in a 2D-square binary random alloy calculated using KineCluE with KiRa = $6\,a_0$ and EnRa = $1\,a_0$ around both the vacancy and the tracer, in the case of a high jump frequency ratio of 10^4, and compared with Manning's RA model [19, 20] and with our Monte Carlo simulations.

3.9.2 Case of an interacting binary alloy

We calculate the tracer correlation factors and the vacancy correlation factor in the case of an interacting binary alloy with a 2D-square structure within the pair interaction approximation[1]as a function of the ordering energy W normalized by k_BT. The absolute value of the maximum tested normalized ordering energy, $|W|\,/\,(k_BT) = 1.96$) corresponds to the average ordering energy of the FeCr alloy (taken from [8] and integrated over the whole range of concentrations) at 500°C. Note that here, positive values of W correspond to alloys with an ordering tendency, while negative values represent alloys with a clustering tendency. We plot

---

[1] Not to be confused with the PPM's pair approximation. The interaction model used here, which relies on first nearest-neighbors pair interactions, was presented in Sec. 3.7.4.2.

the correlation factors in Fig. 3.30 for different compositions of the alloy. In each case, we run Monte Carlo simulations to compare our results with. We calculate the correlation factor in a 2×2 Monte Carlo box with 9×10^4 sites and we let the system reach its equilibrium. We start measuring the diffusion coefficient after 10^8 jumps have been made, and we verify that our results converge with 5×10^3 AKMC blocks of 10^4 AKMC steps, and we make sure that both species jump at least 400 times in each block. In KineCluE and in the AKMC simulation, we calculate saddle-point energies using the Kinetically Resolved Activation (KRA) approximation [147], and we consider all activation energies to be equal and all attempt frequencies to be equal. We show in Fig. 3.31 the AKMC microstructure at different values of concentrations and energies, which helps to see the level of ordering and clustering in each case.

In both our model and the AKMC simulations, the tracer correlation factors f_{A^*} and f_{B^*} are symmetric to each other with respect to the alloy's composition (i.e. f_{A^*} at X_A is equal to f_{B^*} at $1 - X_A$). Therefore, it is sufficient to draw the correlation factors at compositions of A below or equal to 0.5. The first noticeable comparison points are that correlation factors are less precise for higher absolute values of ordering energies and when the alloy's composition approaches an equiatomic distribution. Taking AKMC simulations as the reference calculations, tracer correlation factors calculated with KineCluE are underestimated in alloys with positive ordering energies, and overestimated in alloys with negative ordering energies. Vacancy correlation factors are however always overestimated, except in the case of $X_A = 0.1$ and $W/(k_BT) = -1.96$. For values of $W/(k_BT)$ between -0.5 and $+0.5$, the three correlation factors are in good agreement with the AKMC calculations, such that the relative error is below 20% at all concentrations.

In alloys with high ordering tendencies ($W/(k_BT) = +1.96$), the correlation factor of the dilute species is in very good agreement with the AKMC (relative error below % at all concentrations), while that of the concentrated species is less accurate. At this energy, the vacancy correlation factor deviates the most from the AKMC value which decreases with the A concentration towards a null value. When the ordering energy is high, atom distribution tends to maximize the number of $A - B$ interactions, and A and B atoms are distributed in a highly ordered manner such that A atoms are surrounded only by B atoms, and vice-versa (see Fig. 3.31). In highly ordered alloys, a vacancy which exchanges with any atom will decrease the level of order in the structure and lead to the creation of anti-sites and anti-phase boundaries which decrease the efficiency of its diffusion. A vacancy which exchanges with an A atom for example, breaks $A - B$ bonds and is more likely to exchange with it again to re-increase the number of $A - B$ bonds rather than exchanging with one of its neighboring B atoms. This high probability of jumps and reverse jumps leads to an almost null net displacement of the atoms and the vacancy, and therefore to correlation factors close to 0. This effect is not reproduced by our model because of the small environment radius. With an environment radius consisting of only first nearest-neighbors, in most configurations (all configurations in which the tracer and vacancy environments do not interact) there are no interactions between the environment atoms. Interactions are mainly between the tracer and the environment atoms around it, and between the environment atoms and the mean-field. A vacancy exchanging with an A atom around it needs to break an $A - M$ bond, which is not the same as breaking an $A - B$ bond and is energetically less costly. The reverse jump is also not necessarily more probable than any other jump, and the vacancy's diffusion is therefore not as correlated as it is in the AKMC simulation. This is also the reason why tracer correlation factors are in good agreement. When the vacancy is near the tracer, its exchange frequency with the tracer and its escape frequency both take into account the breaking and forming of bonds. These two frequencies are properly calculated by our model for two reasons: 1. environments include first nearest-neighbors and interaction energies are limited to pair first nearest-neighbors; 2. as explained, in this type of alloys kinetic correlations arise from back and forth vacancy exchanges with atoms, and therefore short trajectories contain most of the information on kinetic correlations.

All this highlights the importance of having sufficiently big environments for thermodynamic and kinetic interactions to be well represented. Large environments are not necessarily needed, as long as the interactions which are the most representative of the system and its thermodynamic energy are properly described.

In alloys with high clustering tendencies, long-range order is needed to properly characterize the decomposition of the system (see Fig. 3.31). This situation is similar to the percolation case, except that jump frequency ratios are not infinite. The discrepancy between our results and the AKMC simulation lies in KineCluE not being able to properly reproduce the connected cluster of A or B atoms, because environments are not being big enough for the short-range order present in them to be well representative of the long-range order of the structure.

Overall, the tracer and vacancy correlation factors calculated with our model are in good agreement with the AKMC simulation for normalized values of the ordering energy between -0.5 and $+0.5$ and for the whole range of alloy composition. Our model is not particularly developed to treat highly ordered alloys as the number of generated environments is small compared to the number of environments one needs to generate in order to reproduce the short-range and the long-range order present in this type of alloys. However, our model reproduces the tracer correlation factor in these alloys with good agreement with the AKMC simulations. Contrary to the vacancy correlation factor, the short-range order around the tracer is well modeled and sufficient for an accurate computation of its correlation factor.

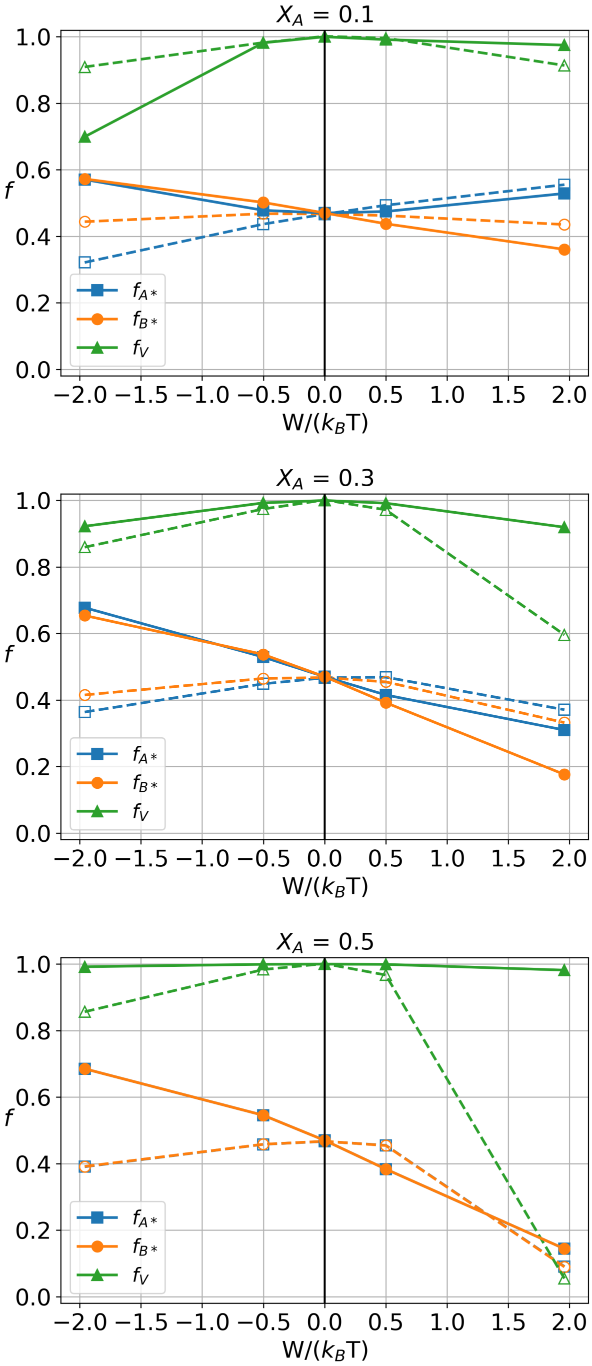

Figure 3.30: Correlation factors (tracers f_{A^*} and f_{B^*}, and vacancy f_V) as a function of ordering energy normalized by k_BT, for three different concentrations of A in the case of a 2D-square binary alloy AB, with clustering (negative W) and ordering (positive W) tendencies. Values obtained from KineCluE (this work) are drawn in solid lines and full symbols, while values obtained from our AKMC simulation are drawn in dashed lines and open symbols. The values of f_{A^*} and f_{B^*} at $X_A = 0.7$ and $X_A = 0.9$ can be deduced from the above figures because f_{A^*} and f_{B^*} are symmetric, and f_{A^*} at a concentration X_A is equal to f_{B^*} at a concentration $1 - X_A$. Note that the error bars on the AKMC results are smaller than the marker's size and therefore not represented.

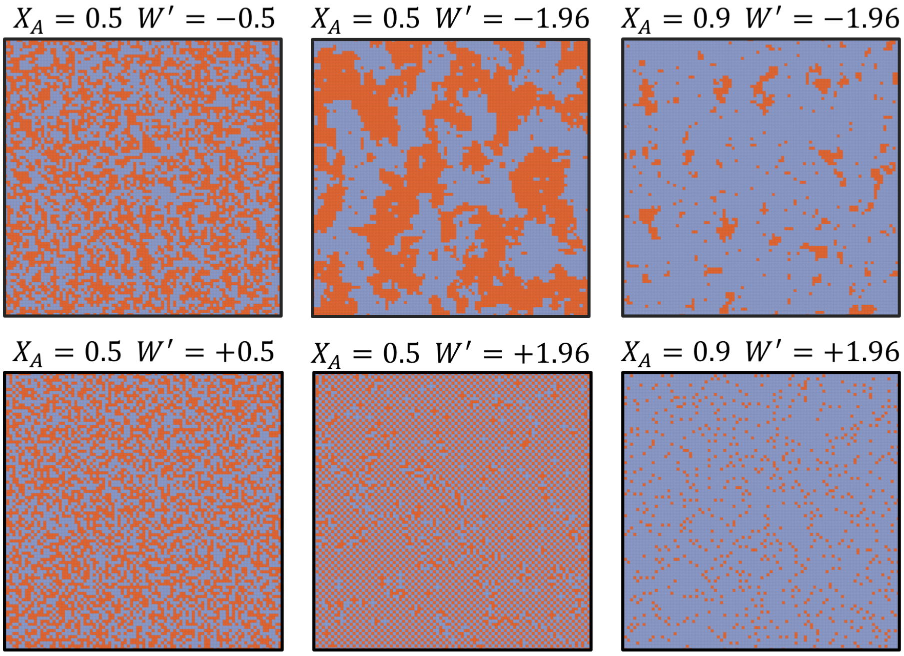

Figure 3.31: AKMC snapshots of the structure at different concentrations and values of the normalized ordering energy ($W' = W/(k_B T)$), in the case of a binary alloy AB with clustering (top) and ordering (bottom) tendencies. A atoms are represented in blue, and B atoms are represented in red. These snapshots were taken using Ovito [142].

3.10 Conclusions of chapter 3

In this chapter, we showed how we extended Schuler's SCMF-d and KineCluE code [18] to concentrated alloys. Our model relies on local environments around cluster components to describe short-range order, and on an original mean-field approximation far from diffusing species in order to simplify the calculations. Despite this, a sampling scheme is necessary to reduce the configuration space which scales with the number of components in the alloy and with the size of the local environments. The computational limitation of the code is its memory requirements, and even though correlation factors converge fast with increasing kinetic radius, the environment radius cannot be increased beyond 3^{rd} nearest-neighbors in the simplest cases and a convergence with respect to the environment radius cannot be achieved. We presented a general sampling scheme and found a good compromise between accuracy and simplicity using a reservoir sampling scheme. The size of the reservoir with respect to the size of the sites we are filling from it controls the local equilibrium approximation that we are imposing on our system and the local configuration composition fluctuations. The reservoir sampling was combined with a pseudo residence-time algorithm which picks configurations based on their thermodynamic weights. We applied our model to the case of an interacting and non-interacting alloy, and we compared our results to the literature results and to our own Monte Carlo simulations. In the case of a random alloy, KineCluE is in agreement with the literature when jump frequency ratios are small, but it cannot reproduce the percolation curve at high jump frequency ratios with a relatively small environment radius. In the case of an interacting alloy, our model is in good agreement with Monte Carlo simulations in both cases of positive and negative ordering energies, with normalized values between -0.5

and +0.5. A larger environment radius is required to reproduce special cases of highly ordered systems and of spinodal decomposition.

3.11 Perspectives of chapter 3

This chapter showed that our model allows for the computation of correlation factors in good agreement with other theories, for a range of exchange frequencies, ordering energies and concentrations. These results are promising because they were obtained using the smallest possible local environments. Increasing the environment radius, even to only second-nearest neighbors, has the potential to improve the accuracy of our model significantly. It is clear however that this is not feasible without sampling the configuration space. We think that our sampling procedure still needs optimization and better understanding of how and what configurations are being sampled at each step.

We saw in Fig. 3.27 that sampling is quite sensitive to the ordering energy. This is most likely related to the combination of both the pseudo residence-time algorithm and the reservoir sampling, which can favor specific couples of initial and final configurations. This needs to be further investigated by analyzing the configurations sampled at each sampling step, by studying whether this occurs at specific concentrations more frequently than others (for example at lower concentrations it is more likely to happen because of the lower number of configurations with local compositions close to the dilute limit). We need to identify whether or not this energy dependency will cause severe trapping in some cases, and if yes, optimize the sampling to deal with such cases. For example, we can allow the code to explore jumps from the same configuration a fixed number of times only.

Additionally, we found in Sec. 3.6, that sampling always overestimates correlations. In some cases, especially when a low percentage of the configuration space is being sampled, we obtain negative correlation factors. It is still not clear if these negative values are physical or an artifact of our sampling procedure. If it is the former, we need to better understand in which cases a subspace of the phase space leads to negative correlation factors in general. If it is the latter, we identified some possible reasons for it. The first one is that, in some cases, the sampled subspace can be a closed system and does not allow diffusion in an infinite volume. This leads to an underestimation of the escape frequency and explains the overestimation of the sampled correlation factor. Intuitively, including all symmetry equivalent configurations and trajectories (which is what we do) seems to be a solution to this problem because it increases the chances of a configuration transitioning into an equivalent version of itself (for example translated version) and creating an open-system. Rigorously, however, there is no guarantee that symmetry equivalents solve the problem in all types of structures and for any jump mechanisms. Additionally, including symmetry equivalent subspaces raises the question of whether or not these subspaces are connected, and at the moment, there is no theoretical evidence that they are. In case they are not, transport coefficients need to be calculated in each subspace separately. Negative correlation factors can also arise as a consequence of simplifications and assumptions made in the formalism, which are no longer valid if not all configurations and trajectories are explored. A simple example is the occupation number Ω_e of an environment e, which depends on the number of sampled environments e and can no longer be written as a function of the number of species and the number of sites in e. Therefore, we need to make sure that the formalism developed for a full configuration space exploration is valid as well in the case of a sampled subspace. As sampling the configuration space is crucial, these studies must be done in a meticulous way.

Currently, computational time is not a limiting problem and it is not expected to be one since the biggest system that can be studied requires around a couple of hours on one processor. Nevertheless, computational time can be optimized for faster calculations which will allow for complete studies of transport coefficients as a function of energies, composition, temperature and strain. Hence, it is advantageous to parallelize the code. Indeed, several parts of the code can be run in parallel, such as the sampling scheme and the construction of the un-correlated and correlated matrices. The configuration space can be sampled in parallel by making sure that the parallel sampling procedures contain at least one cluster-environment configuration in common (to guarantee a connected subspace).

Once the sampling procedure is optimized, it will allow us to test a greater variety of crystalline structures, and to not be limited to a 2D structure. Additionally, in the case of a binary alloy, we can test the effect of not only the ordering energy, but also the energy asymmetry on the transport coefficients (by taking different values of ϵ_{AA} and ϵ_{BB}, ϵ_{AV} and ϵ_{BV}), and we can extend interactions beyond first nearest-neighbors and go on to calculate transport coefficients of FeCr alloys. Eventually, we should be able to test our model in the case of multicomponent alloys beyond the binary limit, in order to see how well the model can predict transport coefficients of high entropy alloys.

Conclusions

The work described in this thesis can be divided in two main parts. Here, we summarize the conclusions obtained in chapters 2 and 3.

- We simulated interdiffusion in nanometric Fe/Cr multilayers using Senninger *et al.*'s Atomic Kinetic Monte Carlo (AKMC) model [9, 16], which was developed to study the $\alpha - \alpha'$ phase separation in FeCr alloys. We compared the concentration profiles and layer thicknesses to experimental multilayers which were studied by our experimental collaborators. We found that the AKMC model reproduces interdiffusion in the Fe-rich region and at the interfaces at 500°C, with overall satisfactory agreement with the experimental results.

- We used the AKMC concentration profiles to simulate X-ray diffraction (XRD) profiles of Fe/Cr multilayers using Pierron-Bohnes' simulation code [138]. We compared the XRD profiles to the experimental profiles and found good qualitative agreement, while experimental XRD profiles exhibit an overall faster decay at 450°C and 500°C.

- We found that an analysis of multilayer XRD profiles based on interference of X-rays allows us to identify the part of the multilayer which affects predominantly each XRD satellite. We also found that, due to diffusion asymmetry, the decay of the logarithm of XRD satellite intensities is linear during specific time ranges of annealing, with a decay rate specific to each satellite. We were therefore able to separated the evolution of the multilayer into separate kinetic regimes, each attributed to diffusion in a specific region of the multilayer.

- We were able to extract, from the simulations and the experiments, interdiffusion coefficients at 450°C and 500°C, and at different concentrations: in high Cr concentration, in high Fe concentration, at the interfaces, and at concentrations close to the solubility limits. We found that the values obtained at 500°C are in satisfactory agreement with values calculated by Senninger *et al.* [9, 16].

- We found that multilayers with strong diffusion asymmetry allow us to extract, from their XRD profiles, interdiffusion coefficients at certain relevant concentrations. Our methodology applies best when interdiffusion coefficients in phases rich in one element are very different, because then, bulk interdiffusion in the different layers happens in separate time-scales and changes the rate of XRD satellite decays in an observable way.

- Experimental observations showed the presence of misfit dislocations and a possible partial coherency growth of the multilayers. For a more complete study, we need to take into account in our simulations the presence of dislocations and the elastic properties of the alloy. This can help improve the simulation results and explain the faster experimental XRD decay at the beginning of annealing.

- We extended the Self-Consistent Mean-Field theory reformulation (SCMF-d) and the KineCluE code to concentrated alloys, and implemented a sampling procedure to reduce the size of the configuration space. The sampling procedure is based on filling environment sites from a reservoir of atoms based on their average composition, combined with a pseudo residence-time algorithm which favors the most thermodynamically stable configurations. Our model introduces an original way to explore a connected configuration space. We start from an initial configuration and extend the configuration space little by little, starting at every step of the sampling from any previously found configuration. The exploration is oriented toward configurations with a high thermodynamic weight and a local composition which fluctuates around the average composition. Then, we are able to reconstruct all possible trajectories between these sampled configurations.

- We applied our model to binary alloys with different ordering energies. In non-interacting alloys, we found good agreement with the literature results when the jump frequencies of the different atomic species were within the same order of magnitude. In interacting alloys with both ordering and clustering tendencies, we found good agreement with AKMC simulations when the ordering energy normalized by $k_B T$ was lower than 0.5 in absolute value.

- In the limit of a very high difference in jump frequencies, the current state of our model does not predict a null diffusion flux when the concentration of the fast diffusing species is below the percolation threshold. We found that our model yields similar results to the original version of the Path Probability Method (PPM), hinting that the long range order (LRO) is constructed from an overlay of copies of the short range order (SRO), and that the SRO of our model is not big enough to be representative of the LRO. We think that this is also the reason why the current implementation of our model cannot be used to study accurately diffusion in alloys undergoing spinodal decomposition or in highly ordered alloys, i.e. systems with high values of ordering energies normalized by $k_B T$.

- We found that correlation factors converge with increasing kinetic and environment radii. A kinetic radius of 6 lattice parameters was enough for our results to converge at different values of ordering energies. Due to computational limitations, we could not increase the environment radius beyond 2 lattice parameters to study in depth the convergence with respect to this parameter.

- We found that the sampling scheme is accurate when more than 1% of the effective interaction classes are sampled. We found that correlations are always overestimated in the sampled configuration space and that the more correlated a system is, the more its correlations are overestimated. Further studies need to be conducted to better understand this effect and construct a reliable sampling scheme in realistic systems where sampling is likely to be well below 1%.

Perspectives

Besides the technical perspectives which were discussed at the end of each chapter, more general perspectives can be suggested in order to complete our study. For a complete understanding of interdiffusion in Fe/Cr multilayers, we need to understand interface mobility and elasticity. This will provide a better understanding of interdiffusion in general, and of interdiffusion as analyzed and quantified from X-ray diffraction (XRD) profiles, as interface mobility and elastic properties are closely linked to the variation of the interplanar lattice spacing profile. On the other hand, in order to be able to calculate transport coefficients in Fe/Cr, among other multi-component alloys, using KineCluE, we need to further optimize and test our sampling procedure. This will allow us to set the convergence parameters to values which ensure the accuracy of the results, while allowing to perform calculations with reasonable computational power. We also need to test the validity of our mean-field model and generalize it to be applicable for a larger variety of applications. In this section, we discuss three perspectives of our work.

Interface mobility model for Fe/Cr multilayers

Interface mobility occurs alongside interdiffusion in multilayers with an asymmetrical miscibility gap and/or asymmetrical diffusion. This can be seen from Kirkendall's experiment (Sec. 2.2.4), and from our AKMC simulations (Sec. 2.11). Interface mobility is therefore closely linked to interdiffusion and it affects layer thicknesses and the lattice spacing profile. It has therefore an effect on the evolution of the XRD profiles. The importance in developing an interface mobility model lies in making the link between the atomic scale (AKMC) and the macroscopic scale (XRD). An interface mobility model can be simple enough to be studied analytically, all while making an explicit link between the atomic and macroscopic scales. The first question which arises it: how can we define the interface unequivocally? Should it be sharp or diffuse? Should the choice be based on a thermodynamic or kinetic argument? Is there or not local equilibrium at the interface?

Available models of interface mobility either assume an interface at a local thermodynamic equilibrium whose mobility is controlled by the slow bulk diffusion [64, 130], or they assume an out-of-equilibrium interface whose mobility is controlled by its deviation from equilibrium concentrations [67]. In each plane of our AKMC simulation, we calculated the gradient of chemical potential difference $\nabla\mu_{\mathrm{CrFe}}$ between the Cr and the Fe chemical potential gradients using Widom's integration scheme [146] and the same AKMC model (Fig. 3.32). We found that $\nabla\mu_{\mathrm{CrFe}}$ is zero at the interface, which is inconsistent with phase-field models which assume a non-null gradient $\nabla\mu_{\mathrm{CrFe}}$ [65]. We suspect that the interface is in a two-phase equilibrium state with different proportions of phases. An example of a model that could apply to Fe/Cr multilayers is presented in Fig. 3.33. In such model, we can express the fluxes as a function of chemical potential gradients, and make the link between the fluxes and Kirkendall's velocity through changes in the reference frames (see Sec. 2.2.4). We need to find a convincing definition of the position of the inner interface which separates the two phases of the interface. We thought of using a lever rule to divide them in a way to keep the average interface concentration C^{nom} constant. This model is conceptually simple, but requires us to better understand the microstructure of the system and the validity of a local equilibrium condition before it is assumed. Further work needs to be done to set meaningful hypothesis, establish the corresponding equations and solve them analytically if possible. An interface mobility model will also require parametrization, and most probably an analytical expression of the interdiffusion coefficient as a function of concentration and temperature. Finally, interface mobility is closely linked to strain and can also be calculated from the lattice parameter variations (calculated in Fig. 2.28) combined with an elasticity theory, which will be discussed in the next paragraph.

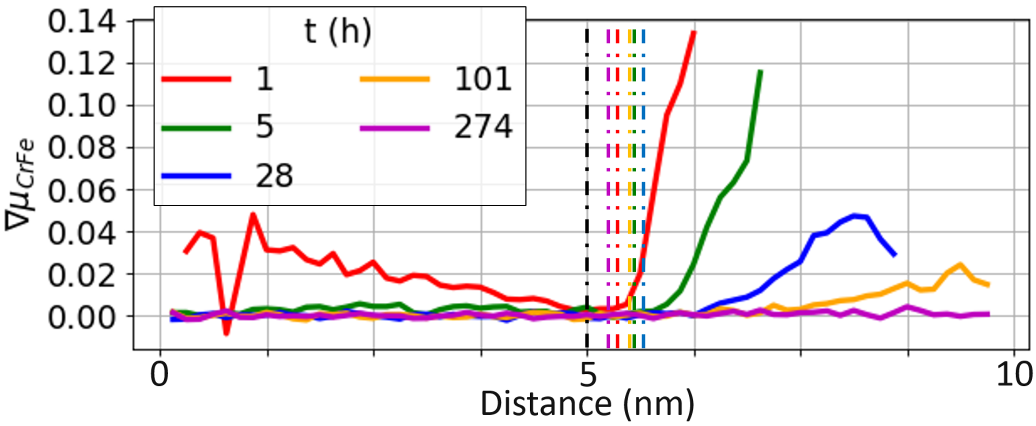

Figure 3.32: Time evolution of the gradient of chemical potential difference $\nabla \mu_{\mathrm{CrFe}}$, at the different planes of the multilayer. The black dashed line indicates the position of the interface before annealing, while colored dashed lines indicate the position of the interface at different annealing times. The position of the interface was determined as the abscissa corresponding to the inflection point of the concentration curve.

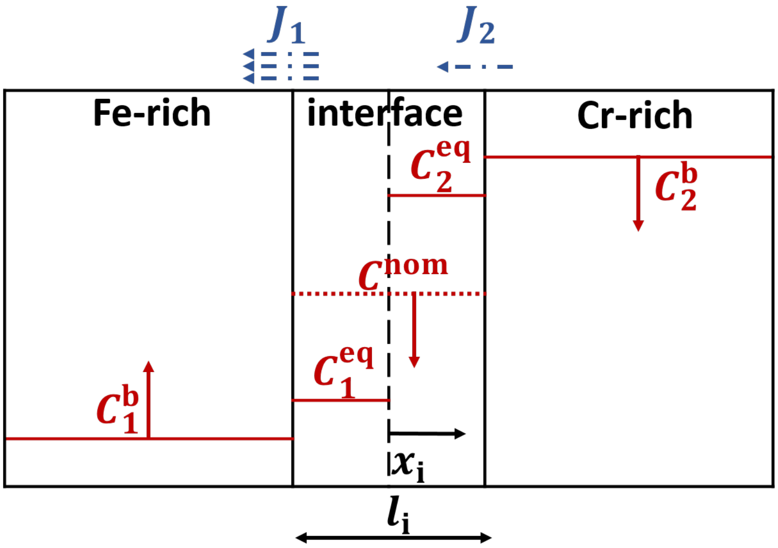

Figure 3.33: Schematic representation of the kind of model which seems relevant to us. J_1 and J_2 are the fluxes between the interface and the layers, C_1^b and C_2^b are the bulk concentrations in the Fe-rich and Cr-rich layers respectively, C^{nom} is the average concentration at the interface, and x_i is the position of the middle interface that splits the two equilibrium phases. Solid line arrows show the evolution of concentrations and plane positions in the case where $J_1 \gg J_2$.

Elasticity of Fe/Cr multilayers

In our AKMC simulations, we assumed a rigid lattice, and in our X-ray diffraction simulations, we assumed a linear Vegard's law to calculate the interplanar spacing profile, which assumes no coherency at the interface [140]. This is a reasonable approximation because loss of coherency is observed in multilayers whose period is larger than approximately 4 nm of thickness [141] (remember that our multilayers have a period of 20 nm). Pierron-Bohnes's measurements of the parallel and perpendicular lattice parameters show a linear relationship between the two and an evolution which is more important at the beginning of annealing (Fig. 2.28). This suggests that misfit dislocations were not enough to relax the multilayers and some residual strain exists in them and leads to a residual stress. With annealing, atoms diffuse across the interface which shifts its position, and the phase proportions at the interface change. Therefore, strain decreases with annealing. Therefore, it is not clear if there is coherency or not at the interfaces, and a partial coherency is the most likely scenario. In this case, the time evolution of the interface mobility can be expressed as a function of the time variation of the ratio of parallel and perpendicular lattice parameters, which provides an additional way to study interface mobility. Transport properties and XRD profiles depend on the degree of coherency in the multilayers and interface mobility, and therefore, for this study to be complete, we must be able to calculate the degree of coherency in our multilayers. Cahn's elasticity model [148], which takes into account surface tension and elastic energy, assumes a completely coherent growth. His model, however, is only valid in multilayers with low composition modulations at the interface, which is not the case of our multilayers in which the concentration gradient varies between approximately the two solubility limits (see Fig. 2.11 for example). Ariosa *et al.* [140] considered the case of partially coherent growth, which is more adapted for a strong composition variation at the interface. Their model relates the strain induced from lattice mismatch to the density of misfit dislocations, which our collaborating experimental teams can measure. This will add a correction to our interplanar spacing profile and modify the simulated XRD profiles. It will be interesting to analyze whether this correction improves the agreement between simulated and experimental XRD profiles, and it will help us to better understand the experimentally measured evolution of the multilayers and make the link between strain, misfit dislocations and interface mobility, and how they affect and are affected by interdiffusion.

Computation of transport coefficients in concentrated alloys using KineCluE

We saw that, in its current state, KineCluE's main limitation is its memory requirements, due to the large size of the configuration space. Optimizing the sampling procedure to be reliable and accurate compared to the full configuration space results, is the number one priority for this work to be complete. In most real applications, the configuration space will be way too large and we will need to sample very small portions of it. Even though it is not a problem, computational time can also be improved by parallelizing some parts of the code. These two points will allow us to test the model in a greater variety of applications, which will help us to better understand the nature and validity of our assumptions and approximations. We need to work some more at getting a deeper understanding of our mean-field definition and what it implies, i.e. what a mean-field atom really represents in our model and how it relates to previous formulations of mean-field interactions. The applications that we presented were made based on a simple energetic model that we developed for theoretical development, and which is not inherent to our SCMF-c model itself. Our energetic model relies on a nearest-neighbors pair interactions and on the first nearest-neighbors pairs CVM for the calculation of chemical potentials, which is probably not a good approximation when second-nearest neighboring pair interactions need to be considered, for instance in the case of FeCr alloys. In such case, we would need to extend the CVM to second nearest-neighbors pairs. We also considered a point approximation when calculating the interactions with mean-field atoms, and we still need to study the effect of the size of the cluster on mean-field energies. There are no conceptual problems for the generalization of our model to any energetic model, except for the treatment of interactions with mean-field atoms. Therefore, our energetic model needs to be further generalized if we want it to be applicable in the case of any concentrated alloy. Ultimately, the application of the code to multi-component alloys (with more than two components) will lead to a better understanding of diffusion in HEA.

Résumé

1. Introduction

Dans la plupart des applications, les métaux ne sont pas utilisés sous leurs formes pures parce que nous pouvons optimiser la composition des alliages en fonction de l'application souhaitée. Il existe une grande variété d'alliages et de propriétés d'alliages, et ces alliages sont utilisés dans différentes applications en fonction des contraintes macroscopiques et des conditions d'utilisation (température, pression, volume, etc...). Alors que les propriétés des alliages étaient autrefois optimisées sur la base d'expérimentations et d'observations macroscopiques, on sait maintenant que les propriétés macroscopiques résultent d'états microscopiques du système. Les atomes sont constamment en mouvement dans un matériau à température finie, ce qui entraîne des sauts atomiques et une redistribution des atomes. La diffusion peut être généralement définie comme le mouvement net de ces atomes. Il est intéressant d'étudier la diffusion parce que ces changements à l'échelle atomique affectent les propriétés macroscopiques des matériaux. De plus, les alliages ont différentes phases à différentes températures et compositions, et chaque phase peut avoir des propriétés différentes. Le phénomène de diffusion permet l'évolution du matériau d'une phase à l'autre et explique comment et à quelle vitesse les propriétés de l'alliage changent.

1.1 Lois de diffusion dans les alliages

Du point de vue phénoménologique, la diffusion est quantifiée par la matrice d'Onsager (ou matrice des coefficients de transport), qui relie le flux macroscopique d'espèces chimiques aux forces motrices de la diffusion (les gradients de potentiel chimique des espèces) [13, 14]. Le flux d'atomes d'espèce β est donné par

$$\vec{J}^{\beta} = -\sum_{\alpha} L_{\beta\alpha} \frac{\vec{\nabla}\mu_{\alpha}}{k_B T}, \tag{3.151}$$

où les $L_{\beta\alpha}$ constituent les coefficients de transport d'Onsager, $\vec{\nabla}\mu_{\alpha}$ est le gradient de potentiel chimique de l'espèce α, k_B est la constante de Boltzmann, et T est la température. Notez que la matrice d'Onsager est une matrice symmétrique définie positive. Il existe toute une zoologie de coefficients de diffusion qui sont utilisés pour quantifier la diffusion dans des conditions spécifiques, comme la diffusion de traceur ou l'interdiffusion. Les coefficients de diffusion représentent alors un cas particulier de la matrice d'Onsager.

Du point de vue atomique, la diffusion est le résultat d'une marche aléatoire des espèces qui se déplacent de proche en proche. Dans le cas d'une diffusion isothèrme sur un réseau de volume total V, en généralisant la formule d'Einstein [79], Allnatt [81] a établi le lien entre les coefficients de transport et les fluctuations d'équilibre des positions atomiques. Les coefficients $L_{\beta\alpha}$ sont calculés en fonction du déplacement quadratique moyen des atomes β et α à l'équilibre,

$$L_{\beta\alpha} = \lim_{t\to\infty} \frac{\left\langle \vec{R}_\beta\left(t\right) \vec{R}_\alpha\left(t\right) \right\rangle}{6Vt}, \tag{3.152}$$

où t est le temps durant lequel le vecteur de déplacement collectif des atomes de l'espèce α est $\vec{R}_\alpha\left(t\right)$. Les $\langle . \rangle$ représentent une moyenne thermodynamique sur un ensemble de réalisation et le temps de calcul doit être suffisamment long pour assurer une bonne statistique et un calcul précis.

Même si les sauts atomiques individuels sont aléatoires et suivent un processus markovien, différentes séquences de sauts ne sont pas nécessairement équiprobables. Ces corrélations entre sauts successifs résultent de la géométrie du système et/ou des interactions entre différentes espèces chimiques. Les corrélations peuvent être quantifiées en introduisant les facteurs de corrélation des espèces qui quantifient l'écart des coefficients de transport totaux par rapport aux coefficients de transport idéaux, c'est-à-dire correspondant à une marche aléatoire sans bias dans les trajectoires. Le facteur de corrélation diagonal $f_{\alpha\alpha}^{(\alpha)}$ peut être calculé en fonction du coefficient de transport diagonal $L_{\alpha\alpha}$ et de sa valeur non corrélée $L_{\alpha\alpha}^0$,

$$f_{\alpha\alpha}^{(\alpha)} = \frac{L_{\alpha\alpha}}{L_{\alpha\alpha}^0}. \tag{3.153}$$

Le facteur de corrélation non-diagonal $f_{\beta\alpha}^{(\gamma)}$ quantifie la déviation du coefficient de transport $L_{\beta\alpha}$, par rapport au coefficient $L_{\gamma\gamma}^0$ où γ est soit α soit β,

$$f_{\beta\alpha}^{(\gamma)} = \frac{L_{\beta\alpha}}{L_{\gamma\gamma}^0}. \tag{3.154}$$

La difficulté du calcul analytique des facteurs de corrélation réside dans le fait de devoir calculer des moyennes de vecteurs de déplacement successifs d'atomes, et de devoir trouver toutes les trajectoires possibles des atomes suivis, ce qui n'est pas faisable dans le cas général de la diffusion à plusieurs corps. Malgré le fait qu'il est difficile de calculer analytiquement les facteurs de corrélation, ils sont importants dans de nombreux cas, notamment à basse température, et doivent être pris en compte pour une description complète du phénomène de diffusion.

1.2 Diffusion dans les alliages concentrés

Dans cette thèse, nous nous sommes intéressés particulièrement à l'étude de la diffusion dans les alliages concentrés. Par définition, un alliage concentré est un alliage avec au moins deux composants présents à des concentrations relativement élevées (c'est-à-dire des concentrations supérieures à 1%). Les alliages concentrés comprennent les alliages à haute entropie (HEA), qui sont un mélange d'au moins cinq éléments présents dans des proportions comparables. L'augmentation du nombre d'éléments dans un matériau ajoute une complexité chimique au problème de la diffusion, notamment des corrélations cinétiques apparaissent en raison de la différence d'espèces chimiques occupant les différents sites du système.

Il est difficile de quantifier les coefficients de transport en général, et en particulier dans le cas des alliages concentrés. Des expériences de diffusion, des approches numériques stochastiques et des modèles théoriques ont tous été utilisés pour une meilleure compréhension des phénomènes de diffusion. Cependant, chacune de ces méthodes a ses propres forces et limites.

Les expériences de diffusion ne sont généralement réalisables qu'à des températures élevées et, dans la plupart des cas, il n'est pas correct d'extrapoler les résultats aux basses températures. Pour surmonter cet obstacle, des expériences de diffusion peuvent être réalisées dans des matériaux présentant une microstructure nanométrique afin de réduire les distances de diffusion pertinentes. Par exemple, les multicouches nanométriques permettent l'étude de l'interdiffusion à des températures relativement basses et en un temps raisonnable. Dans le cas général, les expériences de diffusion deviennent plus difficiles à établir et surtout à analyser avec l'augmentation du nombre de composants, et dans la plupart des cas, elles ne permettent pas de mesurer la matrice d'Onsager entière.

Par ailleurs, les approches numériques stochastiques nécessitent le calcul de moyennes de déplacement, et peuvent donc souffrir de problèmes de piégeage cinétique et de convergence. Cela est particulièrement vrai lors de l'étude de systèmes hautement corrélés d'alliages concentrés et lors du calcul des coefficients de transport hors diagonaux. Ces problèmes peuvent dans de nombreux cas être résolus à l'aide d'algorithmes d'optimisation qui empêchent le système de rester bloqué dans les minima locaux. En revanche, il reste difficile de calculer la matrice d'Onsager dans des systèmes hors d'équilibre car la mesure est faite en parallèle de la décomposition du système et il n'est pas trivial de garantir la convergence des résultats.

Les approches analytiques et théoriques ont tenté de surmonter ces problèmes, mais elles souffrent de devoir calculer explicitement les effets de corrélation. Cela nécessite l'étude exhaustive de toutes les configurations possibles du système et de toutes les trajectoires. Ceci est particulièrement difficile dans les alliages concentrés car le nombre de configurations et de fréquences de saut devient vite gigantesque avec le nombre croissant de composants et de sites dans le système. C'est pourquoi les approches théoriques s'appuient fortement sur des approximations cinétiques et thermodynamiques afin de réduire l'espace de configuration. Actuellement, des modèles théoriques ont été appliqués soit dans le cas d'un alliage sans interactions [19, 20], soit dans le cas d'un alliage avec interactions dans des cas particuliers de structures et de mécanismes de diffusion [21, 22].

1.3 Objectifs de la thèse

Le besoin d'un modèle général pour étudier la diffusion dans un alliage concentré est toujours présent. L'objectif des deux sections suivantes est de fournir des modèles à l'échelle atomique pour calculer les coefficients d'interdiffusion et les coefficients de transport dans les alliages concentrés. Dans la première section, nous avons étudié l'interdiffusion dans le système spécifique des alliages FeCr. Nous avons réalisé une étude d'interdiffusion à basse température dans des multicouches nanométriques afin de mesurer les coefficients d'interdiffusion à partir de profils de diffraction des rayons X (DRX). Ce travail a combiné des expériences et des simulations de Monte Carlo cinétique à l'échelle atomique (AKMC). Dans la deuxième section, nous présentons un nouveau modèle théorique développé pour calculer les coefficients de transport dans le cas général des alliages concentrés, ainsi que son implémentation dans un code de calcul automatisé.

2. Interdiffusion dans les multicouches Fe/Cr

2.1 État de l'art

Le coefficient d'interdiffusion des alliages FeCr dépend fortement de la concentration, et beaucoup de travaux ont tenté de le calculer en fonction de la concentration et de la température, du point de vue expérimental et à partir de simulations AKMC. Senninger et al. ont développé une simulation AKMC et comparé leurs coefficients d'interdiffusion aux valeurs expérimentales et ils ont trouvé un bon accord dans les environnements riches en Fe, en particulier à des températures élevées [9,16]. Il n'y a cependant pas de données expérimentales ou *ab initio* dans les environnements riches en Cr, ce qui rend difficile de juger de la validité des simulations dans cette région, sachant que la simulation est ajustée à la fois sur les données expérimentales et *ab initio*. De plus, il n'y a pas de données expérimentales à des températures inférieures à 642°C. Récemment, G. Magnifouet-Tchinda et V. Pierron-Bohnes de l'IPCMS Strasbourg ont fait croître des multicouches Fe/Cr nanométriques dans la direction (100) en utilisant l'épitaxie par jets moléculaires et les multicouches ont été recuites à basse température (450°C et 500°C) [60]. Des mesures de diffraction des rayons X ont été effectuées à différents temps de recuit et les profils de diffraction ont montré un pic principal de Bragg entouré de quatre satellites, deux de chaque côté. Pendant le recuit, il a été observé que l'intensité normalisée des satellites décroissait. Cependant, la relation entre cette décroissance et l'interdiffusion n'est pas établie, et certaines questions demeurent ouvertes concernant ce que représente chaque pic et sur l'obtention des coefficients d'interdiffusion à partir de la décroissance de l'intensité des pics.

L'objectif de cette partie est de calculer les coefficients d'interdiffusion à partir de profils de diffraction des rayons X simulés et expérimentaux, aux basses températures de 450°C et 500°C.

2.2 Résultats

Nous avons simulé les multicouches nanométrique ainsi que l'évolution de leurs profils de concentration lors du recuit à l'aide de la simulation AKMC développée par Senninger et al. [9, 16]. Nous avons simulé deux bi-couches de FeCr avec des conditions aux limites périodiques aux températures constantes de 450°C et 500°C séparément. Afin de tester la validité de la simulation AKMC, nous avons comparé les profils de concentration simulés aux profils des multicouches caractérisés expérimentalement avant recuit et après recuit à 500°C pendant 4h. Expérimentalement, la sonde atomique tomographique (APT) a été utilisée pour mesurer les concentrations au milieu de chaque couche et le microscope Electronique en Transmission en mode STEM/HAADF a été utilisé pour mesurer les épaisseurs des couches [149]. Dans la simulation et l'expérience, on a observé après le recuit que le Cr diffuse dans la couche riche en Fe alors que le Fe ne diffuse pas au milieu de la couche riche en Cr. On a observé aussi que l'épaisseur de la couche Fe augmente avec le recuit. Ces observations sont à la fois qualitativement et quantitativement en accord entre la simulation et l'expérience. La cinétique d'interdiffusion est alors bien reproduite par la simulation AKMC, au moins à la température de 500°C et après un recuit de 4h.

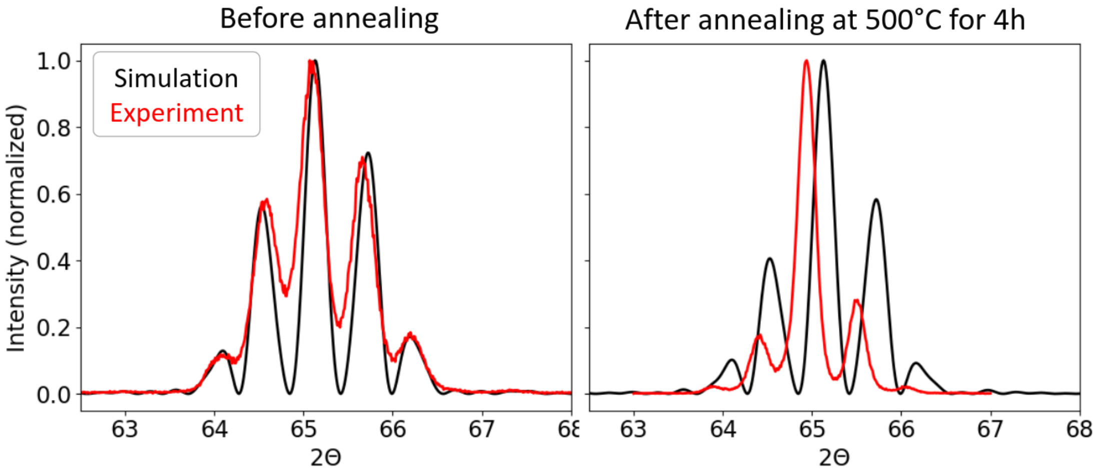

Figure 3.34: Profils DRX simulés (noire) et expérimentaux (rouge), avant recuit (gauche) et après un recuit à 500°C pendant 4h (droite). L'intensité à un temps t, $I\left(t\right)$, est normalisée par l'intensité du pic central au temps t, $I_0\left(t\right)$, tel que l'intensité dessinée correspond à $I\left(t\right)/I_0\left(t\right)$.

Nous avons ensuite utilisé les profils de concentration obtenus par AKMC pour simuler l'évolution du profil DRX avec le recuit. Nous avons utilisé un code DRX précédemment développé qui simule, à partir du profil de concentration, le profil d'espacement du réseau et le profil du facteur de diffusion [138]. Les profils d'espacement entre deux plans consécutifs et du facteur de diffusion de chaque plan sont considérés comme évoluant linéairement avec la concentration. Les distance inter-atomiques du Cr pur et du Fe pur mises en entrée du code ont été obtenues à partir d'une étude précédente [60], et les facteurs de diffusion de Cr et de Fe ont été donnés par Cromer et Mann [139]. L'intensité diffractée en fonction de l'angle 2θ est obtenue à l'aide des lois de diffraction de Bragg. Afin de tester la validité de la simulation DRX, nous avons comparé les profils diffractés simulés aux profils expérimentaux, avant recuit et après recuit à 500°C pendant 4h (Fig. 3.34). Avant recuit, les positions et intensités des pics ont été en bon accord qualitatif et quantitatif. Cela a montré que les paramètres d'entrée de la simulation sont en bon accord avec les conditions expérimentales. Après recuit, les pics satellites expérimentaux avaient des intensités plus faibles et un décalage plus prononcé vers les valeurs inférieures de 2θ. La décroissance des pics de l'expérience plus rapide peut signifier que l'interdiffusion est plus rapide dans l'expérience. Cependant, ceci est en contradiction avec ce que nous avons observé lorsque nous avons précédemment comparé les profils de concentration à la même température et après la même durée de recuit. La décroissance expérimentale plus rapide est une conséquence de quelque chose qui manque soit dans la simulation AKMC, soit dans la simulation DRX, soit dans les deux. Notez que les positions des pics sont généralement liées aux espacements des plans du réseaux (selon la loi de Bragg), ce qui laisse entendre que les simulations pourraient ne pas reproduire correctement l'évolution du profil de distance inter-plans. Afin de mieux comprendre l'écart entre les profils DRX simulés et expérimentaux, nous avons d'abord tenté d'analyser l'origine de chaque satellite.

Afin de quantifier les décroissances d'intensités des satellites et de calculer les coefficients d'interdiffusion à partir de ces décroissances, nous avons utilisé un modèle qui combine la loi de Fick [28] et la théorie de Guinier [25]. Cette théorie combinée suppose un coefficient d'interdiffusion constant et aucune fluctuation des paramètres de réseau [26], ce qui ne s'applique pas au cas des alliages FeCr. Nous avons surmonté ces contraintes en séparant d'abord l'évolution temporelle de notre système en plusieurs régimes cinétiques puis en traitant chaque satellite séparément. Pour identifier les régimes cinétiques, on a trouvé les plages de temps dans lesquelles la décroissance des satellites est linéaire et nous avons supposé donc qu'il n'y a qu'un seul coefficient d'interdiffusion qui domine dans la redistribution des atomes dans le système. Étant donné que chaque satellite provient d'interférences dans une partie du système, nous avons identifié ces parties en fonction de la position de chaque satellite. Nous avons remarqué que les positions des satellites de premier ordre -1 et +1 correspondent respectivement aux espacements de réseau dans le Cr pur et le Fe pur respectivement. Nous pensons que les satellites de premier ordre correspondent aux principaux pics de diffraction des couches de Cr et de Fe respectivement, et que ce sont les seuls pics avec une interprétation physique directe. Dans cette théorie combinée, le logarithme de la décroissance de l'intensité du satellite est linéaire avec le temps et la pente est fonction de la période de la multicouche et d'un coefficient d'interdiffusion constant. Connaissant la période de la multicouche, cette théorie permet le calcul du coefficient d'interdiffusion en traçant le log de la décroissance de l'intensité en fonction du temps de recuit. Nous avons appliqué cette méthodologie aux décroissances d'intensité de satellites de DRX des multicouches recuites à 450°C et 500°C, obtenus par l'expérience et par la simulation.

En analysant l'évolution du profil de concentration dans chaque régime cinétique linéaire, nous avons identifié dans la simulation un premier régime linéaire rapide (régime A) durant lequel le Cr diffuse dans la couche riche en Fe et l'interface se décale vers la couche riche en Cr . Nous avons identifié un second régime linéaire plus lent (régime C) dans lequel le Fe diffuse dans la couche riche en Cr et l'interface se décale en sens inverse, vers la couche riche en Fe. Nous avons également identifié un régime intermédiaire non linéaire (régime B) dans lequel les deux régimes linéaires A et C coexistent.

A 500°C, nous avons comparé les coefficients d'interdiffusion calculés à partir des profils simulés aux valeurs obtenues par Senninger et al. [9, 16] en utilisant la même simulation AKMC combinée à la méthode d'atténuation des ondes (Figure 3.35). Les valeurs que nous avons obtenues à partir du régime A (resp. régime C) correspondent aux valeurs de Senninger dans des environnements riches en Fe (resp. riches en Cr). Cela a validé notre méthodologie et a montré que, en utilisant la même simulation AKMC, nous pouvons calculer les coefficients d'interdiffusion en utilisant une méthode d'atténuation des ondes ou une méthode de décroissance de satellites de DRX.

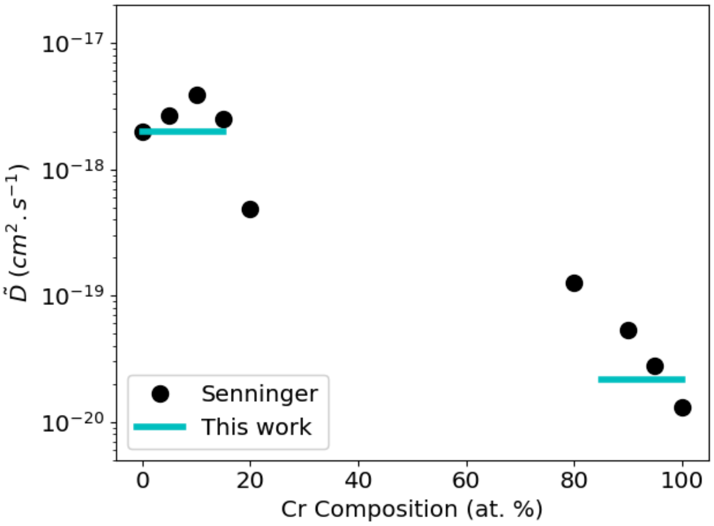

Figure 3.35: Coefficients d'interdiffusion obtenus à 500°C par Senninger [9, 16] (points) et par notre méthodologie à partir des profils de DRX simulés (lignes continues).

A 450°C et 500°C, nous avons comparé les coefficients d'interdiffusion obtenus à partir des profils simulés et expérimentaux en régime A et nous avons trouvé un bon accord aux deux températures, l'expérience donnant des valeurs légèrement supérieures mais restant dans la précision acceptée (Figure 3.36). Notez que l'écart augmente avec la température décroissante, et cela peut être dû au fait que la simulation est ajustée sur des données expérimentales à haute température. Notez également que le régime C n'a pas été étudié expérimentalement car les expériences n'ont pas été assez longues pour l'observer. A 450°C, l'expérience a présenté en plus de ces régimes une très forte décroissance d'intensité au début du recuit qui n'a pas été observée dans la simulation. Nous pensons que ce régime très rapide est dû à la présence de dislocations et d'inclusions riches en Fe traversant les couches riches en Cr, qui ont été observées à l'aide de l'APT et qui ne sont pas modélisées dans la simulation.

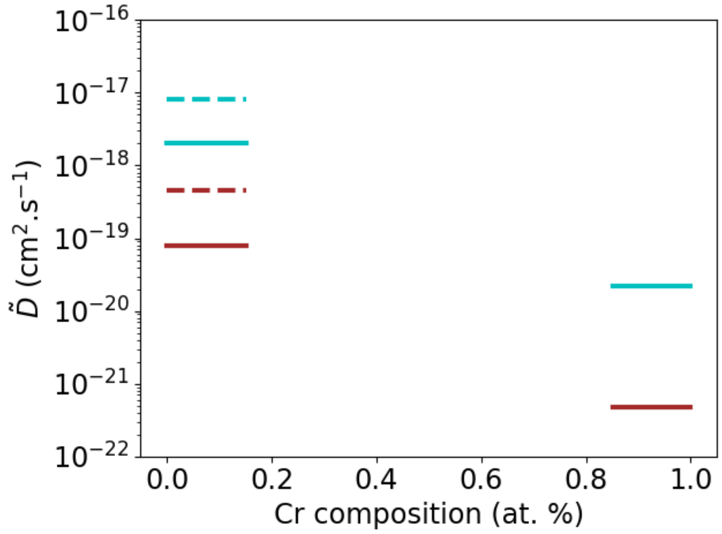

Figure 3.36: Coefficients d'interdiffusion obtenus par notre méthodologie à 450°C (marron) et 500°C (bleu), à partir des profils de DRX simulés (lignes continues) et expérimentaux (lignes pointillées).

2.3 Conclusions et perspectives

Nous avons montré que si les régimes cinétiques dans lesquels un seul mécanisme de diffusion domine sont bien identifiés et si on comprend bien à quelle partie de la multicouche chaque satellite est sensible, des coefficients d'interdiffusion dépendant de la concentration peuvent être obtenus à partir d'une théorie basée sur un coefficient d'interdiffusion constant et un espacement de plans de réseau constant. En l'absence de modèles analytiques qui permettent le calcul des coefficients d'interdiffusion dépendants de la concentration à partir des profils DRX, notre travail fournit une alternative simple et quantitative. Nous avons pu calculer à partir de la simulation et de l'expérience, des coefficients d'interdiffusion à 500°C dans des environnements riches en Fe et riches en Cr, avec une précision satisfaisante par rapport aux travaux de Senninger. Nous avons également pu fournir ces valeurs à 450°C. En utilisant les données expérimentales sur les multicouches nanométriques, nous avons pu fournir des valeurs à 450°C et 500°C dans des environnements riches en Fe, qui correspondent à des températures qui n'avaient jamais été étudiées expérimentalement auparavant. Par conséquent, cette étude peut également aider à fournir des données expérimentales à plus basse température afin de mieux ajuster la simulation AKMC.

Malgré le fait que les expériences ont été réalisées en utilisant des multicouches nanométriques, le régime cinétique lent de la diffusion du Fe dans le Cr n'a pas pu être exploré et pourrait être inaccessible à des températures inférieures à 500°C dans notre système (par example, à 450°C, le temps nécessaire serait de l'ordre d'une année d'après nos simulations AKMC). La validité de la simulation dans des environnements riches en Cr n'a pas pu être vérifiée, et un recuit expérimental plus long serait nécessaire, au moins à 500°C. Les deux limites principales de cette étude sont que, d'une part, elle s'applique mieux aux systèmes dans lesquels il existe une forte asymétrie d'interdiffusion, et d'autre part, elle ne permet pas le calcul du coefficient d'interdiffusion à des concentrations spécifiques, mais plutôt dans des plages de concentration dans notre cas données par limites de solubilité. D'autres travaux théoriques et appliqués doivent être menés afin de tester cette méthode sur d'autres alliages et de déterminer ses limites de validité, et si elle peut ou non être étendue au cas de n'importe quel alliage binaire.

3. Éxtention du SCMF-d et KineCluE aux alliages concentrés

3.1 État de l'art

Actuellement, il existe trois principaux modèles théoriques pour calculer les coefficients de transport dans les alliages concentrés : le modèle d'alliage aléatoire (RA) de Manning [19, 20], la méthode “Path Probability Method” (PPM) de Kikuchi [21] et la théorie de champ moyen auto-cohérent (SCMF-o) de Nastar [22]. Le modèle de Manning a été largement utilisé en raison de sa simplicité, mais il s'applique uniquement aux alliages dans lesquels les interactions thermodynamiques peuvent être négligées. De plus, dans la plupart des cas, le modèle a été appliqué à la diffusion via une faible concentration de lacunes. D'autre part, la PPM et le SCMF-o ont été en théorie développées pour le cas général des alliages avec interactions via n'importe quel mécanisme de diffusion. Ces deux méthodes sont cependant théoriquement difficiles à appliquer et elles étaient principalement appliquées à des systèmes simples spécifiques, tels que l'alliage binaire avec diffusion de lacunes dans un cristal cubique. Le fait que ces deux méthodes soient spécifiques au système n'aide pas puisque les équations analytiques doivent être retravaillées depuis le début pour chaque cas différent. Des approximations thermodynamiques et cinétiques strictes ont également été utilisées dans les deux cas pour simplifier le problème mathématique. Même si la PPM et le SCMF-o partagent de nombreuses similitudes, le SCMF-o offre plus de flexibilité en découplant l'approximation cinétique de l'approximation thermodynamique et traite par conséquent les corrélations cinétiques plus rigoureusement, ce qui a permis son application à une plus grande variété de problèmes de diffusion. Le SCMF-o a été reformulée ces dernières années par Schuler et al. [18], et cette nouvelle formulation que nous appelons SCMF-d, a été implémentée dans un code de calcul open-source appelé KineCluE. Cependant, les hypothèses du SCMF-d ne la rendent valable que dans le cas des alliages très dilués.

Le SCMF-d est basée sur un développement en amas cinétique du système. On suppose que le système est suffisamment dilué pour le diviser en amas indépendants. Chaque amas est constitué d'un groupe d'espèces qui diffusent. Ces espèces sont entourées d'un milieu homogène, c'est-à-dire que chaque site du cristal (autres que ceux occupés par les espèces de l'amas) est occupé par des atomes identiques. Les composants de l'amas diffusent dans un rayon cinétique tel que l'amas se dissocie lorsqu'une des espèces diffusantes s'éloigne au-delà de ce rayon cinétique par rapport à toutes les autres espèces diffusantes. Le coefficient de transport total est alors calculé comme la somme des coefficients de transport de tous les amas, chacun pondéré par la concentration d'amas correspondante. KineCluE calcule les coefficients de transport d'amas, tandis que les concentrations des amas sont calculées séparément par l'utilisateur. Ces concentrations peuvent être des concentrations à l'équilibre ou hors d'équilibre, ce qui permet le calcul des coefficients de transport totaux de systèmes à l'équilibre et hors équilibre. La raison pour laquelle le SCMF-d, ainsi que d'autres théories précédemment développées pour les alliages dilués [38–42], ne peut pas être utilisée dans le cas des alliages concentrés est que le milieu autour des espèces diffusantes est considéré comme homogène. Dans un alliage concentré composé de plusieurs espèces, le milieu autour des espèces qui diffusent est hétérogène, c'est-à-dire que plusieurs espèces peuvent occuper chaque site du système et l'environnement des espèces diffusantes dépend de leur emplacement dans le système. En conséquence, le problème ne peut pas être résolu d'une manière exacte car le nombre de configurations possibles évolue de manière exponentielle avec le nombre d'espèces et de sites dans le système. Cela rend impossible dans la plupart des cas l'énumération complète des toutes les configurations et fréquences de saut dans le système. D'un autre côté, utiliser une approximation en champ moyen et remplacer le milieu hétérogène par un milieu homogène moyen réduit l'alliage concentré à un alliage dilué moyen. Cela fait perdre beaucoup d'informations et empêche une prise en compte correcte des corrélations cinétiques puisque tous les sites deviennent chimiquement équivalents.

Dans ce chapitre, nous montrons comment nous avons étendu le SCMF-d et KineCluE aux alliages concentrés. Notre modèle s'appuie sur des environnements locaux spécifiques autour des composants d'amas pour décrire l'ordre à courte portée, et sur une approximation originale de champ moyen loin des espèces diffusantes afin de simplifier les calculs.

3.2 Résultats

Nous avons étendu le SCMF-d aux alliages concentrés en considérant dans chaque amas une approche intermédiaire entre la solution exacte et l'approximation du champ moyen. Autour des espèces qui diffusent nous avons considéré un "environnement" local et c'est uniquement au sein de ce milieu que nous avons étudié toutes les occupations possibles des sites. Loin des espèces qui diffusent et autour des environnements locaux, nous avons utilisé une approximation de champ moyen en considérant que chaque site est occupé par un atome "moyen". Les propriétés de cet atome "moyen" satisfont une équation mathématique qui permet de remplacer une somme d'exponentielles d'énergie d'un nombre infiniment grand de configurations par une exponentielle d'énergie d'une seule configuration dans laquelle les sites sont remplacés par des atomes "moyens'. En d'autres termes, cela signifie que la contribution au problème de diffusion provenant de différentes configurations ayant la même configuration d'espèces diffusantes et d'environnement est équivalente à la contribution provenant d'une seule et même configuration d'espèces diffusantes et d'environnement entourés d'un milieu homogène d'atomes moyens. Nous avons implémenté notre modèle dans le code KineCluE qui permet désormais l'étude des alliages dilués et concentrés. Dans le cas des alliages concentrés, le code prend une configuration initiale des espèces de l'amas et construit autour d'elles un environnement en fonction du rayon choisi par l'utilisateur. Le code explore ensuite toutes les occupations possibles de ces sites. Pour chaque occupation possible, le code trouve tous les sauts possibles et les configurations accessibles, et calcule toutes les fréquences de saut de telle sorte que, lorsque les atomes sont en position de point-col, l'environnement qui les entoure est une combinaison de l'environnement autour de la configuration initiale et de l'environnement autour de la configuration finale. Une fois le saut effectué, les sites qui ne sont plus à l'intérieur du rayon de l'environnement autour de la configuration finale sont considérés comme occupés par des atomes moyens. De cette façon, le code trouve toutes les configurations connectées possibles pour des rayons cinétique et d'environnement spécifiés par l'utilisateur.

Nous avons appliqué le code pour calculer les facteurs de corrélation des atomes de traceurs dans les alliages binaires pour une large gamme d'énergies d'ordre.

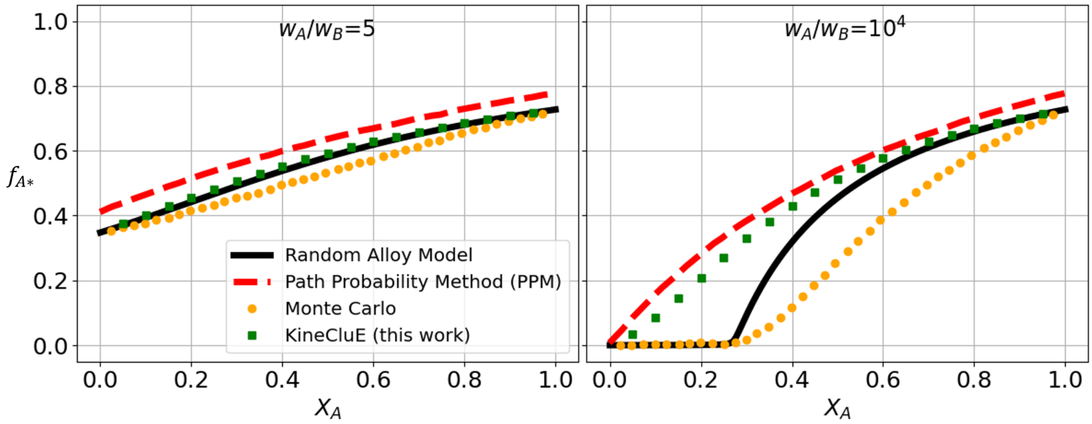

Figure 3.37: Facteur de corrélation du traceur rapide, f_{A^*}, en fonction de la composition, dans le cas d'un alliage binaire aléatoire avec une structure BCC, pour un rapport de fréquence de saut faible (égal à 5, gauche) et pour un rapport de fréquence de saut élevé (égal à 10^4, droite), calculé avec KineCluE (ce travail) et comparé aux résultats de la littérature: modèle de l'alliage aléatoire de Manning [19, 20], la PPM de Kikuchi [46], et les simulations Monte Carlo [29]. Notons que les résultats Monte Carlo sont considérés comme les valeurs de référence.

Dans le cas d'un alliage binaire aléatoire, c'est-à-dire un alliage sans interactions thermodynamiques, ayant une structure BCC et dans lequel le rapport de fréquence de saut est faible ($w_A/w_B = 5$), le facteur de corrélation du traceur calculé par le code est en très bon accord avec les résultats de la littérature à toutes les concentrations (Figure 3.37 à gauche). Dans le cas d'un rapport de fréquence de saut élevé ($w_A/w_B = 10^4$), le facteur de corrélation du traceur calculé par le code ne reproduit pas la courbe de percolation prédite par le modèle de Manning (Random Alloy Model, i.e. RA) et par les simulations AKMC (Figure 3.37 à droite). Cela est dû au fait que les environnements autour de la lacune sont trop petits et conduisent à une surestimation de la fréquence d'échappement de la lacune de l'atome traceur. L'augmentation des rayons d'environnement au-delà des premiers voisins nécessite une mémoire de calcul supérieure à celle disponible sur nos machines.

Dans le cas d'un alliage binaire aléatoire avec une structure carrée 2D, on observe que certaines combinaisons de rayons cinétique et d'environnement permettent la reproduction du facteur de corrélation nul en dessous du seuil de percolation à des concentrations de l'espèce rapide inférieures à 0.15. On observe en outre que certaines combinaisons conduisent à des résultats plus précis avec moins de mémoire de calcul. Par conséquent, il est possible de trouver, dans chaque cas, une combinaison de rayons cinétique et d'environnement pour obtenir les résultats les plus précis avec le moins de ressources de calcul possible.

On a considéré ensuite le cas d'un alliage binaire dans lequel les interactions thermodynamiques ne peuvent pas être négligées. On a considéré des interactions de paires de premiers voisins et on a quantifié les interactions par une énergie d'ordre. Les facteurs de corrélation des traceurs calculés avec notre modèle sont en bon accord avec la simulation AKMC pour les faibles énergies d'ordre (c'est-à-dire avec des valeurs normalisées de l'énergie d'ordre entre -0,5 et +0,5) et pour toute la gamme de composition d'alliage (Figure 3.38).

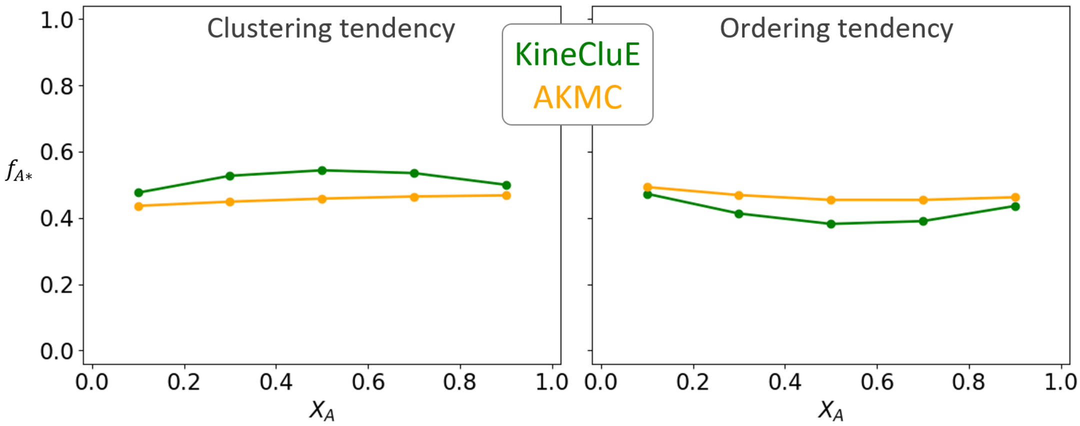

Figure 3.38: Facteur de corrélation f_{A^*} en fonction de la composition dans le cas d'un alliage binaire avec une structure 2D-carrée et un ordre à courte distance (énergie d'ordre normalisée égale à 0.5).

Dans les alliages à forte tendance à la démixion (Figure 3.39 à gauche), un ordre à longue distance est nécessaire pour caractériser correctement la décomposition du système. Cette situation est similaire au cas de la percolation, sauf que les rapports de fréquence de saut ne sont pas infinis. L'écart entre nos résultats et la simulation AKMC réside dans le fait que KineCluE n'est pas en mesure de reproduire correctement l'amas connexe d'atomes A ou B, car les environnements ne sont pas assez grands pour que l'ordre à courte distance qui y est présent soit bien représentatif de l'ordre à longue distance de cette structure.

Notre modèle n'est pas particulièrement développé pour traiter les alliages hautement ordonnés car le nombre d'environnements générés est faible par rapport au nombre d'environnements qu'il faut générer pour reproduire l'ordre à courte distance ainsi que l'ordre à longue distance présents dans ce type d'alliages. Malgré cela, notre modèle reproduit le facteur de corrélation de traceur dans ces alliages avec un bon accord avec les simulations AKMC (Figure 3.39 à droite). En effet, l'ordre à courte distance autour du traceur est bien modélisé par KineCluE et suffisant pour un calcul précis de son facteur de corrélation et pour une bonne reproduction de l'ordre à longue distance.

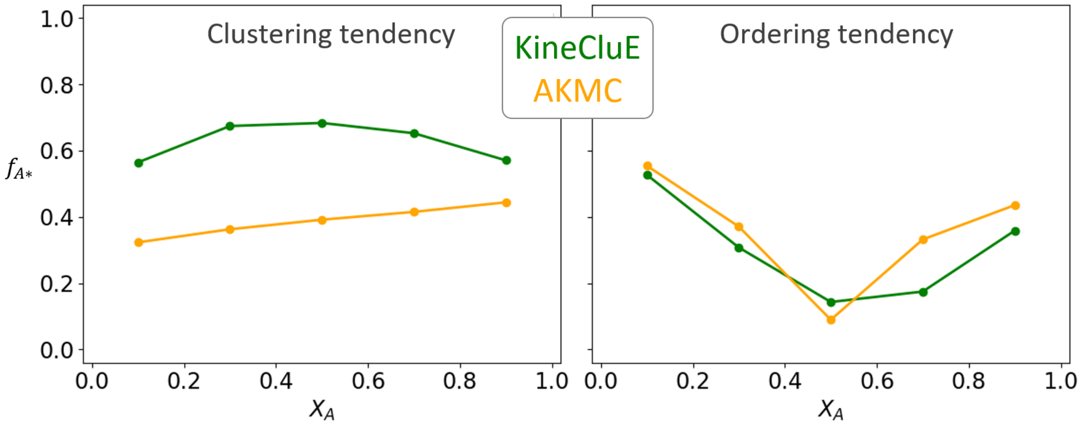

Figure 3.39: Facteur de corrélation f_{A^*} en fonction de la composition dans le cas d'un alliage binaire avec une structure 2D-carrée et un ordre à longue distance (énergie d'ordre normalisée égale à 1.96).

3.3 Conclusions et perspectives

Nous avons appliqué notre modèle au cas d'un alliage avec et sans interactions, et nous avons comparé les facteurs de corrélation du traceur calculés par KineCluE aux résultats de la littérature et à nos propres simulations de Monte Carlo. Dans le cas d'un alliage aléatoire (sans interactions), KineCluE reproduit les facteurs de corrélation de traceurs en accord avec la littérature lorsque les rapports de fréquence de saut sont faibles. KineCluE ne reproduit pas la courbe de percolation à des rapports de fréquence de saut élevés avec les rayons d'environnement relativement petits que nous avons été en mesure de tester. Dans le cas d'un alliage où les interactions thermodynamiques sont non-négligeables, les facteurs de corrélation de traceur calculés par KineCluE sont en bon accord avec les résultats des simulations de Monte Carlo, dans les deux cas d'énergies d'ordre positives et négatives, avec des valeurs normalisées comprises entre -0.5 et $+0.5$. Un rayon d'environnement plus grand est nécessaire pour reproduire des cas particuliers de systèmes hautement ordonnés et de décomposition spinodale. Ces résultats ont montré que notre modèle permet le calcul de facteurs de corrélation en bon accord avec d'autres théories, pour une large gamme de fréquences d'échange, d'énergies d'ordre et de concentrations. Ces résultats sont prometteurs car ils ont été obtenus en utilisant des environnements locaux autour des espèces qui diffusent qui sont les plus petits possibles. L'augmentation du rayon de l'environnement a le potentiel d'améliorer considérablement la précision de notre modèle. Il est clair cependant que cela n'est pas faisable sans échantillonner l'espace de configuration. Nous avons encore à optimiser une procédure d'échantillonnage et à mieux comprendre comment et quelles configurations sont échantillonnées à chaque étape. Une fois la procédure d'échantillonnage optimisée, elle nous permettra de tester une plus grande variété de structures cristallines, et de ne pas nous limiter à une structure 2D. De plus, dans le cas d'un alliage binaire, on peut tester l'effet non seulement de l'énergie d'ordre avec des interactions premiers voisins, mais aussi de l'asymétrie énergétique sur les coefficients de transport et des interactions au-delà des premiers plus proches voisins. Cela nous permettra de passer au calcul des coefficients de transport des alliages FeCr par exemple. A terme, nous devrions pouvoir tester notre modèle dans le cas d'alliages multi-composants au-delà de la limite binaire, afin de voir dans quelle mesure le modèle peut prédire les coefficients de transport des alliages à haute entropie.

Bibliography

[1] F. Onimus, T. Jourdan, C. Xu, A. Campbell, and M. Griffiths, "Irradiation creep in materials," 2020. (document)

[2] E. M. e. a. M. Nastar, L.T. Belkacemi, "Thermodynamic model for lattice point defect-mediated semi-coherent precipitation in alloys," *Commun Mater 2*, vol. 32, 2021. (document)

[3] K. Russell, "Phase stability under irradiation," *Progress in Materials Science*, vol. 28, no. 3, pp. 229–434, 1984. (document)

[4] G. S. WAS, *Fundamentals of Radiation Materials Science: Metals and Alloys.* 2016. (document)

[5] M. Nastar and F. Soisson, *1.18 – Radiation-Induced Segregation*, vol. 1, p. 471–496. 12 2012. (document)

[6] A. J. Ardell and P. Bellon, "Radiation-induced solute segregation in metallic alloys," *Current Opinion in Solid State and Materials Science*, vol. 20, no. 3, pp. 115–139, 2016. (document)

[7] T. Schuler, M. Nastar, and F. Soisson, "Towards the modeling of the interplay between radiation induced segregation and sink microstructure," *Journal of Applied Physics*, vol. 132, no. 8, p. 080903, 2022. (document)

[8] E. Martínez, O. Senninger, C.-C. Fu, and F. Soisson, "Decomposition kinetics of fe-cr solid solutions during thermal aging," *Phys. Rev. B*, vol. 86, p. 224109, Dec 2012. (document), 1.1, 1.5.1, 2.1, 3.9.2

[9] O. Senninger, *Ségrégation et précipitation dans les alliges fer-chrome hors et sous irradiation.* 2013. (document), 1.5.2.3, 1.5.3, 1.5.5, 2.1, 2.3.1, 2.3, 2.4, 2.4.2, 2.8, **??**, 2.18, 2.8, 2.33, 2.34, 3.11, 3.11, 3.11, 3.11, 3.35

[10] S. V. Divinski, A. Pokoev, N. Esakkiraja, and A. Paul, "A mystery of "sluggish diffusion" in high-entropy alloys: the truth or a myth?," 2018. (document)

[11] J. Dabrowa and M. Danielewski, "State-of-the-art diffusion studies in the high entropy alloys," *Metals*, vol. 10, no. 3, 2020. (document)

[12] K.-Y. Tsai, M.-H. Tsai, and J.-W. Yeh, "Sluggish diffusion in co–cr–fe–mn–ni high-entropy alloys," *Acta Materialia*, vol. 61, no. 13, pp. 4887–4897, 2013. (document)

[13] L. Onsager, "Reciprocal relations in irreversible processes. i.," *Phys. Rev.*, vol. 37, pp. 405–426, Feb 1931. (document), 1.1, 1.2.1, 3.11

[14] L. Onsager, “Reciprocal relations in irreversible processes. ii.,” *Phys. Rev.*, vol. 38, pp. 2265–2279, Dec 1931. (document), 1.1, 1.2.1, 3.11

[15] M. Nastar, *Une théorie atomique de la diffusion dans les alliages, HDR.* (document)

[16] O. Senninger, F. Soisson, and M. Nastar, “Atomistic simulations of the decomposition kinetics in fe-cr alloys: Influence of magnetism,” *Acta Materialia*, vol. 73, p. 97–106, 07 2014. (document), 1.1, 1.5.1, 1.5.5, 2.1, 2.3.1, 2.3, 2.3.2, 2.5, 2.6, 2.4, 2.4.2, 2.8, **??**, 2.18, 2.8, 2.6.4, 2.33, 2.34, 3.11, 3.11, 3.11, 3.11, 3.35

[17] H. Mehrer, *Diffusion in Solids.* Springer Berlin, Heidelberg, 2007. (document), 1.1, 1.4

[18] T. Schuler, L. Messina, and M. Nastar, “Kineclue: A kinetic cluster expansion code to compute transport coefficients beyond the dilute limit,” *Computational Materials Science*, vol. 172, p. 109191, 2020. (document), 1.1, 1.7.4, 1.8, 3.1, 3.2, 3.2.1, 3.2.5, 3.5, 3.8.2.1, 3.10, 3.11

[19] J. R. Manning, “Correlation factors for diffusion in nondilute alloys,” *Phys. Rev. B*, vol. 4, pp. 1111–1121, Aug 1971. (document), 1.1, 1.6.4, 1.7, 1.7.1, 1.7.1, 3.9.1, 3.28, 3.29, 3.11, 3.11, 3.37

[20] J. R. Manning, “Correlation effects and activation energies for diffusion in alloys,” *Zeitschrift für Naturforschung A*, vol. 26, no. 1, pp. 69–76, 1971. (document), 1.1, 1.7, 1.7.1, 3.9.1, 3.28, 3.29, 3.11, 3.11, 3.37

[21] R. Kikuchi, “The path probability method,” *Progress of Theoretical Physics Supplement*, vol. 35, 01 1966. (document), 1.1, 1.6.4, 1.7, 1.7.3, 1.7.3, 3.11, 3.11

[22] M. Nastar, V. Dobretsov, and G. Martin, “Self-consistent formulation of configurational kinetics close to equilibrium: The phenomenological coefficients for diffusion in crystalline solids,” *Philosophical Magazine A-physics of Condensed Matter Structure Defects and Mechanical Properties - PHIL MAG A*, vol. 80, pp. 155–184, 01 2000. (document), 1.1, 1.6.4, 1.7, 1.7.4, 1.7.4, 3.1, 3.11, 3.11

[23] M. Nastar, “Atomic diffusion theory challenging the cahn-hilliard method,” *Phys. Rev. B*, vol. 90, p. 144101, Oct 2014. (document), 1.7.4

[24] A. Debelle, A. Michel, M. Loyer-Prost, T. Rieger, A. Billard, and M. Nastar, “Determination of the interdiffusion coefficient at low temperature in ni/nicr nanometer-scale multilayers using x-ray reflectivity,” *Materialia*, vol. 25, p. 101528, 2022. (document)

[25] A. Guinier, *X-ray diffraction in crystals, imperfect crystals, and amorphous bodies.* San Francisco, W.H. Freeman, 1963. (document), 2.2, 2.2.2, 3.11

[26] M.-C. Benoudia, *Interdiffusion et déformations dans des multicouches Cu/Ni et Mo/V: Diffraction des rayons X et simulation de la cinétique.* 2009. (document), 2.2.2, 2.2.3, 2.2.3, 3.11

[27] J. B. J. Fourier, “Théorie de la propagation de la chaleur,” 1807. 1.1

[28] D. A. Fick, “V. on liquid diffusion,” *The London, Edinburgh, and Dublin Philosophical Magazine and Journal of Science*, vol. 10, no. 63, pp. 30–39, 1855. 1.1, 1.2.2.1, 3.11

[29] Y. Mishin and D. Farkas, “Monte carlo simulation of correlation effects in a random bcc alloy,” *Philosophical Magazine A*, vol. 75, no. 1, pp. 201–219, 1997. 1.1, 1.5.1, 1.5.5, 1.7, 1.7.1, 3.9.1, 3.28, 3.37

[30] G. E. Murch and S. J. Rothman, “Diffusion, correlation, and percolation in a random alloy,” *Philosophical Magazine A*, vol. 43, no. 1, pp. 229–238, 1981. 1.1, 1.5.1, 1.5.5, 1.7, 1.7.1

[31] I. V. Belova and G. E. Murch, “Collective diffusion in the binary random alloy,” *Philosophical Magazine A*, vol. 80, no. 3, pp. 599–607, 2000. 1.1, 1.5.1, 1.5.5, 1.7, 1.7.1

[32] I. V. Belova and G. E. Murch, “Tracer correlation factors in the random alloy,” *Philosophical Magazine A*, vol. 80, no. 7, pp. 1469–1479, 2000. 1.1, 1.5.1, 1.5.5, 1.7, 1.7.1

[33] I. V. Belova, A. R. Allnatt, and G. E. Murch, “Collective and tracer diffusion kinetics in the ternary random alloy,” *Journal of Physics: Condensed Matter*, vol. 14, pp. 6897–6907, jul 2002. 1.1, 1.5.1, 1.5.1, 1.7.1

[34] F. Soisson and C.-C. Fu, “Atomistic simulations of copper precipitation and radiation induced segregation in -iron,” *Solid State Phenomena*, vol. 139, pp. 107–112, 04 2008. 1.1, 1.5.1

[35] O. Senninger, F. Soisson, E. Martínez, M. Nastar, C.-C. Fu, and Y. Bréchet, “Modeling radiation induced segregation in iron–chromium alloys,” *Acta Materialia*, vol. 103, pp. 1–11, 2016. 1.1, 1.5.1, 1.5.5, 2.1

[36] T. R. Paul, I. V. Belova, and G. E. Murch, “Random alloy diffusion kinetics for the application to multicomponent alloy systems,” *Philosophical Magazine*, vol. 96, no. 12, pp. 1228–1244, 2016. 1.1, 1.5.1, 1.5.1, 1.7.2

[37] K. Ferasat, Y. N. Osetsky, A. V. Barashev, Y. Zhang, Z. Yao, and L. K. Béland, “Accelerated kinetic monte carlo: A case study; vacancy and dumbbell interstitial diffusion traps in concentrated solid solution alloys,” *The Journal of Chemical Physics*, vol. 153, no. 7, p. 074109, 2020. 1.1, 1.5.1

[38] A. Lidiard, “Cxxxiii. impurity diffusion in crystals (mainly ionic crystals with the sodium chloride structure),” *The London, Edinburgh, and Dublin Philosophical Magazine and Journal of Science*, vol. 46, no. 382, pp. 1218–1237, 1955. 1.1, 1.6.3.2, 1.6.3.2, 3.11

[39] A. D. Leclaire and A. B. Lidiard, “Liii. correlation effects in diffusion in crystals,” *The Philosophical Magazine: A Journal of Theoretical Experimental and Applied Physics*, vol. 1, no. 6, pp. 518–527, 1956. 1.1, 1.6.3.2, 1.6.3.2, 3.11

[40] A. B. Lidiard, “The influence of solutes on self-diffusion in metals,” *The Philosophical Magazine: A Journal of Theoretical Experimental and Applied Physics*, vol. 5, no. 59, pp. 1171–1180, 1960. 1.1, 1.6.3.2, 1.6.3.2, 3.11

[41] A. Le Claire, "Solute diffusion in dilute alloys," *Journal of Nuclear Materials*, vol. 69-70, pp. 70–96, 1978. 1.1, 1.6.3.2, 1.10, 1.6.3.2, 3.11

[42] D. R. Trinkle, "Automatic numerical evaluation of vacancy-mediated transport for arbitrary crystals: Onsager coefficients in the dilute limit using a green function approach," *Philosophical Magazine*, vol. 97, no. 28, pp. 2514–2563, 2017. 1.1, 3.11

[43] P. C. W. Holdsworth and R. J. Elliott, "Correlated random walk in a multicomponent alloy self-consistent decoupling approximation," *Philosophical Magazine A*, vol. 54, no. 5, pp. 601–618, 1986. 1.1, 1.7, 1.7.2

[44] L. K. Moleko, A. R. Allnatt, and E. L. Allnatt, "A self-consistent theory of matter transport in a random lattice gas and some simulation results," *Philosophical Magazine A*, vol. 59, no. 1, pp. 141–160, 1989. 1.1, 1.7, 1.7.2

[45] A. R. Allnatt, T. R. Paul, I. V. Belova, and G. E. Murch, "A high accuracy diffusion kinetics formalism for random multicomponent alloys: application to high entropy alloys," *Philosophical Magazine*, vol. 96, no. 28, pp. 2969–2985, 2016. 1.1, 1.7.2

[46] R. Kikuchi and H. Sato, "Correlation factor in substitutional diffusion in binary alloys," *The Journal of Chemical Physics*, vol. 53, no. 7, pp. 2702–2713, 1970. 1.1, 1.7, 1.7.3, 3.9.1, 3.28, 3.37

[47] H. Sato and R. Kikuchi, "Theory of many-body diffusion by the path-probability method: Conversion from ensemble averaging to time averaging," *Phys. Rev. B*, vol. 28, pp. 648–664, Jul 1983. 1.1, 1.7, 1.7.3, 3.9.1

[48] M. Nastar, "A mean field theory for diffusion in a dilute multi-component alloy: a new model for the effect of solutes on self-diffusion," *Philosophical Magazine*, vol. 85, no. 32, pp. 3767–3794, 2005. 1.1, 1.7, 1.7.4, 1.7.4

[49] V. Barbe and M. Nastar, "A self-consistent mean field calculation of the phenomenological coefficients in a multicomponent alloy with high jump frequency ratios," *Philosophical Magazine*, vol. 86, no. 11, pp. 1513–1538, 2006. 1.1, 1.7, 1.7.4, 1.7.4

[50] M. Nastar and V. Barbe, "A self-consistent mean field theory for diffusion in alloys," *Faraday Discuss.*, vol. 134, pp. 331–342, 2007. 1.1, 1.7.4, 1.7.4

[51] R. Kubo, "The fluctuation-dissipation theorem," *Reports on Progress in Physics*, vol. 29, pp. 255–284, jan 1966. 1.2.1

[52] L. Huang, T. Schuler, and M. Nastar, "Atomic scale modeling of the effect of forced atomic reactions on the thermodynamic and kinetic properties of dilute alloys under irradiation," 07 2019. 1.2.1

[53] M. G. Grandjean Y, Bellon P, "Kinetic model for equilibrium and nonequilibrium segregation in concentrated alloys under irradiation," *Phys Rev B Condens Matter.*, vol. 50, pp. 4228–4231, 08 1997. 1.2.2.1

[54] Z. Erdélyi, G. L. Katona, and D. L. Beke, "Nonparabolic nanoscale shift of phase boundaries in binary systems with restricted solubility," *Phys. Rev. B*, vol. 69, p. 113407, Mar 2004. 1.2.2.1

[55] Z. Balogh, Z. Erdélyi, D. L. Beke, G. A. Langer, A. Csik, H.-G. Boyen, U. Wiedwald, P. Ziemann, A. Portavoce, and C. Girardeaux, "Transition from anomalous kinetics toward fickian diffusion for si dissolution into amorphous ge," *Applied Physics Letters*, vol. 92, no. 14, p. 143104, 2008. 1.2.2.1, 1.3.2, 2.1

[56] L. Boltzmann, "Zur integration der diffusionsgleichung bei variabeln diffusionscoefficienten," *Annalen der Physik*, vol. 289, no. 13, pp. 959–964, 1894. 1.2.2.3, 1.3.2

[57] C. Matano, "On the relation between diffusion-coefficients and concentrations of solid metals," *Japanese Journal of Physics*, vol. 8, pp. 109–113, 1942. 1.2.2.3, 1.3.2, 2.1

[58] F. Sauer and V. Freise, "Diffusion in binären gemischen mit volumenänderung," *Zeitschrift für Elektrochemie, Berichte der Bunsengesellschaft für physikalische Chemie*, vol. 66, no. 4, pp. 353–362, 1962. 1.2.2.3, 1.3.2

[59] F. den Broeder, "A general simplification and improvement of the matano-boltzmann method in the determination of the interdiffusion coefficients in binary systems," *Scripta Metallurgica*, vol. 3, no. 5, pp. 321–325, 1969. 1.2.2.3, 1.3.2

[60] G. C. M. Tchinda, *Study of epitaxial Femultilayers : structural and magnetic properties, interdiffusion mechanisms.* 2020. 1.3.2, 1.3.2, 1.3.5, 3.11, 3.11

[61] E. Kirkendall, "Reciprocal relations in irreversible processes. ii.," *Trans. AIME*, vol. 147, 1942. 1.3.2, 2.7.6

[62] E. K. A.D. Smigelskas, "Reciprocal relations in irreversible processes. ii.," *Trans. AIME*, vol. 171, 1947. 1.3.2, 2.7.6

[63] L. Darken, "Reciprocal relations in irreversible processes. ii.," *Trans. AIME*, vol. 175, 1948. 1.3.2, 2.7.6

[64] P. Maugis and G. Martin, "Interface transfer coefficient in second-phase-growth models," *Phys. Rev. B*, vol. 49, pp. 11580–11587, May 1994. 1.3.2, 2.1, 3.11

[65] S. G. Kim, W. T. Kim, and T. Suzuki, "Phase-field model for binary alloys," *Phys. Rev. E*, vol. 60, pp. 7186–7197, Dec 1999. 1.3.2, 2.1, 3.11

[66] D. Beke, Z. Erdelyi, Z. Balogh-Michels, C. Cserhati, and G. Katona, "Non parabolic shift of interfaces and effect of diffusion asymmetry on nanoscale solid state reactions," *Journal of Nano Research - J NANO RES*, vol. 7, pp. 43–49, 07 2009. 1.3.2, 2.1

[67] J. Langer, *Fluctuations, Instabilities, and Phase Transformations.* 1975. 1.3.2, 2.1, 2.5, 3.11

[68] T. R. Anthony, "Ratio of vacancy jump frequencies around and away from copper impurity atoms in aluminum," *Phys. Rev. B*, vol. 2, pp. 264–270, Jul 1970. 1.3.4

[69] T. R. Anthony, "Segregation of zinc to vacancy sinks in aluminum," *Journal of Applied Physics*, vol. 41, no. 10, pp. 3969–3976, 1970. 1.3.4

[70] E. Roduner, "Size matters: why nanomaterials are different," *Chem. Soc. Rev.*, vol. 35, pp. 583–592, 2006. 1.3.5

[71] M. Lübbehusen and H. Mehrer, "Self-diffusion in -iron: The influence of dislocations and the effect of the magnetic phase transition," *Acta Metallurgica et Materialia*, vol. 38, no. 2, pp. 283–292, 1990. 1.4

[72] Y. Iijima, K. Kimura, and K. Hirano, "Self-diffusion and isotope effect in -iron," *Acta Metallurgica*, vol. 36, no. 10, pp. 2811–2820, 1988. 1.4

[73] F. Buffington, K. Hirano, and M. Cohen, "Self diffusion in iron," *Acta Metallurgica*, vol. 9, no. 5, pp. 434–439, 1961. 1.4

[74] C. M. WALTER and N. L. PETERSON, "Isotope effect in self-diffusion in iron," *Phys. Rev.*, vol. 178, pp. 922–929, Feb 1969. 1.4

[75] H. Eyring, "The activated complex in chemical reactions," *The Journal of Chemical Physics*, vol. 3, no. 2, pp. 107–115, 1935. 1.5.1, 1.6.3.2

[76] N. Metropolis, A. W. Rosenbluth, M. N. Rosenbluth, A. H. Teller, and E. Teller, "Equation of state calculations by fast computing machines," *The Journal of Chemical Physics*, vol. 21, no. 6, pp. 1087–1092, 1953. 1.5.1, 1.5.2.1

[77] A. Bortz, M. Kalos, and J. Lebowitz, "A new algorithm for monte carlo simulation of ising spin systems," *Journal of Computational Physics*, vol. 17, no. 1, pp. 10–18, 1975. 1.5.1, 1.5.2.2, 2.4.2.1

[78] M. Nastar and F. Soisson, "Atomistic modeling of phase transformations: Point-defect concentrations and the time-scale problem," *Physical Review B*, vol. 86, p. 220102, 12 2012. 1.5.3, 2.4.2.1

[79] A. Einstein, "Über die von der molekularkinetischen theorie der wärme geforderte bewegung von in ruhenden flüssigkeiten suspendierten teilchen," *Annalen der Physik*, vol. 322, no. 8, pp. 549–560, 1905. 1.5.4.1, 3.11

[80] M. von Smoluchowski, "Zur kinetischen theorie der brownschen molekularbewegung und der suspensionen," *Annalen der Physik*, vol. 326, no. 14, pp. 756–780, 1906. 1.5.4.1

[81] A. R. Allnatt, "Einstein and linear response formulae for the phenomenological coefficients for isothermal matter transport in solids," *Journal of Physics C: Solid State Physics*, vol. 15, pp. 5605–5613, sep 1982. 1.5.4.2, 3.11

[82] M. A. Novotny, "Monte carlo algorithms with absorbing markov chains: Fast local algorithms for slow dynamics," *Phys. Rev. Lett.*, vol. 74, pp. 1–5, Jan 1995. 1.5.5

[83] M. Athènes, P. Bellon, and G. Martin, "Identification of novel diffusion cycles in b2 ordered phases by monte carlo simulation," *Philosophical Magazine A*, vol. 76, p. 565, 1997. 1.5.5

[84] A. Chatterjee and A. F. Voter, “Accurate acceleration of kinetic monte carlo simulations through the modification of rate constants,” *The Journal of Chemical Physics*, vol. 132, no. 19, p. 194101, 2010. 1.5.5

[85] B. Puchala, M. Falk, and K. Garikipati, “An energy basin finding algorithm for kinetic monte carlo acceleration,” *The Journal of Chemical Physics*, vol. 132, p. 134104, 2010. 1.5.5

[86] M. Athènes and V. Bulatov, “Path factorization approach to stochastic simulations,” *Physical Review Letters*, vol. 113, 2014. 1.5.5

[87] C. Daniels and P. Bellon, “Hybrid kinetic monte carlo algorithm for strongly trapping alloy systems,” *Computational Materials Science*, vol. 173, p. 109386, Feb. 2020. 1.5.5

[88] K. Ferasat, Y. N. Osetsky, A. V. Barashev, Y. Zhang, Z. Yao, and L. K. Béland, “Accelerated kinetic monte carlo: A case study; vacancy and dumbbell interstitial diffusion traps in concentrated solid solution alloys,” *The Journal of Chemical Physics*, vol. 153, p. 074109, Aug. 2020. 1.5.5

[89] L. K. Béland, P. Brommer, F. El-Mellouhi, J.-F. m. c. Joly, and N. Mousseau, “Kinetic activation-relaxation technique,” *Phys. Rev. E*, vol. 84, p. 046704, Oct 2011. 1.5.5

[90] J. R. Manning, “Correlation effects in impurity diffusion,” *Phys. Rev.*, vol. 116, pp. 819–827, Nov 1959. 1.6.3.2, 1.6.3.2

[91] J. R. Manning, “Correlation factors for impurity diffusion. bcc, diamond, and fcc structures,” *Phys. Rev.*, vol. 136, pp. A1758–A1766, Dec 1964. 1.6.3.2

[92] T. Schuler, P. Bellon, D. Trinkle, and R. Averback, “Modeling the long-term evolution of dilute solid solutions in the presence of vacancy fluxes,” *Physical Review Materials*, vol. 2, 07 2018. 1.6.3.2

[93] C. Varvenne, A. Luque, W. G. Nöhring, and W. A. Curtin, “Average-atom interatomic potential for random alloys,” *Phys. Rev. B*, vol. 93, p. 104201, Mar 2016. 1.6.4

[94] R. Kikuchi and H. Sato, “Substitutional diffusion in an ordered system,” *The Journal of Chemical Physics*, vol. 51, no. 1, pp. 161–181, 1969. 1.7, 1.7.3

[95] J. K. McCoy, R. Kikuchi, K. Gschwend, and H. Sato, “Extension of the path-probability method beyond the pair approximation. triangle approximation,” *Phys. Rev. B*, vol. 25, pp. 1734–1748, Feb 1982. 1.7, 1.7.3

[96] V. Y. D. V. G. Vaks, S. V. Beiden, “Mean-field equations for configurational kinetics of alloys at arbitrary degree of nonequilibrium,” *Jetp Lett.*, vol. 61, 01 1995. 1.7

[97] V. G. Vaks, “Master equation approach to the configurational kinetics of nonequilibrium alloys: Exact relations, h-theorem, and cluster approximations,” *Jetp Lett.*, vol. 63, pp. 471–477, 03 1996. 1.7, 1.7.4, 1.7.4

[98] M. Nastar and E. Clouet, “Mean field theories for the description of diffusion and phase transformations controlled by diffusion,” *Phys. Chem. Chem. Phys.*, vol. 6, pp. 3611–3619, 2004. 1.7, 1.7.4, 1.7.4

[99] M. Nastar and V. Barbe, “From the atomic jump frequencies to the phenomenological transport coefficients,” *Advanced Engineering Materials*, vol. 8, no. 12, pp. 1239–1243, 2006. 1.7, 1.7.4, 1.7.4

[100] K. Compaan and Y. Haven, “Correlation factors for diffusion in solids. part 2.—indirect interstitial mechanism,” *Trans. Faraday Soc.*, vol. 54, pp. 1498–1508, 1958. 1.7.1

[101] I. V. Belova and G. E. Murch, “The manning relations for atomic diffusion in a binary ordered alloy,” *Philosophical Magazine A*, vol. 75, no. 6, pp. 1715–1723, 1997. 1.7.2

[102] J. Bocquet, “Diffusion of dumb-bell interstitials in concentrated random alloys: An effective field approximation,” *Acta Metallurgica*, vol. 34, no. 4, pp. 571–597, 1986. 1.7.2, 1.7.5

[103] L. K. Moleko and A. R. Allnatt, “Atomic transport in a random alloy at arbitrary vacancy concentration,” *Philosophical Magazine A*, vol. 57, no. 1, pp. 115–125, 1988. 1.7.2

[104] R. Kikuchi, “A theory of cooperative phenomena,” *Phys. Rev.*, vol. 81, pp. 988–1003, Mar 1951. 1.7.3, 3.7.1, 3.7.4.2

[105] H. Sato, “Path probability method of irreversible statistical mechanics,” *Materials Transactions, JIM*, vol. 32, no. 6, pp. 509–525, 1991. 1.7.3

[106] S. A. Akbar, “The path probability method: An atomistic technique of diffusion,” *Journal of Materials Science*, vol. 27, p. 3125–3132, 06 1992. 1.7.3

[107] H. Sato and R. Kikuchi, “Kinetics of order-disorder transformations in alloys,” *Acta Metallurgica*, vol. 24, no. 9, pp. 797–809, 1976. 1.7.3

[108] K. Gschwend, H. Sato, and R. Kikuchi, “Kinetics of order–disorder transformations in alloys. ii,” *The Journal of Chemical Physics*, vol. 69, no. 11, pp. 5006–5019, 1978. 1.7.3

[109] K. Gschwend, H. Sato, R. Kikuchi, H. Iwasaki, and H. Maniwa, “Kinetics of order–disorder transformations in alloys. iii,” *The Journal of Chemical Physics*, vol. 71, no. 7, pp. 2844–2852, 1979. 1.7.3

[110] K. Wada, T. Ishikawa, H. Sato, and R. Kikuchi, “Time evolution of fluctuations in the path-probability method. ii,” *Phys. Rev. A*, vol. 33, pp. 4171–4178, Jun 1986. 1.7.3

[111] V. Barbe and M. Nastar, “Phenomenological coefficients in a concentrated alloy for the dumbbell mechanism,” *Philosophical Magazine*, vol. 86, no. 23, pp. 3503–3535, 2006. 1.7.4, 1.7.4

[112] V. Barbe and M. Nastar, “Split interstitials in an interacting bcc alloy. ii. transport coefficients,” *Phys. Rev. B*, vol. 76, p. 054206, Aug 2007. 1.7.4, 1.7.4

[113] M. Nastar, "Diffusion and coupled fluxes in concentrated alloys under irradiation: a self-consistent mean-field approach," *Comptes Rendus Physique*, vol. 9, no. 3, pp. 362–369, 2008. Materials subjected to fast neutron irradiation. 1.7.4, 1.7.4

[114] T. Garnier, M. Nastar, P. Bellon, and D. R. Trinkle, "Solute drag by vacancies in body-centered cubic alloys," *Phys. Rev. B*, vol. 88, p. 134201, Oct 2013. 1.7.4, 1.7.4

[115] J. Sanchez, F. Ducastelle, and D. Gratias, "Generalized cluster description of multicomponent systems," *Physica A: Statistical Mechanics and its Applications*, vol. 128, no. 1, pp. 334–350, 1984. 1.7.4, 3.2.1

[116] L. L. Chang and B. C. Giessen, *Synthetic modulated structures.* Academic Press, 1985. 2.2

[117] J. DuMond and J. P. Youtz, "An x-ray method of determining rates of diffusion in the solid state," *Journal of Applied Physics*, vol. 11, no. 5, pp. 357–365, 1940. 2.2

[118] R. M. Fleming, D. B. McWhan, A. C. Gossard, W. Wiegmann, and R. A. Logan, "X-ray diffraction study of interdiffusion and growth in (gaas)n(alas)m multilayers," *Journal of Applied Physics*, vol. 51, no. 1, pp. 357–363, 1980. 2.2, 2.2.3

[119] J. Chaudhuri, S. Alyan, and A. Jankowski, "X-ray characterization of au/ni multilayer thin films," *Thin Solid Films*, vol. 219, no. 1, pp. 63–68, 1992. 2.2, 2.2.3

[120] J. Chaudhuri, S. Alyan, and A. Jankowski, "Analysis of ni/ti multilayers by x-ray diffraction," *Thin Solid Films*, vol. 239, no. 1, pp. 79–84, 1994. 2.2, 2.2.3

[121] T. Tsakalakos, "Spinodal decomposition in cuni alloys by artificial composition modulation technique," *Scripta Metallurgica*, vol. 15, pp. 255–258, 1981. 2.2

[122] T. Tsakalakos, "Composition-modulated films: New materials for studying stability and critical phenomena in solid solutions," *Thin Solid Films*, vol. 86, no. 1, pp. 79–90, 1981. 2.2

[123] T. Tsakalakos and J. E. Hilliard, "Effect of long-range interaction on diffusion in copper-nickel composition-modulated alloys," *Journal of Applied Physics*, vol. 55, no. 8, pp. 2885–2894, 1984. 2.2

[124] D. Aubertine, N. Ozguven, P. McIntyre, and S. Brennan, "Analysis of x-ray diffraction as a probe of interdiffusion in si/sige heterostructures," *Journal of Applied Physics*, vol. 94, pp. 1557–1564, 08 2003. 2.2

[125] T. Tsakalakos, "Nonlinear diffusion," *Scripta Metallurgica*, vol. 20, no. 4, pp. 471–478, 1986. 2.2, 2.2.4.2

[126] N. I. C. JB., *Residual Stress : Measurement by Diffraction and Interpretation.* New York: Springer-Verlag, 1987. 2.2.1, 2.7.4.2

[127] M. Glicksman, *Diffusion in Solids: Field Theory, SolidState Principles, and Applications.* Wiley, 1999. 2.2.4.1

[128] P. Grünberg, R. Schreiber, Y. Pang, M. B. Brodsky, and H. Sowers, "Layered magnetic structures: Evidence for antiferromagnetic coupling of fe layers across cr interlayers," *Phys. Rev. Lett.*, vol. 57, pp. 2442–2445, Nov 1986. 2.3

[129] M. N. Baibich, J. M. Broto, A. Fert, F. N. Van Dau, F. Petroff, P. Etienne, G. Creuzet, A. Friederich, and J. Chazelas, "Giant magnetoresistance of (001)fe/(001)cr magnetic superlattices," *Phys. Rev. Lett.*, vol. 61, pp. 2472–2475, Nov 1988. 2.3

[130] "A model for 1d multiphase moving phase boundary simulations under local equilibrium conditions, volume=47, journal=Calphad, author=Larsson, H., year=2014, pages=1-8," 2.3.1, 3.11

[131] G. Bonny, D. Terentyev, and L. Malerba, "New contribution to the thermodynamics of fe-cr alloys as base for ferritic steels," *Journal of Phase Equilibria and Diffusion*, vol. 31, pp. 439–444, 10 2010. 2.3.1

[132] W. Xiong, P. Hedström, M. Selleby, J. Odqvist, M. Thuvander, and Q. Chen, "An improved thermodynamic modeling of the fe–cr system down to zero kelvin coupled with key experiments," *Calphad*, vol. 35, no. 3, pp. 355–366, 2011. 2.3.1

[133] G. Bonny, D. Terentyev, and L. Malerba, "On the α–α' miscibility gap of fe–cr alloys," *Scripta Materialia*, vol. 59, pp. 1193–1196, 12 2008. 2.3

[134] W. Xiong, M. Selleby, Q. Chen, J. Odqvist, and Y. Du, "Phase equilibria and thermodynamic properties in the fe-cr system," *Critical Reviews in Solid State and Materials Sciences*, vol. 35, no. 2, pp. 125–152, 2010. 2.3

[135] G. Bonny, D. Terentyev, L. Malerba, and D. Van Neck, "Early stages of $\alpha-\alpha^{'}$ phase separation in fe-cr alloys: An atomistic study," *Phys. Rev. B*, vol. 79, p. 104207, Mar 2009. 2.5

[136] F. Vurpillot, D. Larson, and A. Cerezo, "Improvement of multilayer analyses with a three-dimensional atom probe," *Surface and Interface Analysis*, vol. 36, no. 5-6, pp. 552–558, 2004. 2.4.1.3

[137] M. Levesque, E. Martínez, C.-C. Fu, M. Nastar, and F. Soisson, "Simple concentration-dependent pair interaction model for large-scale simulations of fe-cr alloys," *Phys. Rev. B*, vol. 84, p. 184205, Nov 2011. 2.4.2.1

[138] V. Pierron-Bohnes, "Private communication," 2.4.2.2, **??**, 2.28, 3.11, 3.11

[139] D. T. Cromer and J. B. Mann, "X-ray scattering factors computed from numerical hartree–fock wave functions," *Acta Crystallographica Section A*, vol. 24, pp. 321–324, 1968. 2.4.2.2, 2.4.2.2, 2.2, **??**, 3.11

[140] D. Ariosa, O. Fischer, M. G. Karkut, and J.-M. Triscone, "Elastic model for the partially coherent growth of metallic superlattices. i. interdiffusion, strain, and misfit dislocations," *Phys. Rev. B*, vol. 37, pp. 2415–2420, Feb 1988. 2.4.2.2, 2.7.4.2, 2.9, 3.11

[141] E. M. Philofsky and J. E. Hilliard, "Effect of coherency strains on diffusion in copper-palladium alloys," *Journal of Applied Physics*, vol. 40, no. 5, pp. 2198–2205, 1969. 2.4.2.2, 3.11

[142] A. Stukowski, "Visualization and analysis of atomistic simulation data with OVITO-the Open Visualization Tool," *MODELLING AND SIMULATION IN MATERIALS SCIENCE AND ENGINEERING*, vol. 18, JAN 2010. 2.6.2, 3.31

[143] R. Kikuchi and H. Sato, "Correlation factor in substitutional diffusion in binary alloys," *The Journal of Chemical Physics*, vol. 53, no. 7, pp. 2702–2713, 1970. 3.1

[144] T. Schuler, F. Christien, P. Ganster, and K. Wolski, "Ab initio investigation of phosphorus and hydrogen co-segregation and embrittlement in -fe twin boundaries," *Applied Surface Science*, vol. 492, pp. 919–935, 2019. 3.2.1, 3.7.1

[145] "Note sur une méthode de résolution des équations normales provenant de l'application de la méthode des moindres carrés a un système d'équations linéaires en nombre inférieur a celui des inconnues. — application de la méthode a la résolution d'un système defini d'équations linéaires," *Bulletin géodésique*, vol. 2, pp. 67–77, 1924. 3.5

[146] B. Widom, "Some topics in the theory of fluids," *The Journal of Chemical Physics*, vol. 39, no. 11, pp. 2808–2812, 1963. 3.7.1, 3.11

[147] A. Van der Ven and G. Ceder, "First principles calculation of the interdiffusion coefficient in binary alloys," *Phys. Rev. Lett.*, vol. 94, p. 045901, Feb 2005. 3.9.2

[148] J. W. Cahn, "On spinodal decomposition," *Acta Metallurgica*, vol. 9, no. 9, pp. 795–801, 1961. 3.11

[149] E. M. M. Valet, "Private communication," 3.11